JOURNAL OF APPLIED PHYSICS

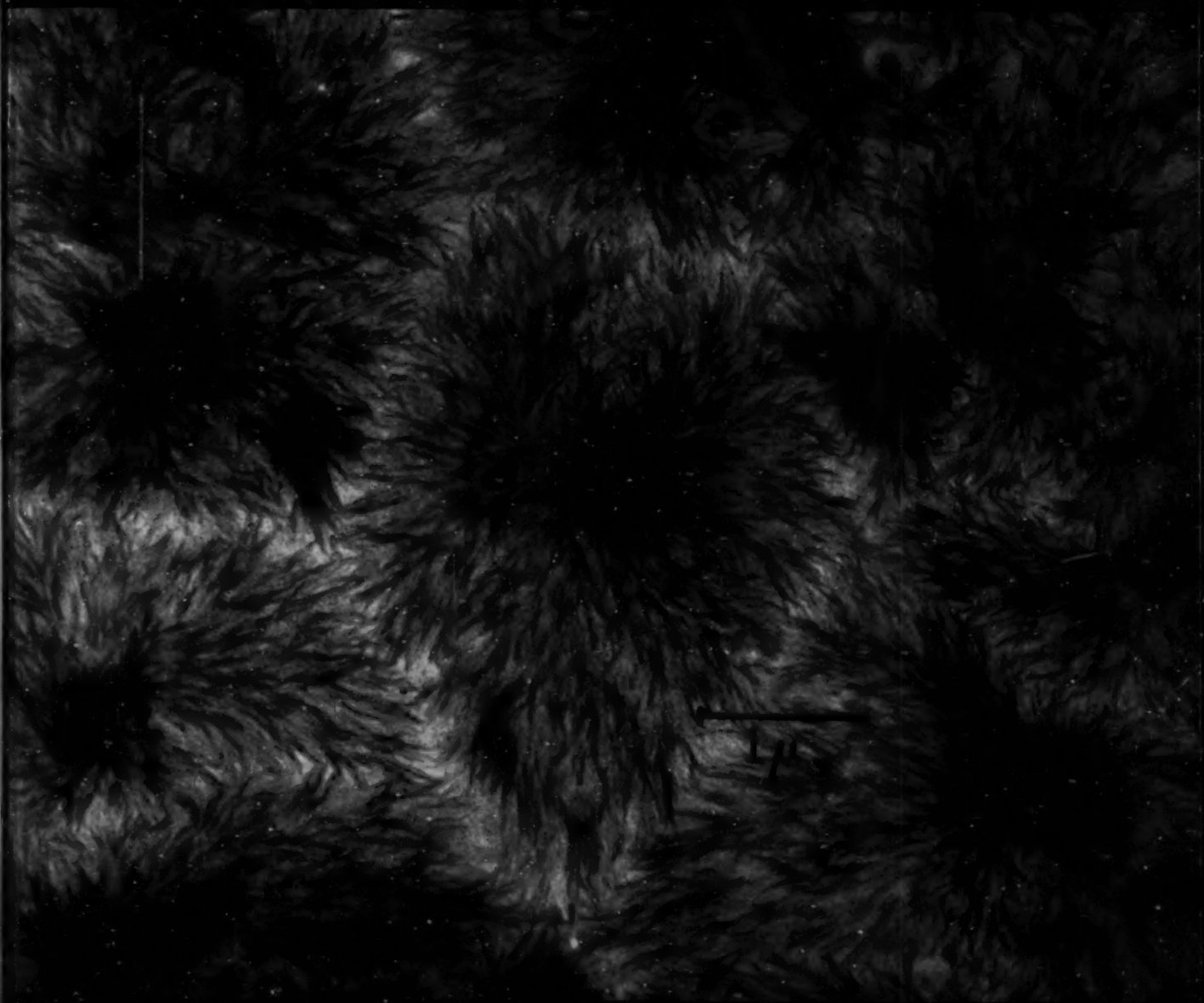

JOURNAL OF APPLIED PHYSICS

Vol. 20, No. 6 JUNE, 1949

In This Issue

Special Issue on High Polymers

Page

Propagation of Audiofrequency Sound in High Polymers R. S. Witte, B. A. Mrowca, and E. Guth 481
Propagation of Ultrasonic Bulk Waves in High Polymers Donald G. Ivey, B. A. Mrowca, and E. Guth 486
Dynamic Measurements of Polymer Physical Properties J. W. Ballou and J. C. Smith 493
Equation of State for Polystyrene R. S. Spencer and G. D. Gilmore 502
Creep and Damping Properties of Polystyrene J. A. Sauer, J. Marin, and C. C. Hsiao 507
Scattering by an Inhomogeneous Solid P. Debye and A. M. Bueche 518
Relationship between Gough-Joule Coefficients and Moduli of Vulcanized Rubbers F. S. Conant, G. L. Hall, and G. R. Thurman 526
Polymerization in the Solid State E. Miller, I. Fankuchen, and H. Mark 531
Time and Stress Effects in the Behavior of Rubber at Low Temperature J. R. Beatty and J. M. Davies 533
Compatibility, Efficiency and Permanence of Plasticizers Raymond F. Boyer 540
X-Ray Diffraction Studies of the Stretching and Relaxing of Polyethylene Alexander Brown 552
Infra-Red Absorption Spectra of Some Polymers at Liquid-Helium Temperatures Gilbert W. King, R. M. Hainer, and H. O. McMahon 559
Dilatometric Studies of High Polymers. I. Second-Order Transition Temperature Harry J. Kolb and Emmette F. Izard 564
Dilatometric Studies of High Polymers. II. Crystallization of Aromatic Polyesters Harry J. Kolb and Emmette F. Izard 571

Regular Contributed Original Research

Notes on the Excitation of Electromagnetic Waves in Cylindrical Metallic Wave Guides A. Colino 576
Use of a Mechanical Harmonic Synthesizer in Electric Wave Filter Analysis S. Leroy Brown and James M. Sharp 578
Barkhausen Noise and Magnetic Amplifiers. II. Analysis of the Noise J. A. Krumhansl and R. T. Beyer 582
Elasticity of Zinc Crystals C. A. Wert and E. P. T. Tyndall 587
Electric-Field Modulation of Ultrasonic Signals in Liquids A. W. Nolle 589
Inter-Particle Interference Effects in the Small Angle X-Ray Scattering from Fine Powders Louis H. Lund and George H. Vineyard 593
Synthesis of n-Reactance Networks for Desired Transient Response Pierre R. Aigrain and Everard M. Williams 597
Electro-Mechanical Device for Solving Non-Linear Differential Equations Carl A. Ludeke 600
Torsion Balance for Measuring Forces in Low Density Gas Flows I. Estermann and E. D. Kane 608
Resonance Effect in the Synchrotron E. D. Courant 611
On the Design of Networks for Constant Time Delay M. H. Herb, C. W. Horton, and F. B. Jones 616
Apparatus to Depict the Load-Elongation Diagram of Yarn at Five Cycles per Second Francis Breazeale and John Whisnant 621
Transition Temperatures of Methyl Methacrylate Polymers at Ultrasonic Frequencies Thomas F. Protzman 627

Letters to the Editor:

On Blowing Bubbles for Bragg's Dynamic Crystal Model Cyril Stanley Smith 631
Method of Measuring Spherical Aberration of an Electron Microscope Objective Cecil E. Hall 631
Note on the Maximum Height of Reflection of a Radio Wave in a Curved Ionosphere Layer John M. Kelso 632
Tensor Field Equations in a Region of Variable Refractive Index P. D. P. Smith 633
Comments on Biconical Antennas P. D. P. Smith 633
Formation of Recrystallization Nuclei Paul A. Beck 633
Notes on "Wave Guides for Slow Waves" W. Walkinshaw 634
Ground Plane Field of the Wide Angle Conical Dipole P. D. P. Smith 636

Index to Advertisers xxxvi

BOARD OF EDITORS
Elmer Hutchisson, *Editor*

Associate Editors
R. Bowling Barnes
Otto Beeck
W. James Lyons
Philip Morrison
Paul E. Sabine
Raymond J. Seeger
Frederick Seitz
Charles S. Smith
J. R. Townsend

Publication of the
American Institute of Physics

OFFICERS
George R. Harrison, *Chairman*
Wallace Waterfall, *Secretary*
George B. Pegram, *Treasurer*
John T. Tate, *Adviser on Publications*

GOVERNING BOARD
Luis W. Alvarez
J. W. Beams
Wallace R. Brode
E. U. Condon
W. F. Fair, Jr.
Harvey Fletcher
George R. Harrison
W. V. Houston
Paul Kirkpatrick
Paul E. Klopsteg
F. W. Loomis
Philip M. Morse
J. R. Oppenheimer
George B. Pegram
Harold K. Schilling
John T. Tate
Wallace Waterfall
M. W. White
A. G. Worthing

Consultant on Printing
Melvin Loos

ADMINISTRATIVE STAFF
Henry A. Barton, *Director*
Theodore Vorburger, *Business Manager*
Ruth F. Bryans, *Publication Manager*
Betty Hofstadter, *Office Manager*
Eileen B. Neuberger, *Circulation Manager*

The Journal of Applied Physics, published monthly at Prince and Lemon Sts., Lancaster, Pa., is devoted to physics in its role as the science basic to other natural sciences and to the arts and industries. Previous to 1937 this publication was known as Physics. The Journal of Applied Physics publishes editorials, news of physicists, and reviews, as well as technical papers of applied physics. Articles appearing in it are indexed regularly, according to their field, by Physics Abstracts, Chemical Abstracts, Engineering Index, Inc., Industrial Arts Index, etc.

Manuscripts should be submitted to Elmer Hutchisson, Editor, Case Institute of Technology, Cleveland 6, Ohio. The authors' institutions are requested to pay a **publication charge** of $4 per page which, if honored, entitles them to 100 free reprints. Instructions will be sent with galley proofs.

Subscriptions and orders for back numbers should be addressed to Prince and Lemon Streets, Lancaster, Pa. or to the American Institute of Physics, 57 East 55 Street, New York 22, N. Y.

Subscription Price	U.S. and Canada	Elsewhere
To members and associate members of the American Institute of Physics	$7.00	$ 8.00
To all others	9.00	10.00

Back Number Prices

Complete set: Vol. 1, July, 1931–Vol. 19, 1948—$140.00
Yearly back number rate: $10.00
Single copies: $1.00 each.

Changes of address should be sent to the Business Manager, American Institute of Physics; **corrected proofs** should be sent to the Publication Manager, American Institute of Physics.

Advertising rates supplied on request. Orders, advertising copy, and cuts should be sent to the American Institute of Physics.

Entered as second class matter January 22, 1937, at the Post Office at Lancaster, Pennsylvania, under the Act of March 3, 1879.
Accepted for mailing at the special rate of postage provided for in the Act of February 28, 1925, authorized May 2, 1932.

Copyright 1949, by the American Institute of Physics.

Journal
of
Applied Physics

Volume 20, Number 6 June, 1949

Special Issue on High Polymer Physics

The following fourteen papers were presented at the meeting of the Division of High Polymer Physics of the American Physical Society in New York City, January 27–29, 1949.

Propagation of Audiofrequency Sound in High Polymers*†

R. S. Witte, B. A. Mrowca, and E. Guth
Polymer Physics Laboratory, University of Notre Dame, Notre Dame, Indiana

Velocity and attenuation measurements were made in thin strips of rubber from 0.5 to 5 kc and from −5°C to 90°C to obtain the dynamic viscoelastic constants of butyl and GR-S gum stocks. Above room temperature velocity and attenuation are higher in butyl gum than in GR-S. In all cases, the velocity increases with decreasing temperature and increasing frequency. The attenuation shows a peak with temperature. For butyl the peaks are broad and occur at higher temperatures than for GR-S. For both stocks an increase in frequency gives peaks which are higher and sharper, and shifted to higher temperatures. In some instances, there are indications of peaks in the attenuation *versus* frequency at frequencies beyond our range of measurement. The behavior of the dynamic modulus in the temperature and frequency range studied is similar to that of the velocity. These results combined with low temperature static measurements and very low frequency dynamic measurements indicate a U-shaped modulus-temperature curve whose minimum broadens and shifts to higher temperatures with increasing frequency. This may be explained by a generalization of the kinetic theory of rubber elasticity, taking into account intra- and intermolecular forces, and considering time effects.

INTRODUCTION

THE evaluation of the dynamic viscoelastic properties of a material can be made from measurements of the velocity of transmission and the attenuation of sound in the material. Such methods have been applied chiefly to "low loss" materials such as metals, and to some plastics by Mason, McSkimin, *et al.* A standing wave method for measurement of the dynamic modulus in thin strips was suggested by Bridgeman and Trueblood and was applied by Ballou and Silverman[1] to the measurement of Young's modulus in low loss materials. A modification of this technique can be extended to measure also the internal friction of "high loss" materials. By this method, Nolle[2] obtained the viscoelastic constants of some high polymers. Independently, a method similar to that employed by Nolle has been used in the present work.[3]

The experimental procedure may be best understood by reference to the block diagram shown in Fig. 1. The signal generator drives a crystal, set-

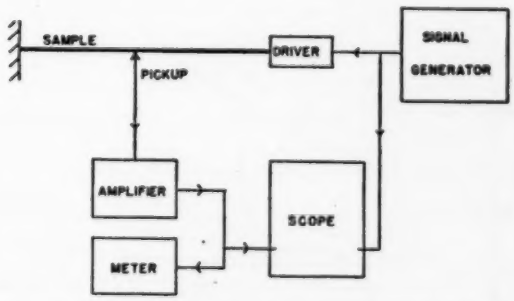

FIG. 1. Schematic diagram of experimental method.

* Supported in part by the ONR.

† Presented at the sixth meeting of the High-Polymer Physics Division, American Physical Society, New York City, January 27–29, 1949.

[1] J. W. Ballou and S. Silverman, J. Acous. Soc. Am. 16, 113 (1944).

[2] A. W. Nolle, J. Acous. Soc. Am. 19, 194 (1947).

[3] Thompson, Mrowca, and Guth, Phys. Rev. 71, 486 (1947).

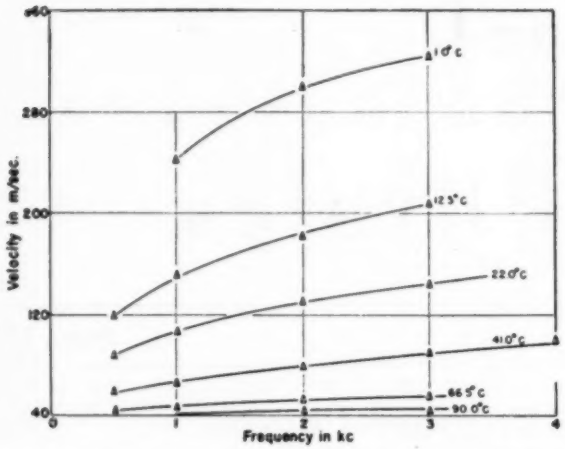

FIG. 2. Velocity *vs.* frequency for a butyl gum stock.

ting up longitudinal waves which are transmitted through the sample and picked up by a reluctance or crystal receiving element. The received signal is amplified and fed to one set of oscilloscope plates, the other set being connected directly to the driving oscillator. Thus, the phase difference between the driven end and the pick-up can be ascertained for any point along the sample. By moving the pick-up along the sample, the distance between two adjacent points in the same phase of motion can be measured, and thus the wave-length of the sonic wave in the sample can be determined. Knowing the frequency of the driving oscillator, the velocity can be directly obtained.

The attenuation is obtained by moving the pick-up along the sample and reading on the wave analyzer, or sound level meter, the amplitude of the received signal as a function of distance.

This method of measurement is limited to a definite frequency range, and is applicable only to certain materials. An upper limit to the frequency range is determined by the fact that the largest cross-sectional dimension of the sample must be kept small in comparison with the wave-length of the propagated wave. At sufficiently low frequencies, the sample length becomes smaller than the half-wave-length of the transmitted sound wave, making velocity measurements impossible. Besides these limitations, it is also apparent that materials of extremely high attenuation cannot be investigated by this method because of the rapid decay of the transmitted wave. Conversely, measurements on materials having very small attenuation are complicated by reflections which tend to produce standing waves, and thus give rise to spurious attenuation readings. The samples used in the present investigation were thin strips 0.45-mm thick and 2 to 3 mm in width. The cross section was thus a very small fraction of the wave-lengths used. The length of the strips was of the order of 20 to 30 cm, and the damping was sufficiently high to prevent standing waves due to reflections from the end of the sample. This length of sample also made it possible to measure the wave-length and attenuation over a considerable distance, thus increasing the accuracy of measurement. The velocity could be measured to an estimated precision of 0.4 percent. The attenuation measurements, particularly those at the higher frequencies, could not be obtained to better than 10 percent due to the rapid rise in absorption with frequency. This confined the measurements to a small portion of the sample.

THEORY

If the cross-sectional dimensions of the strip used are small in comparison with the wave-length, then all points in a given cross section will presumably be in the same phase of motion. The deformation will be of the type encountered in a Young's modulus stress-strain relationship, and acoustically, a plane longitudinal wave is transmitted through the sample. If we also assume that the frictional force is pro-

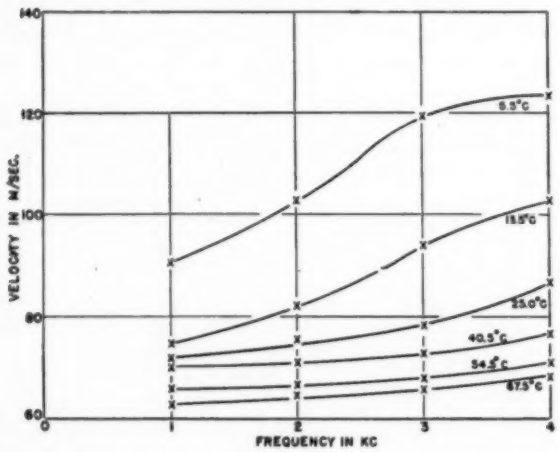

FIG. 3. Velocity *vs.* frequency for a GR-S gum stock.

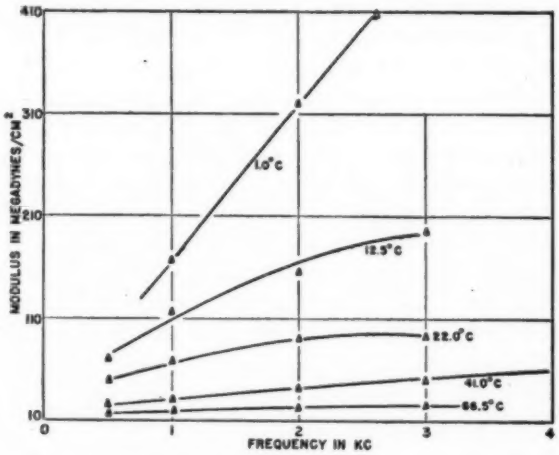

FIG. 4. The dynamic Young's modulus as a function of frequency for butyl gum.

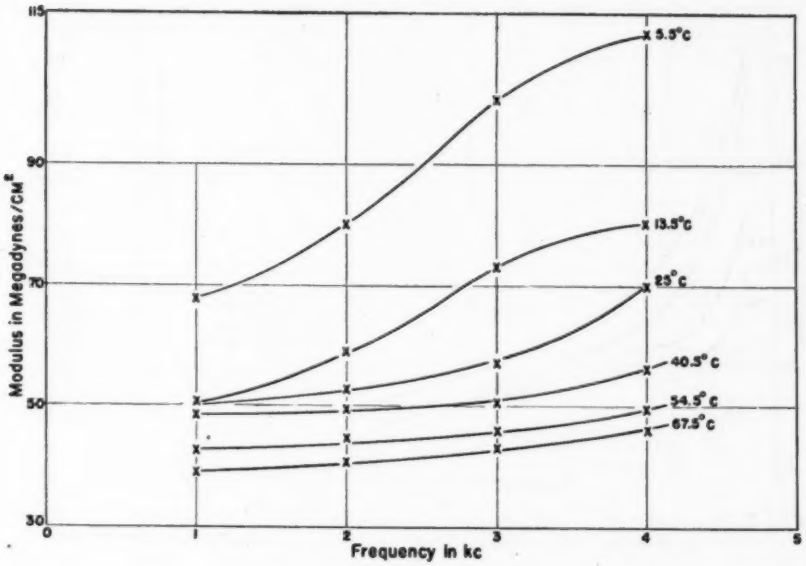

FIG. 5. The dynamic Young's modulus as a function of frequency for GR-S.

portional to the rate of change of strain, the following wave equation results

$$E(\partial^2 u/\partial x^2)+f(\partial^3 u/\partial t dx^2)=\rho(\partial^2 u/\partial t^2), \qquad (1)$$

where u is the instantaneous displacement of a cross section of the sample in the x direction; E is Young's modulus, f the viscosity coefficient, and ρ the density of the material. Assuming a sinusoidal driving force, a solution of the equation yields the following relationships,

$$E=\rho C^2\frac{\omega^2(\omega^2-\alpha^2C^2)}{(\omega^2+\alpha^2C^2)^2} \qquad (2)$$

and

$$f=\rho C^2\frac{2\omega^2\alpha C}{(\omega^2+\alpha^2C^2)^2}, \qquad (3)$$

where ω is the angular frequency and C the phase velocity of the transmitted wave. These equations relate the normal viscosity coefficient f and the dynamic Young's modulus E with the measurable quantities.

EXPERIMENTAL RESULTS

Figure 2 shows the velocity curves for a butyl gum stock as a function of frequency at different temperatures. The velocity increases very slowly with frequency at high temperatures where the values of the velocity are of the order of 40 meters/sec. The increase in velocity with frequency is much more rapid as the temperature is lowered, and the velocity at 0°C is of the order of 300 meters per second. The velocity curves for GR-S are shown in Fig. 3. The general behavior is similar to that in butyl, but the velocity in GR-S is in general lower than that found in butyl at a given temperature and frequency. The corresponding modulus curves derived from the velocity curves, using Eqs. (2) and (3), are presented in Figs. 4 and 5. We note that at all temperatures the modulus increases with frequency. This increase is much more rapid as the temperature is lowered, showing a stiffening of the stock at low temperatures. Data obtained at frequencies in the megacycle range[4] indicate a continuous rise in the modulus with frequency up to 10 or 15 Mc. It would appear then that these curves represent a small portion of a very broad dispersion curve. The temperature variation of the dynamic modulus for butyl and GR-S at different frequencies is plotted in Figs. 6 and 7. At high temperatures the modulus varies only slightly with frequency, but has widely divergent values at temperatures near 0°C.

The curves for butyl and GR-S in Fig. 8 show peaks in the attenuation as the temperature is varied. Two significant facts are obvious from the curves. The attenuation peaks become higher and

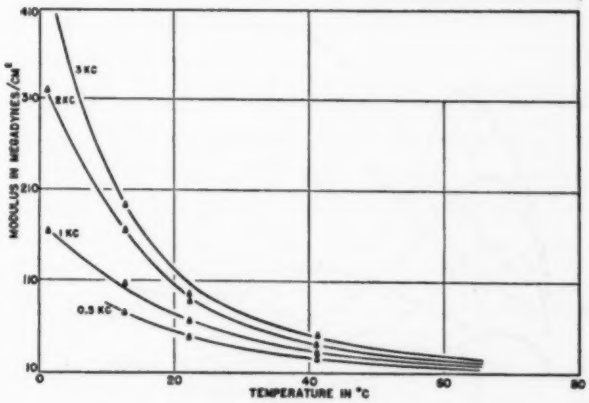

FIG. 6. The variation of the dynamic Young's modulus with temperature for butyl gum.

[4] Ivey, Mrowca, and Guth, J. App. Phys. 20, 486 (1949).

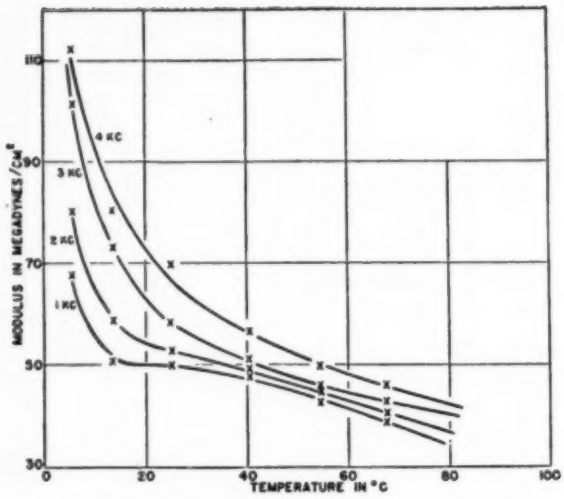

FIG. 7. The variation of the dynamic Young's modulus with temperature for GR-S gum.

are shifted to higher temperatures at higher frequencies. This phenomenon is analogous to the situation encountered in the study of losses in dielectrics. The peaks in butyl are much broader than those found for GR-S, and occur at temperatures about 40°C higher than those for GR-S. Measurements of the transmission of bulk waves from 40 kc to 10 Mc, made on the same materials, showed a similar behavior.[4] At the high frequencies however, the attenuations were one or two orders of magnitude greater.

Figures 9 and 10 show attenuation in db per wave-length as a function of frequency for different temperatures. The curve for GR-S at 5.5°C appears to peak in the frequency range measured. A comparison with the modulus *vs.* frequency curve, Fig. 5, at the same temperature indicates that this peak corresponds roughly to the broad dispersion region in the modulus. The curves at higher temperatures indicate the possible existence of attenuation peaks at frequencies above the range of measurement. In Figs. 11 and 12, the viscosity coefficient f is plotted as a function of frequency for

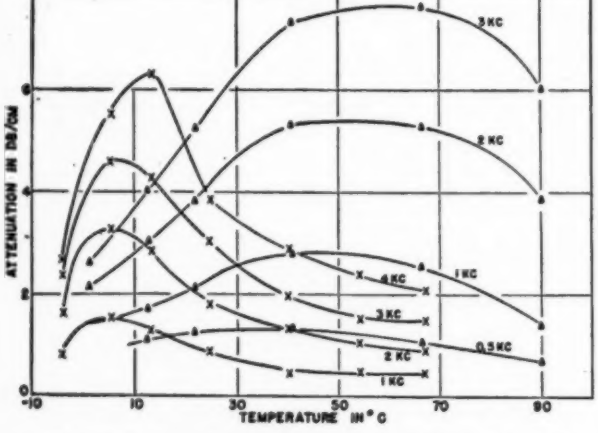

FIG. 8. Attenuation peaks with temperature in butyl and GR-S gum stocks.

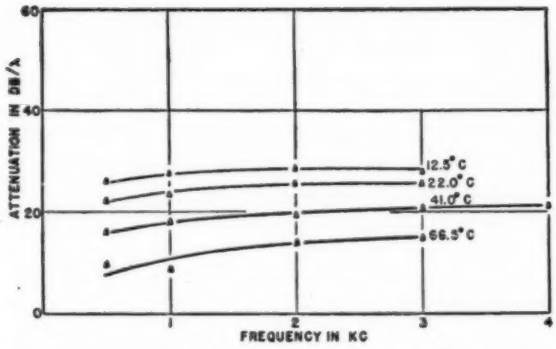

FIG. 9. Attenuation in db/wave-length for a butyl gum stock.

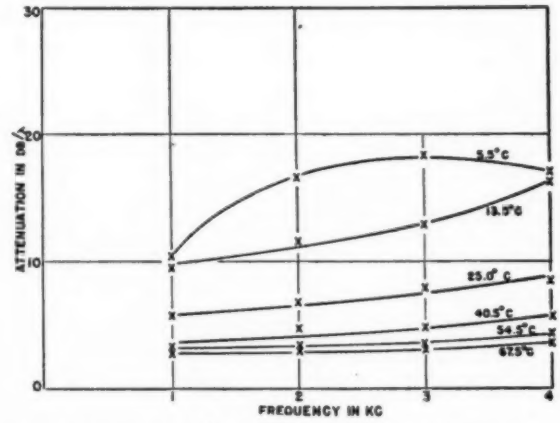

FIG. 10. Attenuation in db/wave-length for a GR-S gum stock.

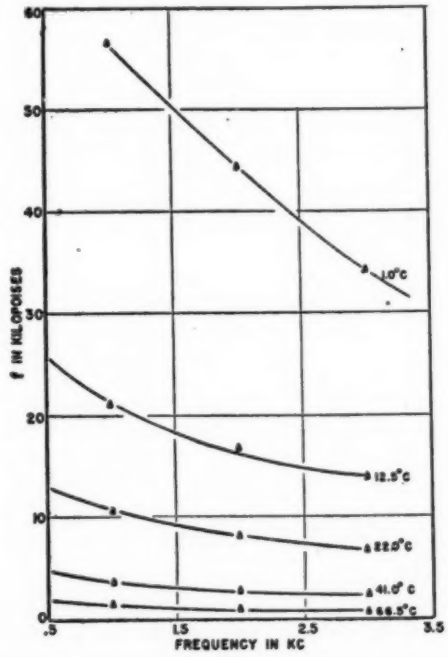

FIG. 11. The normal viscosity coefficient as a function of frequency for butyl gum.

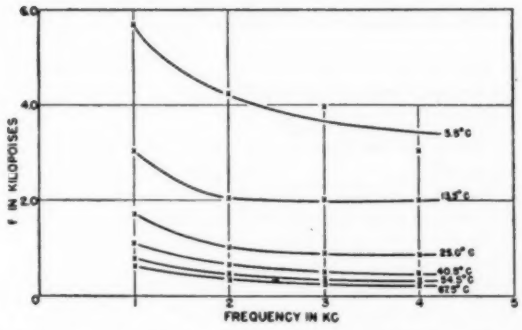

FIG. 12. The normal viscosity coefficient as a function of frequency for GR-S gum.

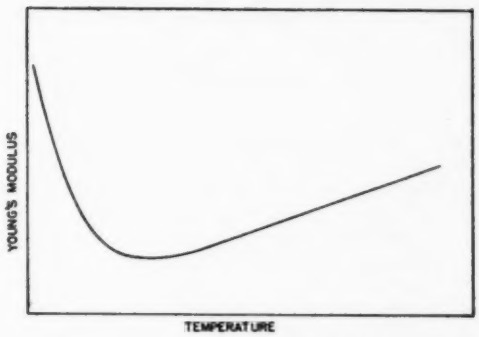

FIG. 13. Schematic diagram showing the inversion of the dynamic Young's modulus with temperature at very low frequencies.

butyl and GR-S at different temperatures. The value of this coefficient decreases with frequency at all temperatures, but does so much more rapidly at low temperatures.

It is apparent from the curves, particularly those for attenuation *versus* frequency and temperature, that an increase in temperature produces the same effect as a decrease in frequency. This generalization might be useful in predicting the behavior of the viscosity and modulus beyond the experimentally accessible range of temperature or frequency.

The modulus *versus* frequency curves for both GR-S and butyl indicate the existence of a dispersion region over the entire frequency range of measurement. The relaxation mechanism responsible for this dispersion would involve the assumption of a number of relaxation times of the order of 10^{-3} second. However, measurements of bulk wave transmission at ultrasonic frequencies indicate that the dispersion region extends to frequencies of the order of 10 Mc or higher.[4] The dispersion over a limited frequency range can be attributed to a mechanism involving relaxation times of the order of $1/\omega$, whereas the entire dispersion range would have to be explained on the assumption of a wide distribution of relaxation times. Composite modulus *versus* frequency and internal viscosity *versus* frequency curves, extending from 1.5 c.p.s. to 10 Mc, are given in a paper by Ivey, Mrowca, and Guth,[4] utilizing the data obtained in the present paper and unpublished material from the Polymer Physics Laboratory at Notre Dame. The relaxation spectrum resulting from these composite curves is also discussed, and the order of magnitude of the activation energies involved is estimated.

At frequencies below 500 cycles, as the static case is approached, the modulus-temperature curves become U-shaped as indicated in the schematic Fig. 13. In the modulus-temperature curves of Figs. 6 and 7, only the descending branch of the U-shaped curve is observed. The minima in such curves become sharper and shift to lower temperatures as the frequency decreases.[5] The inversion in the behavior of the modulus with temperature at very low frequencies can be explained by taking into account both inter- and intramolecular forces. The descending branch of the U-shaped modulus-temperature curves corresponds to the behavior of ordinary elastic materials, whose Young's modulus decreases with increasing temperature. For rubbers below the inversion region, the inter- and intramolecular forces overshadow the effects of the kinetic motion of the chain segments. Above the inversion region, the kinetic effects predominate leading to a linear increase of the modulus with T. The inversion region may be compared with the Curie temperature at which paramagnetic materials become ferromagnetic. This simple picture is complicated by the occurrence of time effects which for some polymers may overbalance equilibrium effects. The generalized kinetic theory can be discussed by analogy to the theory of ferromagnetism.[6]

[5] Anthony, Forster, and Wack, unpublished data, Polymer Physics Laboratory, Notre Dame, Indiana.
[6] E. Guth and H. M. James, Phys. Rev. **75**, 1284 (1949).

Propagation of Ultrasonic Bulk Waves in High Polymers*†

DONALD G. IVEY,** B. A. MROWCA, AND EUGENE GUTH
Polymer Physics Laboratory, University of Notre Dame, Notre Dame, Indiana

The propagation of supersonic waves in bulk rubbers has been studied from 40 kc/sec. to 10 Mc/sec. and from −60°C to 60°C. The wave velocity was found to increase with decreasing temperature, leveling off both at high and low temperatures, and was found to increase slightly with frequency. Peaks in attenuation as a function of either temperature or frequency were observed, the peaks occurring at lower temperatures for lower frequencies. The peaks for butyl, a high loss rubber, are broader and higher than those for GR-S and Hevea, which are lower loss rubbers. The results are in qualitative agreement with data obtained by strip methods at audiofrequencies. However, for bulk waves the real and imaginary parts of two elastic constants, the bulk and shear moduli, determine wave velocity and attenuation; hence, independent measurements of shear wave properties are necessary to evaluate these constants. A three constant theory is discussed, assuming a shear viscosity only, so that an effective modulus $K+4\mu/3$ is obtained, where K and μ are the bulk and shear moduli. Relaxation times of the order 10^{-6} to 10^{-8} second are indicated. Approximate values of the dynamic Young's modulus are obtained from the effective modulus by assuming that the high frequency dispersion is due to the appearance of a "crystalline" shear elasticity. These results are correlated with low frequency data, and the dynamic Young's modulus and the loss factor are plotted. The loss factor exhibits a maximum in the dispersion region. Results are plotted in the range from 1 c.p.s. to 10^7 c.p.s., which covers a wider range of frequency than earlier investigations. The necessary distribution of relaxation times is discussed.

INTRODUCTION

THE viscoelastic constants of rubber at audiofrequencies have been obtained by measurement of traveling or standing waves in strips of the material.[1,2] There are intrinsic difficulties in the extension of these methods to higher frequencies, since, in order that the problem remain one-dimensional, the wave-length must be long compared to the cross section of the sample used. This would involve the use of impossibly thin strips at high frequencies. At ultrasonic frequencies, measurements of bulk wave transmission can be more readily carried out.

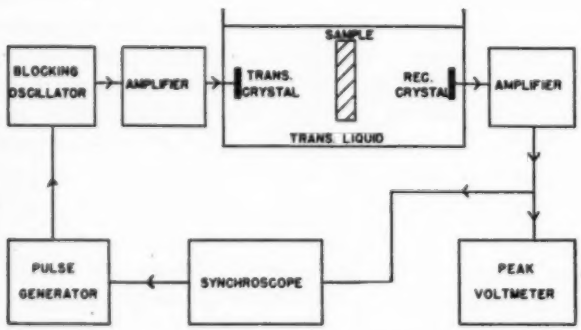

FIG. 1. Schematic diagram of apparatus for measuring bulk wave propagation constants.

Bulk wave properties in glasses have been studied at these frequencies by optical methods.[3] Opaque solids such as metals have been studied by passing a continuous wave train through plane sheets of the material immersed in a liquid.[4] Interference patterns result due to reflections at the interfaces. From a study of the change in these patterns, when the sample thickness is changed by rotation, the elastic constants can be deduced. A more convenient technique is to use a pulsed ultrasonic beam, so that a directly transmitted signal can be observed without the complication of interference. This method has been used extensively for organic[5] and for polymeric[6] liquids. Measurements in rubber using this pulse technique have been made in various polymers at fixed frequencies of 10 and 30 Mc/sec. by Nolle and Mowry.[7] Sack and Aldrich[8] have recently carried out measurements of hysteresis losses in elastomers in the range 0.5 to 6 Mc/sec., using frequency-modulated waves to avoid standing wave effects. In the present work, a pulsed ultrasonic wave was used to investigate the viscoelastic constants of three types of rubbers in the frequency range from 40 kc/sec. to 10 Mc/sec., and the temperature range from −60°C to 60°C.

*† Presented at the sixth meeting of the Division of High-Polymer Physics, American Physical Society, New York City, January 27–29, 1949. Supported in part by the ONR.

** Section of a Dissertation to be submitted to the Graduate School of the University of Notre Dame in partial fulfillment of the requirements for the degree of Doctor of Philosophy.

[1] Witte, Mrowca, and Guth, J. App. Phys. **20**, 481 (1949). Also, Thompson, Mrowca, and Guth, Phys. Rev. **71**, 486 (1947).

[2] A. W. Nolle, J. Acous. Soc. Am. **19**, 19 (1947). Also, M.I.T. Ph.D. Thesis. This manuscript provides an excellent survey of recent work in this field.

[3] L. Bergman, *Ultrasonics* (John Wiley & Sons, Inc., New York, 1938), Chapter 4.

[4] W. C. Schneider and C. J. Burton, J. App. Phys. **20**, 48 (1949).

[5] J. R. Pellam and J. K. Galt, J. Chem. Phys. **14**, 608 (1946).

[6] Mason, Baker, McSkimin, and Heiss, Phys. Rev. **73**, 1074 (1948).

[7] A. W. Nolle and S. C. Mowry, J. Acous. Soc. Am. **20**, 432 (1948).

[8] H. S. Sack and R. W. Aldrich, Phys. Rev. **75**, 1285 (1949).

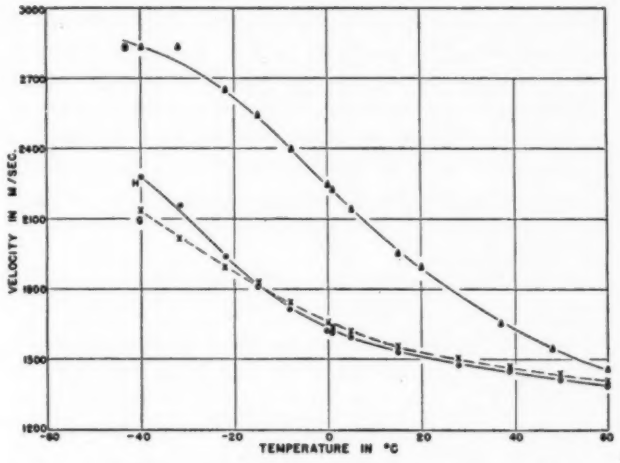

FIG. 2. Bulk wave velocity *vs.* temperature at 1 Mc/sec. for Hevea, GR-S, and butyl rubbers (designated by *H*, *G*, and *B*).

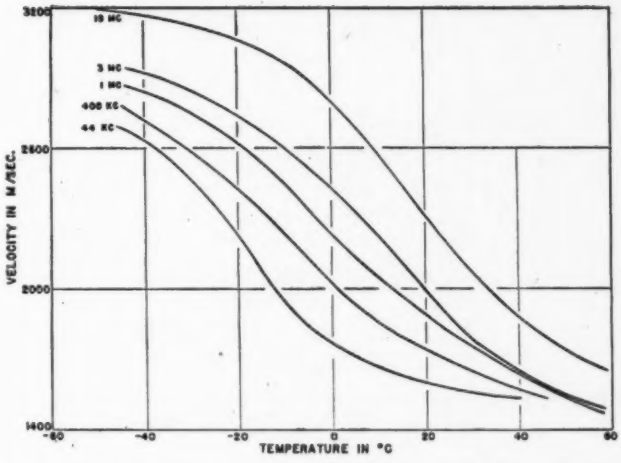

FIG. 3. Velocity *vs.* temperature for butyl at all frequencies.

EXPERIMENTAL METHOD

A pulsed compressional wave is generated and received in a liquid by a pair of crystal transducers. By observing the time shift and amplitude change of the received signal when a rubber sample is inserted in the path of the beam, the bulk wave velocity and attenuation can be calculated. The duration of the pulse is such that interference effects do not occur in the first received signal. However, the pulses used are of sufficient length that the group velocity of the pulse may be assumed equal to the phase velocity of continuous waves of the same frequency.

A schematic diagram of the apparatus is shown in Fig. 1. The synchroscope triggers the pulse generator at the same instant that it starts its sweep. A negative pulse from the pulse generator cuts off a tube which normally short circuits the tank of the oscillator. Thus the oscillator is opened for the duration of the pulse. The oscillations are amplified and fed to the transmitting crystal, which generates an interrupted train of waves in the transmitting liquid. The crystals used are of sufficient cross section to insure a well collimated plane wave. This wave is picked up by the receiving crystal and the resulting signal is amplified and fed into the peak reading voltmeter and the synchroscope. When a rubber sample is inserted in the path of the beam, the wave pattern on the synchroscope screen shifts in position and changes in amplitude. Since a part of the liquid path has been replaced by the sample, the velocity and attenuation in the sample relative to the transmitting liquid can be obtained.

The transmitting liquids used had negligible attenuation compared to that of the rubber, so that the sample attenuation was obtained directly, assuming no reflection at the liquid-sample interfaces. This assumption is valid if liquids of approximately the same acoustic impedance as rubber are used. The discrepancies due to reflections were studied by using samples of varying thickness, and observing the attenuation due to differences in thickness. This also guarded against interpreting pseudo-attenuations due to standing waves as true attenuations, when it was necessary to use very thin samples. It was found that the attenuation at these frequencies is so large that both of these effects may be neglected.

The velocity in the sample was obtained from the relationship

$$C = DC_L/(D \pm C_L\Delta t),$$

where D = sample thickness (measured by a dial micrometer at each temperature), C_L = velocity in the liquid, and $\pm\Delta t$ is the time shift observed on insertion of the sample; C_L was measured by an interferometer method. The relative distance between the crystals could be changed by a calibrated screw drive, and the resultant fringe shift observed on the synchroscope. The velocity in the transmitting liquid was measured at each temperature to an accuracy of 0.5 percent or better. Any desired precision could be obtained in this measurement.

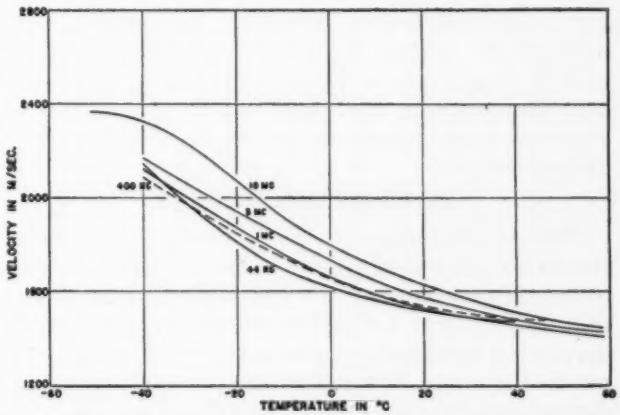

FIG. 4. Velocity *vs.* temperature for GR-S at all frequencies

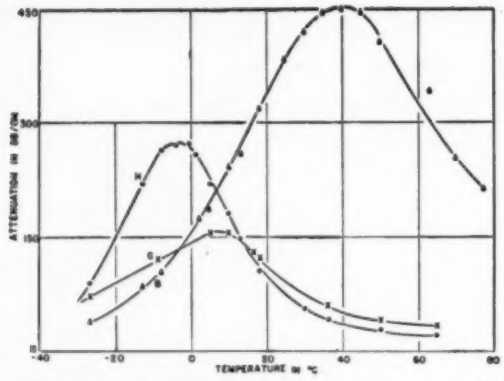

FIG. 5. Bulk wave attenuation *vs.* temperature at 10 Mc/sec. for Hevea, GR-S, and butyl rubbers.

The over-all accuracy of the method was ascertained by measuring the velocity of transmission through several liquids enclosed in a thin-walled cell. Measured values for the velocity in several liquids checked with those reported in the literature to better than 0.2 percent.

Measurements were made in the temperature range −60°C to 60°C. Above 0°C water was used as a transmitting liquid, because of its negligible attenuation and desirable acoustic impedance. Below 0°C an ethylene glycol-water mixture was used which had negligible attenuation down to about −30°C. Below this temperature a small correction had to be made. The velocity in this mixture is higher than it is in water, which is advantageous because the velocity in rubber is higher at lower temperatures. Thus, the mismatch at the interfaces is minimized, and can be neglected. Another advantage is that the error in velocity measurements is a minimum when $C=C_L$, since errors in D and Δt are then eliminated.

X-cut Rochelle salt crystals were used in the frequency range of 40 kc to 1 Mc and X-cut quartz crystals at frequencies from 1 Mc to 10 Mc. Measurements were made at 44 kc, 400 kc, 1 Mc, 3 Mc, and 10 Mc. At each frequency, complete velocity-temperature and attenuation-temperature curves were obtained. Velocity measurements were accurate to within 2 percent at high frequencies and to 5 percent at lower frequencies. Thickness and composition variations made it difficult to measure attenuations to an accuracy better than 10 percent.

EXPERIMENTAL RESULTS

The results for butyl, GR-S, and natural rubber stocks are presented. Figure 2 shows the dependence of velocity on temperature for the three gum stocks at a frequency of 1 Mc. The velocity increases with decreasing temperature, the butyl showing the most marked change. Natural rubber and GR-S are indistinguishable above 0°C. There is some indication that the curves level off at both high and low temperatures. The general behavior is the same at all frequencies. This is shown in Fig. 3, where velocity-temperature curves are plotted for butyl at all frequencies. An increase in velocity with frequency is noted. Figure 4 shows velocity-temperature curves for GR-S at all frequencies, showing much less dispersion. The curves for natural rubber have the same form, with approximately the same values as those shown for GR-S.

Figure 5 shows the dependence of attenuation on temperature for the three stocks at 10 Mc. We observe that these curves all peak in this temperature region. Similar behavior has been observed by Nolle and Mowry[7] for some synthetic rubbers and by Mason[9] for other polymers. These curves have relatively the same form at all frequencies, but as the frequency is decreased the curves decrease in amplitude and shift to lower temperatures, as indicated by Fig. 6, which shows attenuation-temperature curves for butyl at all frequencies. The attenuation per unit length of sample decreases very rapidly with decreasing frequency. The attenuations per wave-length are plotted on the same graph. These were calculated assuming a constant velocity, as the only effect of taking the velocity variation into account is to change the shape of the curves slightly, the over-all behavior remaining the same. The attenuation-temperature curves for natural and GR-S rubbers exhibit a similar behavior.

The velocity-frequency curves for butyl at various temperatures are shown in Fig. 7. We observe that there is a much greater dispersion in the 0°C region than at ±40°C. Figure 8 shows velocity-frequency curves for natural rubber, showing practically no dispersion at 40°C, maximum dispersion at −20°C, but less over-all dispersion than for butyl.

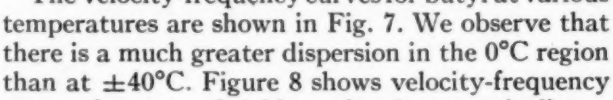

FIG. 6. Attenuation per cm (solid curves); and attenuation per wave-length (dashed curves, arbitrary scale) for butyl at all frequencies.

[9] Warren P. Mason, *Electromechanical Transducers and Wave Filters* (D. Van Nostrand Company, Inc., New York, 1942), pp. 247.

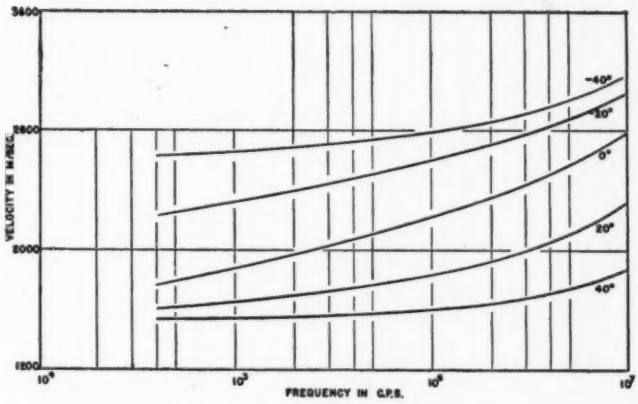

FIG. 7. Velocity *vs.* frequency for butyl at various temperatures.

Figure 9 shows attenuation per wave-length *versus* frequency for butyl at various temperatures. The attenuation shows peaks with frequency, which shift to lower frequency as the temperature is decreased. It is apparent that decreasing the temperature has the same effect on attenuation as increasing the frequency—i.e., a given change in attenuation can be produced by either an increase in frequency or a decrease in temperature.

THEORY

In general, four viscoelastic constants are necessary to characterize a viscoelastic material, since there are shear and compressional viscosities in addition to the shear and bulk moduli. To determine these constants then, we need not only measurements on bulk wave transmission but also the propagation constants for shear waves in the material. Experiments are now being performed to measure these constants at the lower end of the above frequency range, in order to correlate quantitatively the bulk wave data with the lower frequency strip data. As can be seen by comparing the present paper with the low frequency work,[1] the results are qualitatively in agreement, but an exact comparison cannot be made unless the elastic constants themselves can be determined.

In the absence of shear wave data, an approximate three constant theory can be obtained by making Stokes' assumption that there is no viscosity associated with a hydrostatic compression. Recent measurements of viscous losses in ordinary and in polymeric liquids indicate that this assumption is probably not valid for such materials. For instance, Hall[10] has shown that the observed losses in water can be explained by assuming that there is a lag in the rearrangement of the molecules during compression. Mason and co-workers[6,11] also have found it necessary to postulate a compressional viscosity which is an appreciable fraction of the shear viscosity, in order to explain losses associated with longitudinal wave transmission. Hence, the shear viscosities computed here may be upper limits to the true values.

Assuming that the viscous forces are proportional to the time rate of change of strain, and making Stokes' assumption, the effective viscosity may be shown to be[12] $4\gamma/3$, where γ is the coefficient of shear viscosity. The effective modulus for dilatational waves is given by[13] $\lambda+2\mu=K+4\mu/3$, where λ is Lame's constant, and K and μ are the bulk and shear moduli. The one-dimensional wave equation becomes

$$(K+4\mu/3)\partial^2u/\partial x^2+(4\gamma/3)\partial^3u/\partial t\partial x^2=\rho\partial^2u/\partial t^2,$$

where u is the displacement from equilibrium of a transverse plane, and ρ is the density. Assuming a harmonic time dependence, the solution of the amplitude equation gives for the effective modulus,

$$K+4\mu/3=\rho C^2(1-r^2)/(1+r^2)^2,$$

and for the viscosity,

$$4\gamma\omega/3=\rho C^2 2r/(1+r^2)^2,$$

where ω=angular frequency, and the parameter $r=\alpha C/\omega=LC/8.7\omega=L\lambda/54.6$, where α=attenuation in nepers/cm, L=attenuation in db/cm, C=wave velocity in sample, λ=wave-length in sample. Hence, r is the ratio of $L\lambda$, the attenuation

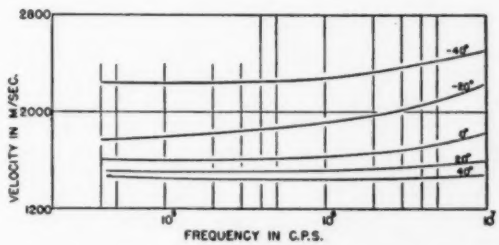

FIG. 8. Velocity *vs.* frequency for Hevea at various temperatures.

[10] L. Hall, Phys. Rev. **71**, 318 (1947).
[11] Mason, Baker, McSkimin, and Heiss, Phys. Rev. **75**, 936 (1949).
[12] Reference 9, p. 304.
[13] A. E. H. Love, *Mathematical Theory of Elasticity* (Cambridge University Press, London, 1927), p. 294.

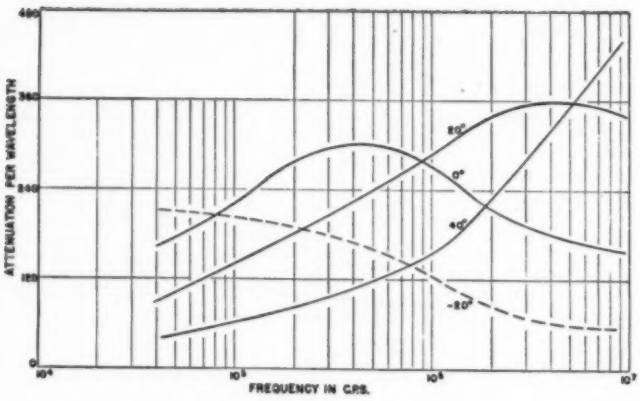

FIG. 9. Attenuation per wavelength *vs.* frequency for butyl at various temperatures.

in db/wave-length, to 54.6, the attenuation of a perfectly viscous medium.

In practice, r is usually less than 0.1 so that $k+4\mu/3$ is approximately equal to ρC^2 and $\gamma \sim LC^3/\omega^2$. Figures 10 and 11 show these quantities plotted as a function of frequency for butyl and natural rubber at three temperatures. The effective loss factor $(4\gamma\omega/3)/(K+4\mu/3)$ is also plotted in Figs. 10 and 11, and is observed to peak with frequency, the peak shifting to lower frequencies at lower temperatures.

In order to discuss quantitatively the distribution of relaxation times for the observed dispersion, it is necessary to know K, μ, or E, Young's modulus, over the entire frequency spectrum. If, for example, μ were known from shear wave measurements, then from the above data the bulk modulus and Young's modulus could be computed, and the values for Young's modulus could be extrapolated to meet the low frequency data obtained by strip methods.[1] However, in the absence of these measurements, the following observations can be made. In general, the relaxation spectrum needed to explain the observed modulus and internal friction is broad in the audiofrequency range, but is sufficiently narrow in the megacycle region to be explained by assuming a few relaxation times. The relaxation mechanisms responsible for dispersion in the frequency region of this work have relaxation times of the order 10^{-6} to 10^{-8} second. The relaxation spectrum, although narrower than in the audio region, is still too broad to be explained by one relaxation time. However, any small portion of the curves could be represented by one or two relaxation times, as has been noted also by Sack and Aldrich.[8] For example, two relaxation times of approximately 5×10^{-6} second and 4×10^{-8} second could be used to explain very roughly the shape of the effective modulus and loss factor curves for butyl at 0°C. Somewhat smaller relaxation times, of the order 10^{-7} to 10^{-9} second, would be necessary to fit natural rubber and GR-S curves at the same temperature. This is indicated in Fig. 11, which shows that dispersion occurs, in a given frequency region, at lower temperatures for natural rubber than for butyl. Thus, at a given temperature, the dispersion would occur at higher frequencies for natural rubber than for butyl. For the butyl rubber loss factor curves, which peak in the frequency region studied, Fig. 10, an approximate value of the activation energy involved at these frequencies may be obtained by considering the change with temperature of the frequency of maximum loss. A value of about 20 kilocalories per mole is obtained for butyl in this way.

An approximate evaluation of the dynamic

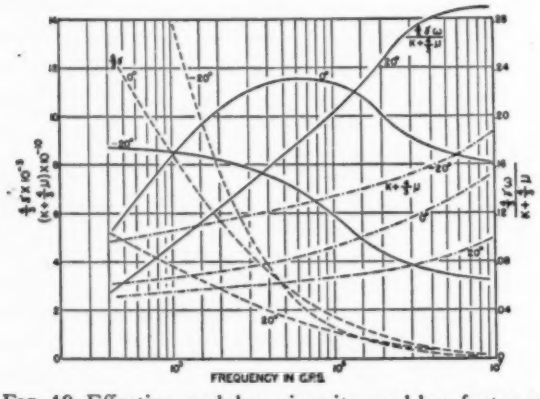

FIG. 10. Effective modulus, viscosity, and loss factor *vs.* frequency for butyl at 20°C, 0°C, and −20°C.

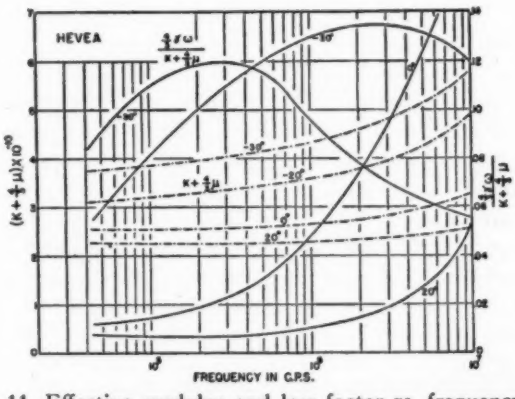

FIG. 11. Effective modulus and loss factor *vs.* frequency for natural rubber at 20°C, 0°C, −20°C, and −30°C.

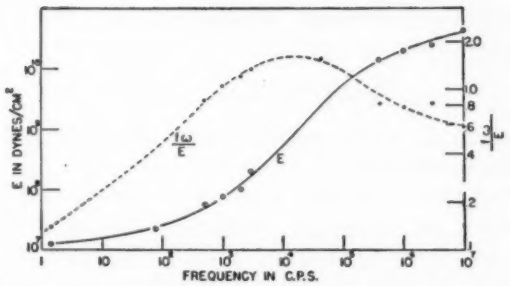

FIG. 12. Young's modulus and loss factor *vs.* frequency for GR-S at 20°C showing correlation with low frequency data.

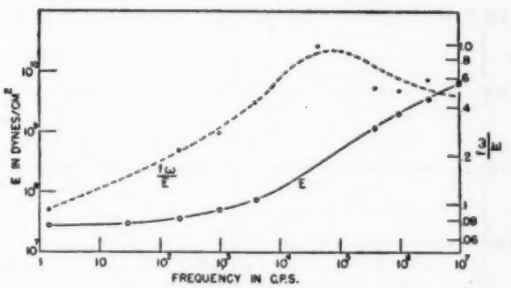

FIG. 13. Young's modulus and loss factor *vs.* frequency for butyl at 20°C showing correlation with low frequency data.

Young's modulus for comparison with low frequency data may be made from the following considerations. Mason and co-workers[11] have shown that the high frequency dispersion in polymeric liquids appears to be due to the appearance of "crystalline" shear elasticity. Nolle and Mowry[7] have assumed that this is also true for rubber, taking the bulk modulus K as equal to that of water. This assumption appears valid in the present work, since the effective modulus curve for natural rubber at 20°C, Fig. 11, appears to level off below 100 kc, approaching as a limit the value 2.25×10^{10} dynes/cm², which is the bulk modulus for water.[14] It is reasonable to assume, then, that at low frequencies, just as in the static case, μ is negligible in comparison with K.[15] Taking K equal to the limiting value of $K+4\mu/3$ at the low frequencies, and assuming it is constant, μ can then be calculated at the high frequencies from the observed change in $K+4\mu/3$. Thus, $E=3K\mu/(K+\mu/3)$ can be computed and compared with low frequency data. The results of such a calculation for GR-S at 20°C are given in Fig. 12. The value of E at 1.5 c.p.s. was obtained from free vibration data,[16] those at 30 and 212 c.p.s. from resonance techniques,[17] and those from 1 to 4 kc from strip method data.[1] Shown also in Fig. 12 is the loss factor $f\omega/E$, where f is the "Young's modulus" viscosity,[1] also obtained at low frequencies from the above sources. Figure 13 shows E and $f\omega/E$ for butyl rubber at 20°C, calculated under the same assumptions. Since the effective modulus curves for butyl, Fig. 10, do not completely flatten out at low frequencies, the value of K must be approximated, and the calculations are therefore less accurate. For both butyl and GR-S the loss factor exhibits peaks, these peaks occurring approximately in the region of maximum change in modulus. The dispersion region for butyl occurs at slightly lower frequencies than that for GR-S.

We observe that dispersion occurs over at least six decades of frequency for both GR-S and butyl rubber. Consequently, a complete spectrum of relaxation times would be necessary to explain the mechanisms involved. For such a relaxation phenomenon,

$$E(\omega)=\sum_{j=0}^{\infty} A_j/(1+1/\omega^2\tau^2),$$

and if we assume a continuous distribution, this becomes

$$E(\omega)=\int_0^{\infty} F(\tau)d\tau/(1+1/\omega^2\tau^2).$$

If the dispersion extends over several decades, then we may treat a given term in the series as a step function,[18] and write

$$E(\omega)\cong\int_{1/\omega}^{\infty} F(\tau)d\tau.$$

The quantity $F(\tau)$ may be called the strength of the relaxation spectrum. Figure 14 shows $F(\ln\tau)$, which is the strength of the relaxation spectrum between

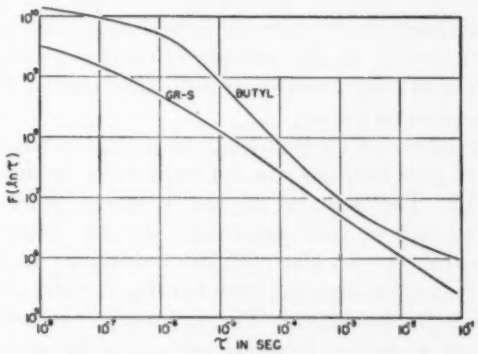

FIG. 14. Approximate strength of the relaxation spectrum *vs.* relaxation time for GR-S and butyl at 20°C.

[14] This value is calculated from the observed bulk wave velocity of 1.5×10^5 cm/sec. in water at 20°C.

[15] This is equivalent to assuming that at low frequencies Poisson's ratio approaches a value of one-half, which is known to be true for rubber.

[16] R. L. Anthony and M. J. Forster, unpublished data, Polymer Physics Laboratory, University of Notre Dame, Notre Dame, Indiana.

[17] R. L. Anthony and L. V. Holroyd, unpublished data, Polymer Physics Laboratory, University of Notre Dame, Notre Dame, Indiana.

[18] T. Alfrey, Jr., *Mechanical Behavior of High Polymers* (Interscience Publishers, Inc., New York, 1948), p. 551.

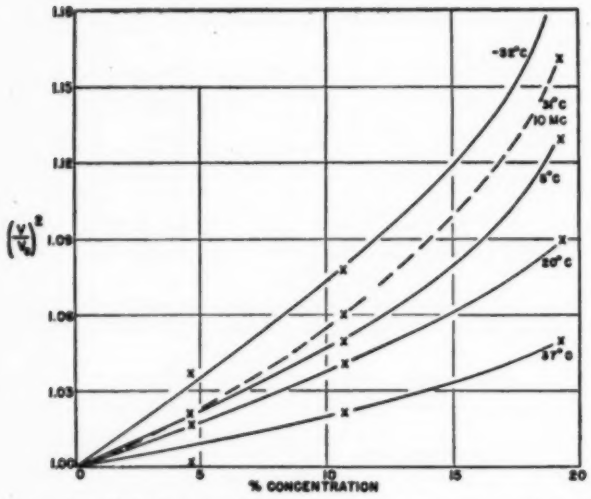

FIG. 15. Relative modulus *vs.* volume concentration for carbon-loaded GR-S at 1 Mc and 10 Mc (dashed curve).

$\ln\tau$ and $\ln\tau+d\ln\tau$, plotted as a function of τ, for GR-S and butyl at 20°C, using E from Figs. 12 and 13. The approximations lead to a distribution which is somewhat broader than necessary. The frequency region in which the modulus would flatten out, and therefore in which $F(\ln\tau)$ would decrease, is apparently just a little above the range investigated.

The satisfactory correlation between the results obtained by low and high frequency methods, as shown in Figs. 12 and 13, would indicate that the assumptions made in the present case are approximately valid. A broad relaxation spectrum was derived by Kirkwood[19] based on the network model of James and Guth,[20] making several simplifying assumptions. For the data embodied in Figs. 12 and 13, however, the inter- and intra-molecular forces play such an important role that Kirkwood's theory cannot be applied quantitatively, since it neglects these forces. The generalization of the kinetic theory of rubber elasticity, including inter- and intra-molecular forces, is being carried out by James and Guth[21] by analogy to the theory of ferromagnetism. It is to be hoped that a relaxation spectrum may be derived based on this generalized theory and compared with the experimental results of the present paper.

The effect of carbon loading in GR-S rubber at various temperatures and frequencies is shown in Fig. 15. The square of the relative velocity is plotted, since this quantity should correspond approximately to the relative modulus. At 1 Mc, the increase in modulus with loading is much greater at lower temperatures. The same effect is achieved by going to higher frequencies, as can be seen from the 10-Mc curve. The curves approach, at low temperature or high frequency, the theoretical curve derived by Guth,[22]

$$E/E_0=1+2.5c+14.1c^2,$$

where E/E_0 is the relative static modulus and c is the concentration.

The effect of cure was also investigated, and found to be negligible. However, the under-cured and over-cured samples used probably did not differ greatly in the amount of cross linking from the optimum-cured samples used. Consequently, little can be said about the effect of cross linking and polymerization.

CONCLUSIONS

The propagation constants of bulk waves in natural, GR-S, and butyl rubbers have been studied as functions of temperature and frequency. From these data, under certain assumptions, values of the dynamic Young's modulus and loss factor have been computed. These results have been extrapolated to the low frequency region where measurements have been made by other methods, and curves drawn over a very wide range of frequency. The resulting correlation indicates that the assumptions made are approximately correct. However, these calculations are only tentative and are dependent for corroboration on measurements of shear wave propagation in the high frequency region. Such measurements are at present being attempted. It is to be hoped that an accurate knowledge of viscoelastic behavior over the entire frequency spectrum will allow a quantitative discussion of the relaxation mechanisms and activation energies involved. From this, a better picture of molecular behavior might be obtained.

APPENDIX

Composition and Cures of Stocks Used

Hevea gum

100.0 g crepe or smoked sheet
3.0 g zinc oxide
1.0 g D.P.G.
5.0 g sulfur

Cured 30 minutes at 50 lb. steam (147°C).

Butyl gum

100.0 g butyl
5.0 g zinc oxide
1.0 g tuads
1.5 g sulfur

Cured 60 minutes at 50 lb. steam (147°C).

GR-S gum

100.0 g GR-S
1.0 g BLE
5.0 g BRT No. 7
5.0 g zinc oxide
1.2 g Santocure
2.5 g stearic acid
1.7 g sulfur

Cured 70 minutes at 40 lb. steam (141°C).

[19] J. G. Kirkwood, J. Chem. Phys. **14**, 51 (1946).
[20] H. M. James and E. Guth, J. Chem. Phys. **11**, 455 (1943).
[21] E. Guth and H. M. James, Phys. Rev. **75**, 1315 (1949).
[22] E. Guth, J. App. Phys. **16**, 20 (1945).

Dynamic Measurements of Polymer Physical Properties*

J. W. Ballou and J. C. Smith
E. I. du Pont de Nemours and Company, Buffalo, New York

Dynamic methods for measuring the elastic and dissipative properties of high polymers in fiber and film form over four decades of frequency (3 to 30,000 cycles per second) are described. The experimental quantities resulting from the three different techniques necessary to cover this range are unified by deriving in each case the parameters of an equivalent Voigt Model (elastic and viscous element in parallel) which would behave in the same way as the polymer sample. Examples of the application of these techniques to the characterization of high polymers are given. The effect of frequency and chemical and physical structure on the derived parameters are discussed, along with the question of heat losses resulting from cyclical differential deformation. In addition, the application of two of the methods to the characterization of the stiffness-temperature behavior of high polymers is described.

INTRODUCTION

DURING the past several years there has been considerable interest in the elastic and dissipative properties of high polymers, in particular those properties which lend themselves to acoustic or other dynamic methods of measurement.[1] In general the approach has been to obtain, at a selected frequency, two experimental quantities from which a dynamic modulus of elasticity and a coefficient of internal viscosity can be derived. These experimental quantities may be, for example, a sound velocity and the associated acoustic attenuation or a resonance frequency and the corresponding logarithmic decrement or band width. The derived quantities then serve to define an equivalent (Voigt) model, consisting of a purely elastic element or spring coupled in parallel with a purely viscous one or dashpot, which will behave in the same way as the sample under the test conditions existing. If the test frequency is changed, a new set of parameters is required in general, since the behavior of high polymers as a function of frequency does not parallel that of a simple linear two parameter model. It is also possible to derive other characteristic numbers to associate with the sample such as a relaxation time, dynamic work recovery, mechanical power factor and other measures of hysteresis which are again a function of frequency.

In contrasting dynamic tests with the usual so-called static tests, it is seen that a unique advantage characterizes the former, because they involve small strains. The large strains associated with stress-strain and creep curves can result in marked increases in orientation and sometimes crystallinity of the polymer sample during the course of the test. Thus the resulting curve is representative of a whole range of physical states and is not characteristic of the material in its starting condition. Dynamic differential tests on the other hand generally involve cyclical strains of a fraction of a percent around some equilibrium strain and can be thought of as characterizing the sample in that state alone.

This paper will describe three techniques which are suitable for investigating the dynamic elastic and dissipative properties of high polymers in fiber and film form over about four decades of frequency (3–30,000 c.p.s.), discuss the effect of frequency and physical state on the derived parameters of a particular high polymer and lastly, indicate the application of these techniques to the study of the stiffness-temperature behavior of high polymers.

HIGH FREQUENCY MEASUREMENTS

An experimental procedure suited to the high frequency range is that of measuring acoustic velocity and attenuation with a sonic interferometer. The equipment used in the present case, which is an extension of that used by Ballou and Silverman[2] and essentially that employed by Nolle,[3] is

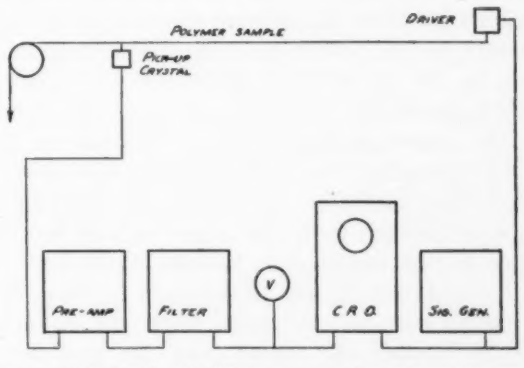

FIG. 1. Schematic of high frequency (sonic) equipment.

* Presented at the sixth meeting of the Division of High-Polymer Physics, American Physical Society, New York City, January 27–29, 1949.

[1] In addition to the other references cited in the text, the following are representative of work in this field: H. Wakeham and E. Honold, J. App. Phys. 17, 698 (1946); H. S. Sack, J. Motz, H. L. Raub, and R. N. Work, J. App. Phys. 18, 451 (1947); W. J. Lyons and I. B. Prettyman, J. App. Phys. 19, 473–480 (1948).

[2] J. W. Ballou and S. Silverman, J. Acous. Soc. Am. 16, 113 (1944).

[3] A. W. Nolle, J. Acous. Soc. Am. 19, 194 (1947).

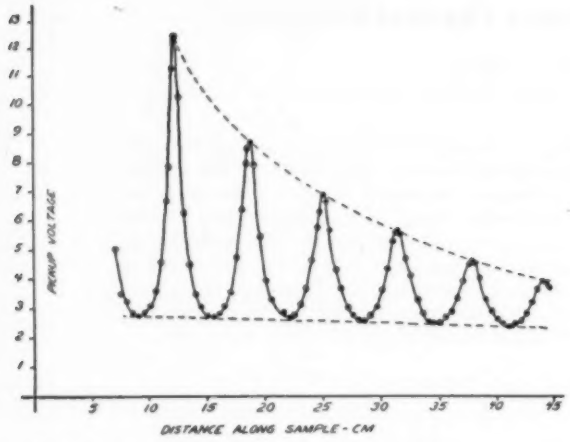

FIG. 2. Pick-up voltage *versus* distance as measured on undrawn 66 Nylon at 12,000 c.p.s. with the apparatus of Fig. 1.

shown in Fig. 1. A signal generator provides a voltage to a driver consisting of a phonograph cutter head. Longitudinal waves are excited in the continuous filament yarn or monofil sample which is attached to the cutter head needle. These waves are picked up by a rochelle salt crystal in contact with the sample and the amplitude and phase (with respect to the driver voltage) of the resulting voltage measured at intervals down the sample. The in-phase positions provide a measure of the wave-length and therefore the velocity. Filters used have pass frequencies of 4, 8, 10, 12, 16, 24 and 32 kc.

Figures 2 and 3 show plots of amplitude *versus* distance along the sample for an undrawn and drawn 66 Nylon, respectively, taken at 12 kc. The presence of standing waves complicates the interpretation of these data and the calculation of the physical attenuation factor involves a somewhat different procedure[4] from that used by Nolle.[3] Appendix I treats the case of standing waves and shows that the attenuation factor is the slope of the plot of the arc hyperbolic tangent of the ratio of points on the lower envelope to corresponding points on the upper envelope *versus* the distance. Figure 4 shows such plots derived from Figs. 2 and 3, with the corresponding values of attenuation α. It may be shown that the y axis intercept is related to the reflection coefficient at the sample-crystal junction, which is seen to be the same for both samples.

Once the attenuation is known, along with the velocity and density, the parameters of the equivalent model can be calculated with the equations given by Nolle.[3] He shows that the modulus of elasticity and coefficient of internal viscosity are

[4] J. C. Smith and J. W. Ballou, J. Acous. Soc. Am. **20**, 586 (1948).

FIG. 3. Pick-up voltage *versus* distance as measured on drawn 66 Nylon at 12,000 c.p.s. with the apparatus of Fig. 1.

given respectively by

$$E=\rho c^2\omega^2(\omega^2-\alpha^2c^2)/(\omega^2+\alpha^2c^2)^2 \quad \text{dynes/cm}^2 \qquad (1)$$

$$\gamma=2\rho\alpha c(\omega c)^2/(\omega^2+\alpha^2c^2)^2 \quad \text{dyne sec./cm}^2 \qquad (2)$$

where ρ=density in g/cc, c=velocity in cm/sec., α=attenuation in nepers per cm, ω=angular frequency in rad./sec. For the case of small damping these expressions reduce to

$$E=\rho c^2 \quad \text{dynes/cm}^2 \qquad (3)$$

$$\gamma=2\rho\alpha c^3/\omega^2 \quad \text{dyne sec./cm}^2. \qquad (4)$$

In addition, the relaxation time is given by

$$\tau=\gamma/E \quad \text{seconds.} \qquad (5)$$

The significance of this relaxation time is not clear at present, but it is a useful characterization parameter as will be shown below. If the two-parameter model obtained at the frequency of measurement also applied in the case of static stresses and strains, the relaxation time would be the time for return to within $1/e$ of equilibrium after release of the yarn sample from a state of longitudinal strain.

Following the above procedure it is possible to associate with a high polymer in yarn or monofil

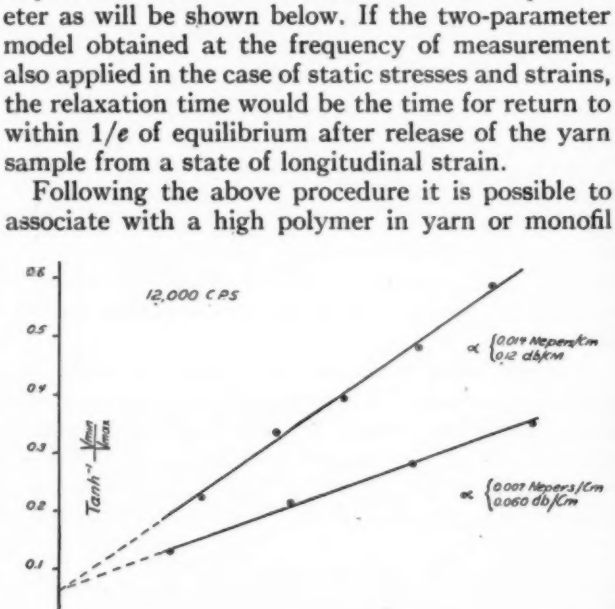

FIG. 4. Plots used in calculating attenuation from the data of Figs. 2 and 3. Upper curve: undrawn Nylon; lower curve: drawn Nylon.

form, at each of the selected frequencies, a two-parameter model which is its equivalent at the particular frequency of measurement.

INTERMEDIATE FREQUENCY MEASUREMENTS

The method described above is not adapted to measurements much below 1 kc because the length of the sample becomes prohibitive. If, however, the high polymer on which such data are desired can be cast into a film or spun into a monofil the method of flexural beam resonance (vibrating reed) may be employed.[5] Olson[6] shows that a clamped-free beam vibrating flexurally will have resonance angular frequencies in rad./sec. given by

$$\omega = M^2 k (E/\rho)^{\frac{1}{2}}/l^2 \qquad (6)$$

where E = modulus of elasticity in dynes/cm^2, ρ = density in g/cc, M = a constant depending on the mode of vibration ($M_1 = 1.8751$ for the fundamental ω_0), k = a cross-sectional shape factor. For circular cross section $k = r/2$ where r is the radius; for the case of rectangular cross sections $k = d/(12)^{\frac{1}{2}}$ where d is the thickness in the plane of vibration, l = length of sample in cm.

This expression properly applies to free vibration with no damping. It does not strictly apply to a driven vibrating reed system because the system is driven at the "fixed" end and further, there is damping present. However, generally only a very small error is introduced in that the resonance frequencies for the two cases differ by only 1 percent for a system with a "Q" of 5. This is relatively large damping compared to that occurring in high polymers. Equation (6) may be used to calculate E from data obtained with an apparatus such as that shown in Fig. 5. Here again a phonograph cutter head is the driver. The pin is slotted to receive the sample, which is held in by compressing the slot. The tip of the reed is observed with a low power microscope and the frequency adjusted for resonance. This method has been used in the region 50–200 c.p.s.

If a value of the coefficient of viscosity is desired, it is necessary to measure the band width of the resonance curve. It may be shown[5] that to a first-order approximation the "Q" of the resonant system treated as a simple system having lumped constants, is given by

$$Q = \omega_0/\Delta\omega \qquad (7)$$

where ω_0 is the resonant angular frequency, $\Delta\omega$ is the band width.

The band width is the angular frequency interval between the angular frequencies on each side of resonance at which the amplitude is 0.707 that at

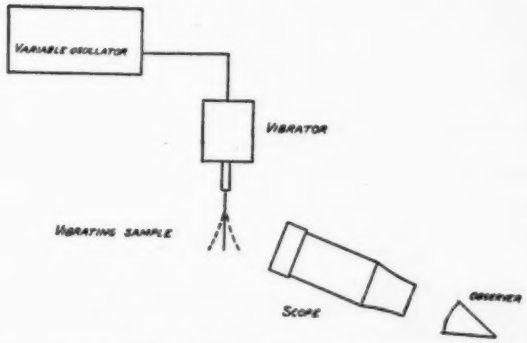

FIG. 5. Schematic of intermediate frequency (flexural vibration) equipment.

resonance. The amplitude may be measured with the aid of a microscope micrometer eyepiece.

Once the Q of the system is measured it is possible to obtain the relaxation time directly. To do this the resonant system (with lumped constants) is replaced by an equivalent network in which the inductance L replaces the lumped mass, the resistance R replaces the coefficient of internal viscosity and the capacity C is associated with the reciprocal of the modulus of elasticity. In this circuit, the following relations hold

$$Q = \omega_0 L/R \qquad (8)$$

$$\omega_0 = (LC)^{-\frac{1}{2}}. \qquad (9)$$

Combining these we obtain,

$$Q = 1/\omega_0 RC \qquad (10)$$

which is equivalent to

$$Q = 1/\omega_0 \tau \qquad (11)$$

since $\tau = RC = \gamma/E$. Thus a knowledge of Q and ω_0 permits the calculation of τ and finally γ since E is known. It is emphasized here that the relations

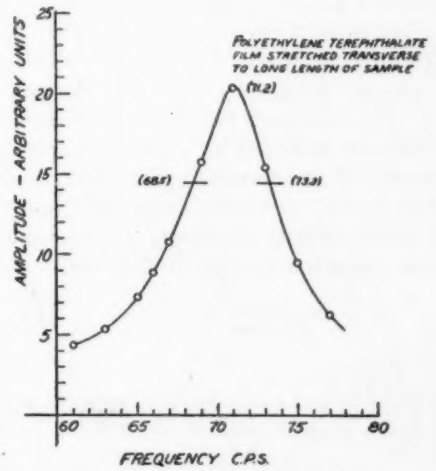

FIG. 6. Example of data taken with the apparatus of Fig. 5; vibration amplitude *vs.* frequency.

[5] A. W. Nolle, J. App. Phys. **19**, 753 (1948).
[6] Harry F. Olson, *Elements of Acoustical Engineering* (D. Van Nostrand Company, Inc., New York, 1947), p. 52.

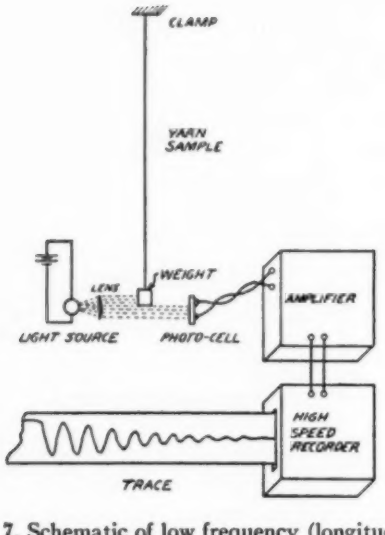

FIG. 7. Schematic of low frequency (longitudinal vibration) equipment.

given are approximate i.e., Eqs. (6) and (7) give errors in E and Q of the order of $1/2Q^2$ or 2 percent for a Q of 5. In most cases the application of these equations to high polymers is justified however. A thorough discussion of this method and the approximations is given in reference 5.

Figure 6 gives a plot of vibration amplitude *vs.* frequency (rather than angular frequency) for a film sample of polyethylene terephthalate polymer stretched four times and measured in the transverse direction with the arrangement of Fig. 5. The film sample was 0.003-cm thick, 0.860-cm long and about 1-mm wide. The band width is 4.8 c.p.s., the resonance frequency 71.2 c.p.s. and the Q is therefore 14.8.

LOW FREQUENCY MEASUREMENTS

For measurements in the frequency range 2–20 c.p.s., a useful technique involves free longitudinal vibrations of a long yarn or monofil sample with an attached mass as shown in Fig. 7. The length of the yarn sample (usually 2–3 meters) is adjusted to give the proper frequency after the desired load is attached. The damped vertical oscillations of the mass, which are induced by a momentary displacement downward, are recorded photoelectrically with the aid of a d.c. amplifier and high speed, fast-response direct inking recorder. The complete system can be adjusted so that it is linear.

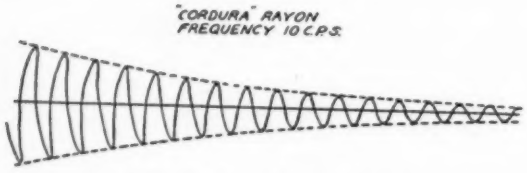

FIG. 8. Example of data taken with the apparatus of Fig. 7; damped oscillation record.

Figure 8 is a typical trace, in this case of a sample of du Pont "Cordura" rayon yarn, and Fig. 9 shows the same data in which the logarithm of the amplitude is plotted *versus* distance. The slope is the logarithmic decrement. Figure 8 also gives the frequency of free oscillation since the chart speed is known.

To convert the resonance frequency and logarithmic decrement into the parameters of the equivalent Voigt model we may first compute the spring constant and dashpot viscosity representative of the sample (rather than the material itself) and then get the modulus of elasticity and coefficient of internal viscosity. It is known[7] that in a system composed of a mass of m grams attached to a spring of constant G dynes/cm coupled in parallel with a dashpot of viscosity η dyne sec./cm the natural angular frequency of free vibration is given by

$$\omega = (G/m - \eta^2/4m^2)^{\frac{1}{2}} \text{ c.p.s.} \qquad (12)$$

Also, the logarithmic decrement is

$$\delta = \pi\eta/m\omega \text{ per cycle.} \qquad (13)$$

From these relations G and η may be computed from measurements of ω and δ; generally the second term under the radical in expression (12) may be neglected.

To convert G and η to a modulus of elasticity E and a coefficient of internal viscosity γ representative of the material itself rather than the sample we note[8] that:

$$E = (l/a)G \quad \text{dynes/cm}^2 \qquad (14)$$

$$\gamma = (l/a)\eta \quad \text{dyne sec./cm}^2 \qquad (15)$$

where l = sample length in cm, a = sample cross-sectional area in cm^2.

As before, the relaxation time is given by

$$\tau = \gamma/E = \eta/G. \qquad (16)$$

OTHER DERIVED QUANTITIES

To summarize the above, we may say that by measurements of α, Q or δ along with measurements of velocity or resonance frequency, it is possible to characterize the viscoelastic part of the experimental arrangement, i.e., the polymer sample, by deriving in each case from these experimental quantities a modulus of elasticity, a coefficient of internal viscosity and a relaxation time representative of the polymer under the conditions of the test. In addition it is possible to derive other quantities having physical significance which are useful in characterizing a polymer such as the mechanical

[7] Leigh Page, *Introduction to Theoretical Physics* (D. Van Nostrand Company, Inc., New York, 1935).

[8] S. D. Gehman, D. E. Woodford, and R. B. Stambaugh, Ind. Eng. Chem. **33**, 1032 (1941).

power factor[3] loss tangent,[5] specific damping capacity,[9] dynamic work recovery or resilience,[8] etc.; and also to compute the power dissipated as heat as well as the heat loss per cycle.[8] The above quantities are, of course, not independent since they are all functions of the relaxation time. To a first approximation the power factor of the mechanical impedance associated with the polymer is given by

$$\cos\theta = \omega\tau. \tag{17}$$

Here θ is the phase angle between velocity and force. For small damping this is identical with the loss tangent, $\tan\phi$, where ϕ is the phase angle between displacement and force. The specific damping capacity is the ratio of the energy dissipated per cycle to the average energy of vibration and is given approximately by

$$\Delta W/W = 1 - e^{-2\pi\omega\tau}. \tag{18}$$

Similarly the ratio of the energy recovered per cycle to the average energy is

$$1 - \Delta W/W = e^{-2\pi\omega\tau}. \tag{19}$$

This has been called the resilience but the term dynamic work recovery is preferred.

If we consider the heating effect of cyclical differential deformations, it is necessary to distinguish between two cases if comparisons between polymers are to be made. We may compare their behavior under the condition where the applied cyclical force per unit area is the same in all cases or under the condition that the differential elongation is held constant. Appendix II shows that the expressions given in Table I apply. It is emphasized that the relaxation time used must be that measured at the frequency in question.

To obtain the heating effect of a cyclical differential oscillation we divide the power expressions given in the top line of Table I by $4.18\times10^{7}\rho s$ where s = specific heat in cal./g/degree, ρ = density in g/cc. The result is the rate of heating in degrees C per second, assuming no conduction or radiation losses from the sample.

$$(\text{Rate})_{T=\text{Const.}} = 2.39\times10^{-8}T^2\omega^2\tau/E\rho s \quad \text{deg./sec.} \tag{20}$$

$$(\text{Rate})_{e=\text{Const.}} = 2.39\times10^{-8}e^2\omega^2\tau E/\rho s \quad \text{deg./sec.} \tag{21}$$

TYPICAL EXPERIMENTAL RESULTS

The Effect of Frequency

Table II presents results which exemplify the application of the techniques discussed. In this particular case the effect of frequency on the dynamic characteristics of a yarn sample of polyethylene terephthalate polymer was determined.

[9] C. Zener, J. App. Phys. 18, 1022 (1947).

TABLE I. Power and energy loss relations.

	Constant force/ unit area	Constant elongation	Units
Power dissipated per unit volume*,†	$T^2\omega^2\tau/E$	$e^2\omega^2\tau E$	ergs/sec./cm³
Energy dissipated per cycle per unit volume*,†	$2\pi T^2\omega\tau/E$	$2\pi e^2\omega\tau E$	ergs/cycle/cm³

* T = applied differential tension in dynes/cm² (r.m.s.).
† e = applied differential elongation in cm/cm (r.m.s.).

The load in each case was just about sufficient to straighten the sample. It is seen that there is a definite increase of dynamic modulus with frequency over the frequency range covered, but that the value at 8.1 c.p.s. is somewhat smaller than the "static" value obtained from a stress-strain curve. As expected the coefficient of internal viscosity and relaxation time decrease with an increase in frequency. It is noted that the attenuations are very much smaller than those encountered with rubber.

The change of relaxation time with frequency is shown in Fig. 10, which combines the results of Tables II and III with other determinations made at various times. The inverse relation exhibited implies the relative constancy of the product $\omega\tau$, a result noted by other investigators.

The Effect of Physical State

Table III compares the dynamic characteristics of this particular polymer for various states of crystallinity and orientation. Orientation has the greatest effect by far and results in an increase in both the dynamic modulus and the coefficient of internal viscosity. This results in a remarkable constancy of relaxation time, the value of which seems to be associated more with the chemical structure of the polymer than its physical state. Other measurements not reported here seem to bear out the suggestion that the relaxation time at a particular frequency is relatively independent of physical state, at least over the frequency range considered here. Figure 10 also illustrates this.

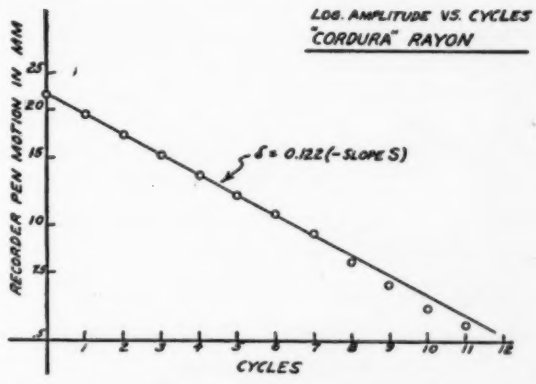

FIG. 9. Plot used in calculating logarithmic decrement from the data of Fig. 8.

TABLE II. Effect of frequency on dynamic characteristics of polyethylene terephthalate polymer (yarn) high orientation, low crystallinity, density 1.4.

Frequency, c.p.s.	Velocity cm/sec.	Attenuation 1/cm	Log dec.	$\omega\tau$	Q	Modulus dynes/cm²	Viscosity dyne sec./cm²	Rel. time sec.	Work rec. %
Static†	—	—	—	—	—	14.5×10^{10}	—	—	—
8.1	**3.0×10^5	* 0.002×10^{-3}	0.087	0.027	37	12.0×10^{10}	648×10^5	540×10^{-6}	85
8,000	3.3×10^5	5.0×10^{-3}	*0.205	0.065	15.3	15.3×10^{10}	2.0×10^5	1.3×10^{-6}	66
12,000	3.3×10^5	7.0×10^{-3}	*0.192	0.061	16.4	15.3×10^{10}	1.24×10^5	0.8×10^{-6}	69
16,000	3.3×10^5	8.5×10^{-3}	*0.173	0.055	18.2	15.3×10^{10}	0.84×10^5	0.55×10^{-6}	72
34,000	3.4×10^5	30×10^{-3}	*0.300	0.096	10.4	16.3×10^{10}	0.73×10^5	0.45×10^{-6}	55

* Calculated from the relation $\delta=\lambda\alpha=c\alpha/f$.
** Calculated from the relation $c=(E/\rho)^{\frac{1}{2}}$.
† Static value at 10 percent per minute elongation rate obtained from stress-strain curve.

Heating Effects

If we apply the expressions for heating rate given in Eqs. (20) and (21) to typical unoriented and oriented yarn samples of polyethylene terephthalate polymer we find the results given in Table IV, for two frequencies and the two methods of comparison. The differences between the two physical states and the two methods of comparison are evident. In the first case where the two states are compared with the differential tension held constant, it is seen that the unoriented state heats up the faster whereas in the second case, the oriented heats up more rapidly.

The absolute magnitudes of the heating rates are also of interest. If we consider a 1 percent elongation, it is seen that the oriented yarn sample has a 0.67 degree C per second rise compared with a 0.15 degree C per second rise in the unoriented case at 8 c.p.s. assuming no conduction or radiation losses. The importance of this aspect of characterization to tire cord behavior is evident.

Modulus *Versus* Temperature Curves

The sonic interferometer and vibrating reed have both been used to measure the temperature dependence of the dynamic modulus; the first with yarns and the second with film samples. In both cases slight modifications of the apparatus are required.

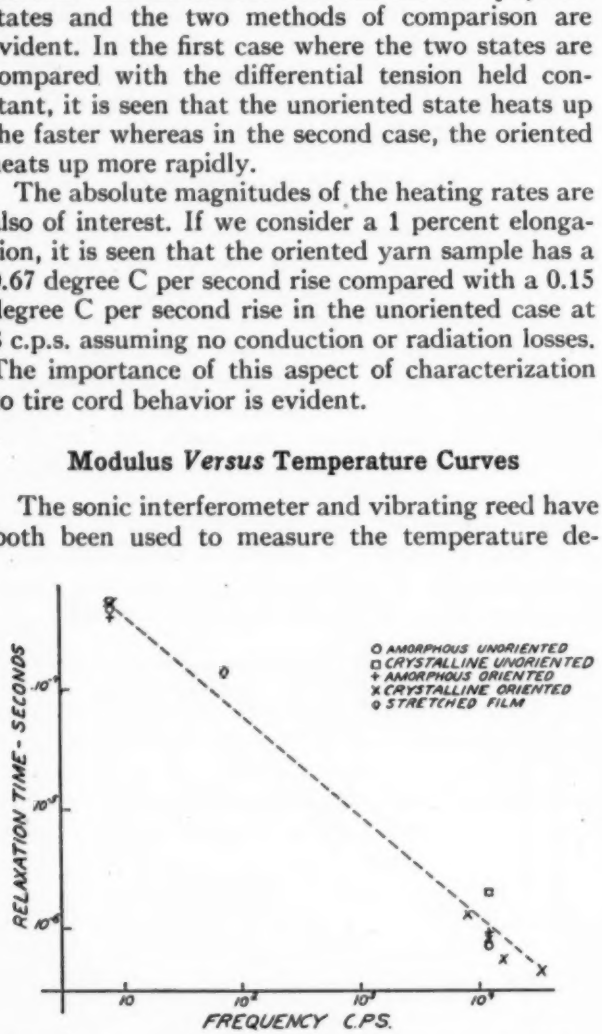

FIG. 10. Relaxation time *versus* frequency for polyethylene terephthalate polymer in various physical states.

In the case of the sonic interferometer (Fig. 1) the device was adapted for fixed path operation rather than fixed frequency, by removing the filters and setting the pick-up crystal 30 cm away from the driver. The 30-cm space is provided with a heater consisting of a Pyrex tube wrapped with wire. The temperature, measured by thermocouples, is controlled by a Variac. Slotted end shields protect the crystal and driver and still permit the yarn sample to be strung through the heater tube and be held in place under a slight tension. This scheme has been used for measurements from room temperature to about 200°C.

With the yarn sample in place the frequency is varied until the yarn is in fundamental longitudinal resonance, as indicated by a maximum voltage reading. Since the velocity is known from a previous determination at room temperature using the fixed frequency method described above, it is possible to estimate the fundamental resonance frequency, as approximately

$$f_0=c/2l \tag{22}$$

where f_0=fundamental resonance frequency c.p.s., c=velocity of sound cm/sec., l=distance between driver and pick-up cm. Generally only fair agreement between the actual resonance frequency and that predicted by (22) is found because of undetermined end effects. However, change in modulus with temperature may be followed by noting how the fundamental resonance frequency changes with temperature and computing the modulus at any temperature T from

$$E_T=E_0(f_T/f_0)^2 \tag{23}$$

where E_T=modulus at temperature T, E_0=modulus at room temperature (measured by fixed frequency method), f_T=resonance frequency at temperature T, f_0=resonance frequency at room temperature.

Figure 11 shows data taken this way on poly-

TABLE III. Effect of orientation and crystallinity at 8 c.p.s. polyethylene terephthalate polymer (yarn).

Sample	Orientation	Crystallinity	Log dec.	$\omega\tau$	Q	Modulus dynes/cm²	Viscosity dyne sec./cm²	Rel. time sec.	Work recovery %
1	None	None	0.075	0.024	42	2.3×10^{10}	11.1×10^{6}	4.8×10^{-4}	86
2	None	High	0.087	0.028	36	0.95×10^{10}	5.3×10^{6}	5.6×10^{-4}	85
3	High	None	0.066	0.021	48	11.4×10^{10}	46.7×10^{6}	4.1×10^{-4}	88
4	High	Low	0.087	0.027	37	12.0×10^{10}	64.8×10^{6}	5.4×10^{-4}	85

ethylene terephthalate in various states. Again orientation has a marked influence on the behavior. It is noted that the first break in the curve (concave downward) occurs in the region of 70°C for the unoriented state, whereas it is near 90°C for the oriented. The second or concave upward break occurs at approximately 130°C and 150°C depending on orientation again. The latter type of break has been referred to as a "cold point"[10] in connection with plastics, but a more descriptive term should be found which would bring out the significance of the break when it is established.

Outside of a small increase in modulus, which is probably due to increased orientation, the crystalline-oriented sample has about the same characteristics as the amorphous-oriented state. It appears that crystallinity has a very small effect on the dynamic behavior of this particular polymer.

To apply the vibrating reed technique (Fig. 5) to the study of the temperature dependence of modulus, it has been found convenient to isolate the driver from the oven or cold chamber. To do this a loudspeaker element is substituted for the phonograph cutter head and provided with a glass rod several inches long connected to the voice coil of the speaker. The sample to be measured is attached to the end of the rod. In this way the sample may be put into a cold or hot chamber and the driver kept at room temperature.

Using a flask surrounded by alcohol-dry ice mixtures as the cold chamber, the data of Fig. 12 were taken. Thermocouples provided measures of the ambient air temperature as well as the temperature of the rod holding the sample. Figure 12 shows that polythene has the same general type of curve exhibited by polyethylene terephthalate except that both breaks are shifted to the region below room temperature.

This type of curve seems to characterize the modulus-temperature behavior of a large number of plastics and high polymers and is also obtained from essentially static measurements.[10]

ACKNOWLEDGMENT

The authors wish to thank the management of the Technical Division, Rayon Department, E. I. du Pont de Nemours and Company for permitting this material to be published.

[10] H. W. Moll and W. J. LeFevre, Ind. Eng. Chem. 40, 2172 (1948).

TABLE IV. Heating rate in degrees C per second polyethylene terephthalate polymer.

Constant differential force per unit area

State	Frequency 8 c.p.s.	Frequency 12,000 c.p.s.
Unoriented	$0.30\times10^{-17}T^2$	$845\times10^{-17}T^2$
Oriented	$0.05\times10^{-17}T^2$	$212\times10^{-17}T^2$

T = Differential tension in dynes/cm² (r.m.s.)

Constant differential elongation

State	Frequency 8 c.p.s.	Frequency 12,000 c.p.s.
Unoriented	$0.15\times10^{4}e^2$	$610\times10^{4}e^2$
Oriented	$0.67\times10^{4}e^2$	$4100\times10^{4}e^2$

e = Differential elongation in cm/cm (r.m.s.)

APPENDIX I

The Measurement of Small Acoustic Attenuation in Fibers

Figure 1 represents the experimental set-up employed in measuring acoustic attenuation in polymers. The driver excites longitudinal oscillations in the sample which progress down it as a wave. Let us assume that the longitudinal displacement is representable by

$$\xi = A_1 e^{-\alpha x}\exp(j(\omega t - 2\pi x/\lambda)) + A_2 e^{\alpha x}\exp(j(\omega t + 2\pi x/\lambda)) \quad \text{(A1)}$$

where ξ = displacement, α = attenuation, x = distance from origin to point considered, λ = wavelength. The first part of the expression represents a wave propagated in the $+x$ direction (from right to left in Fig. 1) and the second part is a wave (reflected) propagated in the $-x$ direction.

Between driver and pick-up

$$\xi_1(x) = A[e^{-\alpha x}e^{-2\pi jx/\lambda} - Re^{-\alpha(2l-x)}e^{j\phi} \times\exp(-2\pi j(2l-x)/\lambda)]e^{j\omega t} \quad \text{(A2)}$$

where l is the distance between the driver and pick-up. To the left of the pick-up

$$\xi_2(x) = Be^{-\alpha x}e^{-2\pi jx/\lambda}e^{j\omega t} \quad \text{(A3)}$$

where we make use of a reflection coefficient de-

fined by

$$\frac{\text{complex amplitude of reflected wave}}{\text{complex amplitude of incident wave}} = -Re^{i\phi} \quad \text{(A4)}$$

here ϕ is an angle whose value depends on the conditions of reflection occurring at the sample-crystal junction. We apply the boundary conditions,

$$\text{at} \quad x=0 \quad \xi_1(0)=\xi_0 e^{j\omega t} \quad \text{(A5)}$$

$$\text{at} \quad x=l \quad \xi_1(l)=\xi_2(l). \quad \text{(A6)}$$

And obtain for the displacement between the driver and the pick-up

$$\xi_1(x)=\frac{[e^{-\alpha x}e^{-2\pi jx/\lambda}-Re^{j\phi}e^{-\alpha(2l-x)}\exp(-2\pi j(2l-x)/\lambda)]\xi_0 e^{j\omega t}}{1-Re^{j\phi}e^{-2\alpha l}e^{-4\pi jl/\lambda}}. \quad \text{(A7)}$$

For our immediate purpose, we need only the displacement at the distance l, which is the displacement of the pick-up crystal. Expression (A7) reduces to (for $x=l$):

$$\xi_1(l)=\frac{[1-2R\cos\phi+R^2]^{\frac{1}{2}}\xi_0 e^{-\alpha l}e^{-j\theta}e^{j\omega t}}{[1-2Re^{-2\alpha l}\cos(\phi-4\pi l/\lambda)+R^2e^{-4\alpha l}]^{\frac{1}{2}}} \quad \text{(A8)}$$

where

$$\tan\theta=\frac{(1-R^2e^{-2\alpha l})\sin(2\pi l/\lambda)+R(1-e^{-2\alpha l})\sin(\phi-2\pi l/\lambda)}{(1+R^2e^{-2\alpha l})\cos(2\pi l/\lambda)-R(1+e^{-2\alpha l})\cos(\phi-2\pi l/\lambda)}. \quad \text{(A9)}$$

If $\phi=0$, then Eq. (A9) reduces to[11]

$$\tan\theta=\frac{1+Re^{-2\alpha l}}{1-Re^{-2\alpha l}}\tan(2\pi l/\lambda). \quad \text{(A9a)}$$

The expression for $\tan\theta$ tells how the phase of the motion varies as we progress down the sample. Calling the product of all terms independent of l in the numerator of (A8) K, we have for the voltage developed by the pick-up crystal [since it is proportional to $\xi_1(l)$]:

$$V=\frac{Ke^{-\alpha l}}{[1-2Re^{-2\alpha l}\cos(\phi-4\pi l/\lambda)+R^2e^{-4\alpha l}]^{\frac{1}{2}}}. \quad \text{(A10)}$$

A similar result is given in reference 11. When $\alpha l>2.3$ nepers i.e. for $l>10$ cm and when $\alpha>0.23$ nepers/cm (>2 db/cm), then expression (A10) approximates to within 1 percent to

$$V=Ke^{-\alpha l}. \quad \text{(A11)}$$

This result may be applied to highly absorbing polymers (e.g. rubber) and α may be measured from a plot of $\log V$ *vs.* distance of pick-up from source. However, when α is small (less than about 0.5 db/cm), the above result will not hold. In this case, we observe that (A8) may be written as

$$V=\frac{K'}{\left[\frac{1}{R}e^{2\alpha l}-2\cos(\phi-4\pi l/\lambda)+Re^{-2\alpha l}\right]^{\frac{1}{2}}}. \quad \text{(A12)}$$

A plot of V against l will have the shape shown in Fig. 13. A number of maxima and minima due to standing waves occur at points given approximately by the condition that:

$$\cos(\phi-4\pi l/\lambda)=\pm 1. \quad \text{(A13)}$$

This occurs every half wave-length. The equations of the envelope curves are, where $R=e^{-2\beta}$:

$$V_{\max}=K'/[e^{2(\alpha l+\beta)}+e^{-2(\alpha l+\beta)}-2]^{\frac{1}{2}}$$
$$=K'/2\sinh(\alpha l+\beta) \quad \text{(A14)}$$

$$V_{\min}=K'/[e^{2(\alpha l+\beta)}+e^{-2(\alpha l+\beta)}+2]^{\frac{1}{2}}$$
$$=K'/2\cosh(\alpha l+\beta). \quad \text{(A15)}$$

Dividing (15) by (14) yields

$$V_{\min}/V_{\max}=\tanh(\alpha l+\beta) \quad \text{(A16)}$$

or

$$\tanh^{-1}(V_{\min}/V_{\max})=\alpha l+\beta. \quad \text{(A17)}$$

Thus, a plot of $\tanh^{-1}(V_{\min}/V_{\max})$ *versus* l gives a straight line whose slope is α and whose intercept is β, from which R may be calculated. The attenua-

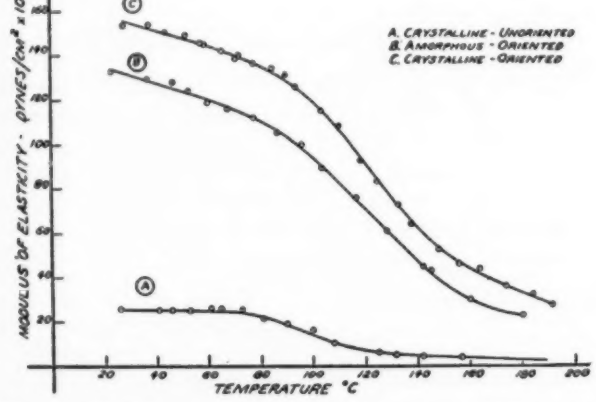
A. CRYSTALLINE - UNORIENTED
B. AMORPHOUS - ORIENTED
C. CRYSTALLINE - ORIENTED
MODULUS OF ELASTICITY - DYNES/cm² x 10⁻⁹
TEMPERATURE °C

FIG. 11. High frequency (sonic) modulus *versus* temperature for polyethylene terephthalate in various physical states.

[11] The same result is given by K. W. Hillier, H. Kolsky and J. P. Lewis, J. App. Phys. **20**, 207 (1949).

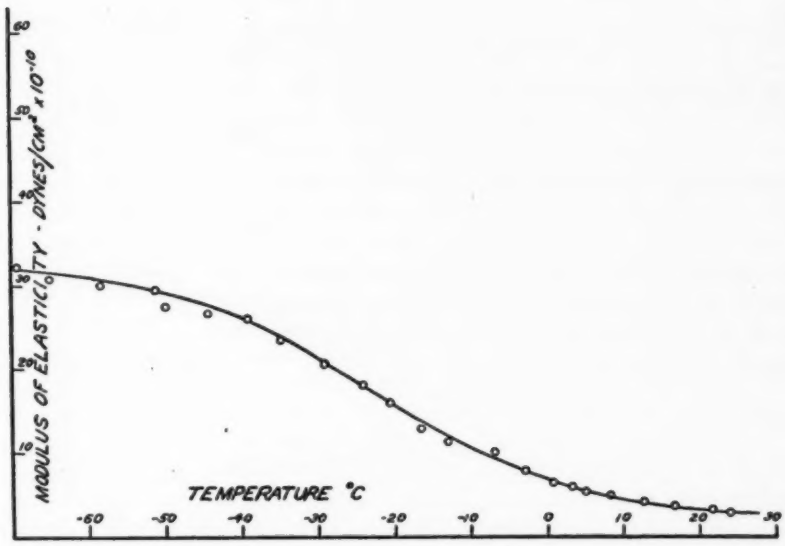

FIG. 12. Intermediate frequency (flexural vibration) modulus *versus* temperature for polythene.

tion so calculated is in nepers per cm. This may be converted to db per cm by multiplying by 8.686.

APPENDIX II

Heating Effects in Yarns During Cyclical Oscillation

Consider a given length of yarn having the following characteristics.

- l length in cm
- a cross-sectional area in cm²
- E modulus of elasticity in dynes/cm²
- γ coefficient of internal viscosity in dyne sec./cm²
- G spring constant in dyne/cm
- η dashpot viscosity in dyne sec./cm.

Here E and γ are representative of the material from which the yarn is made whereas G and η are the constants of the equivalent Voigt model which represents the yarn *sample* under consideration. The following relations hold:

$$G = aE/l \tag{B1}$$

$$\eta = a\gamma/l. \tag{B2}$$

If this yarn sample is subjected at a certain angular frequency ω to a dynamic force F in dynes (r.m.s.), equivalent to a dynamic tension $T = F/a$ dynes/cm² (r.m.s.), a cyclical extension x in cm (r.m.s.) or elongation $e = x/l$ will occur and a certain power dissipation p in ergs/sec. will result. This may also be expressed as the energy dissipated as heat in ergs per cycle h.

If this yarn sample is represented by a series electrical network of a capacity C and resistance R, then G is equivalent to $1/C$, η to R, the force F to the voltage V and the velocity of motion v to the current I, all values being r.m.s. In the network

$$\cos\theta = R/Z \tag{B3}$$

$$Z = (R^2 + (1/\omega C)^2)^{\frac{1}{2}}. \tag{B4}$$

The power dissipation is

$$p = VI\cos\theta. \tag{B5}$$

If $R \ll (1/\omega C)$, then

$$\cos\theta = \omega RC = \omega\tau. \tag{B6}$$

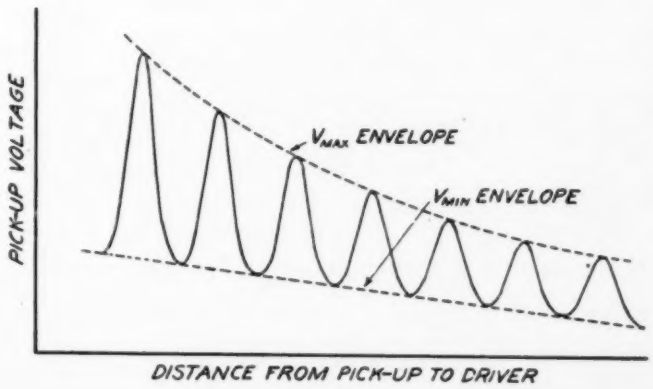

FIG. 13. General type of curve obtained with the sonic interferometer of Fig. 1.

Thus

$$p = VI\omega\tau, \tag{B7}$$

or, in equivalent mechanical terms,

$$p = Fv\omega\tau \tag{B8}$$

and the energy dissipated per cycle is,

$$h = 2\pi Fv\tau. \tag{B9}$$

To throw these relations into useful form we distinguish two cases; (A) where the force F or tension T is explicit and (B) where the extension x or elongation e is explicit.

Case A

For small damping, $v = F\omega/G$ and expression (B8) becomes

$$p = F^2\omega^2\tau/G \tag{B10}$$

or, using (B1) and converting to tension,

$$p = T^2\omega^2\tau al/E. \tag{B11}$$

Thus the power dissipated per unit volume is

$$P = T^2\omega^2\tau/E \text{ ergs/sec./cm}^3, \tag{B12}$$

and the heat loss per cycle per unit volume is

$$H = 2\pi T^2\omega\tau/E \text{ ergs/cycle/cm}^3. \tag{B13}$$

Case B

Since $F = xG$ for small damping and $v = \omega x$ we may write (B8) as

$$p = \omega^2 x^2 G\tau. \tag{B14}$$

Using relation (B1) and converting to elongation, (B14) becomes

$$p = e^2\omega^2\tau al E. \tag{B15}$$

Thus the power dissipated per unit volume is

$$P = e^2\omega^2\tau E \text{ ergs/sec./cm}^3, \tag{B16}$$

and the heat loss per cycle per unit volume is

$$H = 2\pi e^2\omega\tau E \text{ ergs/cycle/cm}^3. \tag{B17}$$

Equation of State for Polystyrene*

R. S. Spencer and G. D. Gilmore
The Dow Chemical Company, Midland, Michigan

Practical considerations emphasize the desirability of formulating an adequate equation of state for polystyrene. A fairly satisfactory one is this simplified version of van der Waals' equation,

$$(P+\pi)(V-\omega) = nRT,$$

where π is the internal pressure (or cohesive energy density) and ω is the volume at absolute zero, by extrapolation. Evaluating constants from thermal expansion data and expressing P in p.s.i., V in cc per gram, and T in degrees Kelvin, this becomes

$$(P+27{,}000)(V-0.822) = 11.6T.$$

Agreement with compressibility measurements, which are described in some detail, is good. Discrepancies with room temperature values of sound velocity and cohesive energy density by swelling measurements are discussed briefly.

INTRODUCTION

VERY little work on the compressibility of high polymers has been reported in the literature, with the notable exception of rubber.[1,2] The volume-temperature relationship for polystyrene has been studied in some detail by a number of workers[3–10] but little has been done on the volume-pressure relationship. This becomes important in the consideration of some problems arising in the fabrication of polystyrene, and thus the present study was initiated.

As was found to be the case with rubber, and indeed with many liquids, the compressibility coefficient was not constant, but depended upon both the temperature and pressure. It was therefore thought desirable to attempt to formulate an equation of state to relate volume to pressure and temperature, and thus correlate thermal expansion

* Presented at the Sixth Meeting of the Division of High-Polymer Physics, American Physical Society, New York City, January 27–29, 1949.

[1] L. H. Adams and R. E. Gibson, J. Wash. Acad. Sci. **20**, 213 (1930).

[2] A. H. Scott, J. Research Nat. Bur. Stand. **14**, 99 (1935).

[3] Alfrey, Goldfinger, and Mark, J. App. Phys. **14**, 700 (1943).

[4] R. F. Boyer and R. S. Spencer, J. App. Phys. **15**, 398 (1944).

[5] R. F. Boyer and R. S. Spencer, J. App. Phys. **16**, 594 (1945).

[6] E. Jenckel and K. Ueberreiter, Zeits. f. physik. Chemie **A182**, 361 (1938).

[7] W. Patnode and W. J. Scheiber, J. Am. Chem. Soc. **61**, 3449 (1939).

[8] R. S. Spencer, J. Colloid Sci., in press.

[9] R. S. Spencer and R. F. Boyer, J. App. Phys. **17**, 398 (1946).

[10] F. Wiley, Ind. Eng. Chem. **34**, 1052 (1942).

and compressibility data. This would seem, *a priori*, a rather large task, inasmuch as the system is not only highly condensed but also involves very complex molecules. It is a little surprising, then, to find that a simplified van der Waals' equation works quite well within the range of variables practical and customary in fabrication. This equation contains two constants to be determined, the irreducible volume, or volume at zero degrees Kelvin, and the internal pressure. Both of these constants can be evaluated from thermal expansion measurements carried out at atmospheric pressure.

In considering the computation of internal pressure from thermal expansion data, cognizance must be taken of the fact, pointed out by Simha,[11] that isothermal or isobaric volume changes are brought about by two mechanisms. One is instantaneous and the other time dependent. The thermal expansion coefficient,[8] and thus the internal pressure, is determined by experimental conditions, insofar as these determine the relative contributions of the two mechanisms in a given circumstance.

Having determined the value of the internal pressure for equilibrium conditions and for the case in which only the instantaneous mechanism contributes, we shall see how well the equation of state describes our compressibility experiments. In addition, comparisons can be made with velocity of sound measurements and with the cohesive energy density of polystyrene as determined by swelling in various solvents.

Refinements in our very simple equation are altogether possible, and indeed probably necessary if any very considerable extension of the range of variables is contemplated. However, we wish to point out that its very simplicity, economy of constants, ease of handling, and reasonably adequate description of experimental behavior, render it convenient for practical work. For this purpose it has been developed, and for this purpose it is now being used.

EXPERIMENTAL METHODS

Figure 1 shows the special mold used for isothermal compression measurements with polystyrene. It consists of a cylindrical specimen cavity one square inch in cross-sectional area, with a close-fitting plunger for compressing the polymer. This plunger also contains a cavity which opens into a groove machined in the wall of the specimen cavity. This plunger cavity is filled with polymer, which is forced into the groove and acts as a seal for the sample in the main cavity. In operation, then, force is applied to the smaller central plunger, and the larger plunger directly contacting the sample "floats."

Specimens were prepared by extruding hot polymer into the mold cavity, taking care to avoid trapping bubbles. After cooling, the piece was removed, inspected for bubbles, and a section $\frac{3}{4}$ inch in length cut from it. Some measurements were made with samples machined from blocks of polystyrene, but no differences attributable to sample preparation technique were noted. The mold was then assembled with the specimen in place, the floating plunger filled with the same polymer, and the whole brought to thermal equilibrium at the desired temperature.

Pressure was applied to the specimen by placing the mold between the platens of a previously calibrated compression press. Change in volume was measured with a dial micrometer mounted between the lower press platen and an indicating arm on the floating plunger. The pressure was increased in increments of about 1300 pounds per square inch, to a maximum pressure of 29,700 p.s.i., the sample volume being recorded at each pressure. Four such runs were made at each set of conditions and the results averaged. Some difficulty was usually experienced in getting a reproducible reading of the micrometer at zero pressure, and a suitable extrapolation of the low pressure data was therefore necessary.

Heat was supplied by an electrical band heater which surrounded the mold. Temperature control, as indicated by the thermocouples shown in Fig. 1, was to about $\pm 1°C$.

The efficiency of the polymer seal in this mold was illustrated by the fact that the weights of the specimens before and after measurements commonly agreed to within 0.1 percent.

No correction was made for change in volume of the cavity due to the elasticity of the metal.

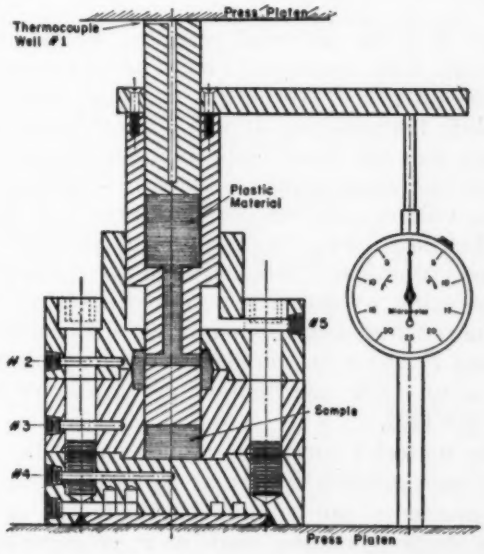

FIG. 1. Mold for compressibility measurements.

[11] R. Simha, Ann. N. Y. Acad. Sci. **44**, 297 (1943).

TABLE I. Internal pressure of 360,000 molecular weight polystyrene from compressibility measurements at 204°C.

$\bar{P}$	π
2,050 p.s.i.	29,250 p.s.i.
3,350	27,950
4,600	26,450
5,900	29,300
7,250	28,150
8,500	27,350
9,850	25,550
11,200	29,000
12,550	25,150
13,850	23,650
15,200	28,600
16,550	24,150
17,850	23,050
19,150	23,850
21,500	20,500
24,850	18,750
28,100	15,900
	Average = 25,100

TABLE II. Internal pressure of 321,000 molecular weight polystyrene from compressibility measurements.

$\bar{P}$	π(177°C)	π(204°C)	π(232°C)
2,050 p.s.i.	28,450 p.s.i.	29,000 p.s.i.	30,350 p.s.i.
3,350	27,150	27,700	29,050
4,600	26,600	27,600	26,300
5,900	29,500	29,500	28,300
7,250	29,550	27,550	27,200
8,550	28,700	28,100	26,850
9,850	27,400	26,150	25,250
11,200	31,800	29,600	28,000
12,550	27,750	27,400	23,950
13,850	29,750	29,650	26,650
15,200	31,600	34,800	31,900
16,550	29,350	30,850	27,450
17,850	28,950	28,650	29,150
19,150	25,250	28,150	27,050
21,500	25,000	26,000	27,400
24,850	23,750	23,050	25,150
28,100	20,300	21,900	20,400
	Average = 27,700	29,000	27,100

Rough calculation showed that this correction amounted to less than 2 percent of the observed volume change, at maximum pressure, and it was subsequently neglected.

The materials used in these measurements were unfractionated, commercial polystyrenes. The molecular weights of two of these are indicated in the tables given in the next section. Observations recorded for a variety of commercial polystyrenes show that there is very little difference in their behavior in compression, it apparently being characteristic for the polymer.

DISCUSSION

The equation of state which we wish to propose for polystyrene is the following,

$$(P+\pi)(V-\omega)=RT,$$

where P is the external pressure, π the internal pressure, V the volume of a basal mole, ω the volume at absolute zero, R the gas constant, and T the absolute temperature. It will be noted that this is merely van der Waals' equation, simplified by the assumption that the internal pressure is independent of the volume over our range of practical interest. The justification for this assumption, and indeed for the equation itself, must rest in its usefulness in representing available experimental observations. In the remainder of this paper we shall most often express P and π in pounds per square inch and V and ω in cubic centimeters per gram, in which case $R=11.6$.

The material constants π and ω may be calculated from published thermal expansion data. Such measurements are commonly made at or near atmospheric pressure, and if π is considerably larger than atmospheric pressure we can let $P=0$ and write

$$V=\omega+11.6T/\pi.$$

Assuming that polystyrene has a density of 1.05 g per cc at 25°C, and using Spencer and Boyer's[9] value of $dV/dT=4.33\times10^{-4}$ under equilibrium conditions, we find that $\omega=0.822$ cc per g. Now

$$\pi=11.6/(\partial V/\partial T)_{P=0},$$

and the question arises as to the value of $(\partial V/\partial T)_{P=0}$ to be used in computing the internal pressure. In considering this question we shall summarize briefly the observed thermal expansion behavior of polystyrene.

It was suggested by Simha,[11] and shown experimentally by Alfrey, Goldfinger and Mark[3] and Spencer and Boyer,[9] that volume changes in polystyrene are accomplished by two mechanisms. In one the "average space" occupied by each molecule changes due to a change in the thermal energy of the molecule. This is analogous to the volume change of a crystalline solid and is practically instantaneous in its response to a change in the variables of state. The second mechanism may be thought of as a change in the equilibrium positions of the molecules, or segments of molecules; Alfrey, Goldfinger, and Mark refer to it as the diffusion of "holes" into or out of the polymer. Such a change is resisted by the "volume viscosity" of the polymer, and thus occurs at a rate which depends upon the temperature in the same manner as does a fluidity. In the neighborhood of room temperature this second mechanism is so slow that most changes involve only the instantaneous mechanism. At higher temperatures and/or under equilibrium conditions both mechanisms operate. Thus the experimental conditions determine whether the instan-

taneous or equilibrium expansion coefficient should be used in computing the internal pressure.

The instantaneous value of $\partial V/\partial T$ may be determined from various published data. Alfrey, Goldfinger, and Mark[3] give 2.40×10^{-4} per °C Spencer and Boyer[9] give 2.58×10^{-4}. The data of Wiley[10] give a value of 2.05×10^{-4}, and those of Patnode and Scheiber,[7] a value of 2.42×10^{-4}. The dilute solution measurements summarized in Table IV result in an average value of 2.29×10^{-4}. On the basis of these, and other results to be discussed later, we shall assume $\partial V/\partial T=2.3\times10^{-4}$ for the instantaneous mechanism. This corresponds to an internal pressure of $\pi=50{,}500$ pounds per square inch.

The equilibrium value of $\partial V/\partial T$ has been reported to be 4.30×10^{-4} by Alfrey, Goldfinger, and Mark, 4.33×10^{-4} by Spencer and Boyer, and 4.40×10^{-4} by Wiley. We shall assume a value of 4.3×10^{-4}, corresponding to an internal pressure of $\pi=27{,}000$ pounds per square inch.

Let us now consider how well these values fit in with other experimental observations. Compressibility measurements, such as those described in the preceding section, should give a value $\pi=27{,}000$ p.s.i., corresponding to equilibrium conditions, as long as the temperature is well above the apparent second-order transition temperature (in the neighborhood of 80°C). The raw data are obtained in the form of the apparent specific volume at various external pressures, where the apparent specific volume deviates from the true value by an amount which is constant throughout a single experiment. To avoid the necessity of extrapolating to zero pressure to determine this correction, we shall compute the internal pressure from the relationship

$$\pi=(-RT(\partial P/\partial V)_T)^{\frac{1}{2}}-P.$$

If sufficiently small intervals of pressure are taken, we can replace the partial derivative by $\Delta P/\Delta V$ and the pressure by $\bar{P}$, the average pressure over the interval in question. In our case, the error introduced is negligible. Table I lists the values of π, computed in this manner, as a function of the average pressure over the respective intervals. The material used was the same polystyrene (of molecular weight 360,000) used by Spencer and Boyer[9] in studying time effects in thermal expansion. It may be seen that the internal pressure remains substantially constant, subject to experimental errors, up to pressures in the neighborhood of 20,000 p.s.i., beyond which it decreases somewhat. The average value of the internal pressure over the entire range was 25,100 p.s.i., and over the range below 20,000 p.s.i. external pressure it was 26,500 p.s.i. These are in rather good agreement with the value of 27,000 p.s.i., calculated from the equilibrium expansion coefficient at atmospheric pressure.

TABLE III. Internal pressure of polystyrene from compressibility measurements at 29°C.

$\bar{P}$	π
3,350 p.s.i.	49,350 p.s.i.
4,600	42,200
5,900	41,200
7,250	45,550
8,550	37,650
9,850	39,250
11,200	37,800
12,550	40,750
13,850	34,150
15,200	31,800
16,550	32,150
17,850	32,150
19,150	37,450
21,500	31,800
24,850	27,550
28,100	23,700

In Table II are presented similar data for a different polystyrene, obtained at three different temperatures. Again, the internal pressures found agree fairly well with the value calculated from thermal expansion measurements. In addition, it is seen that there is apparently no systematic variation of π with temperature in this temperature range. The decrease in π as the external pressure exceeds 20,000 p.s.i. was again found.

Now what will be the expected behavior when only the instantaneous mechanism operates, as, for example, when measurements are made at room temperature? At low pressures the behavior would be described by $\pi=50{,}500$, corresponding to the instantaneous expansion coefficient. In addition, a consideration of the problem in terms of the two types of "free volume" present reveals that the apparent internal pressure will be more sensitive to external pressure in this case than it would if both mechanisms operated. This is shown in Table III, where the apparent internal pressure is computed from isothermal compression measurements carried out at 29°C. Here we see that the value of π at low pressures is apparently rather close to that given by the instantaneous expansion coefficient.

Another comparison can be made by considering the compressibility coefficient at low pressures. In general, the compressibility coefficient at zero external pressure is given by

$$\beta_0=-\frac{1}{V}\left(\frac{\partial V}{\partial P}\right)_T=\frac{11.6T}{\pi(\pi\omega+11.6T)}.$$

If only the instantaneous mechanism contributes to volume changes, then $\pi=50{,}500$ p.s.i., and $\beta_0=1.525\times10^{-6}$ square inch per pound at 25°C. This may be compared with a value of $\beta_0=1.50\times10^{-6}$ square inch per pound, computed by Dillon[12]

[12] R. E. Dillon, The Dow Chemical Company, Midland, Michigan, unpublished observations.

TABLE IV. Expansion of polystyrene in dilute toluene solution

Temperature	Partial specific volume	dV/dT
0°C	0.90868 cc/g	—
20	0.91341	2.365×10^{-4}
40	0.91785	2.220×10^{-4}

from measurements of the velocity of sound in polystyrene at 25°C.

The study by Boyer and Spencer[13] of the swelling of slightly crosslinked polystyrenes in various solvents provides additional information of interest. In the case of a dilute polymer solution, or a polymer swollen with a considerable amount of a good solvent, volume changes in response to temperature or pressure changes will be due in large part to the instantaneous mechanism, insofar as the polymer is concerned. The solvent molecules tend to fill in the "holes" present in the bulk polymer, or, expressed in another way, the only free volume associated with the polymer is the space swept out by the polymer segments due to their thermal energy. This may be seen in Table IV, taken from the paper by Boyer and Spencer, which lists the partial specific volume of polystyrene in dilute toluene solution. It will be noted that the expansion coefficient of polystyrene in dilute solution closely approximates the values obtained for the instantaneous expansion coefficient of the bulk polymer. The corresponding value of 50,500 p.s.i. for the internal pressure may be expressed in different units as a cohesive energy density of 83 calories per cubic centimeter. This compares very favorably with the value of 82 calories per cubic centimeter reported by Boyer and Spencer, obtained by observing the extent of swelling as a function of the cohesive energy density of the solvents employed.

[13] R. F. Boyer and R. S. Spencer, J. Polymer Sci. **3**, 97 (1948).

SUMMARY

Apparatus suitable for isothermal compressibility measurements on polystyrene was described, and its use briefly discussed. A simplified van der Waals' equation of state was proposed to relate the pressure, volume, and temperature of polystyrene, and the values of the constants computed from published data on thermal expansion at atmospheric pressure. It was pointed out that the volume changes by two mechanisms, one essentially instantaneous and one retarded. When the temperature is well above the apparent second-order transition temperature, the system is substantially at equilibrium, both mechanisms operate, and thermal expansion measurements predict an internal pressure of 27,000 p.s.i. This value agreed well with the compressibility behavior in this temperature range. At room temperature, in dilute solution, or in highly swollen gels, most of the volume change is due to the instantaneous mechanism alone, in which case we would expect an internal pressure of 50,500 p.s.i. It was shown that this value was in accord with compressibility measurements at room temperature, sound velocity measurements at room temperature, and the cohesive energy density computed from observations of the swelling of slightly crosslinked polystyrenes in various solvents. It may be concluded that the proposed equation of state adequately describes the behavior of polystyrene within the limits set forth in this study.

Creep and Damping Properties of Polystyrene*

J. A. Sauer, J. Marin, and C. C. Hsiao
Department of Engineering Mechanics, School of Engineering, The Pennsylvania State College, State College, Pennsylvania

The anelastic behavior of polystyrene has been studied by means of creep tests under long-time load application and by means of damping capacity tests under rapidly varying repeated loading. Tensile creep data taken at various stress amplitudes reveal that the log of the creep rate (at 1000 hours) varies linearly with the log of the stress amplitude. A similar type of variation is obtained when damping capacity or energy absorbed per cycle is plotted against stress amplitude. From these two sets of data, the creep rate is found to be proportional to the square of the damping capacity. It would thus appear possible, for polystyrene at least, to predict 1000-hour creep rates from short-time measurements of absorbed energy under dynamic loading conditions.

The data obtained from the creep and damping tests, together with additional data from short-time tension and compression tests, seem to be consistent with an internal structure in which the linear polymer chains and groups of chains are in ordered or partially extended positions, but in which, in the absence of stress, no preference is shown for any particular direction. Under the action of stress—particularly if the stress is maintained for a long period of time—a tendency exists for the ordered regions to orient in the direction of the applied stress. The so-called "crazing" condition which has been observed to occur in the creep specimens is probably a manifestation of this orientation. X-ray evidence appears to support this point of view.

INTRODUCTION

INVESTIGATIONS of anelastic properties of materials are of considerable interest, both because they supply data which are useful for design purposes and also because they shed considerable light on the internal or molecular structure of matter. For metals, this latter aspect has been stressed by Zener,[1] while the former aspect, in particular the importance of high values of damping capacity in reducing stress amplitude for materials subject to resonant vibrations, has been discussed by Foppl[2] and many others. The significance of dynamic modulus and damping capacity values of plastic materials from the engineering point of view has been pointed out by Lazan and Yorgiadis,[3] while many investigators (see Alfrey[4]) have considered the problem of creep, cold flow, or stress relaxation from both points of view.

In the present investigation, measurements are made of the creep and damping properties of stress-free specimens of a thermoplastic material. The measurements are made on fairly large-sized specimens cut directly from molded sheets and are carried out over a broad stress range with maximum stress values as close as possible to static yield strength. The design implications of the data are mentioned, but are considered more fully elsewhere.[5,6] The significance of the test data from the viewpoint of molecular structure is discussed at some length, and an attempt is made to correlate the results with evidence obtained from x-ray diffraction studies of the stressed and non-stressed specimens.

MATERIAL AND TEST SPECIMENS

The material used in this investigation, a grade of polystyrene known commercially as Lustrex, was selected because it could be produced without significant directional properties and because any residual stresses present after molding could be easily detected. The material was molded in the form of flat sheets 12 in.×12 in., with a thickness dimension of ½ in., ¾ in., or 1 in. All of the material was examined under polarized light before use, and sheets showing noticeable internal strains were discarded. The average molecular weight lay between 67,600 and 68,700.**

All test specimens were machined from the flat sheets and kept for at least 72 hours prior to testing in a controlled humidity and temperature room where the relative humidity was held at 50 percent ±2 percent and the temperature maintained at 77°F±2°F. The dimensions of the creep test specimens, the damping test specimens, and the specimens used for obtaining the tensile and compressive behavior under so-called static loading conditions, are shown in Fig. 1.

STRESS-STRAIN PROPERTIES IN TENSION AND COMPRESSION

In order to have available rather complete information on the mechanical properties of the par-

* Presented at the sixth meeting of the Division of High-Polymer Physics, American Physical Society, New York City, January 27–29, 1949.

[1] C. Zener, Tech. Pap. 1992, Metals Tech. (August 1946).

[2] O. Foppl, J. Iron and Steel Inst. **134**, 393 (1936).

[3] B. J. Lazan and A. Yorgiadis, Symposium on Plastics, ASTM (1944).

[4] T. Alfrey, Jr., *Mechanical Behavior of High Polymers* (Interscience Publishers, Inc., New York, 1948).

[5] J. Marin, Tech. Report No. 1, Cont. No. N6onr-269, Task Order 6, for Mechanics and Materials Branch, ONR (August 1948).

[6] J. A. Sauer, Tech. Report No. 2, Cont. No. N6onr-269, Task Order 6, for Mechanics and Materials Branch, ONR (January 1949).

** Data supplied by the Plastics Laboratory, Monsanto Chemical Company, Springfield, Mass.

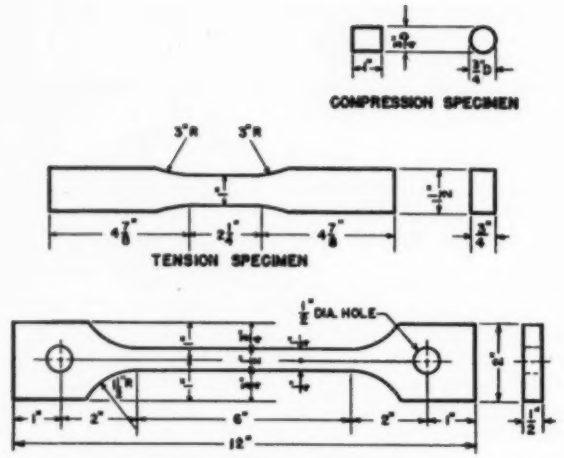

FIG. 1. Types of polystyrene specimens used for tension and compression control tests, tension creep tests, and tension-compression damping tests.

ticular grade of polystyrene selected for the creep and damping tests, it was decided to run rather complete control tests under single load application and at more or less normal testing speeds. At least five separate specimens were tested for each type of loading condition. The stress-strain curves for simple tensile loading are shown in Fig. 2 and for simple compressive loading in Fig. 3. The open circles represent test points and the crossed circles represent fracture.

The tension tests were run on samples proportioned in accordance with ASTM standards for their Type I specimen. Both the tension and compression tests were run on a 60,000-lb. capacity Baldwin Southwark Tate-Emergy hydraulic testing machine.*** Strains were recorded by attaching to the center of the specimen a Type A-1, SR-4 electrical strain gauge connected, in turn, to a standard SR-4 Type K portable strain indicator. In the compression tests, the strain gauge was not attached directly to the specimen, but to a specially designed π-gauge of $\frac{1}{4}$-in. gauge length. The rate of straining was controlled and kept constant throughout the duration of each compressive test, but in the tensile tests only the rate of head separation was kept constant, as it was not thought necessary to accurately control the strain in view of the nearly perfect elastic response of polystyrene to tensile loading.

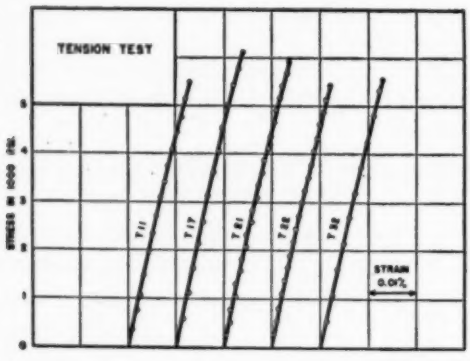

FIG. 2. Tensile stress-strain curves for five samples of polystyrene.

The average values of the significant mechanical properties are summarized in Table I.

It may be noted from this table and from the stress-strain curves of Figs. 2 and 3 that the response of polystyrene to compressive loading is considerably different from its response to tensile loading. Although the elastic modulus is the same, the elastic limit stress or yield strength is much higher in compression; and a comparison of the energy absorptions to yield shows that the material is very much tougher in compression.

It was not found possible to produce fracture under compressive stress. Continued increase of load simply further flattened the specimen until finally longitudinal cracks were produced in the center of the cylinder as a result of development of circumferential tensile stresses. In the specimens subject to tension, the fractured surfaces were amorphous in nature and always perpendicular to the longitudinal axis. The crack or start of failure appeared to originate in a small but visible circular region which usually adjoined the surface, which exhibited concentric circumferential rings, and which showed higher reflectivity than the remainder of the surface.

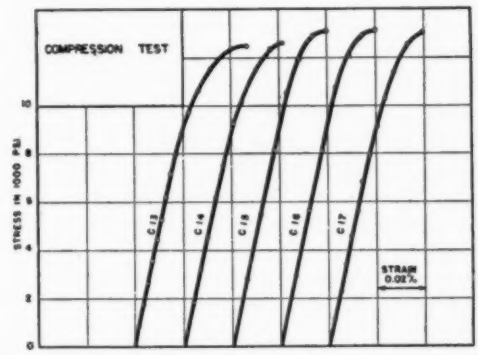

FIG. 3. Compression stress-strain curves for five samples of polystyrene.

*** One tension test and two compression tests were run on a 5000-lb. Dillon Testing Machine. The results were comparable to those obtained by use of the Baldwin Southwark Machine.

CREEP BEHAVIOR OF POLYSTYRENE

The creep tests were carried out on an apparatus (Fig. 4) which permitted nine specimens, all of which were subject to axial tension only, to be tested simultaneously. The entire apparatus was kept in a laboratory whose relative humidity was maintained at 50 percent±2 percent, and whose temperature was kept at 77°F±2°F. The details of the construction and operation of the creep tensile unit has been previously discussed by Marin.[5] The creep strains were measured to 0.00005 in. over a 5-in. gage length by means of a micrometer microscope stand shown in Fig. 4(b).

Each of the specimens was subject to a different stress value ranging from 1760 p.s.i. for the lowest, to 4060 p.s.i. for the highest. Strain readings were taken daily and the test continued for 1000 hours duration, or until the specimen fractured. The total deformation (elastic plus creep) is plotted as a function of time in Fig. 5. The diagram shows that the rate of increase of deformation with time gradually diminishes and appears to become approximately constant even before the 1000-hour period is reached. The values of these constant creep rates C_r are given in Table II for all specimens except those subject to the three highest stresses.

TABLE I. Mechanical properties of polystyrene (Lustrex).

Specific mechanical property	Value obtained from tension test	Value obtained from compression test
Modulus of elasticity (p.s.i.)	4.5×10^5	4.5×10^5
Yield strength (p.s.i.) (0.005 offset)	—	12,400
Fracture strength (p.s.i.)	5700	—
Ductility at fracture (%)	1.35	
Energy to yield (in. lb./cu. in.)	—	171
Energy to fracture (in. lb./cu. in.)	37.1	—

These were omitted as they fractured too early to obtain an accurate creep rate estimate.

The data of Table II show that both the creep and the creep rate increase with increasing stress. It is difficult to find an empirical relation to accurately fit these data, but it is found that the creep rate varies approximately linearly with the stress when the data are plotted on log-log paper (Fig. 6). The creep-rate stress relation may thus be written $C_r = Bs^n$, where B and n are experimental constants which take the values $B = 6.66\times10^{-22}$ and $n = 4.53$, and s is the applied tensile stress.

Discussion of the nature of the fracture under creep conditions and the phenomena of crazing that is associated with long duration of load application will be withheld until the results of the damping capacity tests have been summarized.

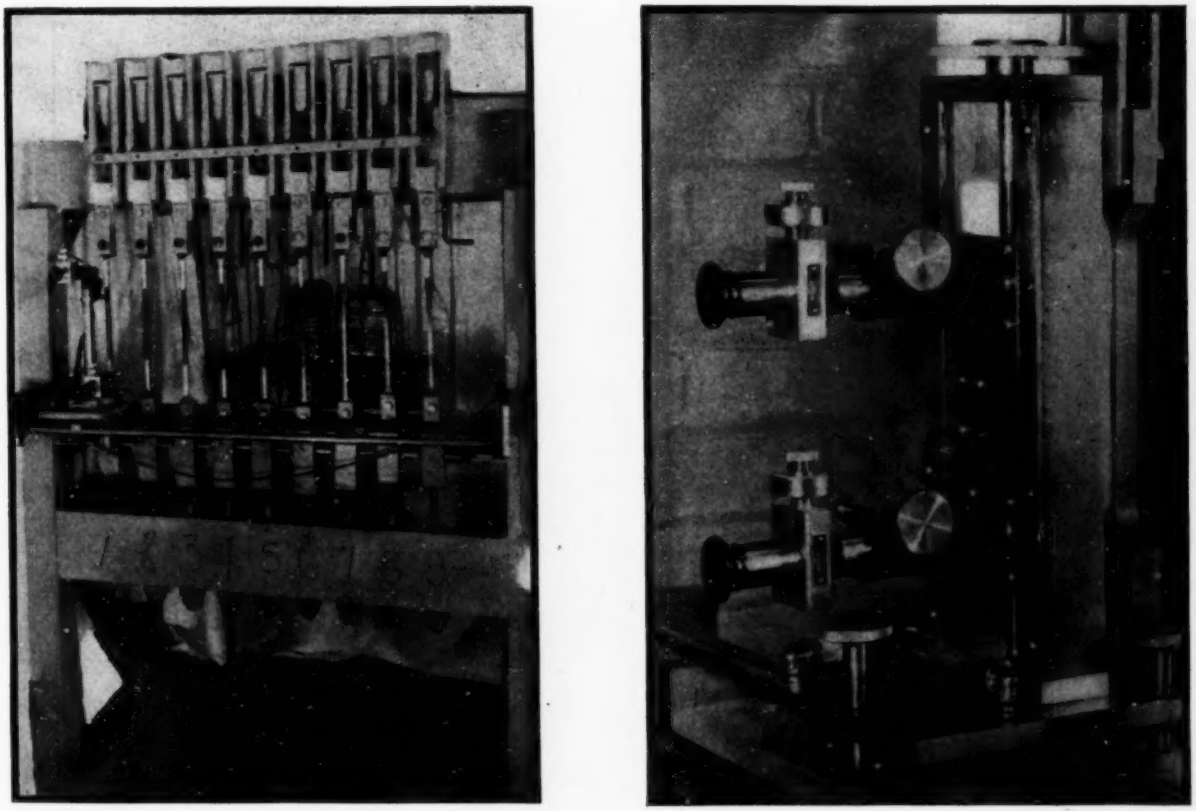

(a) (b)

FIG. 4. (a) Apparatus for obtaining tension creep data. (b) Micrometer microscope unit for measuring creep deformation.

TABLE II. Static tension creep test data for polystyrene (Lustrex).

Spec. No.	Area sq. in.	Load lb.	Stress p.s.i.	Creep rate in./in./hr. units of 10^{-7}	Creep at 1000 hr. in./in. units of 10^{-3}
1	0.250	857	3420	66	—
2	0.220	715	3250	60	—
3	0.264	830	3140	40	—
4	0.213	550	2580	22	9.3
5	0.390	988	2525	20	8.9
6	0.362	808	2240	10	7.2
7	0.363	629	1760	3	4.9

DAMPING BEHAVIOR OF POLYSTYRENE

The method used in the present investigation to measure damping capacity, i.e., the energy absorbed under cyclic stress, per cycle, per unit volume, is a resonant-vibration method originally developed by Lazan[7] and used later by Robertson and Yorgiadis.[8] It consists essentially of measuring the energy input of a centrifugal force mechanical oscillator rigidly attached to a single-degree-of-freedom spring-mass system. The experimental set-up is diagrammatically shown in Fig. 7. The specimen whose internal friction is desired acts as the spring, and the masses M_1 and M_2 are varied by addition or removal of the small masses m until the natural frequency of the longitudinal vibrations of the specimen-mass system is identical with the frequency of the oscillator.

The entire apparatus is mounted on hardened, smooth rollers so as to minimize the energy loss to the supports. The specimen is held in place by means of collet chucks attached to the two large masses M_1 and M_2. The condition of resonance is obtained by adding or subtracting small weights until there exists a 90° phase lag between the oscillator force and the longitudinal displacement. The actual phase lag is observed by stopping the vibratory motion at zero displacement and simultaneously observing, under the action of stroboscopic light of twice the oscillator frequency, the angle of the applied force.

The numerical value of the damping capacity is obtained from the measured value of the total displacement ($2a$) and the amplitude of the oscillator force (F) by the use of the formula for the energy absorbed by a single-degree-of-freedom system operating at resonance, *viz.*,

$$\Delta W = \pi F a / AL.$$

Here ΔW is actually the energy input, but since

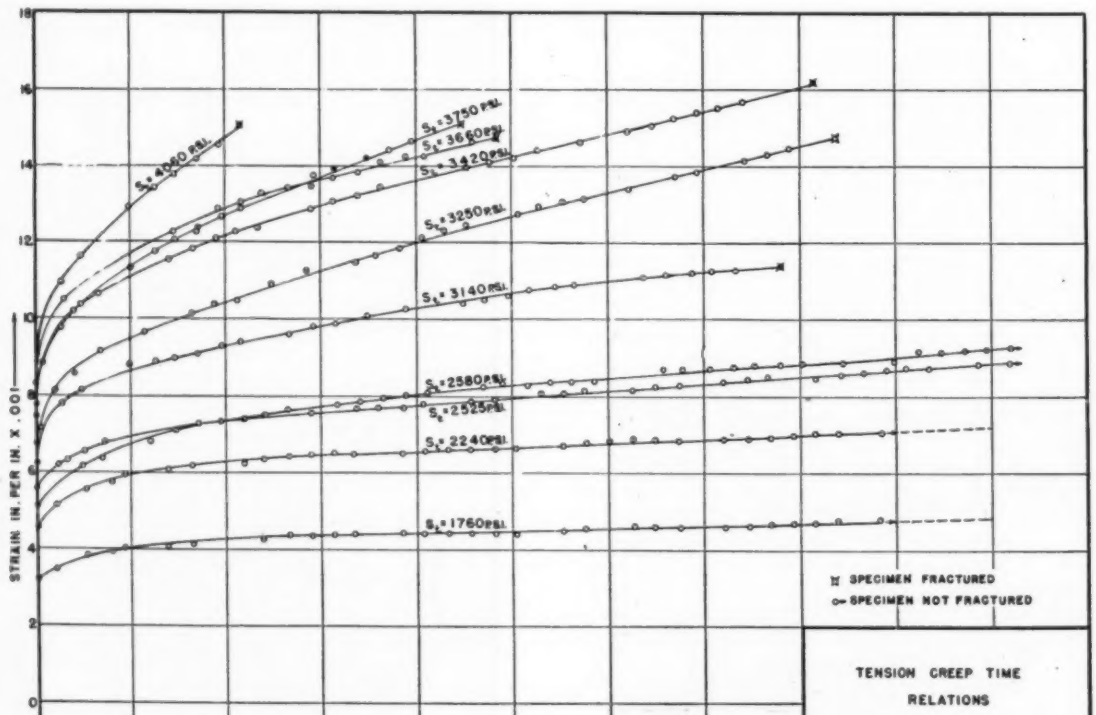

FIG. 5. Tensile creep curves at various stress levels.

[7] B. J. Lazan, Trans. A.S.M.E. 65, 87 (1943).
[8] J. M. Robertson and A. Yorgiadis, J. App. Mech., Trans. A.S.M.E. 68, A173 (1946).

heat losses to surroundings have been kept small, it may also be taken as the energy absorbed.[8] A is the cross-sectional area of the specimen, and L the length of the specimen. The magnitude of the maximum stress (σ) produced in the specimen by the oscillating force is

$$\sigma = M_2\omega^2 a/A,$$

where M_2 is the total mass on the right-hand side of the specimen in Fig. 7 and ω is the circular frequency of the oscillator.

For each specimen, readings of a and F were taken at a number of progressively increasing stress levels varying from 329 p.s.i. to 2105 p.s.i. Measurements at higher stresses were not made because of the danger of fatigue failure. Even at low stresses it is difficult to keep the specimen at constant temperature, since the absorbed energy appears as heat. Fortunately, however, the test data can be taken rather rapidly, and whenever the surface temperature rises more than two or three degrees the test can be discontinued until the specimen cools down.

The results of a typical test are shown in Table III. The damping capacity values from the last column, as well as for two other test specimens, are plotted as a function of stress amplitude in Fig. 8. The test points clearly follow a straight line trend on this plot, indicating that the relation between absorbed energy due to internal friction and stress amplitude is given by an equation of the form

$$\Delta W = C\sigma^n,$$

where C and n are constants which can be readily found from the data. The constant n is simply the slope of the damping capacity-stress amplitude curve on the log-log plot, and takes the value 2.3 for the data of Fig. 8.

Figure 9 indicates the good agreement obtained with previous results when additional measurements are made on the same specimen after completion of the tests at high stress amplitudes. This agreement would appear to indicate that no noticeable change in specimen properties has occurred. Whether the specimens stand one hour or twenty hours before being retested apparently makes little difference.

COMPARATIVE DAMPING QUALITIES OF POLYSTYRENE AND OTHER HIGH POLYMERS

In order to correlate experimental values of damping capacity with internal molecular structure, it seemed appropriate to determine values of internal friction for some other plastic materials. Additional tests were therefore made on several other thermoplastic materials and several thermosetting ones. The complete results, together with a more precise description of the different materials, is given elsewhere by Sauer.[6] For our purposes, it is sufficient to show the results for two other thermoplastic materials and four thermosetting phenolic laminates.

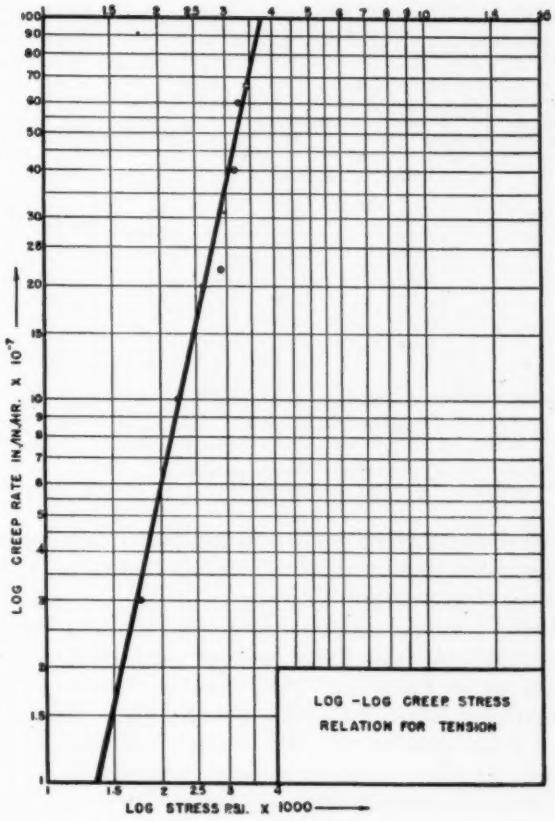

FIG. 6. Relation between tension creep rate and stress amplitude.

Table IV gives values of the experimentally determined dynamic modulus together with dimensional data, and Table V gives comparative values of the damping capacity at two different stress loads for both the Lustrex and the six other high polymers. The data illustrate the increase in damping capacity with increase of stress amplitude, and show also that the damping capacity of polystyrene is considerably below that of cellulose

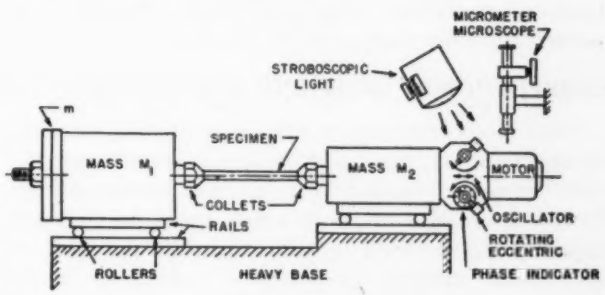

FIG. 7. Diagrammatic sketch of apparatus for measuring damping capacity.

TABLE III. Results of damping capacity measurements on polystyrene (Lustrex). (Specimen No. 10.)

Run No.	Amplitude of oscillator force (lb.)	Weights $W_1=M_1g$ (lb.)	Weights $W_2=M_2g$ (lb.)	W^* (lb.)	Amplitude a (in.)	Stress σ (p.s.i.)	Dynamic modulus E^{**} (p.s.i.)	Damping capacity ΔW in. lb. per cu. in.
1	1.63	660	390	245.2	0.00354	329	5.35×10^5	0.00654
2	2.44	656	390	244.5	0.00511	475	5.33×10^5	0.01412
3	3.26	651	390	243.7	0.00649	604	5.31×10^5	0.0239
4	5.18	645	390	243.0	0.00964	897	5.29×10^5	0.0565
5	6.80	640	390	242.3	0.01220	1135	5.28×10^5	0.0941
6	8.45	635	390	241.5	0.01456	1353	5.26×10^5	0.1392
7	11.86	628	390	240.5	0.01869	1740	5.24×10^5	0.251
8	15.25	623	390	239.5	0.02262	2105	5.22×10^5	0.391
9	1.63	645	390	243.0	0.00342	318	5.29×10^5	0.00632
10	3.26	645	390	243.0	0.00669	542	5.29×10^5	0.0212

Auxiliary data:
Oscillator frequency—26.6 c.p.s.
Phase angle ϕ—90°
Specimen length—9¼ in.
Specimen diameter—0.622 in.

Applicable formulas:

$$^*W=\frac{W_1\cdot W_2}{W_1+W_2} \qquad ^{**}E=\frac{L}{A}\frac{\omega^2}{g}W$$

acetate and methyl methacrylate and more nearly comparable to that of the phenolic laminates than to the other thermoplastics.

The damping capacity increases with stress in approximately the same manner for each of the materials of Table V. This is clearly shown by the comparable slopes ($n=2.3\pm$) of the data shown on the log-log plot of Fig. 10 for four phenolic laminates.

The experimental data thus seem to lead, both from the more extensive investigations on Lustrex samples and also from the separate series of tests on other high polymers, to the conclusion that the energy absorbed per cycle varies approximately as the 2.3 power of the maximum stress amplitude. This seems to differ with the conclusion of Robertson and Yorgiadis[8] that for all materials internal friction varies as the third power of the stress amplitude. However, only one of their test materials was similar to ours (Lucite) and for this material their reported data show considerable scatter, so much in fact that a 2.3-power law would appear to give just as good agreement with their data as a third-power law.

With the exception of methyl methacrylate, Table IV and Table V indicate that plastic materials of higher dynamic modulus exhibit, in general, lower energy absorption under dynamic loading. A similar trend has been previously reported by Robertson and Yorgiadis.[8]

CORRELATION OF CREEP AND DAMPING BEHAVIOR

Since both creep and damping are manifestations of anelasticity, it is appropriate to seek a correlation between measurements of the two quantities. In this investigation, both creep rate and damping capacity have been determined for polystyrene specimens subject to various values of stress amplitude. Both these quantities were found to vary as a power law of the stress amplitude, although the stress itself is constant in the creep tests and rapidly alternating from maximum tension to maximum compression in the damping tests. If, for a given stress amplitude, one plots the (1000-hour) creep rate as a function of damping capacity, one gets a straight line on a log-log plot (Fig. 11) having a slope of approximately 2. Thus, there appears to be a relation between creep rate and damping capacity of the form $C_r=K(\Delta W)^2$ where K is a constant.

This interrelationship of creep rate and damping capacity is significant from two points of view.

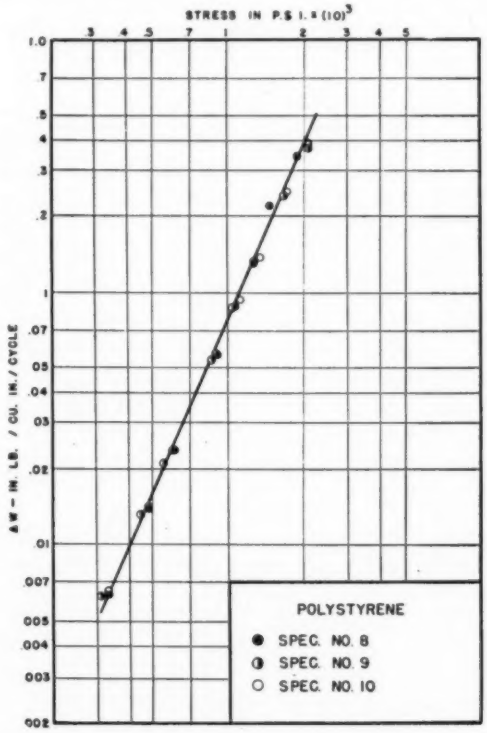

FIG. 8. Relation between damping capacity and stress amplitude.

First of all, if it is found that a similar relationship holds for other materials as well as for polystyrene, it should be possible to obtain knowledge of the deformation-time properties of any given substance by simply making damping capacity measurements at various stress amplitudes. Since damping capacity tests are relatively simple to run, and since measurements of damping capacity at various stress amplitudes can be obtained in a short period of time and from but a single specimen, this procedure would result in a considerable saving of time and effort.

Aside from this important practical consideration of the relationship between creep and damping capacity, the data would seem to imply that the same molecular mechanism must be responsible for both types of behavior. We shall first consider the bearing of the damping test data on molecular structure and then will consider the bearing of the creep data and of the "crazing" aspects of the creep measurements.

STRUCTURE OF HIGH POLYMERS AND DAMPING BEHAVIOR

The anelastic or viscoelastic properties of polystyrene and other high polymers have been considered from the point of view of molecular structure by a number of investigators.[4,9–11] Linear

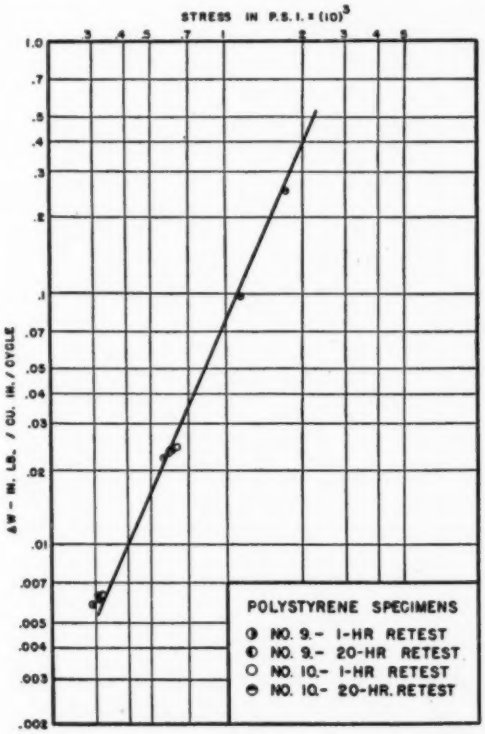
STRESS IN P.S.I. = (10)³
ΔW - IN. LB. / CU. IN. / CYCLE
POLYSTYRENE SPECIMENS
NO. 9.- 1-HR RETEST
NO. 9.- 20-HR RETEST
NO. 10.- 1-HR RETEST
NO. 10.- 20-HR. RETEST

FIG. 9. Damping capacity data taken after one-hour and twenty-hour rest periods.

[9] H. Mark, Ind. Eng. Chem. **34**, 449 (1942).
[10] A. Tobolsky and H. Eyring, J. Chem. Phys. **11**, 125 (1943).
[11] T. Alfrey, Jr., J. Chem. Phys. **9**, 374 (1944).

TABLE IV. Type of specimen and value of dynamic modulus for various high polymers.

Type of plastic	Cross-sectional dimensions (in in.)	Length of specimen L (in.)	Freq. of oscillation (c.p.s.)	Dynamic modulus E (10^5 p.s.i.)
Thermoplastic materials				
Cellulose acetate (FM6)	0.500 round	7.31	18.0	2.7
Methyl methacrylate (Plexiglas)	0.749 round	6.25	37.5	6.1
Polystyrene (Lustrex)	0.622 round	9.12	26.6	5.3
Thermosetting laminates				
Army duck base	0.513 × 0.500	9.00	37.5	13.3
Paper base (Grade XX)	0.500 round	8.00	37.5	14.3
Rayon base	0.508 × 0.615	7.50	60.0	17.2
Paper base (high strength)	0.502 × 0.508	8.94	60.0	33.1

Note: Dynamic modulus calculated on basis of length of specimen between grips (L).

polymers, of which natural rubber is an example, are generally considered to consist of long-chain molecules which, when unstressed, are in random curled positions because of the greater statistical probability of these configurations over extended ones. Under the action of stress, the entire system tends to straighten. This applies to local kinks, intermediate curls, and long range conformations. The rapidity with which each of these units can respond to stress is, however, quite different and depends on the nature of its environment. The local kinks will respond fastest to stress and the long range conformations slowest; there will thus be an elastic and a non-elastic response to applied stress.[4]

In the case of polystyrene, the non-elastic response is not due to any relaxation of primary bonds as, first of all, there are few, if any, primary bonds across chains and, secondly, the relaxation time of primary bonds would probably be quite high. Secondary bonds across chains are by comparison weaker, and slipping of chains or chain segments past one another is one possible mechanism contributing to creep, hysteresis, and internal friction. The mechanical properties are affected, however, not only by the intramolecular forces but also by geometric factors such as mechanical hindrances due to existence of bulky side groups or side chains. In polystyrene, the phenyl group prevents close fitting of chains and thus, the attractive power of the polymer per unit of chain length is reduced from that calculated by Mark[9] based on most efficient packing. Since, in general, internal friction is reported to be greater when the chains are well packed,[10] a reduction of attractive power (specific molar cohesion) should thereby decrease the damping capacity. This would appear to account for the comparatively low value of the damping capacity of polystyrene compared to that of cellulose acetate as shown by the data of Table V.

TABLE V. Comparative values of damping capacity of several thermoplastic materials and several thermosetting materials.

Type of plastic	Values of damping capacity (ΔW) (in. lb./cu. in./cycle) at $\sigma = 500$ p.s.i.	at $\sigma = 1000$ p.s.i.
Thermoplastic		
Cellulose acetate (FM6)	0.156	0.670
Methyl methacrylate (Plexiglas)	0.0882	0.430
Polystyrene (Lustrex)	0.0159	0.0782
Thermosetting phenolic laminates		
Army duck base	0.0129	0.0612
Paper base (Grade XX)	0.0108	0.0534
Rayon base	0.0085	0.0381
Paper base (high strength)	0.00324	0.0153

The still lower value for the thermosetting plastics is accounted for by the fact that they are three-dimensional polymers with primary cross linking and hence are more elastic and less inelastic in their response to load.

CRAZING EFFECTS IN POLYSTYRENE

One of the most striking manifestations of the anelastic behavior of polystyrene, observed particularly in the creep-time tests, was a tendency for the original transparent material to "craze." By crazing we simply imply a clouding or blushing of the originally transparent material which causes some of the light striking the material to be reflected instead of transmitted. Crazing occurs in methyl methacrylate as well as polystyrene and has been reported in the literature to be caused by solvent action as well as by applied stress. Crazing is frequently associated with mechanical cracks, and our tests show that even before fracture occurs crazing marks are sometimes evident at various points on the specimen where stress concentration occurs, such as at regions where the specimen changes its cross-sectional dimensions or at points of concentrated load application. Our observations of this phenomena may be summarized as follows:

(1) Crazing nearly always starts on the surface of the test specimen and works inward toward the center. Though more striking in long-time tests, some crazing seems even to occur in the short-time stress-strain tests. As noted previously, a small circular reflective area is sometimes visible on the otherwise amorphous fractured surfaces of the test pieces. This condition appears to generally occur when a noticeable defect or inhomogeneity is present.

(2) The amount of cross-sectional area of the specimen which crazes appears to be a function of both time of application of load and magnitude of applied tensile stress. For a given time, crazing increases with stress amplitude, and for a given stress, crazing increases with increase of time of load application. Maxwell and Rahm,[12] from measurements of reflected light intensity, report a similar behavior.

(3) Crazing seems to occur both on surfaces which have been machined and surfaces which have been cast without showing any preference for one over the other. In the tensile specimens, it seems also to occur uniformly along the longitudinal axis of the specimen.

(4) In some specimens in which the load remained on the specimen for a fairly long period of time (of the order of 1000 hours) the entire cross-sectional surface of the specimen crazed, but the specimen did not fracture.

(5) Fractured surfaces usually show definite evidences of cracks which appear to grow radially outward from the center of the disturbance, which itself may or may not be on the surface. The center of the cross section of many of the fractured specimens shows an amorphous region similar to that for the unstressed specimens.

(6) Crazing has been found to occur at low stresses and low strains (<0.5 percent elongation for 1000-hour tests) and also has been observed *not* to occur at high stresses and high strains (>1.3 percent) for rapid load application.

(7) Whenever cracks are noticeably present on the crazed surfaces, i.e., when the surface is the actual fracture surface and not a surface which has been cut from the stressed specimen, they occur on planes at right angles to the maximum principal stress direction.

(8) If sections of the specimen showing crazed regions along the edges are cut off and placed under high compressive loading, most of the crazing or cloudiness disappears.

Some of the manifestations mentioned above can be clearly seen in the photographs of Figs. 12 and 13, which depict specimens subject, respectively, to simple tensile creep and pure bending creep. These photographs reveal the highly reflective area which is usually found for a short distance all around the surface of the specimen and also the amorphous center area. They clearly show that the crazing cracks are at right angles to the direction of the maximum principal tensile stress.

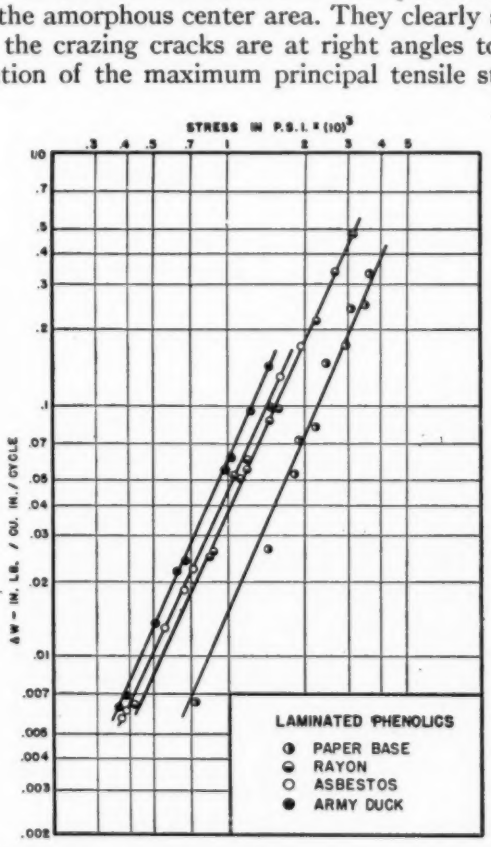

FIG. 10. Damping capacity *vs.* stress amplitude for four phenolic laminates.

[12] B. Maxwell and L. F. Rahm, Tech. Report 11B, Plastics Laboratory, Princeton University, Princeton, New Jersey (September, 1948).

In the case of the sample subject to bending, there is no evidence of crazing on the compression side of the specimen, while crazing is very apparent on the surface edges and for some distance inward on the tensile side of the specimen. Somewhat similar observations have been reported by Maxwell and Rahm,[12] Russell,[13] and others.

CURRENT THEORIES OF CRAZING

Several groups of investigators have studied the phenomena of crazing, have made measurements of crazing by recording the amount of reflected light, and have proposed certain theories to account for its occurrence. According to Maxwell and Rahm,[12] crazing is considered to be a system of very fine mechanical cracks which occur whenever the local deformation of the specimen exceeds a certain critical amount. This critical amount for clean, thermal stress-free samples of the polystyrene material which they tested was reported to be 0.75 percent. If their theory is correct, a clean stress-free specimen subject to tension should show no visible crazing until the local elongation exceeds their critical figure. It is difficult to see, however, why crazing should then occur only on the surface and not in the center, especially since the local elongation is approximately constant over the entire cross-sectional area. Also, in some of the short time stress-strain tests, the specimens were loaded until failure occurred at an elongation of about 1.4 percent and again no visible crazing was evident. It is, of course, quite conceivable that some crazing is present, but the amount is so small that it can be ascertained only by a sensitive light measuring method. Our tests also show that if the load is applied for a long period of time (several hundred hours or so), crazing will become evident at much lower strains than 0.75 percent. Maxwell and Rahm[12] believe this behavior to be due to contamination from the air. It is hoped that further tests under controlled atmospheres will clarify this point, but thus far our tests indicate that crazing is markedly dependent on the time of load application as well as on the stress or strain magnitude.

Some studies on the crazing of methyl methacrylate have been reported by Russell.[13] He noted that crazing cracks seem to be similar in nature whether caused by stress or by solvent action. He assumed that the crazing was produced by the same processes as are involved in normal tensile failure, and that the crazing condition occurs first on the surface because of the presence there of non-uniform randomly-directed residual stresses, which arise as a result of shrinkage due to non-uniform temperature conditions occurring in the casting process. This theory does not appear to be sufficiently adequate to explain our experimental results, *viz.*, that crazing can and does occur even when no appreciable residual stresses are present in the specimens. The presence or absence of residual stresses is determined by polariscope examination of all sheets from which the specimens are cut. Those showing any evidence of internal stresses are discarded. Furthermore, if any residual stress pattern should be present, it would be altered by the machining operation; yet, both the newly machined and the molded surfaces show identical crazing effects.

[13] E. W. Russell, Report No. Chem. 447, Part III, Royal Aircraft Establishment, Farnborough, England (August 1948).

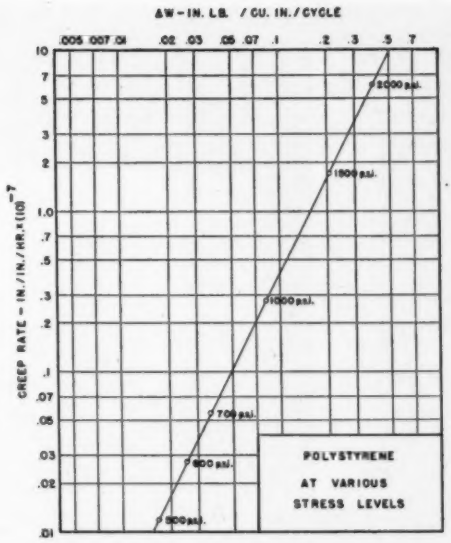
AW - IN. LB. / CU. IN. / CYCLE
.005 .007 .01 .02 .03 .05 .07 .1 .2 .3 .5 .7
10 7 5 3 2 1.0 .7 .5 .3 .2 .1 .07 .05 .03 .02 .01
CREEP RATE - IN./IN./HR. x (10)⁻⁷
2000 p.s.i.
1500 p.s.i.
1000 p.s.i.
700 p.s.i.
500 p.s.i.
300 p.s.i.
POLYSTYRENE
AT VARIOUS
STRESS LEVELS

FIG. 11. Relation between creep rate and damping capacity for polystyrene.

INTERPRETATION OF DATA IN TERMS OF MOLECULAR STRUCTURE

The results of the stress-strain studies, the creep studies, and the damping studies reported herein

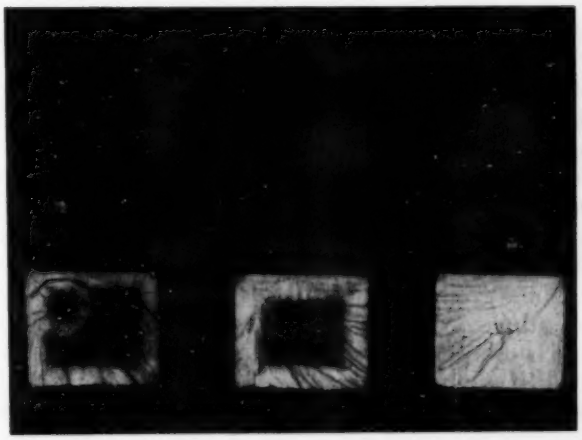

FIG. 12. Fractured surfaces of polystyrene tension creep specimens.

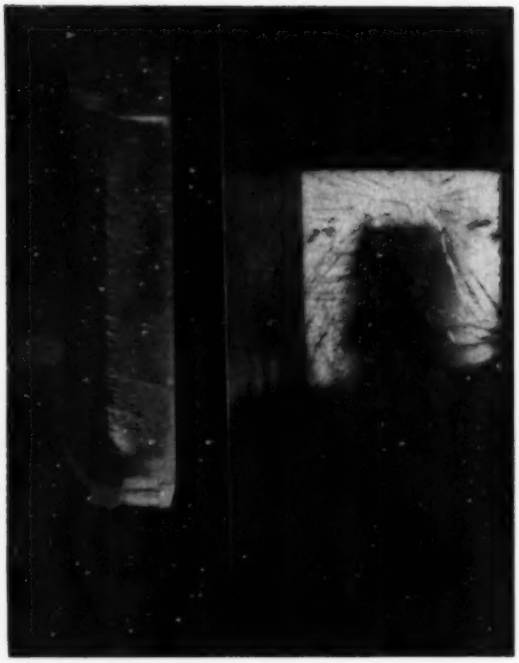

FIG. 13. Fractured surfaces of polystyrene bending creep specimens.

all seem to reveal that the molecular structure of polystyrene must, of necessity, be considerably different, at least at 20°C, from that of other linear super polymers such as synthetic or natural rubbers. First of all, the damping capacity data indicate that polystyrene, despite the absence of primary cross bonds, acts more in the fashion of the the three-dimensional cross-linked thermosetting materials than it does in the manner of the other thermoplastics. Secondly, the total elongation to failure under simple tensile loading is quite small—of the order of 1.4 percent at room temperatures as compared to about 50 percent for cellulose acetate. Thirdly, the material is found to creep under load at low stress values and to show crazing even at low elongations.

All this would seem to indicate that the structure of polystyrene below its second-order transition temperature does not consist of miscellaneous polymer chains that are predominately in the curled-up state. The data would appear rather to be more compatible with a polymer structure in which groups of polymer chains were in more or less ordered or partially extended positions, but the various groups or bundles themselves randomly orientated. In the usual Guth-James theory of rubber-like elasticity, the energy of all configurations is assumed to be alike, and hence, the curled-up state is considered the most likely one simply because of the greater number of ways in which this state can be statistically realized. There is no *a priori* reason why this condition should exist and is most unlikely in polystyrene, for example, in view of its observed mechanical behavior. The most probable state of the system as a whole may well be one in which various polymer chains are in ordered or partially extended positions if energy and stearic considerations as well as entropy ones are taken into account in the analysis.

The difference in behavior under tension and compression loading noted previously would appear to fit with the suggested picture of the polystyrene structure. Under fairly rapid tensile loading, very little additional elongation would be required before some of the already extended chains were stretched to their ultimate extensibility and the applied stress brought to bear on the primary bonds themselves. Under compressive loading, on the other hand, some secondary bonds might be broken and some chain slipping permitted, but no primary bonds would be separated, and hence, the deformation could become quite appreciable before any evidence of failure was observed.

In the tensile creep tests, as load is applied and maintained, some time dependent slipping will occur between chains and groups of chains, due to breakdown of secondary bonds. At the same time, there will be some general orientation of the polymer chains in the direction of the applied stress, although the tendency to orient will probably be restricted by the force field of the surrounding molecular chains and by mechanical hindrances. The longer the duration of load application, the greater will be the amount of orientation. It is

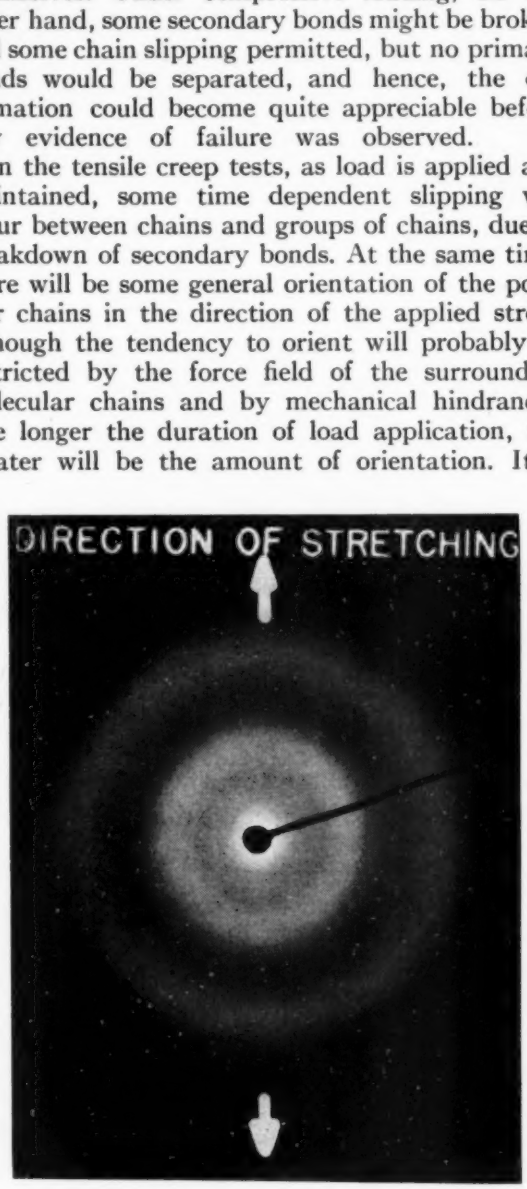

FIG. 14. X-ray diffraction pattern of polystyrene specimens.

possible that orientation will begin on the surface where the restrictive forces of the nieghboring polymer chains are perhaps somewhat less, because of the free air surface, than those acting on internal polymer molecules. Oxygen or moisture absorption may also play a part in reducing the value of these restraining molecular forces (and thereby permitting greater orientation), but sufficient experimental data has not yet been accumulated to decide this point.

If this view is correct, then crazing is a manifestation of orientation and the essential difference between the structure of noncrazed and crazed material is that in the first instance all the ordered regions or chain groups are randomly directed, while in the second instance the ordered regions show a preferred orientation in the direction of stretch. Additional evidence in support of this point of view arises from study of x-ray diffraction patterns taken on sections cut from the polystyrene creep specimens. Both the crazed and noncrazed regions of a specimen such as that shown in Fig. 12 were examined under Copper K radiation with the following results:

(1) The non-crazed regions showed a well defined uniform ring pattern. According to Fankuchen and Mark[14] this is indicative of random orientation of ordered regions or "crystallites" which are responsible for the scattering and in which the polymer chains show a high degree of local order.

(2) Transmission pictures taken on the crazed regions of the specimen with the x-ray beam perpendicular to the direction of stretching reveal a somewhat similar ring pattern with (to the eye) apparently comparable intensities. Figure 14 shows a typical x-ray pattern obtained under these conditions. Similar pictures have been obtained by Katz[15] who shows that the outside ring appears in x-ray pictures of the styrene monomer but the inside ring does not.

(3) However, photometer intensity curves of the crazed regions recorded by use of an x-ray spectrometer (Fig. 15) reveal that variations of diffracted ring intensity do occur (especially for the intense inner ring of Fig. 14) for different directions of the axis of rotation relative to the direction of stretching. This difference of intensity in the directions parallel and perpendicular to the applied stress is a definite indication of the existence of orientation. The photometer graphs also seem to show that the peak intensity of the inner ring shifts slightly inward toward the center as we pass from the parallel to the perpendicular direction. This would indicate an increase in some characteristic spacing caused probably by the same forces that produce the orientation tendency.

[14] I. Fankuchen and H. Mark, *Currents in Biochemical Research* (Interscience Publishers, Inc., New York, 1946), p. 439.

[15] J. R. Katz, Trans. Faraday Soc. **32**, 77 (1936).

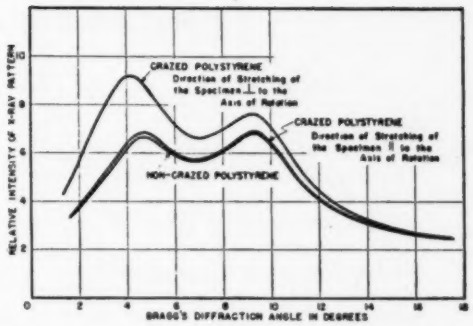
CRAZED POLYSTYRENE
Direction of Stretching of the Specimen ⊥ to the Axis of Rotation
CRAZED POLYSTYRENE
Direction of Stretching of the Specimen ∥ to the Axis of Rotation
NON-CRAZED POLYSTYRENE
RELATIVE INTENSITY OF X-RAY PATTERN
BRAGG'S DIFFRACTION ANGLE IN DEGREES

FIG. 15. X-ray spectrometer curves of crazed and non-crazed sections of polystyrene tension creep specimens.

The x-ray diffraction results thus appear to confirm the concept of the structure of polystyrene already discussed. The existence of the somewhat diffuse but nevertheless well defined rings in the immediate neighborhood of the incident beam indicates that geometrically ordered regions do exist in the otherwise amorphous structure and that within these regions there must be some periodic sequence of fairly well defined spacings. Furthermore, the results obtained on the crazed specimens by use of the x-ray spectrometer indicate the close tie-in between crazing and orientation and lend confirmation to the theory that crazing is essentially an orientation phenomena and not a mechanical crack phenomena, although it may be associated with cracks if the applied stresses are high enough to produce local or complete fracture.

It is hoped that more complete studies will permit the determination of the relative proportion of ordered or orientated regions to amorphous regions; will provide accurate quantitative values of the molecular or chain spacings; and will also shed more light on the effect of the surrounding atmosphere in the development of the crazing or orientated condition.

ACKNOWLEDGMENTS

It is a pleasure to acknowledge our gratitude to the ONR and to the Mechanics and Materials Branch. Without their assistance and cooperation this project could not have been undertaken. We are indebted to Messrs. G. Cuff, D. Lemmon, W. Oliphant, and B. Black for assistance in obtaining the experimental data. Our thanks go also to Drs. E. Saibel and J. M. Robertson for advice and counsel, and to the Monsanto Chemical Company and Mr. H. Adams, in particular, for supplying us with the test material.

Scattering by an Inhomogeneous Solid*

P. Debye and A. M. Bueche
Cornell University, Ithaca, New York

A general treatment of the scattering of radiation by an inhomogeneous material is developed. It is shown how scattering measurements can be used to obtain the average square of the fluctuations in refractive index or electron density and a correlation function which measures the degree of correlation between two fluctuations as a function of their distance of separation.

The scattering of visible light by Lucite and two glass samples has been investigated. The data are analyzed in terms of the quantities mentioned above. It is found that the extensions in space of the inhomogeneities in the Lucite sample are much greater than those in the optical glass samples investigated. The magnitudes of the fluctuations in refractive index are found to be dependent on the composition of the sample.

THE inhomogeneities present in solid materials are of considerable importance in the study of the physical properties such as strength of these materials. Few good methods have been available for investigating the inhomogeneities; therefore a correlation with physical properties has been difficult. The purpose of this paper is to elucidate a method whereby the inhomogeneous regions present in solids may be characterized. It is not necessarily restricted to solids and may be applied to liquids and gases.

The method to be described is based on the scattering power of solids for electromagnetic radiation. A beam of light or x-rays passing through the material will be diminished in intensity even in the absence of real absorption because some of the radiation is scattered to the side. The intensity and angular distribution of this scattering depend on the fluctuations of refractive index (or dielectric constant) in the solid and on the sizes of the regions over which these fluctuations occur. These are the two quantities obtained upon complete application of the following method. In the x-ray case electron-density fluctuations can be substituted for those in refractive index.

For the convenience of the reader, the paper has been written in two parts. In the first part the method as applied to solid Lucite using visible light has been described. The second part contains a detailed development and discussion of the method.

The results reported in Part II were obtained in 1944 by P. Debye and those in Part I in the latter half of 1948 by A. M. Bueche during the course of work supported by the Office of Rubber Reserve, Reconstruction Finance Corporation, in connection with the Government's synthetic rubber program.

PART I

The Lucite sample investigated was obtained[1] in the shape of a rod 37 mm in diameter and about 55 mm long. It was taken from commercial stock. No extra care was exercised in its polymerization. The rod was carefully clamped in a lathe and the curved surface polished with tooth paste and wet flannel. The rod was moved to a milling machine and opposite flat faces 15 mm wide were cut the length of it. These were then polished.

Such a sample could be mounted in our angular scattering instrument.[2] The scattered intensity was measured photoelectrically over the angular range from 35° to 135°. Measurements were made using both the Hg blue ($\lambda = 4358$A) and green ($\lambda = 5461$A) lines of the light source. The scattering at 90° of blue light was compared with the scattering by a toluene solution of polystyrene whose turbidity is known. The galvanometer readings so obtained were corrected (a) for the angular variation expected because unpolarized light was used, i.e., divided by $(1+\cos^2\theta)$, where θ is the scattering angle, and (b) because at each angle the photo-cell received light from a scattering volume of different size.

To measure the scattering in the angular range close to the primary beam a "small angles camera"[3] was used. The camera consists of a single circular compartment 10 cm in diameter with provision for mounting the sample at the center. The primary beam enters through a pinhole-lens system, passes through the sample, and leaves the camera through a hole cut in a 35-mm film clamped against the opposite wall. The scattered intensity as a function of angle is recorded on this film in much the same way as in a circular x-ray camera.

The samples for these low angle experiments were polished disks 8 mm in diameter and 2 mm thick. They were made from a plate of Lucite cut from one end of the rod. Photographs were made using blue light only.

The photographic densities were converted to

---

* Presented at the Sixth Meeting of the Division of High-Polymer Physics, American Physical Society, New York City, January 27–29, 1949.

[1] The authors are indebted to Dr. F. W. Billmeyer, Jr., Plastics Department, E. I. duPont de Nemours and Company for this sample.

[2] P. P. Debye, J. App. Phys. **17**, 392 (1946).

[3] F. W. Billmeyer, Jr., Report to Office of Rubber Reserve (Reconstruction Finance Corporation, March 1, 1945).

relative intensities by means of a step wedge printed on each film. The values so obtained were corrected for reflection and refraction occurring at the face of the sample and for the fact that unpolarized light was used.

The data obtained using blue light by both methods are shown in Fig. 1. The crosses refer to the values obtained photographically and the circles to those obtained by the photoelectric instrument. Since the variation of scattered intensity with angle was so large we have plotted this intensity, i, in arbitrary units times $\sin\theta/2$ *vs.* $(\sin\theta/2)/\lambda$. Here λ is the wave-length in the solid. The index of refraction was taken as 1.50. The photographic intensities were fitted to the curve obtained photoelectrically in such a way as to give a smooth curve in the region of joining. The hump evident in this region was felt not to be real since it occurs at the angular limit of both instruments and was neglected. It may be due to small amounts of stray light in the instruments. For the purpose of further calculations points representing the smooth curve of Fig. 1 were used.

The scattered intensity did not go to zero for the largest values of $(\sin\theta/2)/\lambda$ investigated but approached a small almost constant value at the larger angles. This background scattering is due to very small inhomogeneities in the solid. In the present work they were neglected by subtracting this small intensity from the other points. They could be investigated by measuring the scattering for smaller wave-lengths. The values in arbitrary units of $i\sin\theta/2$ used for the remainder of the investigation are given in Table I as functions of $\sigma=2(\sin\theta/2)/\lambda$.

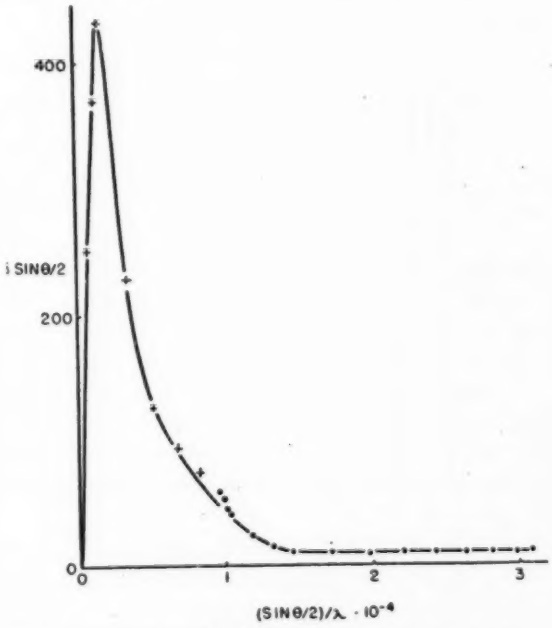

FIG. 1. Scattering of blue light ($\lambda=4358$A) by Lucite.

TABLE I. Angular dependent scattering of blue light ($\lambda=4358$A) by Lucite.

$\sigma\times10^{-4}$	$i\sin\theta/2$
0.0	0.0
0.171	254
0.342	431
0.513	385
0.685	237
0.856	159
1.030	123
1.199	101
1.370	84
1.712	54
2.058	32.5
2.399	17.5
2.740	8.0
3.422	4.1
4.110	2.0
4.790	1.0
5.475	0.0

The extensions of the inhomogeneities, i.e., the sizes of the regions over which they occur, is characterized by the correlation function, $\gamma(r)$ (see Part II, Eq. (1)). To obtain this function it is necessary to find another function $\Phi(\sigma)$. After the intensities have been corrected for the polarization by dividing by $(1+\cos^2\theta)/2$ and for instrumental effects such as shape of the beam, $\Phi(\sigma)$ is proportional to the scattered intensity times $\sin\theta/2$. Therefore the data in Table I represent $\Phi(\sigma)$ in arbitrary units. (See Eq. (7).) It remains then to choose a value of r, multiply Φ by $\sin(2\pi r\sigma)$ and determine the area under the curve of $\Phi\sin(2\pi r\sigma)$ *vs.* σ. This area is proportional to $r\gamma(r)$ for the single r. The process is repeated for several values of r until enough points are obtained to define the function $\gamma(r)$.

Figure 2 contains two curves of $\Phi\sin(2\pi r\sigma)$ for two different r values in the case of Lucite. $\Phi(\sigma)$ is again in arbitrary units. In determining the total area, that which lies below $\Phi\sin(2\pi r\sigma)=0$ must be subtracted from that which lies above.

By definition $\gamma(r)$ is 1 for $r=0$ and approaches 0 for large r. No matter what the units used the points determining $\gamma(r)$ should be normalized so that this is true. Figure 3 is a plot of $\gamma(r)$ *vs.* r for Lucite. The values are given in Table II. This function characterizes the extensions of the inhomogeneities. For a comparison of different samples one could, for example, compare the values for $\gamma(r)=0.5$. In the case of Lucite this could correspond to $r=2250$A. Another perhaps more illuminating way to treat $\gamma(r)$ is to try and fit a mathematical expression to the data. An example of such an expression is

$$\gamma(r)=e^{-r/a}.$$

It is evident from Fig. 4, where $1+\log_{10}\gamma(r)$ *vs.* r is plotted that this is a fairly good approximation. In this case $a=2800$A. For studying different samples, values of a could be compared. The larger the a

TABLE II. The correlation function, $\gamma(r)$.

$r \times 10^8$ cm	$\gamma(r)$
0.00	1.0
0.146	0.992
0.364	0.972
0.727	0.905
1.46	0.681
2.18	0.513
2.91	0.378
4.37	0.217
5.82	0.141

values the larger are the extensions of the inhomogeneities.

Furthermore, if the exponential representation of $\gamma(r)$ is correct, the mathematics in the theory of the method becomes very simple. Then it can be shown (see Eq. (4″)) that a plot of $\log(1/i)$ *vs.* $\log(1+k^2s^2a^2)$ should be a straight line. Here $k=2\pi/\lambda$, $s=2\sin\theta/2$, and a is the characteristic length in the above exponential expression. Thus we have a convenient way of seeing how good the approximation to $\gamma(r)$ is. In Fig. 5 the logarithms of the experimental intensities are plotted in the suggested way. The straight line is what would be expected if the exponential expression were a true representation of $\gamma(r)$. It seems to be a fairly good approximation.

The same type of plot can be used in another interesting and important way. If the angular dependence of the scattering from the solid is a result of interference of the scattered light it should be possible to superimpose the data obtained using green light on that obtained using blue light by a way which considers the difference in wave-length alone. The data for green light have been plotted on the same scale as was used in Fig. 5. The difference being only that the abscissae in this case have been calculated using a value of k corresponding to $2\pi/\lambda$ for green light instead of blue. The refractive index of Lucite has been taken as 1.49 for green light. This curve was then shifted, always keeping the axes of the two plots parallel, until a fit was obtained. The result is shown in Fig. 6. The crosses refer to the points for green light, the circles are for the blue light. It can be seen that it was possible to superimpose the two curves. Therefore, we have evidence that we are really dealing with an interference phenomenon.

Knowing the extensions of the inhomogeneities we would now like to know the average square, $\bar{\eta}^2$, of the fluctuations in dielectric constant which lead to this scattering. This can be done easily since the scattering at 90° of the Lucite has been compared with that of the standard solution whose turbidity, τ_0, is known. The intensity per unit solid angle, dI, of the light scattered by a solution of small molecules is given by

$$dI = I_0 \frac{3}{16\pi} \frac{dV}{R^2} \tau_0 (1+\cos^2\theta),$$

where dV is the scattering volume, R is the distance from the scattering volume to the point of observation and I_0 is the primary intensity. If dV/R^2 is the same for both solid and standard the intensity scattered at 90° by the solid is

$$I = I_0 \frac{3dV}{16\pi R^2} \tau_0 \frac{p}{p_0},$$

where p and p_0 are the galvanometer deflections for the solid and standard, respectively. In the notation of the present work $dV/R^2 = V/R^2$ and $dI = i$. The

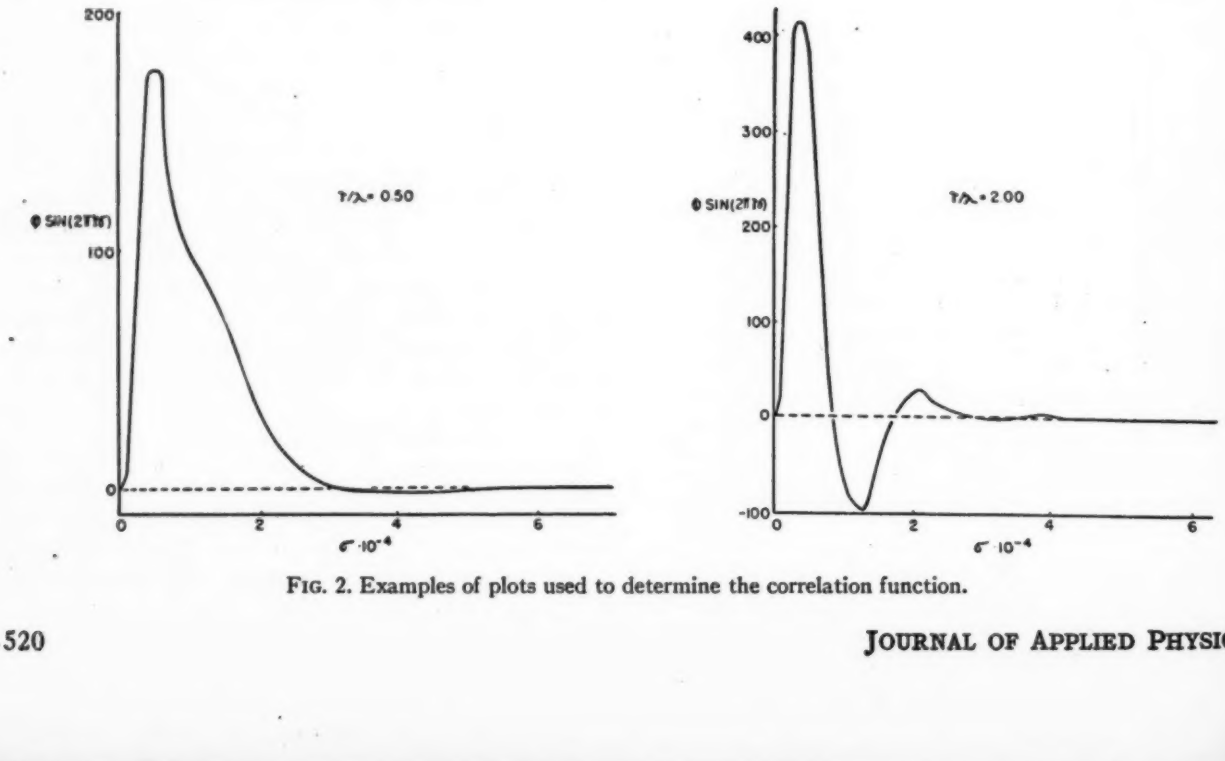

FIG. 2. Examples of plots used to determine the correlation function.

above expression can then be introduced into Eq. (7), and the absolute value of $\Phi(\sigma)$ can be obtained.

Now the surface of the $\Phi(\sigma)\sin(2\pi r\sigma)$ *vs.* σ-curve for a chosen value of r is equal to $2\pi(\bar{\eta}^2/\epsilon^2)r\gamma(r)$, where ϵ is the average dielectric constant of the medium and $\bar{\eta}^2$ is the average square of the dielectric constant fluctuations. Since we know $\Phi(\sigma)$ and thus the surface in terms of absolute values we can pick a value of r, find the corresponding predetermined value of $\gamma(r)$, insert the proper value of ϵ^2 and find $\bar{\eta}^2$. In the case of Lucite, using $\epsilon=2.25$ it was found that $(\bar{\eta}^2)^{\frac{1}{2}}=2.76\times10^{-4}$. This means that fluctuations in dielectric constant of the order of 3 parts in 10,000 cause the observed scattering of this sample. Since the dielectric constant is related to the refractive index, n, $\epsilon=n^2$ it can be shown that this corresponds to fluctuations in refractive index of about 1.7×10^{-4}.

Knowing $\bar{\eta}^2$ and the extensions of the inhomogeneities we can find the turbidity of the Lucite sample. Inserting the proper values in Eq. (6″) we find the turbidity to be 9.53×10^{-3} cm^{-1}. This is the part of the total turbidity of the sample due to the presence of the large inhomogeneities. That due to the smaller fluctuations which we subtracted earlier is 9×10^{-4} which is only one-tenth as large.

We may now compare these experimental values with the turbidity expected because of the changes in optical density due to thermal fluctuations in a fluid. The turbidity, τ, due to these thermal fluctuations has been calculated by Einstein.[4] With the aid of the Lorentz-Lorenz equation it can be written as

$$\tau=\frac{8\pi^3}{27}\frac{kT}{\lambda^4}\beta[(n^2-1)(n^2+2)]^2.$$

Here k is Boltzman's constant, T is the absolute temperature, β is the compressibility of the fluid, λ is the wave-length of the light in vacuum and n is the refractive index of the fluid. Using a compressibility $\beta=3\times10^{-12}$ cm^2/dyne (an average value for glassy substances) and an index of refraction $n=1.5$ we find the expected turbidity to be $\tau=9\times10^{-6}$ cm^{-1}. The observed turbidity corresponding to the small background scattering was 100 times larger. A study of this background scattering using shorter wave-lengths may lead to information regarding molecular configurations in the solid.

A few scattering measurements have been made on two samples of optical glass.[5] The samples were supplied in the shape of octagons with polished faces allowing measurements to be made at 45°, 90°, and 135°. The indices of refraction, n, of the glass for green and blue light are given in Table III.

[4] A. Einstein, Ann. d. Physik. **33**, 1275 (1910).
[5] Supplied by Dr. A. F. Turner, Bausch and Lomb Optical Company.

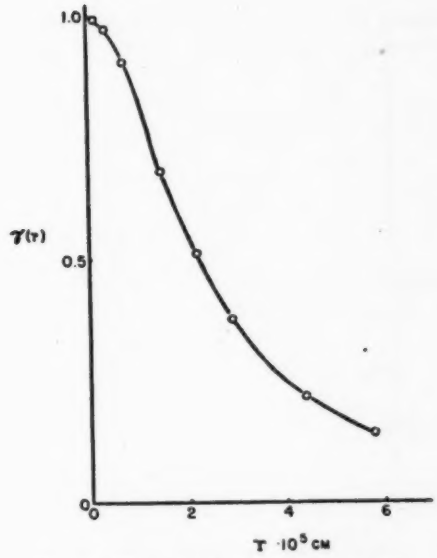

FIG. 3. The correlation function, $\gamma(r)$.

The scattering at 90° was compared with the scattering of our standard. Since the dissymmetry of scattering was low these values are then proportional to the turbidities. In Table IV the turbidities of the samples, the quotients of the scattering at 45° to that at 135°, the products $\bar{\eta}^2\omega_0$ (Eq. (6)) and the average value, $(\bar{r}^2)^{\frac{1}{2}}$, of the radii (Eq. (11′)) of the inhomogeneous regions are given.

An examination of these data shows that the extensions of the inhomogeneities are about the same for both samples and quite small. The difference in turbidities is due almost entirely to the difference in the dielectric constant fluctuations, $(\bar{\eta}^2)^{\frac{1}{2}}$, in the two glasses; these fluctuations are almost twice as large in the flint glass than in the crown glass. As yet no correlation of such data with the strength of the materials has been made but it is felt that this approach may be a useful one.

PART II**

Let us suppose an inhomogeneous solid in which the average dielectric constant is ϵ on which are superimposed local variations η. These variations η will be represented by a highly fluctuating function of the coordinates, the average value of η will be zero. We want to answer 2 questions: Firstly, how big are the variations η, and secondly, which is the average distance over which a variation η can be considered not to change appreciably. We try to answer these questions by observing firstly the intensity of the light scattering by the solid and secondly the angular distribution of the scattered intensity. It is evident from the beginning that

** At the New York Meeting of the American Physical Society in January, 1949, we found that a somewhat similar and independent treatment of the scattering problem herein discussed was attempted by C. L. Pekeris, Phys. Rev. **71**, 268 (1947).

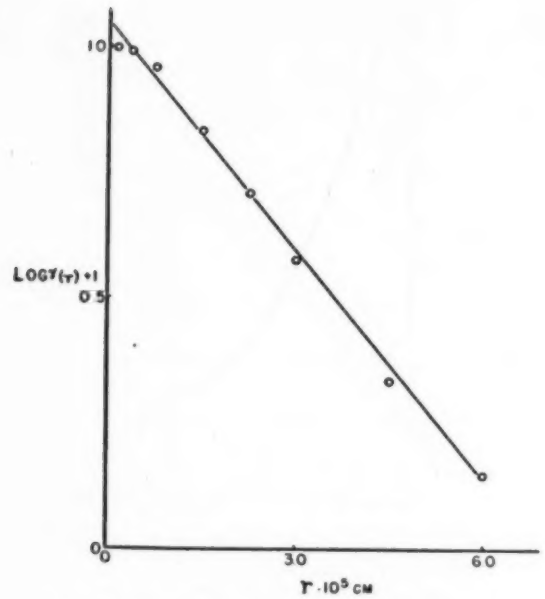

FIG. 4. The correlation function approximated by $\gamma(r)=e^{-r/a}$.

even large fluctuations will only give rise to a small turbidity if the distance over which η can be considered not to change appreciably is small compared with the wave-length. So we see that two quantities will enter in our considerations: (a) What we may call the amplitude of η, which will be conveniently measured by the average value of η^2 indicated by $\bar{\eta}^2$ (b) the average extension of the inhomogeneities. The best method for characterizing this extension seems to be the following. Consider two points 1 and 2 in the solid, situated at a distance r. Now take the product of the two fluctuations η_1 and η_2 the first measured in point 1, the second in point 2. Following this, move the points 1 and 2 around in the solid, always keeping their distance r fixed. In this way we will obtain a large number of values for the product $\eta_1\eta_2$ and we can find the average value of this product indicated by $\langle\eta_1\eta_2\rangle_{Av}$. Obviously this average will depend on the distance r. If $r=0$ we will have $\langle\eta_1\eta_2\rangle_{Av}=\bar{\eta}^2$. For large values of r the average product will be zero, since in this case η_1 and η_2 will vary quite independently. So in general $\langle\eta_1\eta_2\rangle_{Av}$ will be a function of the distance r which begins with $\bar{\eta}^2$ for $r=0$, and goes to zero in some as yet undetermined fashion with increasing values of r. We put

$$\langle\eta_1\eta_2\rangle_{Av}=\gamma(r)\bar{\eta}^2, \tag{1}$$

and call $\gamma(r)$ the *correlation-function*. (It has no physical dimensions, is just a number varying with the distance.) Obviously this function γ which drops from 1 to 0 indicates the average extension of the inhomogeneities. As a measure for their size we could for instance adopt the value of r for which γ becomes equal to $\frac{1}{2}$.

If we assume η/ϵ to be small it can easily be shown that the intensity of the light scattered by a volume V of the solid will be proportional to the average of the square of the absolute value of the following integral over the whole volume with the element of volume $d\tau$

$$F=\int \eta \exp[ik(\mathbf{s},\mathbf{R})]d\tau,$$

which we call F since it is analogous to what we are accustomed to call the *amplitude of the Form factor* of an atom for x-ray scattering.

The integral has to be extended over the whole volume V; k stands for $2\pi/\lambda$ in which λ is the wave-length as measured in the solid; R is the vectorial distance from a fixed point, the position of which will turn out to be immaterial; finally $\mathbf{s}$ is a vector

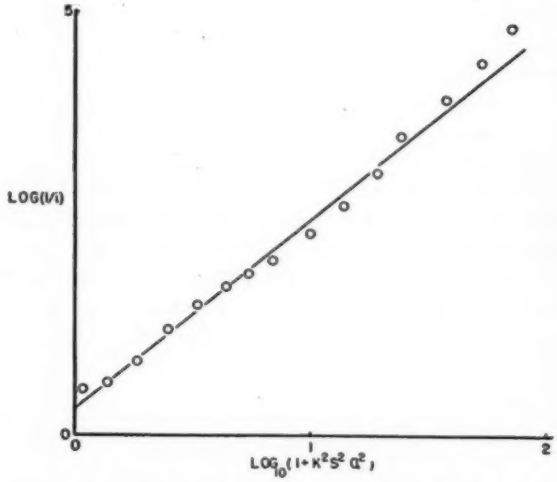

FIG. 5. Comparison of the observed intensities, ○, with those calculated using $\gamma(r)=e^{-r/a}$, —.

characterizing both the direction of incidence of the primary light and the direction of observation. This is done by drawing a unit vector $\mathbf{S}_0$ in the direction of the primary ray, another unit vector $\mathbf{S}$ in the direction of the secondary ray and putting

$$\mathbf{s}=\mathbf{S}-\mathbf{S}_0. \tag{2}$$

From this it follows that the length of the vector $\mathbf{s}$ is

$$s=2\sin\theta/2, \tag{2'}$$

in which θ is the angle between primary and secondary ray. It should be mentioned that the statement neglects the consideration of the polarization-effect in light scattering. That is why the statements in the next following part apply to the scattered intensity after correction for the polarization-effect. This correction can be performed by multiplying the observed scattered intensity by the reciprocal

of $(1+\cos^2\theta)/2$. Accepting the validity of our statement the intensity i of the scattered light will be

$$i=\int\int \eta_1\eta_2 \exp[ik(\mathbf{s}, \mathbf{R}_1-\mathbf{R}_2)]d\tau_1 d\tau_2. \quad (3)$$

Taking into account that $\mathbf{R}_1-\mathbf{R}_2$ is the vector $\mathbf{r}$ connecting the two points 1 and 2 and remembering that $\langle\eta_1\eta_2\rangle_{Av}$ will be zero for distances r which are very small compared with the dimensions of the volume V, we obtain

$$i\sim\bar{\eta}^2 V\int \gamma(r)\exp[ik(\mathbf{s}, \mathbf{r})]d\tau. \quad (3')$$

Since in many cases γ will depend only on the distance r and not on the direction in space of this vector the integration over all directions can be performed and the final result is[6]

$$i\sim 4\pi\bar{\eta}^2 V\int_0^\infty r^2\gamma(r)\frac{\sin ksr}{ksr}dr. \quad (3'')$$

Discussion

Suppose the average extension of the inhomogeneity is so small that in the range in which $\gamma(r)$ is appreciably different from 0 the quantity $ksr=4\pi(r/\lambda)\sin\theta/2$ is small. Our formula reduces then to

$$i\sim 4\pi\bar{\eta}^2 V\int_0^\infty r^2\gamma(r)dr.$$

In this way we note in passing that the scattered intensity is proportional to the illuminated volume V as was to be expected. The most interesting conclusion to be drawn from the formula is however that the scattering is proportional to the product of 2 quantities: $\bar{\eta}^2$ and a volume

$$\omega_0=\int_0^\infty \gamma(r)4\pi r^2 dr \quad (4)$$

which we would like to call the *correlation-volume*. In the limit for inhomogeneities extending over distances small compared with the wave-length it is only the product $\bar{\eta}^2\omega_0$ which matters. This confirms our expectation that in this limiting case large fluctuations combined with small extensions are just as effective as small fluctuations combined with large extensions.

In the more general case in which no assumption is made concerning the extension of the inhomogeneities as compared with the wave-length the result can still be expressed in the same way. The scattered intensity is again

$$i\sim V\bar{\eta}^2\omega$$

that is proportional to the product $\bar{\eta}^2\omega$ with the only difference that now the correlation-volume ω depends on the direction of observation and the wave-length since in general this volume has to be defined by the equation

$$\omega=4\pi\int_0^\infty \frac{\sin ksr}{ksr}r^2\gamma(r)dr. \quad (4')$$

It is this dependence which enables us to draw conclusions about the extension of the inhomogeneities independent of the value of $\bar{\eta}^2$.

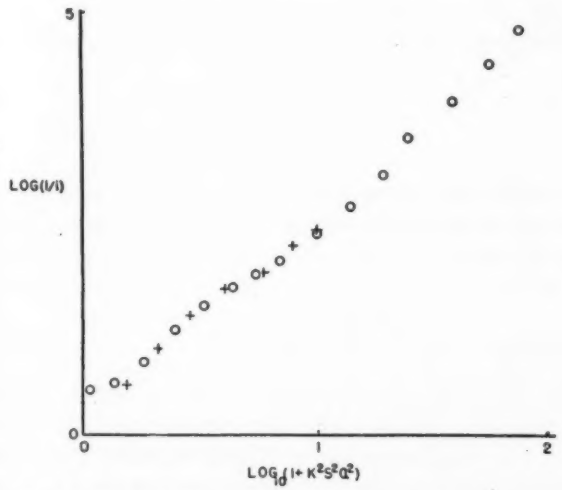

FIG. 6. Superposition of the data for the Hg blue, ○, and green, +, light.

[6] If a medium in which originally γ depended only on r and not on its directions is put under a strain, γ will begin to depend on the direction of r too. In this case the scattered intensity will not have central symmetry around the directions of the primary ray. The same will be true if for instance the inhomogeneities are striations with a common axis.

TABLE III. Refractive indices of glass samples.

Glass	Wave-length	n
BSC-2	489 mμ	1.5170
	436 mμ	1.5269
DF-2	589 mμ	1.6170
	436 mμ	1.6389

TABLE IV. Summary of data for optical glass samples.

Glass	$\tau\times10^4$ cm^{-1}	i_{45}/i_{135}	$\bar{\eta}^2\omega_0\times10^{24}$	$(\overline{r^2})^{\frac{1}{2}}$
BSC-2	1.56	1.22	6.7	296A
DF-2	5.34	1.18	2.3	269A

Example

Let us assume in this example a simple definite function for the correlation, namely,

$$\gamma(r)=e^{-r/a},$$

where the length a will be a measure of the extension of the inhomogeneities.

It can now easily be calculated that (see Eq. (4′))

$$\omega = 4\pi \int \frac{\sin ksr}{ksr} r^2 \gamma(r) dr = \frac{8\pi a^3}{(1+k^2 s^2 a^2)^2}, \quad (4'')$$

and therefore

$$i \sim V\bar{\eta}^2 \omega = V\bar{\eta}^2 \frac{8\pi a^3}{(1+k^2 s^2 a^2)^2}.$$

We will call $1/(1+k^2 s^2 a^2)^2$ the Dissymmetry-factor f, which in the general case is defined as

$$f = \frac{\omega}{\omega_0} = \frac{\int_0^\infty (\sin ksr/ksr) r^2 \gamma(r) dr}{\int_0^\infty r^2 \gamma(r) dr},$$

and we see that in our example this factor f goes from 1 for $s=0$ ($\theta=0°$) to

$$f = \frac{1}{(1+4k^2a^2)^2} = \frac{1}{(1+16\pi^2 a^2/\lambda^2)^2}$$

for $s=2$ ($\theta=180°$). This means that a 50 percent decrease of the scattered intensity is to be expected over the interval 0°–180° if $a/\lambda = 0.051$ which shows that we should be able to detect rather small correlation-distances.

Absolute Value of the Scattered Intensity

So far we have given only an expression which is proportional to the scattered intensity, without fixing the proportionality factor. Amplifying the statement in this respect, it can be shown that the scattered intensity i coming from a volume V under an angle θ at a large enough distance R is to the primary intensity I as

$$\frac{i}{I} = \frac{\bar{\eta}^2}{\epsilon^2} \frac{\pi^2 V \omega}{\lambda^4 R^2} \frac{1+\cos^2\theta}{2} \quad (5)$$

in which ω is as before the correlation-volume (see Eq. (4′)) and λ is the wave-length in the solid. In this formula the polarization effect is included by the introduction of the last factor of Eq. (5).

By integrating over all directions in space an expression for the turbidity τ can be derived from (5). In this way a formula is found which shows a simple dependence on the wave-length only for the limiting case that the size of the correlation-volume is small compared with the wave-length. Under these circumstances we have the familiar Rayleigh law that $\tau \sim 1/\lambda^4$ and we expect blue scattered from white incident light. From Eq. (5) it can easily be seen that for larger sizes of the correlation volume the scattered light will be more nearly white in color. In the limiting case of small size the integration over all directions in space leads to the expression

$$\tau = \frac{8\pi^3}{3} \frac{\bar{\eta}^2 \omega_0}{\epsilon^2 \lambda^4} \quad (6)$$

for the turbidity τ in which the limiting correlation volume is defined by Eq. (4) and λ is the wave-length in the solid. In the special case of our example calculated on the basis of the correlation-function $\gamma = e^{-r/a}$ we would have for small values of a/λ

$$\tau = \frac{64\pi^4}{3} \frac{\bar{\eta}^2 a^3}{\epsilon^2 \lambda^4}. \quad (6')$$

The expression for any value of a/λ can be shown to be

$$\tau = 32\pi^4 \frac{\bar{\eta}^2 a^3}{\epsilon^2 \lambda^4} \left[\frac{(b+2)^2}{b^2(b+1)} - \frac{2(b+2)}{b^3} \log(b+1) \right], \quad (6'')$$

where

$$b = 4k^2 a^2 = \frac{16\pi^2}{\lambda^2} a^2.$$

How to Determine the Correlation Function $\gamma(r)$ from Experiments on the Angular Distribution of the Scattered Intensity

For the scattered intensity i as compared with the primary intensity I we have found (see Eq. (5)).

$$\frac{i}{I} = \frac{\bar{\eta}^2}{\epsilon^2} \frac{\pi^2 V}{\lambda^4 R^2} \frac{1+\cos^2\theta}{2} \omega,$$

in which the correlation volume ω is related to the correlation function $\gamma(r)$ by the formula (see Eq. (4′)).

$$\omega = 4\pi \int_0^\infty \frac{\sin ksr}{ksr} r^2 \gamma(r) dr.$$

Instead of the angle θ itself, we can use the variable $s = 2\sin\theta/2$ and plot the observed values of i as a function of this variable s. This plot being available we can now plot the new function Φ defined by

$$\Phi = \left(\frac{s}{\lambda} \frac{i}{I}\right) \Big/ \left(\frac{\pi}{4} \frac{V}{\lambda^4 R^2} \frac{1+\cos^2\theta}{2}\right), \quad (7)$$

which will have the dimensions of the square of a length. In fact what has been done is to define this

function Φ by putting

$$\Phi=\frac{2\bar{\eta}^2}{\epsilon^2}ks\omega=4\pi\frac{\eta^2}{\epsilon^2}\frac{s}{\lambda}\omega. \tag{7'}$$

From the definition of ω it is clear that Φ is a function of the quotient s/λ. So it will be better to plot Φ as a function of this variable. This means implicitly that in case experiments on the angular distribution have been made with different wave-lengths, we will obtain just one curve for Φ provided it is plotted as a function of s/λ and not of s alone. Let us call the new variable σ, that is

$$\sigma=s/\lambda. \tag{8}$$

Φ is a function of σ and as such determined by experiment (see Eq. (7)).

We now have

$$\Phi(\sigma)=4\pi\frac{\bar{\eta}^2}{\epsilon^2}\sigma\omega=8\pi\frac{\bar{\eta}^2}{\epsilon^2}\int_0^\infty r\gamma(r)\sin(2\pi\sigma r)dr. \tag{9}$$

But this integral-equation can be solved at once by the well-known Fourier Transformation and we obtain

$$2\pi\frac{\bar{\eta}^2}{\epsilon^2}r\gamma(r)=\int_0^\infty\Phi(\sigma)\sin(2\pi r\sigma)d\sigma. \tag{10}$$

The only thing we have to do in order to determine the correlation-function γ is to plot $\Phi(\sigma)$, choose a value of r, plot the product $\Phi(\sigma)\sin(2\pi r\sigma)$ and determine the surface under this curve from $\sigma=0$ to $\sigma=\infty$. This surface is now equal to the product $2\pi(\bar{\eta}^2/\epsilon^2)r\gamma(r)$. In this way we have found $\gamma(r)$ for the definite value of r which has been chosen. We can repeat the process for other values of r and so obtain the whole curve.

It is clear that this procedure is only practical if and when the extension of the inhomogeneities is so large that a pronounced dissymmetry-effect exists. Otherwise we cannot cover with the given wave-length λ a large enough range of σ-values to define the function $\Phi(\sigma)$ adequately.[7]

We may expect that in our case of light scattering the extension of the inhomogeneities may sometimes be too small in this sense. It is of importance to know what the conclusions are which can be drawn in such a case. In order to answer this question we can take our correlation-volume as defined by Eq. (4') and develop the function $(\sin ksr)/ksr$ under the integral in a power-series. If this is done, we obtain

$$\omega=\omega_0\left\{1-\frac{k^2s^2}{3!}\bar{r}^2+\frac{k^4s^4}{5!}-+\cdots\right\}, \tag{11}$$

in which we have used the following definitions;

$$\bar{r}^2=\frac{1}{\omega_0}\int_0^\infty r^2\gamma(r)4\pi r^2dr,$$
$$\bar{r}^4=\frac{1}{\omega_0}\int_0^\infty r^4\gamma(r)4\pi r^2dr. \tag{11'}$$

The scattered intensity i divided by the primary intensity finally becomes

$$\frac{i}{I}=\frac{\bar{\eta}^2}{\epsilon^2}\frac{\pi V\omega_0}{\lambda^4R^2}\frac{1+\cos^2\theta}{2}\times\left\{1-\frac{k^2\bar{r}^2}{3!}s^2+\frac{k^4\bar{r}^4}{5!}s^4-+\cdots\right\}. \tag{12}$$

We can always represent our experimental results by a series of the form

$$\frac{i}{I}=A\frac{1+\cos^2\theta}{2}\{1-\alpha s^2+\beta s^4-+\cdots\}. \tag{12'}$$

Comparison of (12') and (12) shows that the absolute intensity of scattering measured by A determines the product $\bar{\eta}^2\omega_0$. As soon as an angular dissymmetry can be observed the coefficients α, β, $\cdots$ can be evaluated. Perhaps only the first of them, α, if the dissymmetry is slight, more of these coefficients if it is more pronounced. If α alone is available we only learn the value of $\bar{r}^2$ as a measure of the extension of the inhomogeneities. However, the more such coefficients are available, the more we learn about details of the correlation function $\gamma(r)$. The problem how to make approximations for $\gamma(r)$ if r^2, r^4, etc. are known can be handled mathematically. At the present stage of the whole problem we do not think it necessary to discuss this aspect. It may be sufficient to say that in the case of the distribution curve for the molecular weights of a polymer just the same problem occurs.

On the other hand it should be said that the whole discussion also applies to x-ray scattering (with the proper interpretation of η by its corresponding electron-density). In this way it provides a theory for the interpretation of *small-angle x-ray scattering*, which will be important if inhomogeneities occur of about 150 A.U. extension or smaller which cannot be analyzed any more with visible light. The large angle x-ray scattering finally gives evidence of the inhomogeneities on an atomic scale.

[7] The procedure just outlined is the same as the procedure followed in the analysis of x-ray scattering of liquids leading to the so-called radial distribution-function in the liquid.

Relationship between Gough-Joule Coefficients and Moduli of Vulcanized Rubbers*

F. S. Conant, G. L. Hall, and G. R. Thurman
Chemical and Physical Research Laboratories, The Firestone Tire and Rubber Company, Akron, Ohio

The Gough-Joule coefficients (a) at constant stress and (b) at constant strain are defined and methods of measurement of each on vulcanized rubbers are given. It is shown mathematically and experimentally that the ratio of (b) to (a) is equal to the "tangent" modulus. The quotient of the Gough-Joule coefficient at constant stress divided by the stress and the quotient of the Gough-Joule coefficient at constant strain divided by the strain are shown to be constants which are independent of the stress-strain-temperature conditions of the test. Experimental data are given for stocks based on Hevea, GR-S, Neoprene GN, Butyl Rubber, and Butaprene.

INTRODUCTION

THE first reference to the increase in temperature of rubber on stretching was by J. Gough,[1] but this was apparently unnoticed until Joule[2] rediscovered the phenomenon. Joule's experiments showed a decrease in temperature with increase in elongation up to about 2 percent and an increase in temperature with increase in elongation beyond this point. He recognized also that the principles of thermodynamics required that a rubber strip elongated by a constant load must become shorter when heated.

Subsequent investigations have been made on the change in length of a rubber strip with a change in temperature at constant load[3] and on the change in force with change in temperature at constant elongation.[4] The use of three concepts to designate the same phenomenon indicates an awareness of interrelationships among them, but this relationship has not been explicitly stated. The latter two concepts lend themselves most readily to quantitative measurements, and will be referred to as the Gough-Joule effects at constant stress and at constant strain, respectively.

Investigations of the Gough-Joule effect in vulcanized rubber have been very productive of knowledge concerning the physical structure of rubber. The use of rubberlike materials as support members has also emphasized the practical importance of the effect. In such cases it is important to know the interrelationship of the Gough-Joule coefficients and moduli.

The greatest experimental difficulty experienced by investigators in the field has been the attainment of thermodynamic equilibrium, and various methods have been used to minimize creep and plastic flow during experiments. Williams[3] obtained stress-strain curves with extreme rapidity and was able to show the increase in modulus of stretched rubber with increased temperature. Gerke[4] obtained equilibrium deformations by means of either horizontal or vertical vibrations in stretched samples. Meyer and Ferri[5] held the desired elongation at the highest temperature of test until increase in length became negligible. Meyer and Van der Wyk[6] obtained torsional deformations alternately 5°C higher and 5°C lower than test temperature until the plastic deformation tended to disappear. In the present work it was found that a specimen which had been kept under a given shear stress for 16 hours at 35°C was essentially in stress-strain equilibrium (within the time required for the experiment) at temperatures below 35°C. This method of conditioning was therefore used in all of the experimental work described below. The advantages of conditioning at temperatures above test temperatures is apparent from a consideration of the fact that in the absence of chemical changes or crystallization the same equilibrium strain-temperature curve is eventually reached at any temperature at which the test specimen is elastic. Temperatures much above 35°C could not be used because of the accelerated rate of chemical changes.

Most of the early work on the Gough-Joule effect was done in tension.[7,8] The disadvantages of this type of deformation have recently been pointed out by Meyer and Van der Wyk.[6] They show that the apparent change of sign of the effect at 0.10 strain is due to volume change and hence is eliminated when shear deformation is used.

Another time-dependent factor besides creep and plastic flow often influences the attainment of thermodynamic equilibrium. This is crystallization. A second important advantage of a shear type specimen for work of this nature is that shear does

* Presented at the Sixth Meeting of the Division of High-Polymer Physics, American Physical Society, New York City, January 27–29, 1949.

[1] J. Gough, Memoirs of the Lit. and Phil. Society of Manchester 1, 288 (1805).

[2] J. P. Joule, Trans. Roy. Soc. (London) 149, 91 (1859).

[3] Ira Williams, Ind. Eng. Chem. 21, 872 (1929), Rubber Chem. and Tech. 3, 74 (1930).

[4] R. H. Gerke, Ind. Eng. Chem. 22, 73 (1930).

[5] K. H. Meyer and C. Ferri, Helv. Chim. Acta 18, 570 (1935). Rubber Chem. and Tech. 8, 319 (1935).

[6] K. H. Meyer and A. J. A. Van der Wyk, Helv. Chim. Acta 29, 1842 (1946). Rubber Chem. and Tech. 21, 314 (1948).

[7] L. Hock, "Physics of rubber," *The Science of Rubber*, K. Memmler, Am. Ed. (Dunbrook & Morris, Reinhold Publishing Corporation, New York, 1934).

[8] W. W. Vogt, "The physics of vulcanized rubber," *Chemistry and Technology of Rubber*, Davis & Blake (Reinhold Publishing Corporation, New York, 1937).

not appear to induce crystallization to the same extent as does equivalent tension or compression. It has been shown in this laboratory, for example, that a particular Hevea stock did not crystallize during a period of six hours at −20°C under a shear strain of 1.07. The same stock, by its low recovery rate, showed definite evidence of crystallization after 6 hours storage at 40 percent compression at −20°C.

MATHEMATICAL DEVELOPMENT

Suppose a specimen of rubber is acted upon by a stress σ which produces a strain γ at absolute temperature T. Let C be the thermal capacity of the specimen, H its intrinsic energy or enthalpy. Assuming no significant difference between C_σ and C_γ a single symbol may be used for either.

Case I. Constant Strain

Let T and σ be changed by small amounts with γ held constant, then the heat received by the strip

$$dQ = CdT + C(\partial T/\partial\sigma)d\sigma. \tag{1}$$

The work done on the strip is $\gamma d\sigma$, hence

$$dH = dQ + \gamma d\sigma = CdT + C(\partial T/\partial\sigma)d\sigma + \gamma(\partial\sigma/\partial T)dT,$$

or

$$dH = [C + \gamma(\partial\sigma/\partial T)]dT + C(\partial T/\partial\sigma)d\sigma. \tag{2}$$

The change in entropy is

$$dS = \frac{dQ}{T} = \frac{C}{T}dT + \frac{C}{T}\left(\frac{\partial T}{\partial\sigma}\right)d\sigma. \tag{3}$$

Since dS and dH are perfect differentials the Euler equations may be applied to Eqs. (2) and (3) to yield

$$\frac{\partial C}{\partial\sigma} + \left(\frac{\partial\gamma}{\partial\sigma}\right)\left(\frac{\partial\sigma}{\partial T}\right) = 0, \tag{4}$$

and

$$\frac{\partial C}{\partial\sigma} = \frac{\partial C}{\partial T}\frac{\partial T}{\partial\sigma}. \tag{5}$$

Eliminating $\partial C/\partial\sigma$ between (4) and (5) and solving for $\partial\sigma/\partial T$ we have

$$\frac{\partial C}{\partial T}\frac{\partial T}{\partial\sigma} = -\frac{\partial\gamma}{\partial\sigma}\frac{\partial\sigma}{\partial T}. \tag{6}$$

The quantity $(\partial\sigma/\partial T)_\gamma$ will be called the Gough-Joule coefficient at constant strain.

Case II. Constant Stress

Following a similar development for the case of constant stress we may show that

$$\frac{\partial C}{\partial T}\frac{\partial T}{\partial\gamma} = -\frac{\partial\sigma}{\partial\gamma}\frac{\partial\gamma}{\partial T}. \tag{7}$$

The quantity $(\partial\gamma/\partial T)_\sigma$ will be called the Gough-Joule coefficient at constant stress. From Eqs. (6) and (7) we obtain

$$\left(\frac{\partial\sigma/\partial T}{\partial\gamma/\partial T}\right)^2 = \left(\frac{\partial\sigma}{\partial\gamma}\right)^2,$$

or

$$\frac{\partial\sigma/\partial T}{\partial\gamma/\partial T} = -\frac{\partial\sigma}{\partial\gamma}. \tag{8}$$

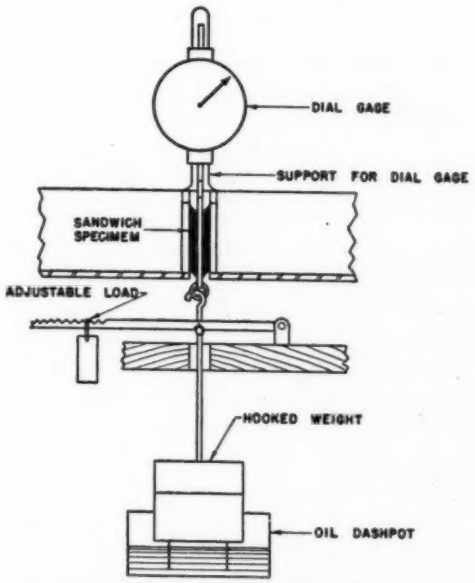

FIG. 1. Diagram of apparatus.

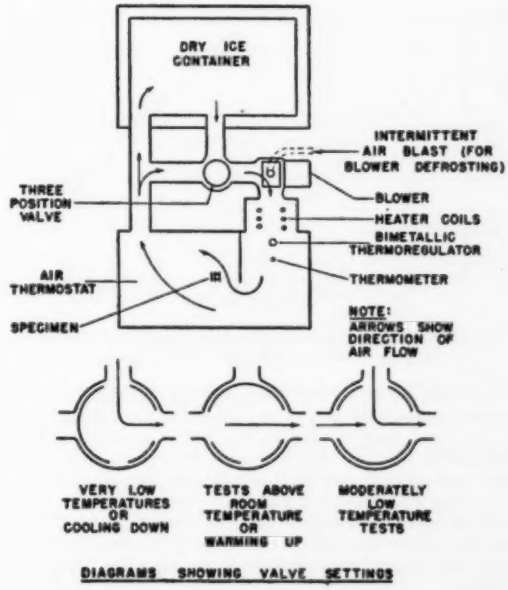

FIG. 2. Air thermostat.

TABLE I. Compounding formulas.

Pigment Cure	Hevea *A* 35′/288°F	Hevea *B* 50′/280°F	Hevea *C* 35′/288°F	Butyl GR-I 30′/312°F	Neoprene GR-M 60′/280°F	GR-S 60′/280°F	Butaprene (medium acrylonitrile) 60′/280°F
Polymer	100	100	100	100	100	100	100
Sulfur	3	3	3	1.5	—	2	2
Zinc oxide	3	5	3	4	5	5	5
Stearic acid	0.5	3	3.5	—	0.5	—	1
Channel black	—	15	50	30	20	20	45
SRF black	—	15	—	—	20	15	—
Mercaptobenzothiazole	1	—	1	1	—	—	—
PBNA	1	1	1	—	—	—	2
Pine tar	—	—	3	—	—	—	—
808 accelerator	—	—	—	—	—	0.25	—
Dibutyl sebacate	—	—	—	—	—	—	20
Medium process oil	—	2.5	—	—	—	—	—
Paraffin	—	—	—	2	—	—	—
Lt. calcined magnesia	—	—	—	4	4	—	—
Methyl tuads	—	—	—	1	—	—	—
Benzothiazyl disulfide	—	0.75	—	—	1	—	1
Neozone D	—	—	—	—	2	—	—
Lt. process oil	—	—	—	—	15	—	—
Petrolatum	—	—	—	—	2	—	—
Paraflux	—	—	—	—	—	5	—
Turgum S	—	—	—	—	—	8	—
Santocure	—	—	—	—	—	1.25	—

In the case of a rubber-like material $\partial\gamma/\partial T$ is negative, and all other terms in Eq. (8) are positive. Hence only the negative sign is applicable to the right hand member of the equation.**, [9]

The second member of Eq. (8) is the slope of the stress-strain curve at the point (σ, γ) and may be termed the "tangent" modulus of the stock at this point. It has thus been shown that the ratio of the Gough-Joule coefficient at constant strain to that at constant stress is equal to the tangent modulus.

If it is initially assumed that there exists some function of σ, γ, and T and no other thermodynamic variable such that

$$f(\sigma, \gamma, T) = 0, \tag{9}$$

then Eq. (8) may be derived much more simply. By a well-known mathematical theorem it follows from Eq. (9) that

$$\left(\frac{\partial\sigma}{\partial\gamma}\right)\left(\frac{\partial\gamma}{\partial T}\right)\left(\frac{\partial T}{\partial\sigma}\right) = -1 \tag{10}$$

which is equivalent to Eq. (8).

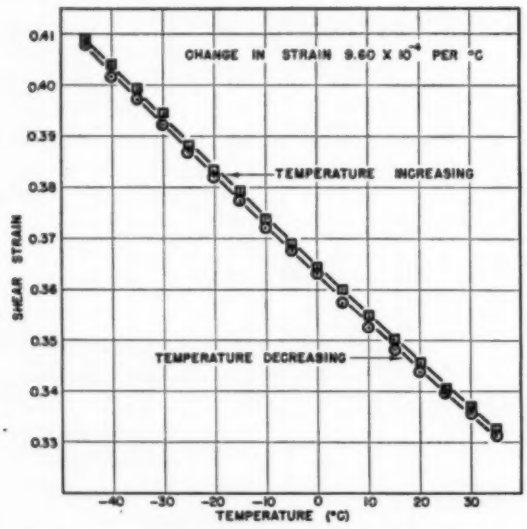

FIG. 3. Gough-Joule effect under constant stress of 35.6 lbs./sq. in., Hevea compound *B*.

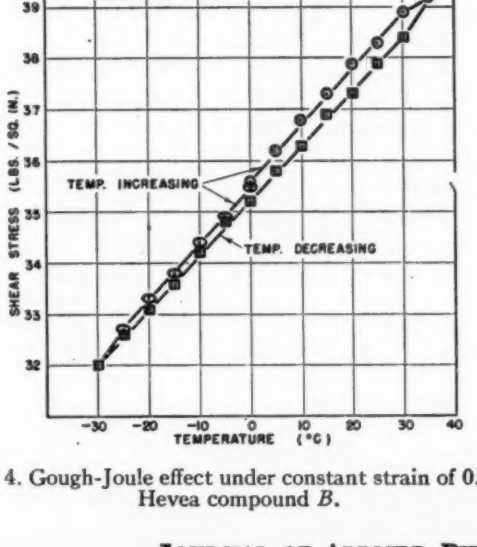

FIG. 4. Gough-Joule effect under constant strain of 0.365, Hevea compound *B*.

** It should be observed that the Gough-Joule coefficient at constant stress may be calculated from the tangent modulus at a given stress and temperature. It has been pointed out by Gee (reference 9) that $(\partial H/\partial\gamma)_{T,\sigma}=0$ for shear deformations. Making use of this relation it may be readily shown that $(\partial\gamma/\partial T)_\sigma=\sigma/T\cdot 1/(\partial\sigma/\partial\gamma)$. Values of $(\partial\gamma/\partial T)_\sigma$ calculated from this formula are not, however, in close agreement with observed coefficients given in Table II. The difference between the observed and calculated values is as high as 30 percent in some cases.

[9] G. Gee, Quart. Rev. Chem. Soc. 1, 265 (1947).

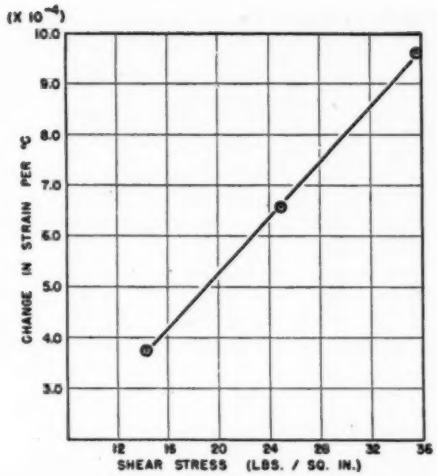

FIG. 5. Effect of degree of stress on Gough-Joule effect at constant stress, Hevea compound *B*.

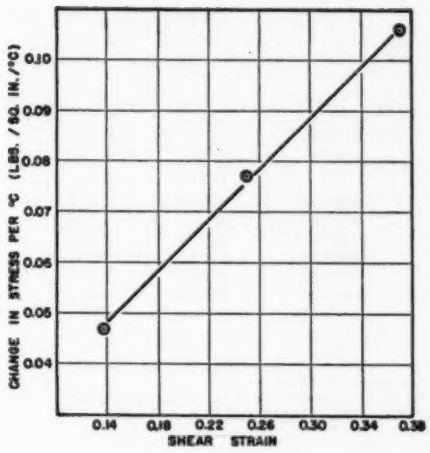

FIG. 6. Effect of degree of strain on Gough-Joule effect at constant strain, Hevea compound *B*.

It will be shown later that over a wide temperature range the magnitude of the Gough-Joule coefficient at constant stress is directly proportional to the stress (Fig. 5), and that the Gough-Joule coefficient at constant strain is directly proportional to the strain (Fig. 6). The quotients $(\partial\sigma/\partial T)_\gamma/\gamma$ and $(\partial\gamma/\partial T)_\sigma/\sigma$ are thus constant over considerable portions of the stress-temperature and strain-temperature curves. From Eq. (8) we obtain

$$\frac{(\partial\sigma/\partial T)_\gamma \cdot (1/\gamma)}{(\partial\gamma/\partial T)_\sigma \cdot (1/\sigma)} = -\left(\frac{\partial\sigma}{\partial\gamma}\right)_T \frac{\sigma}{\gamma}. \qquad (11)$$

The member on the right of Eq. (11) is the product of the "tangent" modulus and the "secant" modulus, where "secant" modulus is used to denote the quotient of the total stress to the strain produced by that stress.

The following experimental work was performed to test the validity of Eqs. (8) and (11) as applied to a variety of compounds. Both the type of polymer and the pigmentation was varied.

DESCRIPTION OF APPARATUS

The apparatus used was basically one developed by Dr. H. Leaderman and one of the authors*** for use in the study of creep and recovery. The diagram in Fig. 1 shows that the apparatus consists essentially of a means of applying a constant shear stress or a constant shear strain to a double sandwich type of specimen, and of observing the deformation of the specimen as test conditions are varied. The side plates of the test specimen are firmly gripped in slots in a jig. An extension rod clamped to the central steel member of the specimen passes through the housing; the dial gage spindle rides on this extension rod. The dial gage used has graduations of 0.0001 inch.

The load is applied by lowering a hooked weight so that it engages with a ring attached to the central member of the sandwich. The basic hooked weight is provided with an oil "dashpot" at its lower end to damp out horizontal oscillations.

The housing or air thermostat in which the jig is placed is shown in Fig. 2. Air is blown into the thermostat by means of a centrifugal blower over heater coils, part of which are controlled by a bimetallic thermoregulator through a lock-in type relay, and part of which are uncontrolled. According to the setting of the gate valve shown in Fig. 2, the air leaving the thermostat may either

(*i*) pass through the dry ice container, and then through the gate valve to the blower, or
(*ii*) pass directly through the gate valve to the blower, or
(*iii*) follow both of these paths.

The three settings of the gate valve are shown in Fig. 2.

A thermocouple inserted into the center metal member of the test specimen was used to measure the actual temperature of the specimen at all times.

METHOD OF TEST

Each specimen tested was conditioned overnight (16 hours) at 35°C under the load to be used in the constant stress test. Unless otherwise stated, this load was 100 lbs. or 35.6 lbs./sq. in. on the specimen.

In the constant stress test the temperature of the housing was lowered at such a rate that a constant temperature differential of 15°C was maintained

*** G. L. Hall.

TABLE II. Relationships of Gough-Joule coefficients to moduli.

Compound	$\left(\frac{\partial\gamma}{\partial T}\right)_\sigma$ (°C^{-1})	$\left(\frac{\partial\sigma}{\partial T}\right)_\gamma$ (lbs./in.^{2}/°C)	$\frac{(\partial\sigma/\partial T)_\gamma}{(\partial\gamma/\partial T)_\sigma}$ [a] (lbs./in.^{2})	$\frac{\Delta\sigma}{\Delta\gamma}$ [b] (lbs./in.^{2})	$\frac{\sigma}{\gamma}$ (lbs./in.^{2})	Ref. temp. °C	$\frac{(\partial\gamma/\partial T)_\sigma}{\sigma}$ ($\times 10^{-4}$) (in.^{2}/lb./°C)	$\frac{(\partial\sigma/\partial T)_\gamma}{\gamma}$ (lbs./in.^{2}/°C)	$\frac{(\partial\sigma/\partial T)_\gamma}{\gamma}\Big/\frac{(\partial\gamma/\partial T)_\sigma}{\sigma}$ [c] (lbs./in.^{2})^2	$\frac{\Delta\sigma}{\Delta\gamma}\cdot\frac{\sigma}{\gamma}$ [d] (lbs./in.^{2})^2
Hevea *B*	0.00096	0.1060	110.4	111.2	97.5	0	2.70	0.293	10,850	10,710
GR-S	0.00139	0.1642	118.1	112.4	87.8	20	3.91	0.398	10,180	9,860
Butaprene	0.000835	0.1120	134.4	135.2	74.2	10	2.34	0.237	10,130	10,030
Butyl	0.00150	0.1300	86.7	85.8	61.9	15	4.21	0.226	5,370	5,310
Neoprene	0.00120	0.1350	112.5	114.1	64.1	0	3.37	0.243	7,210	7,310
Hevea *A*	0.00167	0.1053	63.1	67.0	65.5	0	4.58	0.194	4,240	4,390
Hevea *C*	0.000148	0.0872	588	596	319	0	0.416	0.781	188,000	190,000

[a] Theoretical tangent modulus obtained from Eq. (8).
[b] Measured tangent modulus.
[c] Theoretical value of the product of the tangent and secant moduli from Eq. (11).
[d] Product of measured tangent and secant moduli.

between the housing and the specimen. Dial gage readings were obtained at 5°C intervals down to the temperature at which the strain-temperature curve departed from linearity. The temperature was then raised to 35°C at such a rate that a 15°C temperature differential was maintained between the housing and the specimen and again making dial gage readings at 5°C intervals. The slopes of the resulting strain-temperature curves are almost identical and only very slightly displaced from one another. The temperature gradient within the specimen when the temperature of the housing is being raised or lowered, thus appears to be relatively unimportant. Figure 3 shows typical data obtained in this manner. The compound used in this case was Hevea compound *B* (Table I). The average slope of the straight line portions of the two curves is taken as the Gough-Joule coefficient at constant stress.

In the constant strain tests the same specimen as previously tested under constant stress was first brought to a temperature corresponding to the center of the linear portion of the strain-temperature curve. The resulting strain was then maintained constant by varying the position of the load on the lever arm shown in Fig. 1. The temperature was altered in the manner previously described and the load recorded at 5°C intervals. The data shown in Fig. 4 on the Hevea compound *B* is typical of stress-temperature curves obtained in this manner. Duplication of the original stress after traversing the temperature cycle shows the system to have been in equilibrium during the process.

The tangent modulus was obtained at a temperature corresponding to the middle point of the linear portion of the strain-temperature curve. A 10-lb. additional load (3.56 lbs./sq. in.) was added to the specimen and the resulting deflection noted after 30 minutes. This 10 lb. and another 10 lb. were then removed from the specimen and the recovery noted after 30 minutes. The tangent modulus was taken as the mean of the moduli obtained upon addition and subtraction of the 10-lb. loads. In the case of the Hevea Compound *B* the modulus obtained upon addition of the 10-lb. load was 108.5 lbs./sq. in. and that obtained upon removal of the load was 114.0 lbs./sq. in.

Table I shows the formulas and cures of the compounds employed in these tests. Five commonly known polymers are represented. Three degrees of black content of Hevea compounds are included to show the effect, if any, of these compounding changes on the validity of Eqs. (8) and (11).

RESULTS

In every case investigated the Gough-Joule coefficient at constant stress was directly proportional to the stress and that at constant strain was directly proportional to the strain. A typical illustration of this behavior is shown in Figs. 5 and 6 for the Hevea low black stock. Within rather wide limits, then, the quotients $(\partial\gamma/\partial T)_\sigma/\sigma$ and $(\partial\sigma/\partial T)_\gamma/\gamma$ are independent of the stress and strain at which they were obtained. These values are thus characteristic of the particular compound and are not dependent on test conditions.

Table II shows the relevant data obtained on the compounds given in Table I. The close agreement of columns 4 and 5 shows that Eq. (8) is true experimentally for the compounds studied. In the same manner, the agreement of the last two columns verifies Eq. (11) experimentally.

In Table II:

$(\partial\gamma/\partial T)_\sigma$ = Gough-Joule coefficient at constant stress for 100 lb. (35.6 lbs./sq. in.) load. Change in strain per degree C.

$(\partial\sigma/\partial T)_\gamma$ = Gough-Joule coefficient at constant strain (that produced by 35.6 lbs./sq. in. load at reference temperature). Change in stress (in lbs./sq. in.) per degree C.

$\Delta\sigma/\Delta\gamma$ = Tangent modulus at reference temperature (in lbs./sq. in.).

σ/γ = Secant modulus at reference temperature (in lbs./sq. in.).

$(\partial\gamma/\partial T)_\sigma/\sigma$ = Gough-Joule coefficient per unit stress at constant stress.

$(\partial\sigma/\partial T)_\gamma/\gamma$ = Gough-Joule coefficient per unit strain at constant strain (in lbs./sq. in.).

ACKNOWLEDGMENTS

The authors wish to acknowledge the assistance of discussions on the Gough-Joule effect with Dr. J. W. Ballard and Mr. W. E. Loue. The continued interest of Dr. E. W. Ford is much appreciated as is the permission of The Firestone Tire and Rubber Company to publish these results.

Polymerization in the Solid State*

E. MILLER, I. FANKUCHEN, AND H. MARK

Polytechnic Institute of Brooklyn, Brooklyn, New York

The melting point of ϵ-carbobenzoxy-α-carboxyl-*l*-lysine anhydride stored at room temperature for one year (I) rises considerably above that of the freshly prepared compound (II) (m.p. 100°). X-ray diffraction studies indicate: (II) is probably monoclinic, $a \simeq 90$A, $b = 5$A, $c \simeq 10$A; (I) suffered disorientation giving diagrams similar to those of bulk polymer (III); threshold conditions for the disorientation process are heat-treatment of (II) at 70° for 24 hours; the change appears to be complete when (II) is heat-treated at 85° for 24 hours since the diagrams are similar to those of (III) and no further change is observed in the diagrams of samples treated under more severe conditions below the melting point. The largest Bragg spacing of 29A observed for (II) is of the same order of magnitude as the over-all length of a fully extended hydrogen-bonded dimer of (II). The smallest refractive index of (II) is parallel to the *b* axis. The structure of (II) is concluded to be a triple dimer layer arrangement which would involve a relatively small entropy change on polymerizing in the solid state to give (I) and (III).

EVIDENCE for polymerization in the solid state has been observed in the course of physical studies of the N-carboxy anhydrides. This phenomenon has been described by other workers. Valyi, Janssen, and Mark[1] have observed that $p-p'$-divinybiphenyl polymerizes when allowed to stand in the crystalline state for several days at room temperature. Letort, Duval, and Rollin[2] have reported that liquid acetaldehyde maintained at a temperature slightly above its freezing point or supercooled below its freezing point showed no tendency to polymerize. Only with the onset of crystallization did a polymer form.

We have studied ϵ-carbobenzoxy-α-carboxyl-*l*-lysine anhydride in some detail. The synthesis of this compound and the method for bulk polycondensation at its melting point of 100°C have been described by Katchalski, Grossfeld, and Frankel.[3] The observation of Bergmann, Zervas, and Ross[4] that the melting point of this compound rises considerably when allowed to stand at room temperature for several months has been confirmed.

X-ray diffraction studies[5] of freshly prepared lysine N-carboxy anhydride at room temperature indicate that the compound is typically crystalline (Fig. 1). The x-ray powder pattern for a sample of the compound which was allowed to stand for one year at room temperatures in a stoppered vial (Fig. 2) has an appearance similar to that for polyparbobenzoxy-lysine (Fig. 5) prepared by bulk coly-condensation at the melting point. In order to study the effects of the aging process under accelerated conditions, samples of the freshly prepared monomer were heat-treated at various temperatures below the melting point for periods up to 168 hours. The threshold conditions for line-broadening in the x-ray powder pattern were heat-treatment at 70°C for 24 hours (Fig. 3). The process appears to be complete after heating the monomer at 85°C for 24 hours (Fig. 4) for no further change is noted in the powder diagrams for samples heated at temperatures higher than 85°C or for periods more prolonged than 24 hours. Figure 4 for lysine monomer, heat-treated at 85°C, is similar in appearance to Fig. 5 for the bulk polymer.

The largest Bragg spacing observed for freshly prepared lysine monomer was 29A (Fig. 6). The

---

* Presented at the Sixth Annual Meeting of the Division of High-Polymer Physics, American Physical Society, New York City, January 27–29, 1949.

[1] I. Valyi, A. G. Janssen, and H. Mark, J. Phys. Chem. **49**, 461 (1945).

[2] M. Letort, X. Duval, and Y. Rollin, Comptes Rendus **224**, 50–1 (1947).

[3] E. Katchalski, I. Grossfeld, and M. Frankel, J. Am. Chem. Soc. **70**, 2094 (1948).

[4] M. Bergmann, L. Zervas, and W. F. Ross, J. Biol. Chem. **111**, 245 (1935).

[5] E. Miller, I. Fankuchen, and H. Mark, Research **1**, 720 (1948).

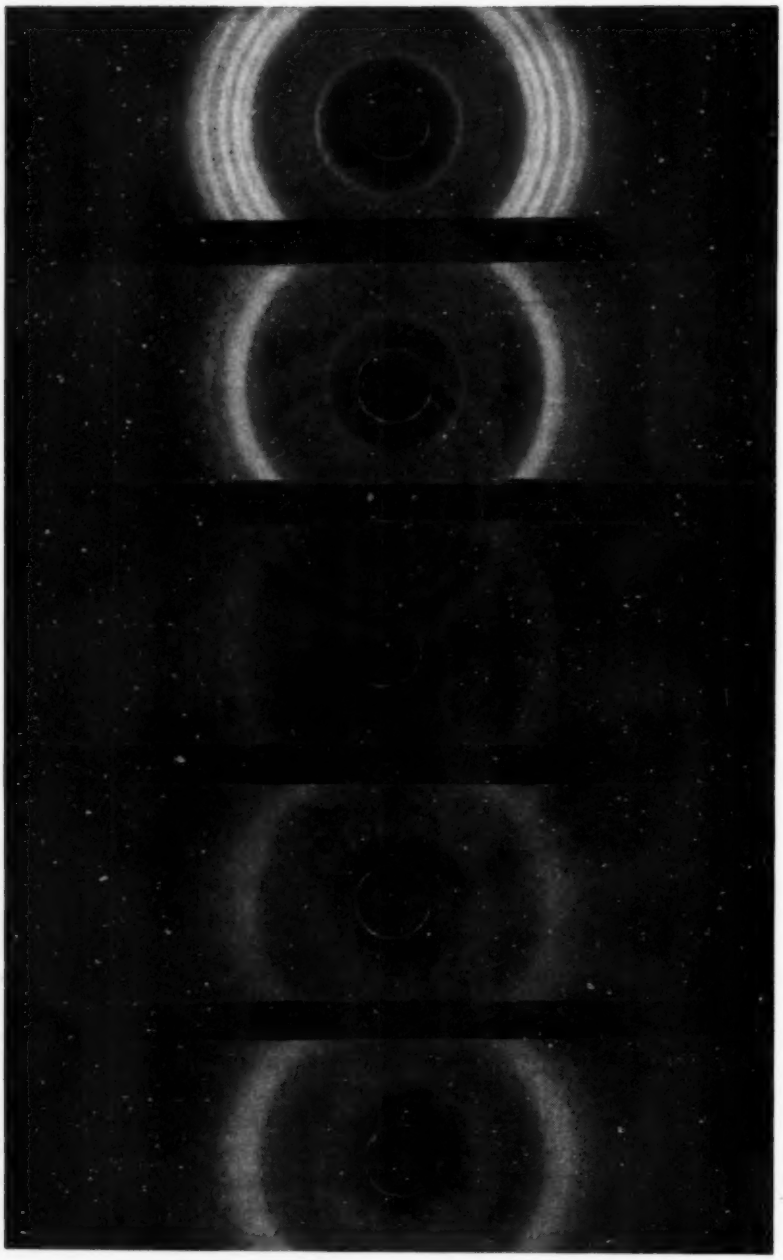

FIG. 1. Fresh lysine monomer at room temperature.

FIG. 2. Lysine monomer, one year at room temperature.

FIG. 3. Lysine monomer, 24 hours at 70°C.

FIG. 4. Lysine monomer, 24 hours at 85°C.

FIG. 5. Poly-carbobenzoxy-lysine at room temperature.

over-all length of the fully extended monomer molecule is calculated to be about 17A (Fig. 7). If association of two monomer molecules is assumed by hydrogen-bonding, a lateral bridge results which causes foreshortening producing an over-all length for the fully extended dimer of about 30A. It would appear that the largest Bragg reflection observed of 29A is of the same order of magnitude.

A diagrammatic representation is given in Fig. 8 for the molecular structure of the freshly prepared crystalline lysine monomer at room temperature. Determination of the exact periodicities by oscillation technique was made difficult by the minute size of the fragile, needle-like crystals available; the periodicities were found to be $a \simeq 90$A, $b = 5$A, $c \simeq 10$A. The a axis periodicity suggests a triple

FIG. 6. Fresh lysine monomer; small angle scatter at 29A.

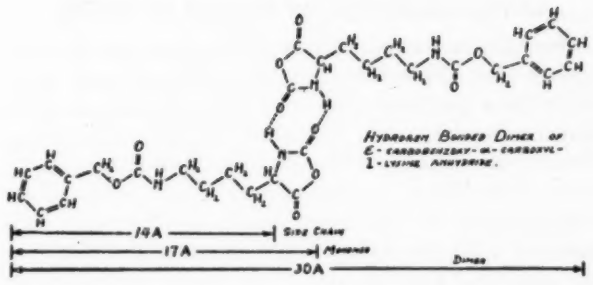

FIG. 7.

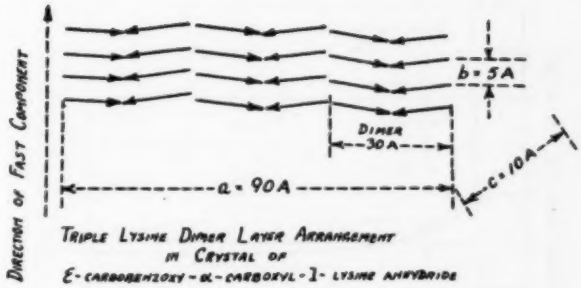

FIG. 8.

dimer arrangement. The smallest refractive index was observed to be parallel to the needle axis, the *b* axis. The general direction of greatest concentration of bonds is probably at 90° to the smallest refractive index. Hence the structure is presumed to be a triple dimer layer arrangement. The high ordering and convenient arrangement of monomer molecules suggests the possibility of polymerization in the solid state since a relatively small entropy change would be involved in the opening of the anhydride ring to form peptide linkages of the resulting polymer.

Time and Stress Effects in the Behavior of Rubber at Low Temperature

J. R. BEATTY AND J. M. DAVIES
B. F. Goodrich Research Center, Brecksville, Ohio

The stiffening of rubber-like materials at low temperature involves several different phenomena, sometimes with their effects superimposed. One of these is crystallization. This is a rate process which is generally very fast at high stresses and very slow at zero stress. In these experiments at temperatures near −25°C and under a shear stress of about 148 p.s.i. the dynamic modulus of the rubber increased at a rate convenient to study. Correlation with x-ray data showed that crystallization was very likely responsible for the increase in stiffness. The rate of change of stiffness increased rapidly with increase in applied stress, and there was no optimum rate at −25°C as has been found for unstressed rubber. The degree of vulcanization influenced the rate of change, tighter cures giving smaller changes. Neoprene FR, GR-S and polybutadiene, which ordinarily show little evidence of crystallization showed very definite, but small increases in stiffness. Mixing GR-S with natural rubber seems to limit the crystallization of the natural rubber rather effectively, but apparently Neoprene FR does not mix intimately enough with natural rubber to affect the crystallization of the latter appreciably.

INTRODUCTION

THE behavior of rubber at low temperature is complicated, the over-all performance representing the combined effects of several entirely different phenomena. These have been studied rather thoroughly by many investigators and the general principles will be illustrated here only by way of review.

Generally, near room temperature the modulus of elasticity increases with increasing temperature in agreement with the usual kinetic theory of molecular motion.[1] This is illustrated in Fig. 1 which shows the dependence of dynamic modulus on temperature for a lightly loaded carbon black stock under two conditions, with no shear stress and with considerable shear stress. Above 15°C, although the change is very small, the slope is positive. Below room temperature the curve deviates from the predictions of kinetic theory, and the rubber becomes progressively stiffer until, in the region of −55 to −65°C, the modulus is very high, in the neighborhood of 10^6 p.s.i. This is the region of the second order transition,[2] and apparently the flexibility of the individual chains has decreased and the attraction between neighboring chains has increased to such an extent that the material no longer has rubber-like properties. Just above the second order transition temperature the rubber has leather-like properties and shows high hysteresis.[3]

[1] (a) Guth, James, and Mark, *Advances in Colloid Science*, Volume II (Interscience Publishers, Inc., New York, 1946), p. 253. (b) E. Guth and H. Mark, Monats. f. Chem. 65, 93 (1934). (c) W. Kuhn, Colloid Zeits. 76, 258 (1936).

[2] R. F. Boyer and R. S. Spencer, *Advances in Colloid Science*, Volume II (Interscience Publishers, Inc., New York, 1946), p. 1.

[3] (a) H. A. Schultz, unpublished work. (b) F. S. Conant and J. W. Liska, J. App. Phys. 15, 767 (1944).

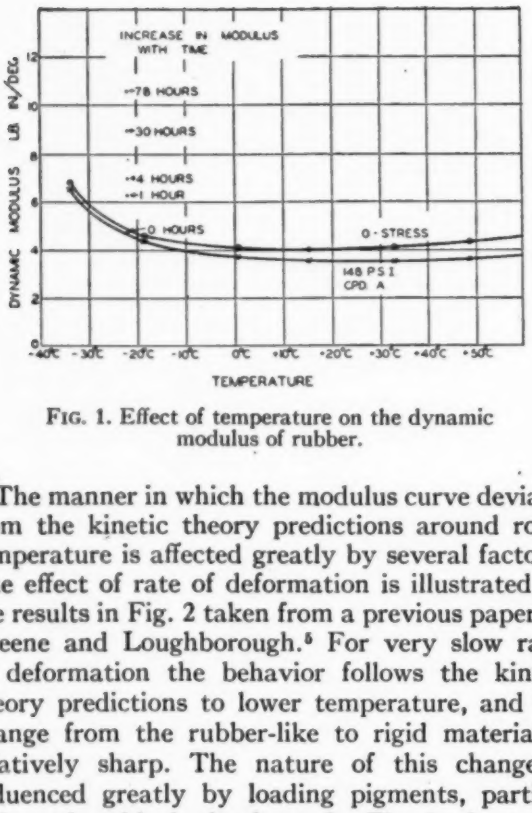

FIG. 1. Effect of temperature on the dynamic modulus of rubber.

The manner in which the modulus curve deviates from the kinetic theory predictions around room temperature is affected greatly by several factors.[4] The effect of rate of deformation is illustrated by the results in Fig. 2 taken from a previous paper by Greene and Loughborough.[5] For very slow rates of deformation the behavior follows the kinetic theory predictions to lower temperature, and the change from the rubber-like to rigid material is relatively sharp. The nature of this change is influenced greatly by loading pigments, particularly carbon black. As shown by Fig. 3, also taken from the paper referred to above, these loading pigments have the same general effect as increasing the speed of deformation.

All rubber-like polymers act essentially alike but there is quite a difference in the second order transition temperature, and the stiffness on approaching this temperature[2] as shown in Fig. 4.[5] For the materials shown, Neoprene FR stiffens at the highest temperature and butyl, GR-S, natural rubber, and polybutadiene stiffen at progressively lower temperatures.

The effects are instantaneous, that is, the rubber exhibits these properties immediately upon cooling. In addition, there is an effect of time of exposure as shown in Fig. 1. At −22°C the dynamic rate was about 4.8 lb.-in./degree, originally. After an hour under stress at this temperature the rate had increased to 6.3, a change of nearly 30 percent. Increasing the exposure changed the rate to 7.1 at 4 hours, 9 at 30 hours, and 10.5 at 78 hours, a total increase of nearly 120 percent in a little over three days. Obviously, this is the effect of another kind of mechanism superimposed on the effects of the two discussed above.

[4] A. P. Alexandrov and J. S. Lazurkin, Acta Physicochimica, U.S.S.R. **12**, 648 (1940). *Rubber in Engineering* (Chemical Publishing Company, Inc., 1946), p. 12.

[5] H. E. Greene and D. L. Loughborough, J. App. Phys. **16**, 3 (1945).

CRYSTALLIZATION OF RUBBER IN SHEAR

One obvious explanation of this increase in stiffness is that the rubber has crystallized, and x-ray diffraction patterns for rubber under shear show that to be the case. The sample was a thin slice, about $\frac{1}{4}$-in. thick, of the sample shown in Fig. 5. Using a holding jig, the central shaft was turned with respect to the outer shell and held in that position with the x-ray beam perpendicular to the flat surface. The shear stress varies considerably throughout this sample, and so diffraction patterns were obtained for the region near the shell and near the shaft. In Fig. 6A and B show the patterns for these two regions at room temperature. There is very little evidence of crystallization—none at all in the low shear region, and perhaps just a slight indication in the high shear region. After 48 hours at −22°C the patterns shown in C and D were obtained. The pattern for the high shear region shows rather sharp arcs indicating considerable crystallization. The low shear region is not quite as sharp, but again there is no doubt that considerable crystallization has taken place. This was accepted as sufficient proof that the gradual increase in stiffness shown in Fig. 1 was actually due to crystallization of the rubber.

The crystallization of rubber has been studied rather extensively.[6] Generally, this has emphasized the crystallization on stretching[6b] or on exposure to low temperature.[6c] On a few occasions the slow changes that take place after stretching have been studied,[7] but generally the experiments have been

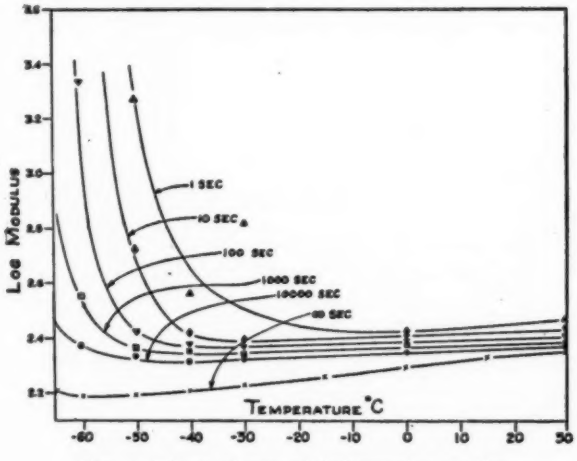

FIG. 2. Effect of rate of deformation on the modulus of rubber.

[6] (a) L. A. Wood, *Advances in Colloid Science*, Volume II (Interscience Publishers, Inc., New York, 1946), p. 57. (b) J. R. Katz, Naturwiss. **13**, 410 (1925). (c) E. Bunschoten, Mededeel Van den Rijksvoorlichtingsdienst ten Behoeve von den Rubberhandel Rubber nij Verheid te Delft No. 337 (1921). (d) N. Bekkedahl and L. A. Wood, Ind. Eng. Chem. **33**, 381 (1941).

[7] (a) L. R. G. Treloar, Trans. Faraday Soc. **37**, 84 (1941). Rubber Chem. Tech. **15**, 251 (1943). (b) L. R. G. Treloar, Rubber Age **63**, 195 (1948).

arranged to emphasize either the instantaneous crystallization or the relatively slow crystallization which takes place at low temperature under no stress. In the present experiments the conditions were just right to emphasize the crystallization taking place in a stressed sample on further exposure to low temperature.

Further comparisons of the elasticity measurements and diffraction patterns indicated that the dynamic modulus test provided a much more sensitive measure of the changes that were taking place. Fairly large changes in modulus occur without corresponding detectable changes in diffraction patterns. Accordingly, the modulus test was used for studying these changes and the effects were generally interpreted as resulting from crystallization, or at least incipient crystallization.

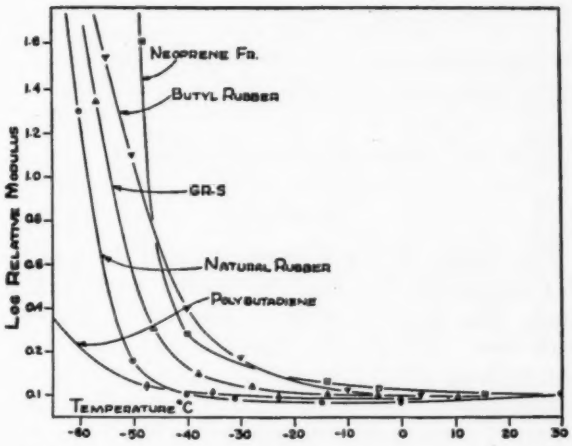

FIG. 4. Comparison of modulus of various polymers at low temperature.

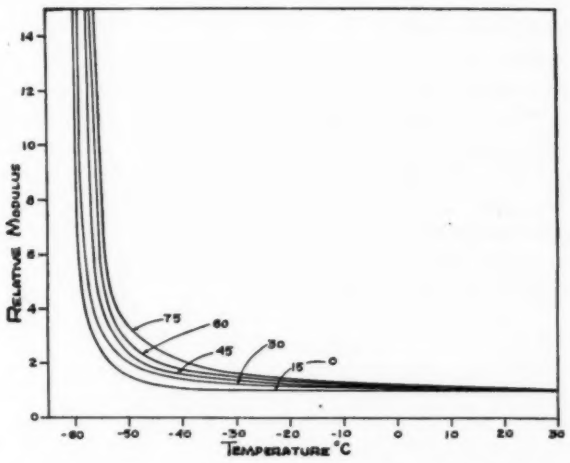

FIG. 3. Effect of carbon black on the modulus of rubber.

EXPERIMENTAL METHOD

The sample used in all cases was that shown in Fig. 5 and the test equipment, that shown in Fig. 7. These have been described previously.[8] The sample is mounted horizontally with the shaft held rigidly. Attached to the shell is an arm about 30 inches long with provision for adding weights up to about 26 pounds at each end. When the loading arm is displaced and released, the resulting free vibration provides a convenient measure of the dynamic elastic properties. The dynamic spring rate is given by

$$k = \frac{4\pi^2 I f^2}{g}$$

where k is the spring rate, I the moment of inertia of the vibrating system, g the acceleration due to gravity, and f the frequency of free vibration. For the loads generally used $k = 33.6 \times 10^{-4} f^2$, where k is in lb.-in. per degree, and f is in vibrations per minute. The frequency, in the neighborhood of 1 vibration per second, is determined from an autographic chart made by a stylus which is fastened to the center of the loading arm and which scribes a record of the motion of the arm on moving wax paper driven by a synchronous motor. One end of the shaft is held by the driven shaft of a gear reducer and with balanced or unbalanced weights on either end of the loading arm, this gear reducer provides a convenient way of winding up the sample to keep the loading arm horizontal. For example, in many of the experiments to be described, the load on one end was 19 pounds and on the other end 7 pounds, giving a steady torque of 180 lb.-in. or a stress at the shaft of 148 p.s.i. The vertical load on the sample undoubtedly has some slight effect on the results, but the major effect results from the wind-up. This wind-up is measured on a circular scale.

In all cases the sample was cooled to the desired temperature under no stress. Time effects were measured from the instant torque was applied.

The shear stress throughout the sample varies inversely with the square of the radius, and with this sample the range is about 4/1 from the inside layer near the shaft to the outside layer near the shell. For this reason it is difficult to express the results as a dynamic modulus of the rubber. Moreover, the dynamic modulus is not uniform throughout the sample. Crystallization very likely proceeds much more rapidly near the shaft. Accordingly, the results are left in the less definite form of a dynamic rate for the particular test sample. This is essentially an average modulus for all the rubber in the sample but this average is determined mainly by the rubber near the shaft.

[8] D. H. Cornell and J. R. Beatty, Trans. A.S.M.E. 69, 799 (1947); Rubber Age 60, 679 (1947).

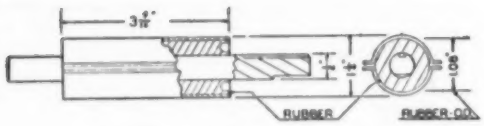

FIG. 5. Diagram of sample.

RESULTS

The results in Fig. 1 were obtained for a sample of Compound A, a lightly loaded carbon black stock. The same results are plotted in Fig. 8 to show more directly the effect of time and stress. The striking effect here is the rapid rate of change of modulus at 148 p.s.i. At zero stress there is no apparent change. Bekkedahl and Wood[6d] found for unstressed samples that it required about 200 days for an appreciable amount of crystallization to take place at this temperature. At 148 p.s.i. the effect seems to be at least 50 times faster.

State of Vulcanization

Figure 9 shows the effect of time of cure for Compound B, a pure gum natural rubber stock. Increasing the number of bonds between chains should decrease the tendency to crystallize, and this is the effect found. There is a great deal of difference between the 20-min. and the 40-min. cures but little change near the optimum as shown by the 80-min. cure.

Since the degree of vulcanization has a large effect on the manner in which the rubber crystallizes, it is difficult to study some of the factors which influence the rate and amount of crystallization. There is always some uncertainty as to whether other effects are not overbalanced by effects of cure. In the examples which follow, it seems certain that the other effects are much greater than those that might be expected from variations in cure.

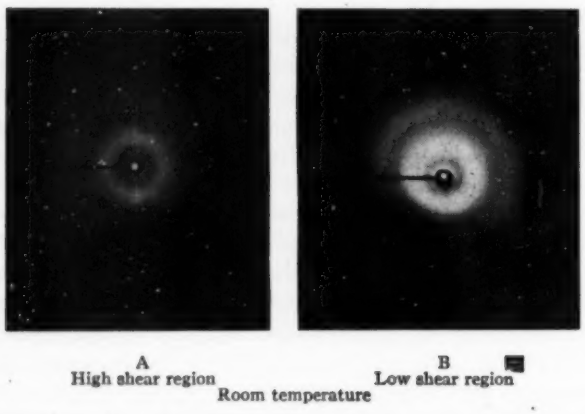

FIG. 6. X-ray diffraction patterns of ¼-in. thick slices of sample shown in Fig. 5.

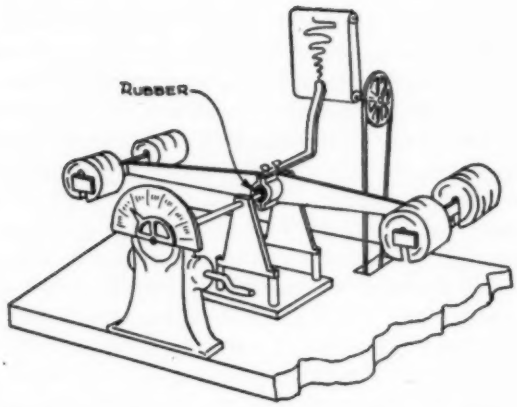

FIG. 7. Equipment for measuring dynamic modulus.

CARBON BLACK

Carbon black has been found to affect the crystallization of rubber. Gehman and Field[9] found a difference in the shape of the arcs as the amount of channel black was increased. The effect of fine thermal and easy processing channel black on the crystallization as determined by modulus changes is shown in Fig. 10. Table I gives a summary of the effects of the blacks.

Temperature

For unstressed rubber the rate of crystallization depends very greatly on the temperature. There is an optimum rate at about −25°C with very slow crystallization at +10°C and −50°C.[6a] Figure 11 shows the effect of temperature for rubber under shear. The sample in this case was Compound E, a lightly loaded natural rubber stock. There is very large increase in the rate as the temperature is lowered, but there is no evidence of any optimum temperature in this region. The same results are shown in Fig. 12, where the dynamic rate at the end of 30 hours is plotted as a function of temperature. Here an attempt is made to separate out the effect of instantaneous stiffening. This effect is

[9] S. D. Gehman and J. E. Field, Ind. Eng. Chem. **32**, 1400 (1940). Rubber Chem. Tech. **14**, 85 (1941).

relatively small, and it is obvious that there is a very rapid increase in crystallization in the region of −30°C.

Stress

Figure 13 shows the effect of stress on the rate of stiffening for the sample. These results are also plotted in Fig. 14, again separating out the instantaneous effects. The remaining curve shows a very great effect of increasing stress, especially above 200 p.s.i.

Release of Stress

Figure 15 shows the effect of releasing the stress. This sample was of the same lightly loaded carbon black stock as shown in Figs. 1 and 8. After the stiffness increased from 4.8 to 10.5, or about 120 percent, over a period of about 78 hours, the load was removed and after 32 hours, still at a temperature of −24°C, the dynamic rate had returned to 5.3, or only about 10 percent above the original value. On reloading, the rate increased about as before and on removing the load again there was a slight decrease. On reloading again, the rate increased roughly as before, but presumably somewhat more slowly.

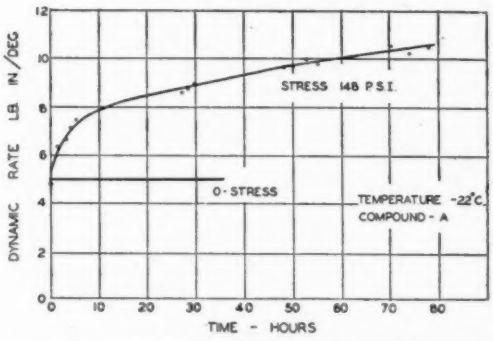

FIG. 8. Change in dynamic modulus of rubber with time and stress.

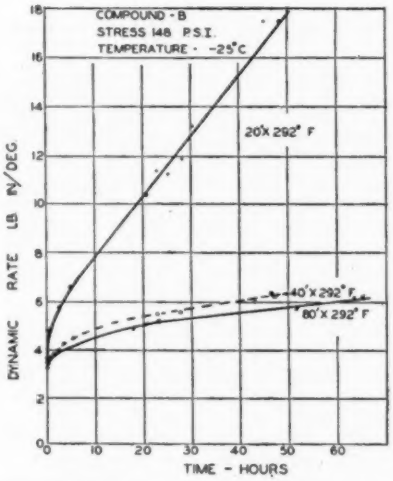

FIG. 9. Effect of cure on the rate of stiffening.

TABLE I. Summary of effect of low temperature on carbon black stocks.

Compound	Dynamic rate—lb. in./deg. Room temp.	−25°C 0 hrs.	−25°C 24 hrs.	Percent increase of dynamic rate Instantaneous R. T. to −25°C	After 24 hrs. (a) −25°C
B	2.2	3.2	5.1	45	59
C	3.7	5.5	10.7	49	95
D	6.8	10.9	21.5	60	97

Apparently during release of the stress there is a tendency to break up any alignment of the rubber molecules and at zero stress, of course, the rate of crystallization is very slow. On reapplying stress the process either starts from the beginning or if some residual alignment remains, as for example at 134 hours, proceeds from that point about parallel to the previous curve.

COMPARISON OF POLYMERS

It is commonly known that some polymers, such as polybutadiene and in particular copolymers such as Neoprene FR and GR-S, do not crystallize nearly as readily as natural rubber. In fact it is only recently that x-ray evidence for such crystallization has been obtained, and for this it has been necessary to cool the sample to low temperature before stretching.[10]

Figure 16 shows the change in dynamic rate for several polymers compared with the natural rubber

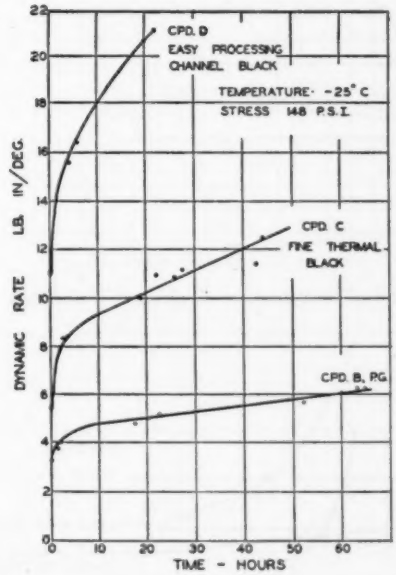

FIG. 10. Effect of carbon black loading on modulus changes at low temperature.

[10] E. E. Hanson and G. Halverson, J. Am. Chem. Soc. **70**, 779 (1948). Rubber Chem. Tech. **21**, 627 (1948).

TABLE II. Summary of changes in dynamic rate of various polymers on exposure to low temperature.

Compound	Polymer	Dynamic rate in lb. in./deg. Room temp.	−25°C 0 hrs.	−25°C 24 hrs.	Percent increase of dynamic rate Instantaneous R. T. to −25°C	After 24 hrs. (a) −25°C
B	Natural rubber	2.2	3.2	5.1	45	59
F	Polybutadiene	7.4	11.3	14.4	53	27
G	Polybutadiene	4.5	5.7	8.8	27	54
H	Neoprene FR	3.5	4.9	6.6	40	35
I	60% conv. GR-S	5.5	5.8	6.6	5.5	14
J	Reg. GR-S	4.0	8.1	9.9	102	22
K	L.t. polymerized GR-S	3.5	6.0	7.9	71	32

stock, Compound B. Polybutadiene, both in a soft black and in a channel black recipe, shows a typical crystallization curve. Neoprene FR seems to show a definite increase in dynamic rate. Three types of GR-S polymers were investigated. They all show crystallization; an unmodified 60 percent conversion GR-S least, the standard GR-S slightly more, and a low temperature polymerized GR-S most. The results are summarized in Table II. In all cases the effects of crystallization are appreciable, but less than shown by natural rubber stocks. Moreover, all of these synthetic polymers show a much greater tendency to level off at some definite value.

MIXTURES OF POLYMERS

Figures 17 and 18 show the effect of mixing polymers. It might be expected that on mixing a polymer that does not crystallize readily with natural rubber the amount of stiffening would be decreased merely by dilution. However, with the matrix predominately natural rubber this effect should be small. Figure 17 shows the crystallization curves for a natural rubber stock, a GR-S stock, and one in which 25 parts of GR-S replaced an equivalent amount of natural rubber. There was a definite tendency for the GR-S to reduce the crystallization. This is not so readily apparent from the curves. During the first 24 hours the increase in modulus for the natural rubber stock was from 4.8 to 8.5, or 77 percent, and the corresponding change for the GR-S stock was from 8.1 to 9.9, or 22 percent. With the mixture, however, the increase was only from 5.7 to 9.0, or 58 percent. This drop from 77 to 58 percent is more than is expected on the basis of dilution alone. Apparently, the GR-S actually interferes with the crystallization of the natural rubber. Such interference would be expected on mixing two materials which have different repeating periodicities, or which tend to crystallize in unlike patterns. X-ray diffraction patterns of similar mixtures bear out the idea that

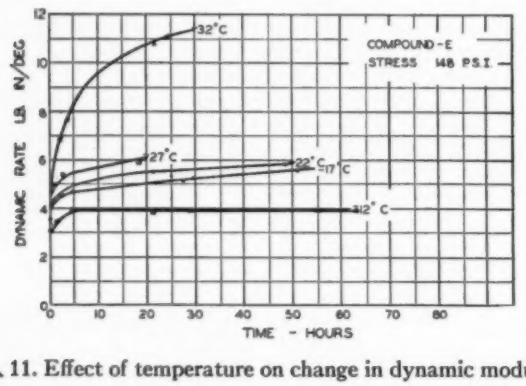

FIG. 11. Effect of temperature on change in dynamic modulus.

DYNAMIC RATE LB IN/DEG
TEMPERATURE °C
COMPOUND-E
STRESS 148 P.S.I.
I-DYN. RATE AFTER 30 HOURS
I-DYN. RATE OF SPRING DUE TO TEMPERATURE CHANGE ALONE
X=I-I-Δ DYN. RATE DUE TO CRYSTALLIZATION

FIG. 12. Effect of temperature on crystallization.

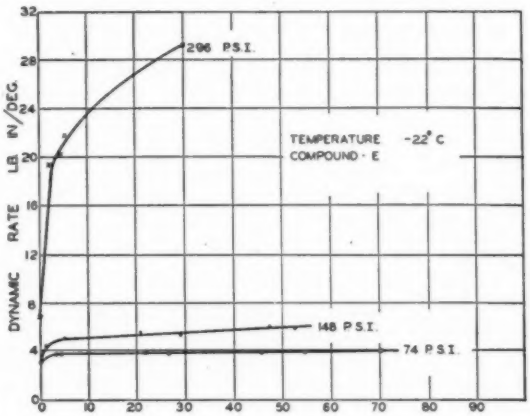

FIG. 13. Effect of stress on the change in dynamic modulus.

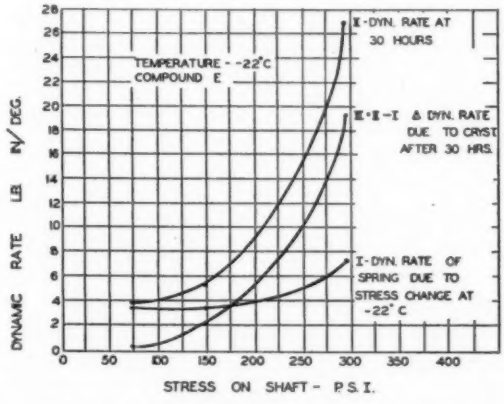
DYNAMIC RATE LB IN/DEG
STRESS ON SHAFT - P.S.I.
TEMPERATURE - -22°C
COMPOUND E
I-DYN. RATE AT 30 HOURS
X=I-I Δ DYN. RATE DUE TO CRYST AFTER 30 HRS.
I-DYN. RATE OF SPRING DUE TO STRESS CHANGE AT -22° C

FIG. 14. Effect of stress on crystallization.

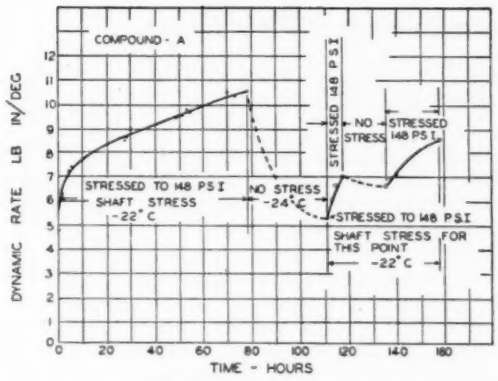
COMPOUND - A
STRESSED 148 P.S.I.
NO STRESSED STRESS 148 P.S.I.
STRESSED TO 148 P.S.I
SHAFT STRESS -22° C
NO STRESS -24° C
STRESSED TO 148 P.S.I.
SHAFT STRESS FOR THIS POINT -22° C
DYNAMIC RATE LB IN/DEG
TIME - HOURS

FIG. 15. Effect of repeated stressing on modulus changes.

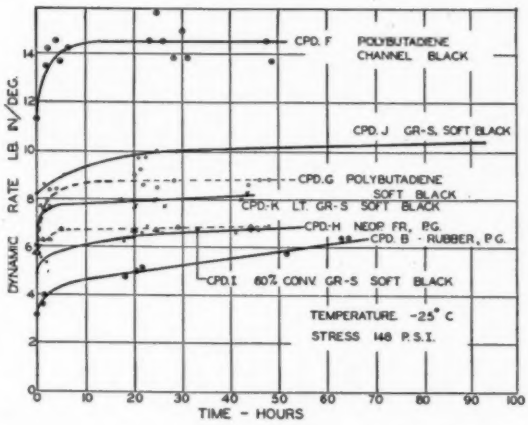
CPD. F POLYBUTADIENE CHANNEL BLACK
CPD. J GR-S, SOFT BLACK
CPD.G POLYBUTADIENE SOFT BLACK
CPD.K LT. GR-S SOFT BLACK
CPD.H NEOP FR, P.G.
CPD. B - RUBBER, P.G.
CPD.I 60% CONV. GR-S SOFT BLACK
TEMPERATURE -25° C
STRESS 148 P.S.I.
DYNAMIC RATE LB IN/DEG.
TIME - HOURS

FIG. 16. Comparison of polymers.

GR-S actually interferes with the crystallization of natural rubber.

In Fig. 18 a similar experiment with Neoprene FR gave different results. In this case a natural rubber and a Neoprene FR stock are compared with one made from a combination of 75 parts of natural rubber and 25 parts of Neoprene FR. Since Neoprene FR contains an inhibitor which acts as an accelerator of vulcanization for natural rubber in this case, the Neoprene FR was extracted with acetone before mixing. Here apparently the mixture crystallizes just as rapidly as does the natural rubber stock. The reason is not exactly clear but likely it is a question of thoroughness of mixing.

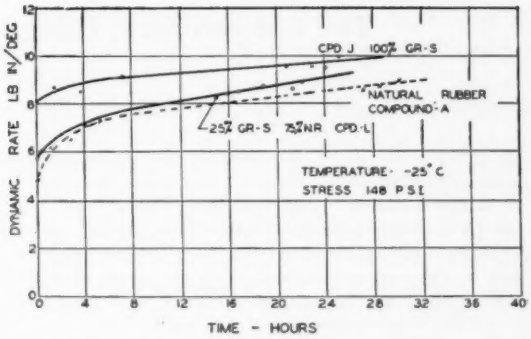

FIG. 17. Stiffening of mixtures of natural rubber and GR-S.

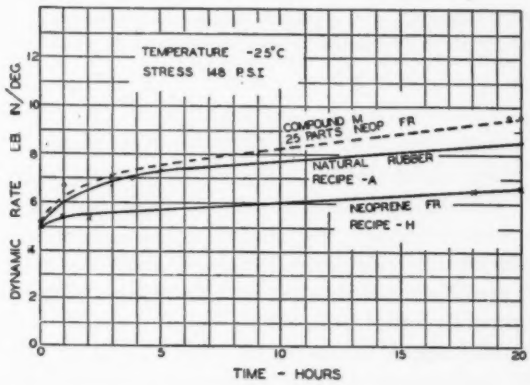

FIG. 18. Stiffening of mixtures of natural rubber and Neoprene FR.

Natural rubber and GR-S appear to be compatible and form an intimate mixture on a molecular scale. If the Neoprene exists in small discrete particles, then the only interference to crystallization would be at the interfaces, which would effect only a small part of the volume of the natural rubber. This would account for the effects shown in Fig. 18.

ACKNOWLEDGMENT

The authors wish to express their appreciation for assistance in this work. Dr. W. L. Davidson did the x-ray analysis, Mr. A. E. Juve advised on compounding problems, Mr. K. Pearce assisted in preparing samples and taking data, and Dr. D. L. Loughborough and Dr. H. A. Schultz assisted the authors by their discussions of the results.

The Compatibility, Efficiency and Permanence of Plasticizers

RAYMOND F. BOYER
The Dow Chemical Company, Midland, Michigan

This paper attempts to interrelate three important aspects of plasticizer behavior: *compatibility* or how much plasticizer can be added without causing phase separation; *efficiency*, or how much a given amount of plasticizer lowers the brittle temperature; and *permanence*, or how well a plasticizer is retained by the polymer on heat aging or solvent treatment.

Compatibility is discussed in terms of the Flory-Huggins theory of the thermodynamics of polymer solutions, which relates the activity of the plasticizer to its concentration in the polymer. Efficiency is measured by how the plasticizer lowers the melt viscosity of the polymer. An empirical relationship between efficiency and μ (the Huggins polymer-solvent interaction constant) is shown. Loss of plasticizer at elevated temperatures depends in part on the effective vapor pressure of the plasticizer, and in part on how rapidly diffusion of plasticizer from the interior of the sample replenishes that lost from the surface. From the fact that diffusion constant times viscosity is a constant, it is possible to correlate measured diffusion rates with plasticizer content and with plasticizer efficiency. A linear relationship is predicted and found experimentally between logarithm of the diffusion constant and the brittle temperature. In this sense, the more efficient a plasticizer is, the more rapidly it can diffuse out of the polymer and be lost. Consideration is given to the effect of plasticizer on electrical resistance and tensile strength. A preliminary discussion of polymeric plasticizers is presented.

INTRODUCTION

THE technological importance of plasticizers for natural and synthetic high polymers is now widely recognized, and a quick survey of the nature of the problems involved may be gleaned from two recent symposia on this topic.[1,2] Theoretical aspects of the problem have trailed behind industrial applications until very recently. Of the many fundamental facets of the problem, we should like to emphasize here only three—compatibility, efficiency, and permanence—because it is now possible to outline some interesting and significant inter-relationships among these three properties.

Compatibility refers to the maximum amount of plasticizer which can be added to a polymer without causing phase separation. More broadly, it is necessary to recognize that the compatibility is not a fixed quantity but may vary in a cyclical fashion with temperature, or in a secular fashion because of chemical or physical changes in the polymer such as oxidation, aging, or slow crystallization.

Efficiency concerns how much a given property of the plastic—brittle point, second-order transition temperature, hardness, stiffness, etc.—is altered by the addition of a fixed amount of plasticizer.

Permanence refers to how well the plasticizer is retained by the polymer during aging in an air, vacuum, or liquid medium, either at normal use temperatures or elevated test temperatures.

Frith and Tuckett[3,4] were the first to show that questions of compatibility can be answered on the basis of the thermodynamics of polymer-solvent systems. At the same time, they recognized efficiency as a separate problem. Many workers have been concerned with efficiency of plasticizers. Boyer and Spencer[5] have attempted to summarize prior work and theories in this field in addition to presenting a new approach to the problem. The basic aspects of permanence have been clarified by Small[6] who resolved the problem into two components:

(1) Loss of plasticizer from the surface layers of the polymer which is an equilibrium or thermodynamic problem depending on the effective vapor pressure of the plasticizer—this effective vapor pressure is the product of the vapor pressure of the pure plasticizer times its activity in the polymer at the concentration and temperature involved; and
(2) diffusion of plasticizer from the interior of the specimen to replenish surface loss, which is a dynamic problem depending on the diffusion rate of the plasticizer which, in turn, depends primarily on the viscosity of the medium.

We shall now examine each of these three problems in greater detail for the express purpose of developing:

(1) an empirical relationship between efficiency and compatibility,
(2) a formal relationship between permanence and compatibility,
(3) an equation for the rate of diffusion of plasticizer as a function of plasticizer content,
(4) a relationship between diffusion of plasticizer and plasticizer efficiency,
(5) effect of plasticizers on tensile strength, and
(6) an extension of these principles to polymeric plasticizers.

[1] J. Polymer Sci. **2**, 113–198 (1947).
[2] Washington, D. C. meeting, American Chemical Society, September 1, 1948, Abstracts of Paint and Varnish Section.
[3] E. M. Frith and R. F. Tuckett, Nature **155**, (1945).
[4] E. M. Frith, Trans. Faraday Soc. **41**, 90 (1945).
[5] R. F. Boyer and R. S. Spencer, J. Polymer Sci. **2**, 157 (1947).
[6] P. A. Small, J. Soc. Chem. Industry **66**, 17 (1947).

COMPATIBILITY

While Frith and Tuckett must be credited with the first formal recognition of a scientific basis for compatibility, yet the ideas were implicit in the Flory[7]-Huggins[8] treatment of the thermodynamics of polymer-solvent systems. They showed that the activity of the solvent is given by

$$\ln a_1 = \ln(1-v_2) + \left(1 - \frac{1}{x}\right)v_2 + \mu v_2^2, \qquad (1)$$

where v_2 is the volume fraction of polymer, x is the ratio between volume of polymer molecule and solvent molecule, and μ is a semi-empirical constant. They showed that phase separation or incompatibility occurs as soon as μ exceeds a certain critical value. This critical value is 0.5 for a polymer of infinite molecular weight, and will lie between 0.5 and 0.55 for most polymers of technical importance. It is merely necessary to translate their term "solvent" as "plasticizer" and their conclusions can be applied directly to the plasticizer problem. These conclusions are essentially no different from those of Frith and Tuckett, but it is more convenient for our purpose to use the nomenclature of Eq. (1) and particularly the μ concept.

Figure 1, adapted from Huggins,[9] shows plasticizer activity as a function of composition for four different values of μ. $\mu=-0.5$ is characteristic of very strong bonding between polymer and plasticizer, $\mu=0$ would be a good solvent, $\mu=0.5$ is a borderline solvent, and $\mu=1$ is a non-solvent of limited compatibility. As long as the activity curves lie completely below the line for unit activity, polymer and plasticizer are miscible in all proportions. However, when the activity curve crosses the $a=1$ line, the point of intersection measures the maximum limit of compatibility for the polymer-plasticizer system having that μ value. In general μ increases, and hence compatibility decreases, as the temperature is lowered. According to μ values given by Doty and Zable[10] for plasticized polyvinyl chloride, the four curves of Fig. 1 would correspond approximately, from left to right, to tributyl phosphate, dibutyl phthalate, tricresyl phosphate, and butyl acetyl ricinoleate in polyvinyl chloride.

For borderline solvents—say in the μ-range from 0.5–0.6—a slight drop in temperature may cause phase separation, leading to cloudiness or "perspiration," depending on the plasticizer content. Even in the absence of these external signs, one concludes from Guggenheim's treatment of the thermodynamics of polymer solutions[11] that such "poor solvents" show a tendency to cluster into groups, thus giving plasticizer-rich areas on a microscopic scale. We believe, as will be discussed later, that this plays an important role in the diffusion of plasticizer and moisture vapor through polymers.

If the polymer crystallizes on aging, or is initially crystalline but slowly increases in crystalline content, this may also alter the compatibility for two reasons. First, the crystalline areas are physically inaccessible for plasticizer molecules, so that the effective composition must be computed on the basis of the amorphous content of polymer. It is conceivable that some types of plasticizer molecules might form mixed crystals with the polymer. Secondly, the crystallites act as points of cross-linkage. This is quite evident in supercooled saran which is soluble in solvents which will not affect the crystalline polymer. The presence of cross-links will change the basic thermodynamics. For one thing, the effective value of μ increases with increasing amount of cross-linking, as shown by Boyer and Spencer[12] and by Doty.[13] This in itself would reduce compatibility, but there is a second and even more important factor acting in the same direction. The network chains in a cross-linked polymer are stretched by the addition of solvent and this leads to an unfavorable entropy effect which limits the maximum amount of swelling. Flory and Rehner[14] have developed the expression, analogous to Eq. (1), which holds for a cross-linked polymer, namely

$$\ln a_1 = \ln(1-v_2) + v_2 + \rho\frac{V_1}{M_c}v_2^{\frac{1}{3}} + \mu v_2^2, \qquad (2)$$

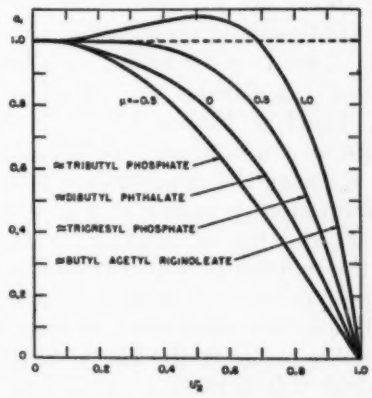

FIG. 1. Activity of plasticizer in polymer as a function of composition for several values of the thermodynamic polymer-solvent interaction constant, μ, according to Eq. (1). The curves would hold approximately for polyvinylchloride containing the indicated plasticizers. a_1 is the plasticizer activity, v_2 is the volume fraction of polymer.

[7] Paul J. Flory, J. Chem. Phys. 9, 660 (1941); 10, 51 (1942); 12, 114 (1944); 12, 425 (1944).
[8] M. L. Huggins, Annals N. Y. Acad. Sci. 43, 1 (1942).
[9] M. L. Huggins, J. Am. Chem. Soc. 64, 1712 (1942).
[10] P. Doty and H. Zable, J. Polymer Sci. 1, 90 (1946).
[11] E. A. Guggenheim, Proc. Roy. Soc. A183, 203, 213 (1944).
[12] R. F. Boyer and R. S. Spencer, J. Polymer Sci. 3, 97 (1948).
[13] Doty, Brownstein, and Schlener, in Press.
[14] P. Flory and J. Rehner, Jr., J. Chem. Phys. 11, 521 (1943).

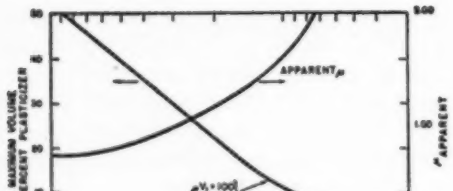

FIG. 2. Volume percent of plasticizer compatible with crystalline polymers which are characterized by M_c, the molecular weight between junction points of the crystalline regions. The curve marked "apparent μ" shows the μ-value which would give these same compatibility limits for a linear, non-crystalline polymer.

where ρ is the density of the dry polymer, V_1 is the molar volume of the solvent, and M_c is the molecular weight of the polymer chains between points of cross-linkage. In general, it will be difficult to find and exact value of M_c for a crystalline polymer, although we have calculated a value for polythene based on the swelling measurements reported by Richards.[15] Thus, a polythene of molecular weight 14,000 had a volume swelling ratio in n-heptane of 1.15 ($v_2=0.87$). Assuming a μ value of 0.3, M_c is calculated from Eq. (2) to be about 140. This calculation neglects the fact that swelling occurs only in the amorphous areas. However, the general order of magnitude is probably correct. Even if crystallation occurs to the extent of only 10–20 percent, it would seem that rather small M_c values will prevail, and that the structure would be tightly cross-linked. The exact situation can differ widely between a few large crystallites or many small ones at the same total crystalline content.

Figure 2 shows the maximum amount of plasticizer compatible with a cross-linked polymer as a function of M_c for $\mu=0.4$, assuming μ is independent of M_c. These calculations are based on Eq. (2) with $\rho=1$, $V_1=100$. Figure 2 also shows the apparent value of μ which one would calculate from Eq. (1) by ignoring the cross-linking and assuming that the compatibility values of Fig. 2 arose from chemical factors, that is, μ alone. Figure 2 then illustrates the manner in which crystallinity might influence compatibility. It is to be understood that such calculations are valid only to the extent that it is permissible to apply the Flory–Rehner theory of cross-linked polymers to a crystalline polymer. The curves are intended primarily for illustrative purposes.

It seems probable, and in the case of saran, it is experimentally verified, that increasing crystallinity has the net effect of decreasing plasticizer compatibility. It is not unlikely that some of the stiffening problems encountered with plasticized vinyls may have a similar origin. Increasing crystallization alone will increase the rigidity; whether plasticizer is exuded, leading to still greater rigidity, will depend on μ, the amount of plasticizer initially present, and the magnitude of the crystallinity change.

[15] R. B. Richards, Trans. Faraday Soc. **42**, 20 (1946).

EFFICIENCY

We shall follow here the approach developed by Boyer and Spencer[5] for the effect of plasticizers in lowering the second-order transition temperature, namely

$$(\omega_2)^{\frac{1}{2}}=A'+E/BRT, \tag{3}$$

where ω_2 is the weight fraction of polymer in the plasticized mixture, T is the transition temperature or brittle temperature, R is the gas constant, A' and B are constants, and E is an activation energy for viscous flow. Figure 3 shows some typical plots of this type. Also included are the theoretical lines for zero and infinite efficiency. The rationale behind this equation and some possible objections against it have been discussed previously.[5] Here we shall simply take the position that this equation describes with adequate accuracy a fair number of sets of experimental data. The physical significance of such a linear plot may be transcribed as follows: The efficiency of a plasticizer can be measured by how rapidly it lowers the melt viscosity of the system.

Jones[16, 17] has made extensive correlations between the viscosity of the plasticizer itself and its efficiency in the polymer. He argues that the melt viscosity of the plasticized mix will depend on the viscosity of the pure plasticizer and pure polymer through an Arrhenius type of plot. Equation (3) is, we believe, a more precise way of formulating quantities based on the melt viscosity of the plas-

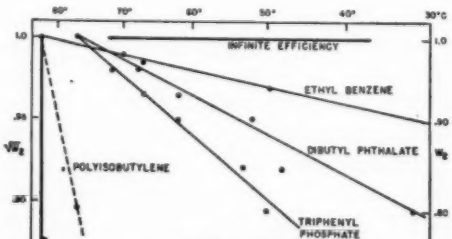

FIG. 3. Plots of Eq. (3) expressing dependence of the transition temperature, $T°$K, of polystyrene on various amounts of plasticizers of increasing molecular weight. The ethyl-benzene and polyisobutylene data are true second-order transitions; those for the other two curves are A.S.T.M. heat distortion values. ω_2 is the weight fraction of polymer.

[16] H. Jones, Trans. Inst. Rubber Ind. **21**, 298 (1946).
[17] H. Jones and E. Chadwick, J. Oil Colour Chemists Assoc. **30**, 199 (1947).

ticized polymer since it is related to Flory's[18,19] experimental work on melt viscosity.

One of the major questions previously raised against Eq. (3) concerns whether or not the activation energy is really independent of plasticizer content. One set of data examined by Boyer and Spencer[5] indicated that the energy of activation for dielectric dispersion decreased markedly with increasing plasticizer content. A study of the results of Parks and Gilkey[20] on the measured viscosity of glucose glass plasticized with glycerol showed that E was essentially constant up to 20 percent plasticizer and had decreased only 10 percent on going to 40 percent plasticizer. Some data by Dienes and Klemm[21] on the measured melt viscosity of Vinylite VYNS plus dioctyl phthalate at 160°C showed that Eq. (3) was followed exactly between 10 and 40 percent plasticizer, although the point for pure polymer was off the straight line. Thus, it appears that in two cases where the melt viscosity of plasticizer systems have been measured, Eq. (3) is reasonably reliable.

Fox and Flory[22] have criticized the use of Eq. (3) because their recent melt viscosity studies on polystyrene and polyisobutylene indicate that the original Flory equation for pure polymers is not valid for wide ranges of molecular weights on some polymers. Actually, in the sense that we have been using the equation, the effective weight average molecular weight is not greatly decreased in the range of 0 to 50 percent plasticizer. Even if Eq. (3) can no longer be considered an extension of Flory's melt viscosity work, one can fall back on the fact that as an empirical equation, it does describe the data rather well in many cases. This, of course, would detract from the value of the equation. Fox and Flory showed with pure polystyrene that the apparent energy of activation for viscosity increases markedly as the temperature is lowered. It may be that the addition of a plasticizer offsets this increase in activation energy of the pure polymer, and thus makes Eq. (3) operate as well as it does.

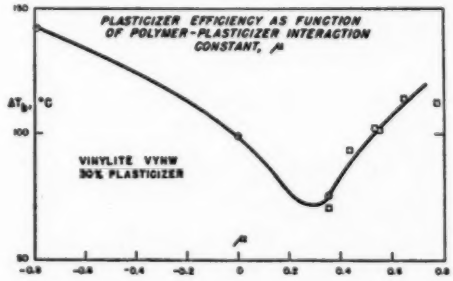

FIG. 4. Correlation of plasticizer efficiency with μ where Δt_b is the lowering of the brittle temperature of Vinylite VYNW by the addition of 30 percent of plasticizer of the indicated μ-value. Circles are data of Clash and Berg (see *Symposium on Plastics*, American Society for Testing Materials, Philadelphia, 1944, pp. 54 *et seq.*; squares are from Reed (see reference 23). μ-values are from Doty and Zable for polyvinyl chloride at 53°C (see reference 10). The left-hand branch ($\mu<0.5$) refers to solvent type plasticizers; the right-hand branch to oil type plasticizers.

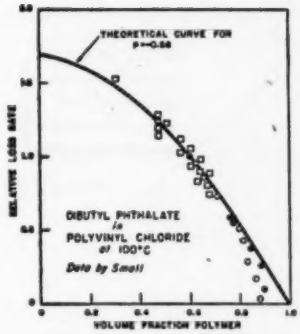

FIG. 5. Circles and squares represent Small's (see reference 6) data on relative rate of plasticizer loss for dibutyl phthalate in polyvinyl chloride at 100°C. The solid curve is calculated from Eq. (1) for $\mu=-0.56$.

Still another objection is that Eq. (3) was developed to give the effect of plasticizers on the second-order transition temperature, assuming that such transitions are connected with the melt viscosity of the polymer. We have subsequently applied it to brittle point data which should follow a high elasticity mechanism and not a melt viscosity process.

Finally, as Boyer and Spencer observed, Eq. (3) is mathematically equivalent, for low plasticizer content and moderate temperatures ($t \ll 273$), to Zhurkov's Theory, which predicts a linear decrease of softening point with number of molecules of plasticizer. It is interesting to note in Fig. 3 that the curves move toward the line for zero efficiency with increasing molecular weight of the plasticizer. This is what Zhurkov's Theory would predict, and also what we shall predict later by a logical extension of Eq. (3).

Thus, while one cannot be emphatic about the exact significance of Eq. (3), we wish to retain it because of a parallelism to be seen presently with the dependence of diffusion rate on plasticizer content, and the correlation of diffusion rate with brittle temperature.

Boyer and Spencer[5] demonstrated an empirical relationship between plasticizer efficiency (as measured by the brittle temperature) and the constant, μ. This relationship is presented in Fig. 4, using a different type of plot from that originally employed, and only part of the data. While this empirical plot needs very much to be verified with additional data, it does appear to divide plasticizers into the two well-known groups, solvent and oil-type plasticizers ($\mu<0.5$ and $\mu>0.5$, respectively).

[18] Paul J. Flory, J. Am. Chem. Soc. **62**, 1057 (1940).
[19] P. J. Flory, J. Phys. Chem. **46**, 870 (1942).
[20] G. S. Parks and W. A. Gilkey, J. Phys. Chem. **33**, 1428 (1929).
[21] G. J. Dienes and H. F. Klemm, J. App. Phys. **17**, 458 (1946).
[22] T. G. Fox, Jr. and P. J. Flory, J. Am. Chem. Soc. **70**, 2384 (1948).

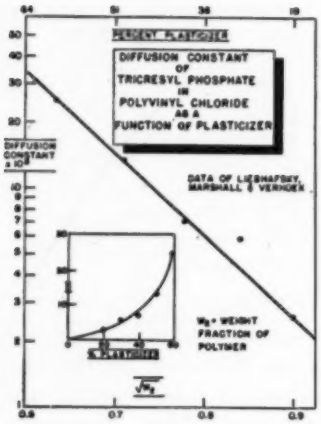
DIFFUSION CONSTANT OF TRICRESYL PHOSPHATE IN POLYVINYL CHLORIDE AS A FUNCTION OF PLASTICIZER
DIFFUSION CONSTANT × 10⁶
DATA OF LIEBHAFSKY, MARSHALL & VERHOEK
w_2 = WEIGHT FRACTION OF POLYMER
$\sqrt{w_2}$

FIG. 6. Diffusion rate of tricresyl phosphate in polyvinylchloride plotted according to Eq. (6). The inset shows the original data on a linear scale. w_2 is the weight fraction of polymer.

PERMANENCE

We are interested in the permanence question only as it refers to loss of plasticizer vapor into vacuum or an air stream, or liquid plasticizer into a liquid medium, i.e., an oil bath surrounding the sample, or into an adjacent polymer specimen. When the rate of loss of plasticizer is slow, it will be governed, as Small[6] has indicated, by its effective vapor pressure or activity. When the loss rate is high, internal diffusion of plasticizer then becomes the dominant factor.

Small has given data on the relative evaporation rate of dibutyl phthalate from polyvinyl chloride at 100°C as a function of composition. His experimental points are reproduced in Fig. 5. This represents in effect, an activity composition curve of the type shown in Fig. 1 if we assume that rate of vapor loss is a measure of effective vapor pressure. We have calculated from this data a μ value of -0.56 by using Eq. (1) and neglecting $1/x$. This μ value of -0.56 is lower than that given by Doty and Zable,[10] namely -0.04, although their values were for 53°C and 73°C, and on a cross-linked polyvinylchloride. It is seen that Small's data does not go to the lower right-hand corner of Fig. 5 as theory would predict, but drops off more rapidly. He interprets this as indicating control by diffusion at low plasticizer content. We have attempted to calculate μ values in similar fashion from other sets of vapor loss data, such as that of Reed,[23] which are not as extensive as Small's data. In general, one gets a μ-value which is smaller than those of Doty and Zable, indicating that the plasticizer is more firmly held. This could arise if diffusion were playing a minor role in all cases. We feel that such vapor loss measurements, if sufficiently refined, may constitute a new and valuable method of estimating μ-values for polymer-plasticizer systems, particularly at higher plasticizer contents. At any rate, it is evident from Fig. 5 that this one aspect of plasticizer permanence is related to the activity curves of Fig. 1.

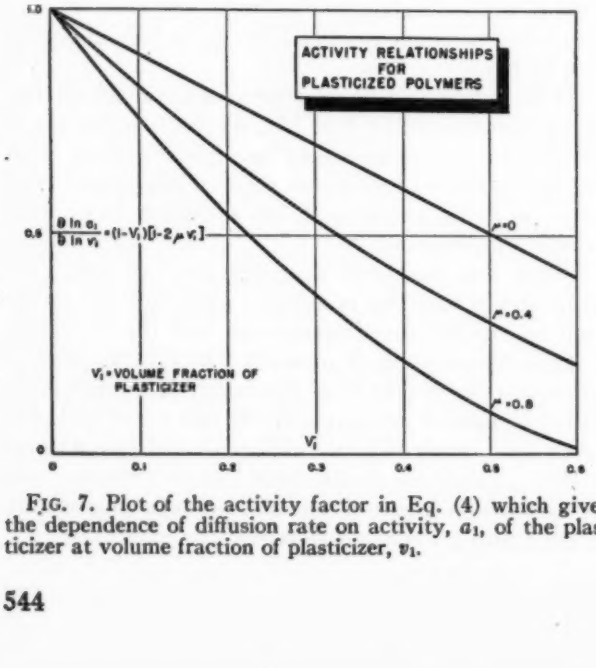
ACTIVITY RELATIONSHIPS FOR PLASTICIZED POLYMERS
$\frac{\partial \ln a_1}{\partial \ln v_1} = (1-V_1)[1-2\mu V_1]$
$\mu = 0$
$\mu = 0.4$
$\mu = 0.6$
V_1 = VOLUME FRACTION OF PLASTICIZER
V_1

FIG. 7. Plot of the activity factor in Eq. (4) which gives the dependence of diffusion rate on activity, a_1, of the plasticizer at volume fraction of plasticizer, v_1.

In the case of cross-linked polymers (and also, according to our previous assumptions, crystalline polymers), Eq. (2) predicts that the activity, or effective vapor pressure of the plasticizer, will be greater than for a linear polymer having the same plasticizer content. Thus, the presence of crystallinity not only decreases the effective compatibility of a plasticizer, but tends also to decrease its permanence by raising its effective vapor pressure.

The diffusion of plasticizers through polyvinyl chloride has been studied by Liebhafsky, Marshall, and Verhoek[24] and by Small[6] as a function of temperature, composition, and plasticizer type. Diffusion rate is presumably governed by an equation proposed by Stearn and Eyring[25]

$$D\eta = K\frac{\partial \ln a_1}{\partial \ln c}, \tag{4}$$

where D is the diffusion constant, η the viscosity of the medium, K a constant, a_1 the activity of the plasticizer at concentration c. Neglecting the variation in the activity term, and assuming that η is given by Flory's equation for the melt viscosity of concentrated polymer solutions, namely

$$\log\eta = A + B(w_2)^{\frac{1}{2}}, \tag{5}$$

where A and B are constants and w_2 is again the weight fraction of polymer, it follows that

$$\log D = a - b(w_2)^{\frac{1}{2}}. \tag{6}$$

Figure 6 is a plot of the Liebhafsky, Marshall, and Verhoek data for tricresyl phosphate in polyvinyl

[23] M. C. Reed, Ind. Eng. Chem. **35**, 896 (1943); **40**, 1414 (1948).

[24] Liebhafsky, Marshall, and Verhoek, Ind. Eng. Chem. **34**, 704 (1942).

[25] A. E. Stearn and H. Eyring, J. Chem. Phys. **5**, 113 (1937); Chem. Rev. **28**, 301 (1941).

chloride over the range of 20–60 percent plasticizer. The insert shows their original plot. Judging from this example, Eq. (6) describes quite well the dependence of the diffusion constant on plasticizer content. It is recognized that Flory's melt viscosity equation refers to the gross or macroscopic viscosity of the whole sample. One would expect a diffusing plasticizer molecule to be concerned not with this gross viscosity, but rather with some local or microscopic viscosity. One would conclude then, from the linearity of Fig. 6 that the local melt viscosity is proportional to the gross viscosity of the plasticized mass. Such a statement would not hold for a homologous series of unplasticized polymers. We have, of course, neglected the activity factor in Eq. (6). This can be calculated from Eq. (1), and several typical plots are shown in Fig. 7. If melt viscosity and diffusion rates are both known as a function of plasticizer content, one should be able, in principle, to calculate μ.

There is now an interesting consequence which can be realized by comparing Figs. 3 and 6, or Eqs. (3) and (6) in that two variables each are linear functions of $(w_2)^{\frac{1}{2}}$. From this, one derives the result that

$$\log D = \alpha + \beta/(t_b + 273), \tag{7}$$

which simplifies, when t_b in °C is much less than 273, to

$$\log D = \gamma - \delta t_B, \tag{8}$$

where α, β, γ, and δ are constants. Figure 8 is a plot based on this equation, where the diffusion rates come from Fig. 6 and the brittle temperatures are those reported by Boyer and Spencer.[26] Figure 9 is a similar plot except that here the plasticizer content is fixed, but different plasticizers are employed. The diffusion data is that of Small[6] while the brittle points are from Jones.[16] These latter are not true brittle points, but are taken from deformation—load curves at 5 g/mm².

We thus reach the significant conclusion that the more successful one is in lowering the brittle temperature, either by using more of a given plasticizer or by selecting more efficient plasticizer, the more readily can that plasticizer diffuse through the sample. To the extent that diffusion controls plasticizer loss, the more efficient plasticizers will be lost more readily from the sample. This tendency is compensated in some degree by the fact that of two plasticizers with the same boiling point, the more efficient one (smaller μ-value) will have a lower effective vapor pressure or activity. In many practical problems, this relationship between diffusion rate and brittle temperature may not be as serious as it appears. Instead, the factor-limiting plasticizer loss will be evaporation rate from the surface, and this is rather well controlled by choosing a high boiling plasticizer. If, however, the plasticized sample is immersed in an organic liquid, or is in intimate contact with another polymer which will readily absorb the plasticizer, then volume diffusion can become quite important. The data of Small[6] and Reed[23] show that vapor pressure of the plasticizer tends to be the most important factor. However, Table I, based on Small's results, illustrates some marked exceptions, particularly in the case of butyl acetyl ricinoleate.

There is one obvious exception in Fig. 9 since butyl acetyl ricinoleate falls well off the curve. Small has commented that it diffuses much faster than one would expect on the basis of its molecular weight and structure. This material is a poor solvent-type plasticizer. As such, it probably exists in the form of clusters rather than as a molecularly uniform dispersion in the polymer. A diffusing molecule of buty acetyl ricinoleate would therefore move alternately through regions of slightly plasticized polymer and of almost pure plasticizer. It may be that the non-solvent plasticizers will fall on a curve of their own which is different from the plot for solvent plasticizers.

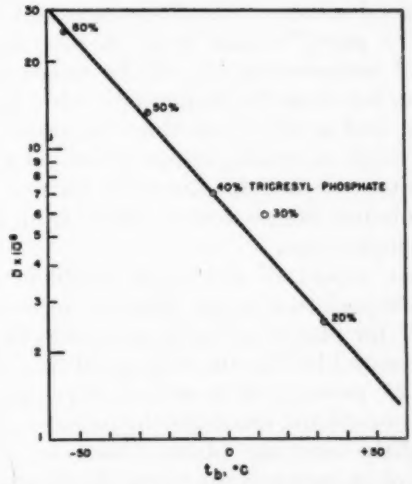

FIG. 8. Correlation between plasticizer diffusion rate at constant temperature (153°C) and the brittle temperature, in accordance with Eq. (8). The weight percent of plasticizer is indicated at each point on the curve.

If consideration is given to the activity factors of Fig. 7 and the data of Fig. 9 is replotted as $\log(D/(\partial \ln a_1/\partial \ln v_1))$ *versus* t_b, there is no substantial improvement in the fit of the data. The point for butyl acetyl ricinoleate does come more closely to lying on a common line with the other four plasticizers. More extensive data, both on solvent and non-solvent type plasticizers, are needed to check these ideas in detail. There is this further inconsistency about butyl acetyl ricinoleate: at the

[26] R. F. Boyer and R. S. Spencer, J. App. Phys. 16, 594 (1945).

TABLE I. Data and calculations for plasticizer loss from polyvinylchloride at 100°C.

Plasticizer	μ at 53°C[a]	Relative vapor pressure of plasticizer[b]	Relative loss rate of plasticizer from 50 parts plasticizer: 100 parts PVC at 100°C[b]	Diffusion constant at 100°C $\times 10^9$[b]	Activity of plasticizer at given concentration and 53°C[c]	Relative escaping tendency = relative vapor pressure $\times$ activity[c]	Brittle temperature for 33% plasticizer °C[d]
Dibutyl phthalate	−0.04	1	1	5.6	0.73	1	−2
Dibutyl sebacate	0.15	0.25	0.25–0.52	—	0.72	0.25	−70
Dihexyl phthalate	−0.13	0.077	0.24–0.40	1.77	0.73	0.077	8
Dioctyl phthalate	0.01	0.023	0.12–0.30	1.25	0.76	0.024	10
Butyl acetyl ricinoleate	0.65	0.021	0.37–0.74	3.16	0.94	0.027	−30
Tricresyl phosphate	0.38	0.013	0.05–0.10	0.9	0.91	0.016	22

[a] From Doty and Zable (see reference 10).
[b] From Small (see reference 6).
[c] Calculated by the author.
[d] From Jones (see reference 16).

brittle point (say −30°C) this plasticizer is quite incompatible with the polymer, and is an oil-type plasticizer; however, at 100°C, where diffusion rates were measured, this same plasticizer is probably a fairly good solvent. Indeed, if one examines Fig. 4 of Small's paper[6] where log$D$ is plotted against reciprocal temperature, it will be noted that this plasticizer has a much smaller activation energy for diffusion; and at the same time the slope tends to decrease with increasing temperature, which might be consistent with a fundamental change in plasticizer-polymer interaction on going from lower to higher temperature.

Another aspect of this same problem may be seen in the moisture vapor diffusion measurements of Doty[27] for plasticized polyvinyl chloride, which are represented in Fig. 10. It is noted that the addition of 25 percent of a solvent-type plasticizer, tricresyl phosphate, increases the moisture diffusion only slightly over the blank. However, the same amount of a non-solvent-type plasticizer, glycol ester of C_8 to C_{10} fatty acids, greatly enhances the moisture transmission. This arises, again, we believe, because the water vapor is diffusing partly through regions of almost pure plasticizer.

We wish to point out now a conclusion reached by Aiken, Alfrey, Janssen, and Mark[28] which antipates our results in some respects; namely, that the most efficient plasticizers are those of highest mobility in the polymer. By plotting rate of plasticizer loss into an oil medium against brittle temperature, they obtained a straight line and concluded that the most efficient plasticizers are those that diffuse most readily through the sample. This is, of course, the conclusion reached from Figs. 8 and 9. However, we have redrawn their curve, using only the plasticizers for which Doty and Zable gave μ-values. The results are shown in Fig. 11. There is a strong tendency for high rate of loss to be associated with a high μ-value. This would mean that those plasticizers which are least compatible with the polymer are most readily extracted by the oil. There is one marked exception in trioctyl phosphate (tri-2-ethylhexyl phosphate) with a μ-value of −0.76. Even here the affinity of the oil for the 2-ethylhexyl groups may be the dominant cause for rapid extraction. In any event, these results appear to emphasize Small's point about the dual factors of thermodynamics and dynamics in plasticizer loss.

Now there still remains a paradox in interpreting the diffusion data of Fig. 9. Thermodynamic studies would say that the most efficient solvent-type plasticizers (being, according to Fig. 4 those with a small or negative μ-value) are the ones most firmly held to the polymer. For dibutyl phthalate ($\mu = -0.06$) and certainly for tri-2-ethylhexyl phosphate ($\mu = -0.76$), it is almost necessary to postulate specific interaction or binding forces between polymer and plasticizer. Yet these are precisely the plasticizers which can diffuse most rapidly. Presumably in such cases, active groups along the polymer chain are completely shielded by firmly attached plasticizer molecules, thus leaving other plasticizer molecules free to diffuse in the regions between such solvated shells. This is in

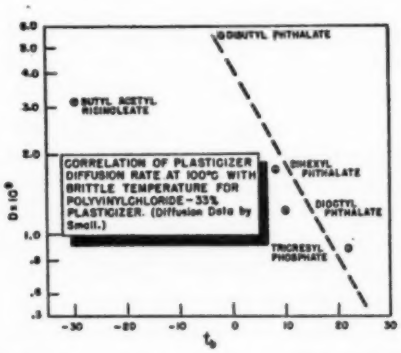

FIG. 9. Plasticizer diffusion rate *versus* brittle temperature for several different plasticizers. These values have not been corrected for the activity factors plotted in Fig. 7. Butyl-acetyl ricinoleate is an oil-type plasticizer; the others are solvent type.

[27] Paul Doty, J. Chem. Phys. 14, 244 (1946).
[28] Aiken, Alfrey, Janssen, and Mark, J. Polymer Sci. 2, 178 (1947).

accord with ideas expressed by Aiken, Alfrey, Janssen, and Mark.

There is one other aspect of diffusion which is assuming greater importance following work by Würstlin,[29] Fuoss,[30] and more recently Richards[31] on the direct current electrical conductivity of plasticized polyvinyl chloride. Addition of plasticizer has a marked effect in increasing conductivity, presumably by decreasing melt viscosity so that ionic impurities present in the polymer can diffuse more rapidly. Figure 12 is a low molecular weight analog of this situation, using mixtures of a viscous material, hexachlorodiphenyl oxide, and carbon tetrachloride. Both compounds have the same resistivity in the pure state, but a much lower resistance at intermediate compositions. A log-log plot of resistivity against viscosity for the mixtures on the left-hand branch of the curve is linear, thus indicating that viscosity is the controlling factor. The major impurities are in the hexachlorodiphenyl oxide, but they cannot attribute appreciably to the conductivity because of the high viscosity of the medium.

Assuming that ionic impurities reside mainly in the polymer, that the melt viscosity of the plasticized mix is given by Flory's relation, Eq. (5), and that resistivity is proportional to the melt viscosity and inversely proportional to the polymer concentration, one can deduce the equation

$$\log Rw_2 = \sigma + \tau(w_2)^{\frac{1}{2}}, \qquad (9)$$

where σ and τ are constants, R is the resistivity,

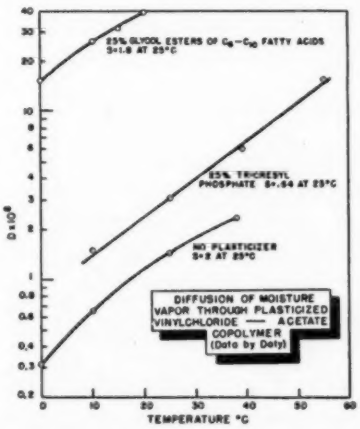
25% GLYCOL ESTERS OF C_8–C_{10} FATTY ACIDS
S=1.8 AT 25°C
25% TRICRESYL PHOSPHATE S=1.64 AT 25°C
NO PLASTICIZER
S=2 AT 25°C
DIFFUSION OF MOISTURE VAPOR THROUGH PLASTICIZED VINYLCHLORIDE — ACETATE COPOLYMER (Data by Doty)
D×10⁸
TEMPERATURE °C

FIG. 10. Dependence of moisture vapor diffusion rate on temperature and plasticizer type for a vinylchloride-vinylacetate copolymer. The S values on each curve represent the solubility of water in the system. Tricresyl phosphate is a solvent type, the glycol ester is an incompatible or oil type plasticizer.

[29] F. Würstlin, Kunststofftechnik 11, 269 (1941).
[30] R. M. Fuoss, J. Am. Chem. Soc. 61, 2334 (1939).
[31] R. G. Richards, The Monsanto Chemical Company, private communication. Data presented at conference on Electrical Insulation, Cambridge, Massachusetts, September 1947.

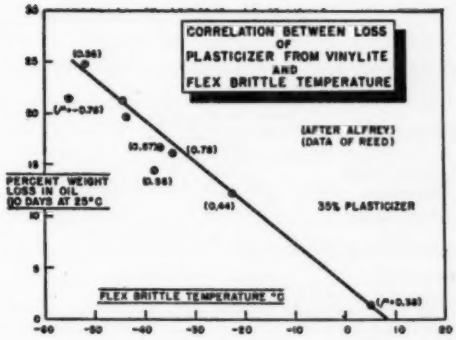
CORRELATION BETWEEN LOSS OF PLASTICIZER FROM VINYLITE AND FLEX BRITTLE TEMPERATURE
(AFTER ALFREY)
(DATA OF REED)
PERCENT WEIGHT LOSS IN OIL (10 DAYS AT 25°C)
35% PLASTICIZER
FLEX BRITTLE TEMPERATURE °C

FIG. 11. Weight loss of plasticizer into oil from plasticized vinylite as correlated with flex brittle temperature. μ-values associated with these plasticizers are indicated at each point.

and w_2 is the weight fraction of polymer. Figure 13 represents such a plot using data by Fuoss.[30] The agreement is only fair, in part because the contribution of plasticizer impurities has been neglected. A similar plot is obtained using Würstlin's data. Richards has recently reported some very interesting electrical resistivity values for plasticized polyvinyl chloride.[31] Part of his data on three different plasticizers is summarized in Table II where we added μ-values and brittle points for comparison. Both the volume resistivity of the mixture and its temperature coefficient run parallel with μ and the brittle points.

Actually, the work of Mead and Fuoss[32] on electrical conductance in plasticized polyvinylchloride to which a known electrolyte has been added reveals complicated voltage-time effects, and a conductance which increases very slowly with concentration of electrolyte. Similar results appear in studies by Fuoss and Elliot for tributyl ammonium picrate in tricresyl phosphate.[33] Hence, the relationship attempted in Fig. 13 is undoubtedly much too simple. Moreover, Fuoss[30] had attempted to prepare the samples used in Fig. 13 in such a way that the electrolyte content would be constant from sample to sample.

INTERRELATIONSHIPS BETWEEN COMPATIBILITY, EFFICIENCY, AND PERMANENCE

Several interrelationships between pairs of the factors, compatibility, efficiency, and permanence have been mentioned at appropriate points already. However, it is believed that the full importance of these interconnections can best be appreciated by representing them on a tri-linear chart, such as is done in Fig. 14. This correlation chart should be self-explanatory since each of its elements has been discussed individually. The most

[32] D. J. Mead and R. M. Fuoss, J. Am. Chem. Soc. 67, 1566 (1945).
[33] R. M. Fuoss and M. A. Elliot, J. Am. Chem. Soc. 67, 1339 (1945).

TABLE II. Effect of plasticizer type on the electrical resistivity of polyvinyl chloride. Data by Richards.*

Plasticizer	Parts plasticizer per 100 parts resin[a]	Specific resistivity at 25°C in ohms. Plasticizer	Compound	$E/2.3R$ compound cal./mole	μ[b]	t_B°C[c]
Tricresyl phosphate	60	1.55×10^{9}	5.4×10^{13}	6970	0.38	−30
Dioctyl phthalate	50	5.6×10^{10}	1.22×10^{13}	4680	0.01	−50
Trioctyl phosphate	50	2.25×10^{8}	2.94×10^{9}	2868	−0.76	−70

* See reference 31.
[a] Also contained one part santicizer.
[b] μ-values by Doty and Zable on cross-linked polyvinyl chloride at 53°C.
[c] Brittle points on Vinylite VYNW by Fligor and Sumner (see reference 49).

important single conclusion to be stated after inspecting Fig. 14 would appear to be this; the chemical composition (and perhaps the size and shape) of the plasticizer molecule determines its thermodynamic interaction with the polymer, which interaction constant can be expressed by means of a single, semi-empirical constant, μ. μ is sufficient to characterize the two thermodynamic properties, compatibility and effective vapor pressure of the plasticizer. The same factors which determine μ are also very largely responsible for the dynamic properties of the plasticized system; namely, the efficiency and diffusion characteristics. It is necessary here to recognize that solvent and oil type plasticizers give essentially different behaviour both with efficiency and diffusion. We realize that the actual physical data leading to Fig. 14 is so scarce and widely scattered as to give this plot more the character of suggestions for future work rather than conclusions to be adopted. Specially designed plasticizer molecules, and particularly polymeric plasticizers, should allow one to avoid the seemingly closed cycle of relationships indicated by Fig. 14.

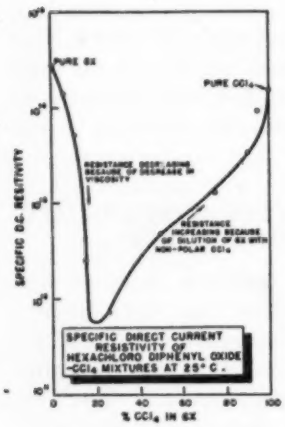
PURE 6X
PURE CCl4
SPECIFIC DIRECT CURRENT RESISTIVITY OF HEXACHLORO DIPHENYL OXIDE -CCl4 MIXTURES AT 25° C.
SPECIFIC D.C. RESISTIVITY
% CCl4 IN 6X

FIG. 12. Measured electrical resistivity in the system, hexachlorodiphenyl oxide (6×)-carbon tetrachloride. This is a low molecular weight analog of the behavior of plasticized polyvinyl chloride.

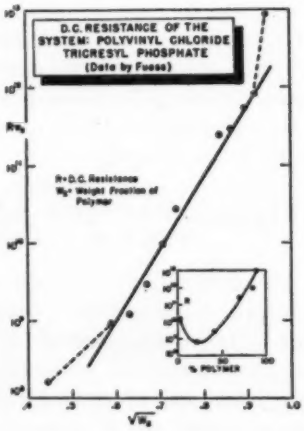

FIG. 13. Direct current resistivity times weight fraction of polymer, Rw_2, as a function of plasticizer content for tricresyl phosphate in polyvinylchloride. The original data from Fuoss is shown in the insert.

EFFECT OF PLASTICIZERS ON TENSILE STRENGTH

While this topic has no formal connection with the major purpose of our article, yet a preliminary attack can be made along lines used by Flory to develop Eq. (5).

Flory has demonstrated[34] a linear relationship between tensile strength, T.S., and reciprocal number average molecular weight, $\bar{M}_n$

$$\text{T.S.} = a - b/\bar{M}_n, \tag{10}$$

where a and b are constants. Assuming that the plasticizer can be treated as a low molecular weight species of the polymer, its presence will lower the number average molecular weight of the mixture such that

$$\bar{M}_n\,(\text{mixture}) = M_1M_2/[M_1+w_1(M_2-M_1)], \tag{11}$$

where M_1 is the molecular weight of the plasticizer and M_2 is the number average value for the original polymer, and w_1 is the weight fraction of plasticizer. Substitution in Eq. (10), and approximating M_2-M_1 by M_2 leads to

$$\text{T.S.} = a - b/M_2 - bw_1/M_1, \tag{12}$$

which reduces to Eq. (10) when $w_1=0$, and otherwise predicts a linear decrease in tensile strength with plasticizer content. Moreover, the rate of decrease of tensile strength is greater the lower the molecular weight of the plasticizer. Data by Rider and Sumner[35] for polyvinylchloride and vinylchloride-acetate copolymers follow roughly this

[34] Paul J. Flory, J. Am. Chem. Soc. 67, 2048 (1945).
[35] D. K. Rider and J. K. Sumner, Abstract of paper presented before the Division of Paint, Varnish and Plastics Chemistry, American Chemical Society, Chicago, September 1946.

linear relationship. However, tricresyl phosphate and paraplex G-25 fall on the same curve, even though differing in molecular weight. Thus, in analogy with the experience gained in using Eq. (5) for the melt viscosity of plasticized polymers, Eq. (12) may predict the general behaviour but provides no basis for distinguishing between different plasticizers.

POLYMERIC PLASTICIZERS

There has been a marked tendency in the past few years toward the use of polymeric plasticizers. This has resulted because of difficulties encountered with migration and vapor loss of low molecular weight plasticizers and is one practical solution to the cycle of properties portrayed in Fig. 14.

Perhaps the first commercial use of a polymeric plasticizer was the incorporation of polyisobutylene with polystyrene to form a semiflexible insulation for coaxial cables during the early days of the war before polythene became available. Details of the exact composition employed have appeared in a recent patent.[36] Polyisobutylene was also used as a plasticizer or softening agent for polyethylene. Toward the end of the war, polyester resins were used in the vinylite jacket on coaxial cables to replace conventional plasticizers which migrated into and ruined the dielectric properties of the polythene cable core.[37] The general significance of

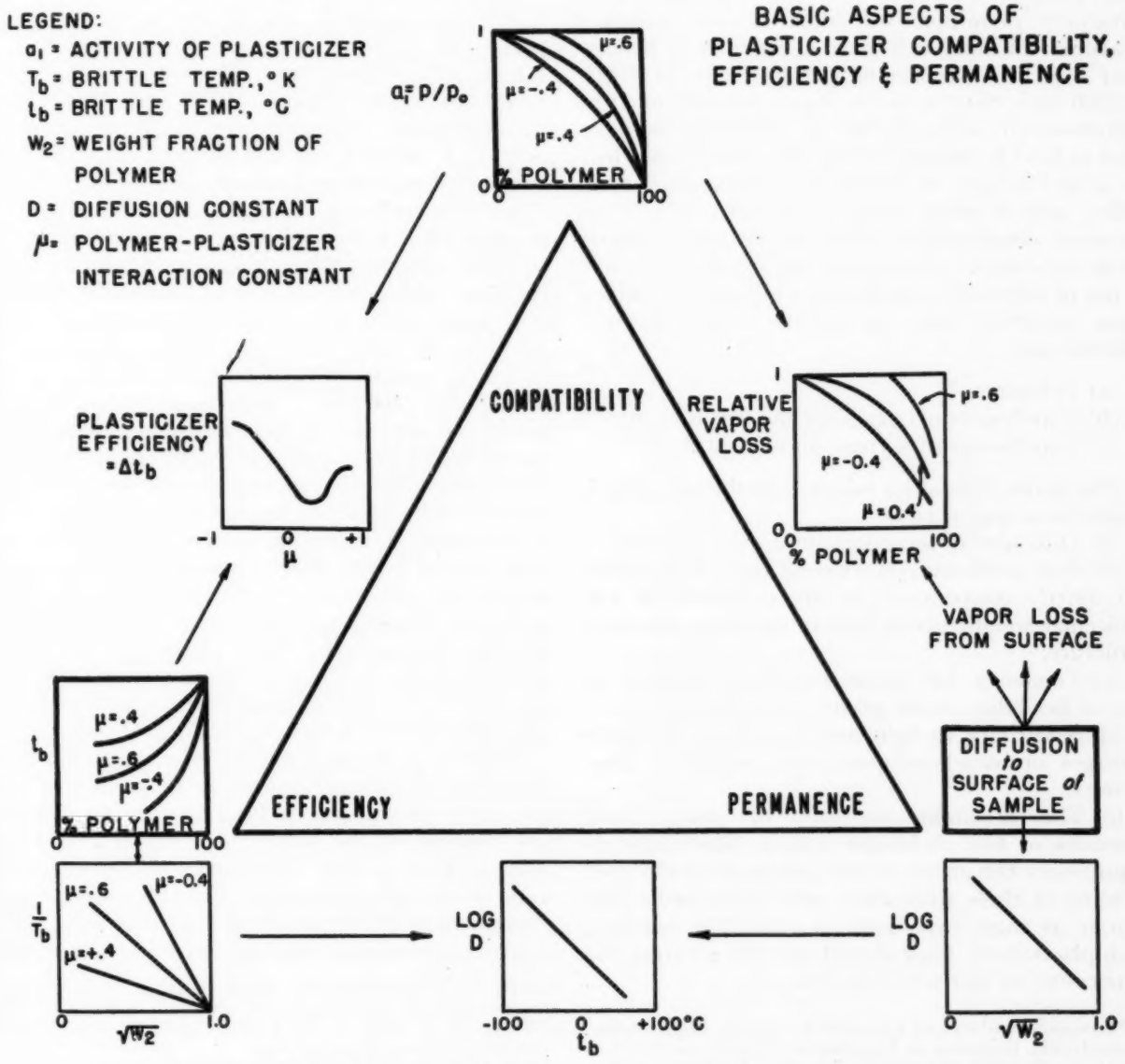

FIG. 14. Interrelationships between pairs of the three factors, compatibility, efficiency, and permanence.

[36] U. S. Patent 2,436,842, March 2, 1948, A. J. Warner and Myron Bakst, Federal Telephone and Radio Corporation.
[37] A. J. Warner, Electrical Communications 23, 63 (March 1946).

TABLE III. Entropy of mixing of two components according to Gee.

Mixture	$T \cdot \Delta S$ at room temperature
Two liquids	8.3 cal.
Liquid plus polymer	4.15
Two polymers	0.0083

Molal volume of liquids, 100 cc.
Molal volume of polymers, 100,000 cc.
1 cc of each material is mixed.

this development to all types of plasticizer problems was soon realized with the result that an important new trend in plasticizers is now evident.

An exact definition of a polymeric plasticizer has not been formulated. The following somewhat arbitrary definition will describe the essential features: an inherently flexible polymer or copolymer with a molecular weight in excess of 1000–10,000 such that both the vapor pressure and the diffusion rate are negligible. In general, a combination of flexible elements along the chain (methylene or ester linkages) to ensure low temperature flexibility, and of polar groups ($-C=O$, $-C\equiv N$) to promote compatibility with the polymer, appear to be necessary, at least with the vinyls. The three types of polymeric plasticizers which have received most attention thus far for use with polyvinyl chloride are:

(a) Polyesters.[38]
(b) Copolymers of butadiene and acrylonitrile[39, 40]
(c) Copolymers of styrene and isobutylene.[41]

The major difficulties inherent in the use of such plasticizers appear to be:

(a) Difficulty of incorporation in the polymer.

(b) Not as efficient, on a weight basis, in lowering the brittle temperature as are conventional low molecular weight plasticizers of the same chemical structure.

(c) Tendency for phase separation leading to loss of flexibility of the plasticized polymer.

(d) Sensitivity to light and oxygen of the olefin linkages in butadiene containing polymeric plasticizers.

(e) The apparent necessity of using small amounts of low molecular weight plasticizers to supplement the action of the polymeric plasticizer.

Some of these difficulties will undoubtedly disappear as more experience is gained in handling such plasticizers. They should not detract from the importance of this new development.

[38] Resinous Product and Chemical Company, Philadelphia, Pennsylvania, literature on Paraplex G-25, G-40, and G-50.
[39] B. F. Goodrich Chemical Company, Cleveland, Ohio, literature on geon polyblends.
[40] Modern Plastics **25**, 81, (Sept. 1947); **25**, 91 (Oct. 1947).
[41] D. W. Young and R. G. Newberg, Ind. Eng. Chem. **39**, 1446 (1947).

TABLE IV. Some cohesive energy densities for rubbers and polymers.

Polymer	Cohesive energy density cal./cc
Silicone rubber	54[a]
Polyisobutylene	60[b]
Polyethylene	62[c]
Hevea rubber	64[d]
GR-S rubber	65.5[d]
Neoprene GN	67[d]
Polystyrene	80[a]
Thiokol F and FA	88[d]
Buna N rubber	88[d]
Polyvinylchloride	90[b]

[a] Measured by Boyer and Spencer.
[b] Estimated by the author.
[c] Richards (see reference 15).
[d] Gee (see reference 48).

What is probably one of the basic polymeric plasticizer patents[42] claims a linear polyester of 1,2-propylene glycol and sebaccic acid having a molecular weight between 1700 and 20,000 as a non-migrating plasticizer for polyvinylchloride, polyvinyl acetate, or copolymers thereof. The condensation of phenyl phosphorous dichloride with dihydroxy aromatic compounds such as hydroquinone gives linear polymers which are said to be suitable, among other things, as plasticizers for cellulose plastics.[43] A special variation on the polymeric plasticizers consists in using a vinyl chloride—20 percent vinyl acetate copolymer of molecular weight 8000–15,000 as a processing aid for vinylite copolymers containing up to 7 percent vinyl acetate and having molecular weights in excess of 18,000.[44] Internal polymeric plasticizers have been used to toughen phenol formaldehyde resins.[45] Polyolefins, or low molecular weight vinyl or butadiene polymers, or fatty acids are condensed with phenol in the presence of BF_3 to form compounds having two or more phenol groups per molecule. These in turn are condensed with formaldehyde. Conventional inert plasticizers added to phenolic resins do not give elastic products whereas the internally linked plasticizers appear able to take deformation forces elastically and reversibly.

There is as yet no scientific interpretation of the behaviour of polymeric plasticizers, partly because the subject is new, partly because even the descriptive aspects of the subject are scarce. We shall attempt here a very preliminary examination of some of the factors involved. For this purpose, it is convenient to divide the subject into the same three catagories previously used for low molecular weight

[42] British Patent 586,826, April 1, 1947, The Resinous Products and Chemical Company; see also U. S. Patent 2,437,657 (March 9, 1948) to H. J. West and H. M. Enterline, American Cyanamid Corporation.
[43] A. D. F. Toy, U. S. Patent 2,435,252, February 3, 1948 assigned to Victor Chemical Works.
[44] British Patent 576,110, March 19, 1946, to W. T. Henley's Telegraph Works, Ltd. and W. F. O. Pollet.
[45] F. J. Hermann, Verfabronick **20**, 168 (1947).

plasticizers—namely, compatibility, efficiency, and permanence.

Compatibility

Dobry and Boyer-Kawenoki[46] have recently examined the mutual compatibilities of a number of pairs of polymers and find that compatibility is an exception rather than a rule. Even when two polymers can be mixed together in the presence of a mutual solvent, they tend to unmix. Gee[47] has interpreted this behaviour by pointing out that the entropy gain on mixing two polymers will be quite small as compared with that for mixing polymer and solvent. Table III lists his calculations. This being so, then even a slightly unfavorable heat of mixing will be sufficient to cause phase separation. This is probably the basis for the common practice of adding some low molecular weight plasticizer, or a compatibility agent like cyclized rubber, along with the polymeric plasticizer.

One might expect Gee's concepts about the role of the cohesive energy density to be a valuable guide for estimating compatibility. Gee[48] showed that the swelling of a cross-linked rubber is a maximum in those solvents having the same cohesive energy density as that of the rubber. This idea might be paraphrased for our case to read that two polymers of the same cohesive energy density will tend to be compatible. Table IV lists cohesive energy densities for several common rubbers and plastics from which it can be seen, at least on the basis of practice that the above idea is roughly true. Thus, butadiene-acrylonitrile copolymers are used in polyvinyl chloride. Even the low molecular weight dimethyl silicone fluids are completely incompatible with polystyrene, but show a slight compatibility with natural rubber. GR-S rubber and polystyrene are incompatible.

While Table IV may serve as a general guide, it seems probable that subtle differences in local force fields and structures may still have an important role. For example, when a copolymer of styrene-1 percent divinyl benzene is swelled in styrene monomer and polymerized, the final product is hazy, even though there has been no change in the gross chemical composition. In polyvinylchloride, local force fields between polymer and plasticizer will probably dominate these general considerations about cohesive energy densities.

Aside from the question of whether two polymers are intrinsically compatible, there is still the problem of achieving perfectly uniform mixtures using two high molecular weight materials. This is a purely mechanical problem; however, it appears that a polymeric plasticizer should be able to function either as a soluble or an oil-type material. The present state of the art can hardly predict which is the more desirable type, unless optical clarity is required. An incompatible polymeric plasticizer is present in its natural and most flexible form, while at the same time the polymer being plasticized should preserve a continuous structure whose heat distortion temperature is not appreciably lowered by the plasticizer. A compatible polymeric plasticizer might be expected to lower the heat distortion temperature of the parent polymer.

Efficiency

Jones[16,17] has shown that the higher the viscosity of a plasticizer, the lower will be its efficiency, but that efficiency approaches asymptotically a limiting value even for infinite viscosity. This asymptotic behaviour apparently arises becauses the longer chain molecules exhibit segmental behaviour.

Here again, we would like to approach this question by Flory's melt viscosity equation for the effect of an addition agent on the viscosity of the parent polymer. When Flory derived Eq. (5), he could safely neglect the molecular weight of the solvent in comparison to that of the polymer. With a polymeric plasticizer, this is no longer permissable.

In general, as Flory showed,

$$\bar{Z}_w' = Z_1 + w_2(\bar{Z}_2 - Z_1), \tag{13}$$

where $\bar{Z}_w'$ is the weight average chain length of the mixture, Z_1 that of the plasticizer, and Z_2 that of the pure polymer. Substitution in the Flory melt viscosity equation

$$\log\eta = A + B(\bar{Z}_w')^{\frac{1}{2}} + E/RT, \tag{14}$$

and making the assumption $\log\eta = \text{constant}$, leads to the following approximate equation which is sufficiently valid to show trends under the rather restricted conditions of $w_2 > 0.9$ and $\bar{Z}_2 > 10Z_1$

$$(w_2)^{\frac{1}{2}} = A'' - Q/T[1 - Z_1/2\bar{Z}_2], \tag{15}$$

where A'' and Q are constants. Evidently, the larger Z_1, the steeper the slope of the curves as in Fig. 3 and the less efficient the plasticizer. The plots of Fig. 3 appear to follow this type of behavior approximately.

Permanence

In the sense that we have been using the term, the problem of permanence is, like that of the famous snakes of Ireland, somewhat trivial since both the vapor pressure and the diffusion rate are vanishingly small. There may be a question whether the degree of dispersion initially obtained between

[46] A. Dobry and F. Boyer—Kawenoki, J. Polymer Science 2, 90 (1947).
[47] G. Gee, Quarterly Rev. Chem. Soc. 1, 265 (1947).
[48] G. Gee, Trans. Inst. Rubber Ind. 18, 266 (1943); Trans. Faraday Soc. 38, 418 (1942).

polymer and polymeric plasticizer is permanent. Localized diffusion may result in aggregation of polymer-polymer chains and plasticizer-plasticizer molecules which would alter the efficiency.

ACKNOWLEDGMENT

This material was presented before The Berkshire Plastics Club, September 1947; the Akron Polymer Group, April 1948; and the Division of High Polymer Physics of the American Physical Society, January 1949—each time in a different form. It is a pleasure to acknowledge the benefit derived from informal discussions. We should also like to thank C. Milton, H. Coles and his collaborators, T. Alfrey, and H. Mark for specific suggestions.

X-Ray Diffraction Studies of the Stretching and Relaxing of Polyethylene*

ALEXANDER BROWN
Carbide and Carbon Chemicals Corporation, South Charleston, West Virginia

The orientation of the crystallites when polyethylene is stretched at 96°C is normal in that, from the onset of stretching, the preferred orientation is that wherein the long chain axis is parallel to the direction of stretch. At low extensions the preference for this orientation is weak, but it progressively becomes stronger as stretching proceeds.

When polyethylene is stretched at room temperature, the crystallite behavior is more complicated. The first 20 percent extension produces no preferred orientation of the crystallites. From 30 percent to 200 percent extension the preferred orientation is that wherein the 011 "axis" is parallel to the direction of stretch, and the long chain axis therefore inclined to this direction at an angle of 64°. From 200 percent extension to the break (about 600 percent extension), the tilt of the crystallites in the preferred orientation progressively lessens and almost vanishes at the break. The stress-strain diagram of polyethylene is interpreted in the light of these findings. The preferred orientation of the crystallites in the region of the shoulder in necked-down polyethylene is also that wherein the 011 "axis" aligns with the stretching direction.

When stretched polyethylene is relaxed by shrinking at elevated temperatures, the crystallites become disoriented but in a non-random manner. This behavior is described qualitatively.

INTRODUCTION

POLYETHYLENE is a "crystalline" polymer. It is estimated that no less than 55 percent,[1] perhaps as much as 73 percent,[2] of the CH_2 groups are present in crystallites. The structure of the crystallites has been elucidated by Bunn.[3] He found that the long chains are restricted to a planar, extended zig-zag configuration while in the crystallites, and that the chains constitute a major axis of the orthorhombic crystals. The "fringed micelle" concept of a crystallite has been described by Mark[4] and Bunn,[5] and the spherulitic nature of the aggregates of the crystallites has been reported by Bunn[6] and Bryant.[2]

In a sample of unstressed polyethylene the crystallites are randomly oriented. When a stress is applied, however, the crystallites tend to line up in a preferred orientation relative to the direction of the applied stress. Figure 1 is an electron micrograph of a very thin, cast film of polyethylene. The random orientation of the crystallites and the spherulitic nature of their aggregates are readily seen.

This film was cast hot on a microscope slide from a 0.2 percent solution of polyethylene in trichlorethylene. After drying, the film was floated off in water and caught on a specimen screen. The film was not shadowed, but the crystallites are visible because they are both denser and thicker than the rest of the film. The micrograph was obtained by an RCA model EMU-2A electron microscope using a 0.001-in. objective aperture and an unbiased gun. It is estimated that the average thickness of the film does not exceed 200 angstroms. Figure 2 shows what happens when this film was stretched. The crystallites are no longer randomly oriented in the stressed regions and the aggregates have lost their identity. Such a thin film cannot be stretched by mechanical means. It was stretched in the microscope when the electron beam hit dust particles which had been impregnated in the film. The particles become charged by the beam and jump. This usually tears the film but occasionally only stretches it. The dark mass in the bottom right-hand corner of Fig. 2 is a dust particle.

---

* Presented at the sixth meeting of the Division of High-Polymer Physics, American Physical Society, New York City, January 27–29, 1949.

[1] E. Hunter and W. G. Oakes, Trans. Faraday Soc. **41**, 49 (1945).

[2] W. M. D. Bryant, J. Polymer Sci. **2**, 547 (1947).

[3] C. W. Bunn, Trans. Faraday Soc. **35**, 482 (1939).

[4] H. Mark, J. Phys. Chem. **44**, 764 (1940).

[5] C. W. Bunn, Proc. Roy. Soc. **A180**, 82 (1942).

[6] C. W. Bunn and T. C. Alcock, Trans. Faraday Soc. **41**, 317 (1945).

Figure 3 is the x-ray diffraction pattern of unstretched polyethylene. The pattern is one of concentric, complete circles similar to that yielded by a crystalline powder. This indicates that the crystallites in unstretched polyethylene are randomly oriented.

Figure 4 is the x-ray diffraction pattern of polyethylene which has been stretched 500 percent at 96°C. The circles of the previous figure have degraded to very short arcs. The shortness of these arcs indicates that the crystallites are not randomly oriented, but rather are essentially all oriented in a preferred direction. The location of these short arcs on the circumferences reveals that the particular orientation of the crystallites that is so highly preferred is that wherein the long chain axis is parallel to the direction of stretch. The other two major axes of the crystallites are randomly oriented in all directions perpendicular to this.

In the present paper we are primarily interested in the behavior of the crystallites under conditions intermediate to the two extremes illustrated by Figs. 3 and 4.

EXPERIMENTAL

Commercial grade polyethylene monofils, of extruded diameter 0.9 mm, were used throughout this investigation, and the x-ray diffraction patterns were obtained using a General Electric XRD-1 x-ray diffraction unit. Since the purpose of the investigation was to discover the behavior of the crystallites under conditions intermediate to the unoriented and "fully" oriented states, diffraction patterns were obtained at intermediate degrees of stretch. These intermediate extensions are easily obtained when a sample is stretched hot, as at 96°C. However, polyethylene necks down when stretched normally at room temperature, and one

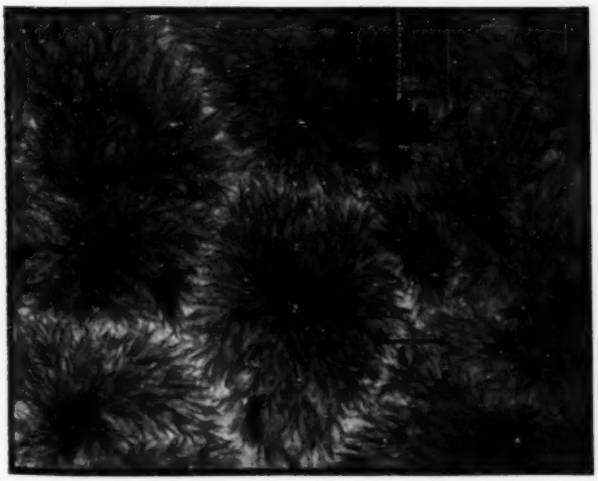

FIG. 1. Electron micrograph of an unstretched film of polyethylene.

FIG. 2. Electron micrograph of a partially stretched film of polyethylene.

is left with a sample, a part of which is stretched about 500 percent, and separated by an abrupt shoulder from the rest of the sample which is essentially unstretched. However, if the room temperature stretching is carried out slowly and carefully, with the sample in a jig, it is possible to achieve any desired extension, up to the 500–600 percent at which the sample breaks, without any necking-down occurring. This technique of sample preparation was used in this investigation, though a necked-down sample was also investigated with a crude micro x-ray camera. Another method which was also used to obtain intermediate conditions is to first stretch the sample to about 500 percent, then allow it to shrink back by exposing it to elevated temperatures. A Leeds and Northrup microdensitometer, equipped with a rotatable plate holder, was used in analyzing the diffraction patterns.

RESULTS AND DISCUSSION

I. Stretching of Polyethylene

Figures 5 and 6 are the x-ray diffraction patterns of polyethylene stretched 50 percent and 100 percent, respectively, at 96°C. These patterns are truly intermediate to those yielded by the unoriented (Fig. 3) and the highly oriented (Fig. 4) crystallite systems. The degradation of the full circles to short arcs is seen to be a smooth process, and the centers of the arcs, however long, are the locations of the final very short arcs or spots. It may be said, then, that when polyethylene is stretched at 96°C, the preferred orientation of the crystallites from the onset of stretching, is that wherein the long chain axis is parallel to the direction of stretch. At low extensions the preference for this orientation is slight, but as stretching proceeds, more and more

of the crystallites are pulled into alignment. This behavior of the crystallites is entirely reasonable in the light of current theories, and it contributes nothing new to our concept of the texture of polyethylene.

When polyethylene is stretched at room temperature, however, a more complicated crystallite behavior obtains. The crystallites act in three different ways, characterizing three different zones of extension. At low degrees of stretch, 0–20 percent, the extension is obtained without any preferred orientation of the crystallites. In the range of 30–200 percent extension, a preferred orientation is evidenced, but it is not that wherein the long chain axis is parallel with the direction of stretch. Rather, the preferred orientation is that wherein the long chain axis of the crystallite is inclined at an angle of 64° to the stretching direction. At 30 percent extension the preference for this orientation is weak, but it becomes progressively stronger till at 200 percent extension, the crystallite system is almost as well ordered as it is at full extension, but with the crystallites closely distributed about a preferred orientation which has its long chain axis inclined at 64° to the stretching direction. From 200 percent extension to the break, about 600 percent stretch, the crystallites turn into near parallelism with the stretching direction, the angle of inclination of the long chain axis to the stretching direction changes, more or less smoothly, from 64° to nearly 0°.

In the region of the 0–20 percent stretch the diffraction patterns were obtained after only a few minutes exposure. They consisted of only the 110 circle (the strongest and innermost reflection), and it was intentionally kept weak so that any intensification on its circumference could be noted. None was, until an extension greater than 20 percent was obtained. Thus, it appears that the first 20 percent extension is achieved without effecting the random orientation of the crystallites at all. Rather, this deformation is accommodated by the amorphous portion of the sample. It is reasonable to expect some sort of abnormal crystallite behavior in this extension range, since extensions of this order in polyethylene are completely recoverable, whereas greater ones are not.

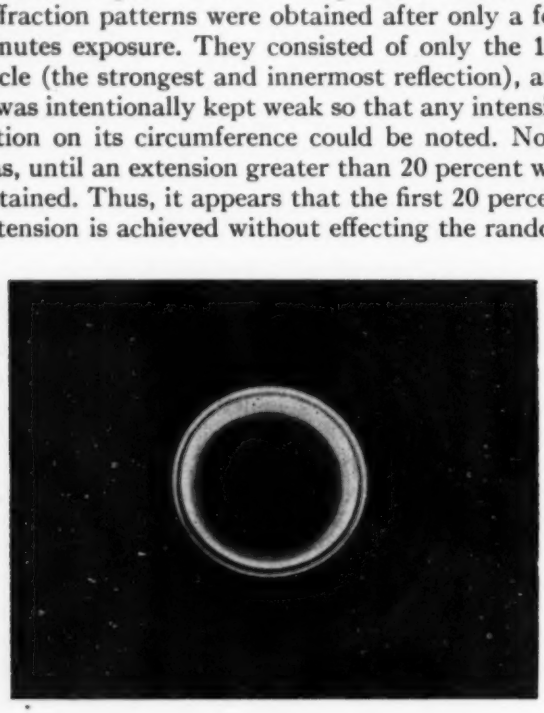

FIG. 3. X-ray diffraction pattern of unstretched polyethylene.

Before discussing the inclined orientation of the crystallites in the intermediate extension range, the procedure used to measure it will be presented. Figure 7 is the x-ray diffraction pattern of polyethylene stretched 150 percent at room temperature. The difference between this pattern and those of the other stretched samples is in the location of the spots or short arcs on the diffraction circles. These different locations are most readily detected in the case of the equatorial reflections where they result in a splitting of the spots, with one exception. This, of course, indicates a different orientation which can be readily evaluated, using the reciprocal lattice method.[7,8] The reciprocal lattice method is generally applied in rotating crystal x-ray studies, but it can also be used in the interpretation of fiber diagrams, since the unidirectional orientation of the crystallites in such materials causes them to be equivalent to a single crystal rotated about an axis during exposure to the x-ray beam. Figure 8 shows the reciprocal lattice configuration which gives rise to the normal type of fiber diagram, like Fig. 4. As the lattice turns about its axis of rotation (in

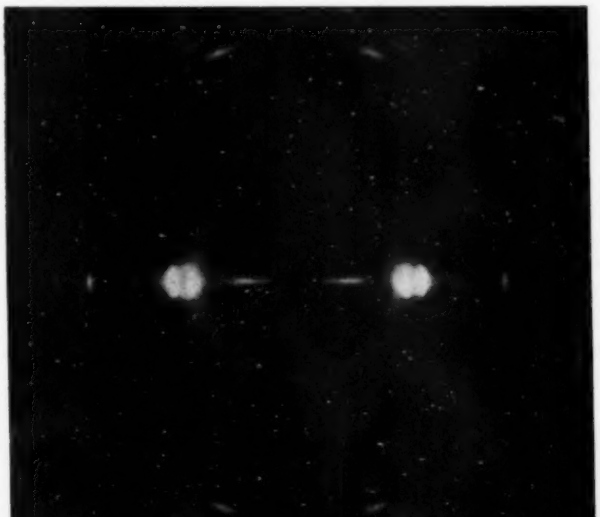

FIG. 4. X-ray diffraction pattern of polyethylene stretched 500 percent at 96°C.

[7] M. J. Buerger, *X-Ray Crystallography* (John Wiley & Sons, Inc., New York, 1942), Chapter 8.
[8] C. W. Bunn, *Chemical Crystallography* (Clarendon Press, Oxford, 1945), pp. 162–164.

this case both the long chain axis, and the fiber axis or stretching direction) the *hk*0 lattice points cut the sphere of reflection on its equator. Therefore, the *hk*0 reflections are on the equator of the diffraction pattern. For simplicity the equator of the sphere of reflection is indicated by a straight line.

If the long chain axis is not coincident with the axis of rotation of the reciprocal lattice, a tilted configuration results as in Fig. 9. This configuration is the particular one which yields the pattern of Fig. 7. In the general case the only restriction is

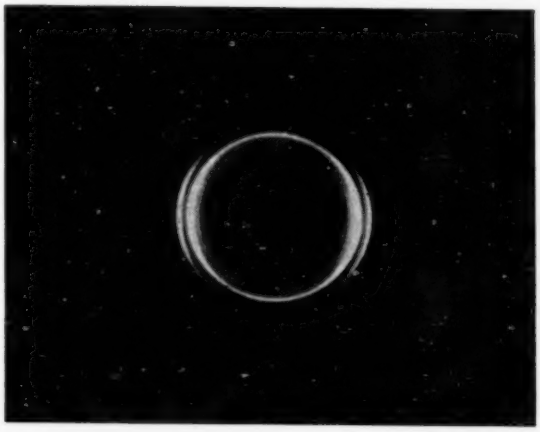

FIG. 5. X-ray diffraction pattern of polyethylene stretched 50 percent at 96°C.

that the lattice origin be on the equatorial plane. As this tilted lattice turns about its axis of rotation, the *hk*0 lattice points will not cut the sphere of reflection on its equator. Instead, they cut it above and below the equator, resulting in split spots in the diffraction pattern. Note that the *h*00 reflections will not split with this configuration. The second equatorial spot, the 200 reflection, is not split in Fig. 7. The tilt of the lattice, and from that the angle of inclination between monofil axis and long chain axis, can be ascertained by determining the ζ and ξ coordinates of the normally equatorial reflections. This was accomplished by scanning the patterns azimuthally with the microdensitometer and transferring the results to a Bernal chart. The angle of inclination was found to be $64° \pm 1°$.

There is a unique direction in the crystal lattice which is also inclined to the long chain axis at an angle of 64°. This is the 011 direction. Examination of Fig. 7 reveals that this reflection has indeed moved over to the meridian from its normal position in the first layer line. Thus, the inclination of the long chain axis of the crystallite in the preferred orientation is due to the fact that the 011 "axis" of the crystallite is parallel with the direction of stretch. It may then be stated that, when polyethylene is stretched at room temperature, the

FIG. 6. X-ray diffraction pattern of polyethylene stretched 100 percent at 96°C.

preferred orientation of the crystallite at intermediate extension is that wherein the 011 direction is parallel to the direction of stretch. As a consequence of this, the 001 direction, or long chain axis, is inclined to the stretching direction at an angle of 64°.

When attention is removed from the inclination of the long chain axis and focused on the direction in the crystallite that is parallel with the stretching direction, the phenomenon appears more reasonable. As Baker has pointed out,[9] this behavior is reminiscent of the "fibering" of metals. When wires are cold drawn, the crystalline grains become preferentially oriented with directions like 011, 111, etc., being parallel to the stretching direction. However, the end effect, aligning a minor axis with the stretching direction is the only way in which this behavior in polyethylene resembles other polycrystalline materials like metals. The mechanism by which the crystallite changes its orientation is different. In metals the intergrain boundaries are supposedly more resistant to deformation than the crystal grains are, and the change of orientation of a grain is presumably due to the slipping of rows of atoms. In polyethylene, the intergrain boundary is made up of the rubbery, amorphous regions, and the particular atoms whose slipping might effect a net turning of the crystallite are not free to do so. Moreover, while this "tilting" of the crystallites in polyethylene is justified only by a precedent, there is not this justification for the "tilting" of an isolated long chain or a short section of one. Such a section would almost certainly be aligned with an applied stress, if free to do so, rather than inclining itself to it at an angle of 64°. Therefore, a stripping off of chains from the crystallites and reformation of new crystallites in the desired orien-

[9] W. O. Baker, *Advancing Fronts in Chemistry* (Reinhold Publishing Corporation, New York, 1945), Vol. 1, p. 108.

FIG. 7. X-ray diffraction pattern of polyethylene stretched 150 percent at room temperature.

tation cannot be the mechanism. We are thus forced to present as a mechanism the only other one of which the author is aware—the actual turning of the crystallites, as units, into the preferred orientation.

As mentioned before, polyethylene necks down when stretched normally at room temperature. A diffraction pattern of the stretched portion is an imperfect Fig. 4, while that of the unstretched portion is the same as Fig. 3, of course. Figure 10 is the x-ray diffraction pattern of the region of the neck itself. This pattern was obtained using a crude micro camera with a pinhole system not fine enough to study surface structure or skin effects, but fine enough that the total irradiated portion was entirely included in the neck. To the best of our knowledge the preferred orientation of the crystallite in the region of the neck is the same tilted orientation that is preferred in the 30–200 percent slowly stretched samples. That is, when polyethylene is necked down, the preferred orientation of the crystallites in the region of the neck is that wherein the 011 direction is parallel to the long axis of the sample. To make certain that the gross physical features of the neck did not contribute to this orientation, a necked-down monofil was annealed at 96°C under tension, and the region of the neck again examined by x-ray diffraction. Though the gross appearance of the neck was the same, the preferred orientation in this region was found to be the normal one of parallelism of the long chain axis with the stretching direction (or long axis of the sample). Furthermore, the lengths of the arcs in the pattern indicated that the degree to which this orientation was preferred was about the same as that in polyethylene which had been stretched 150–300 percent at 96°C.

It would appear then that the behavior of the crystallites in polyethylene, stretched at room temperature, is independent of the rate of stretch, and that scanning the region of the neck with a proper micro camera would yield the same series of patterns as we have obtained by slowly and continuously stretching a sample.[10]

It is interesting to compare these results with the stress-strain behavior of polyethylene. When polyethylene is loaded, it first of all stretches rather grudgingly (and reversibly) to extensions which vary with the sample but average about 20 percent. Increased loading produces a "release" of the sample where small increases in load result in relatively large extensions. The length and slope of this "flat" portion in the stress-strain curve is dependent on the nature of the sample and its history. Most samples, however, start to stiffen again at 200–300 percent extension. From there to the break the curve rises more steeply again. These three zones of mechanical behavior are believed to be intimately related to the three zones of crystallite behavior. The initial reversible extension is accommodated by the amorphous component of the sample, the "yield" region is associated with the crystallites turning such that their 011 "axes" are parallel with the stretching direction, and the final stiffening region is where the crystallites again turn, this time trying to make their long chain axes parallel to the stretching direction.

II. Relaxing of Polyethylene

This portion of the paper describes the results obtained when intermediate conditions were achieved by shrinking polyethylene which had been previously stretched 500 percent at 96°C. The samples were shrunk by exposing them to elevated temperatures. Not much shrinkage results until temperatures considerably in excess of the stretching temperature are reached. For example, a monofil stretched 500 percent at 96°C shrinks by an amount

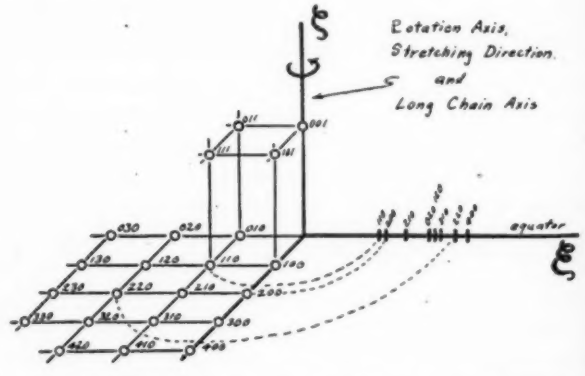

FIG. 8. Reciprocal lattice configuration conforming to normal fiber patterns. Zero level of reciprocal lattice in parallel orientation.

[10] I. Fankuchen and H. Mark, J. App. Phys. 15, 364 (1944).

equal to 3 percent of its stretched length by later exposing it, untensioned, to a temperature of 85°C. The same monofil shrinks 50 percent at 105°C and 75 percent at 110°C. Complete recovery of the 500 percent impressed stretch (83 percent shrinkage) is obtained when the sample is exposed to 115°C.

The starting material, then, is the same sample that has the highly oriented crystallite system indicated by Fig. 4. Since this sample is to be exposed to temperatures of 95–115°C, it would be expected that the shrinkage that will result should be accompanied by a gradual disorientation of the crystallites in a manner just the reverse of the orientation process that accompanies the stretching at 96°C. The patterns would be expected to show simply increasing arc lengths and no complications. However, the following figures show that this is not the case.

Figure 11 is the x-ray diffraction pattern of polyethylene which had been first stretched 500 percent at 96°C, and then allowed to shrink as much as it would, 50 percent of its stretched length, at a temperature of 105°C. Figure 12 is the pattern after shrinking 75 percent at 110°C. The pattern after shrinking at 115°C is identical with Fig. 3. As was expected, the arcs of the patterns become progressively longer as the stretched sample is progressively relaxed, indicating an increasing randomness of the crystallite orientations. However, the locations of the centers of these growing arcs indicate that the preferred orientation in the first place is not that of parallelism with the original stretching direction, and, in the second place, changes with the extent of relaxation of the stretched sample. This means that, while the crystallites become disoriented during the relaxation, they do so in a non-random manner.

Again the preferred orientations are best determined using the reciprocal lattice method. Since no particular orientation is preferred over a range, in

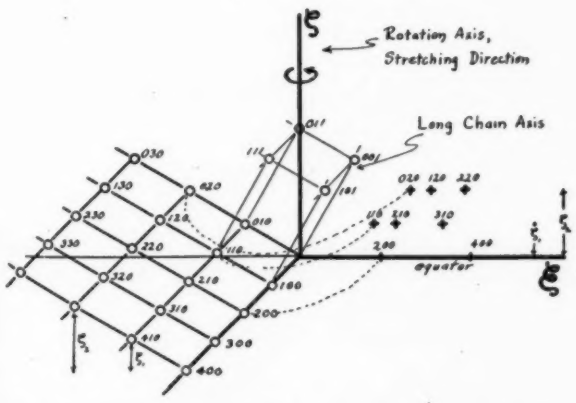

FIG. 9. Tilted configuration of reciprocal lattice conforming to split spot pattern of Fig. 7. Zero level of reciprocal lattice in inclined orientation.

FIG. 10. X-ray diffraction pattern of the region of the neck in necked-down polyethylene.

contrast to the cold stretching process, the following is merely a qualitative picture of the behavior of the crystallites during the relaxation process. The reciprocal lattice configuration conforming to the preferred orientation in the starting material (500 percent stretch at 96°C) is given in Fig. 8. The $h00$, $0k0$, and $hk0$ lattice points are in the equatorial plane, and the corresponding planes are therefore parallel to the stretching direction, or monofil axis. The rotation axis is the 001 axis, long chain axis, of the crystallite. As the sample is relaxed, the reciprocal lattice tilts to conform to the new preferred orientation. This tilt is such that the $0k0$ lattice points are restricted to remain in the equatorial plane (in contrast to the cold stretching process where the $h00$ points are so restricted). The axis of rotation of the lattice is restricted to be in the $h01$ plane of the lattice. The tilt of the lattice increases as the sample is relaxed, so much so that the configuration corresponding to Fig. 12 has a rotation axis almost coincident with the 100 axis of the crystallites. Superimposed on the tilting of the reciprocal lattice, indicating the changing preferred orientation, is an increasing wobble in its rotation corresponding to the disorientation of the crystallites.

In terms of the real lattice of the crystallites, the relaxation process can be described in terms of two of the major axes. In the 500 percent stretched sample the c axis, long chain axis, is parallel with the stretching direction, monofil axis, in the preferred orientation. The mutually perpendicular a and b axes are perpendicular to the monofil axis. As the sample is shrunk back by relaxing at elevated temperature, the behavior of the b axes of the crystallites is normal in that the preferred orientation remains perpendicular to the monofil axis and the distribution about it progressively broadens. The a axes act "abnormally" in that the

FIG. 11. X-ray diffraction pattern of polyethylene, stretched 500 percent then shrunk back at 105°C.

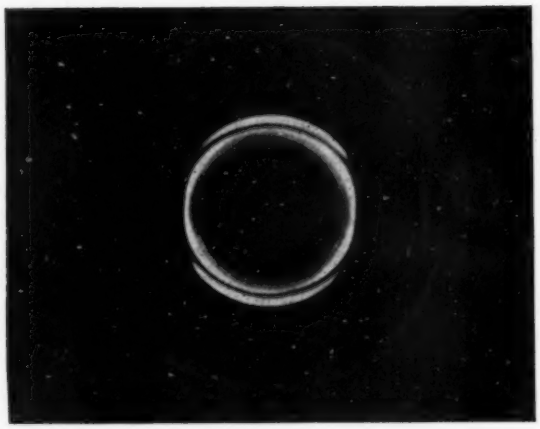

FIG. 12. X-ray diffraction pattern of polyethylene, stretched 500 percent then shrunk back at 110°C.

preferred orientation does not remain perpendicular to the monofil axis but rather continuously changes and approaches parallelism with it; also the distribution of orientations about the preferred one broadens as relaxation continues. The *c* axis is, of course, defined by the positions of the *a* and *b* axes. The foregoing description may be read in terms of the planes of the crystallites by noting, of course, that the *b* axis is perpendicular to the 0*k*0 planes, the *a* axis perpendicular to the *h*00 planes, and the *c* axis to the 001 planes.

It is of interest that the 0*k*0 planes are the last to be brought into parallelism with the stretching direction when polyethylene is stretched at room temperature, and that they are the last to leave parallelism when the stretched sample is shrunk back.

Though radically different in crystallite orientations, the samples which yielded the diffraction patterns, illustrated in Figs. 5 and 12, have something in common. Both have been 'stretched' 50 percent; that of Fig. 5 was directly stretched this amount at 96°C, while that of Fig. 12 had 50 percent of the original 500 percent extension still in it after shrinking back 75 percent of its stretched length at 110°C. It would be interesting to compare the mechanical properties of such materials.

In addition to what significance these results may have in the study of polyethylene itself, they also offer a technique which might profitably be applied in the x-ray crystallography of other crystalline polymers. In the determination of unit cell dimensions from patterns like Fig. 4, the long chain axis (*c* axis) dimension can be obtained directly from the layer line separations. The *a* and *b* dimensions must be obtained by trial, since the *hk*0, *h*00, and 0*k*0 reflections are all on the equator. However, these may be resolved into "layer lines of the third kind" wherein the *h* (or *k*) index is constant, by causing a tilted reciprocal lattice configuration by either of the two methods described here—intermediate cold stretching or partially shrinking of the stretched material. That such behavior in the case of stretching may well be general has been noted by Baker,[9] and more recently investigators of polyethyleneterephthalate[11] and low temperature polymerized polybutadiene[12] have noted "split spots." Fankuchen and Mark[10] however, have reported a different stretching behavior in the case of Nylon. Baker[9] has studied the relaxation of stretched Nylon and found behavior similar to these results on polyethylene.

[11] W. T. Astbury and C. J. Brown, Nature **4024**, 871 (1946).
[12] K. E. Beu, J. Polymer Sci. **3**, 465, 801 (1948).

Infra-Red Absorption Spectra of Some Polymers at Liquid-Helium Temperatures*

GILBERT W. KING, R. M. HAINER, AND H. O. MCMAHON
Arthur D. Little, Inc., Cambridge, Massachusetts

Infra-red absorption spectra of polythene, rubber, polystyrene and polyvinyl chloride have been obtained at 4° absolute, in the rocksalt region, in a specially designed transmission cell containing liquid helium. No unusual changes occur on cooling which considerably alter the absorption. Some sharpening and improvement in resolution occurs, but the widths of most bands in polymers remain wide.

In polythene one component of the doublet at 720 cm^{-1} becomes very sharp (possibly even less than the experimental value of the slit width, 1 cm^{-1}). Its companion remains broad, about 4 cm^{-1}. The two components are interpreted as CH_2 wagging in *trans*- and *cis*-configurations of the hydrocarbon chain.

INTRODUCTION

IT has been generally believed that infra-red spectra of molecules at very low temperatures would be of great interest in the problem of interpretation. At very low temperatures the system is in its ground state, and transitions from thermally-agitated states are absent, thereby clarifying the spectrum. The well-established theory of the structure of absorption bands of molecules in the gas phase predicts a band would be composed of only few lines, if it were possible to observe them with the gas at a very low temperature, instead of the several hundred or thousand lines present at room temperature. In the laboratory it is, of course, impossible to observe gaseous spectra at low temperatures because of the contingent extremely low vapor pressures and consequent requirement of astronomical path lengths for appreciable absorption. One is forced, therefore, to observe low temperature spectra of molecules in the solid state, which, although affording new information about the solid state, is disadvantageous in the study of molecular structure because of the attendant mutual perturbations of the closely packed molecules. Nevertheless, many of the modifications of infra-red spectra introduced by the condensed phase have been considered to be of second order, especially from the point of view of molecular vibrations. In general, the liquid and solid have nearly the same infra-red bands as the gas, sometimes shifted in position, and, of course, always with loss of discrete rotational structure. On the other hand, the conservation of the general envelope of an infra-red band on condensation (as shown in HCl) led[1,2] to the belief that the band was broadened by transitions associated with the basic activation of a vibration frequency, of a nature very similar to rotational transitions in the gas phase. These transitions were supposed[3] to be, in fact, restricted rotation, if not in some cases, free rotation, the various new modes of motions being due to coupling of rotation and translation modes of the molecule in the gas. On the strength of this similarity in position and width between bands of the gaseous and condensed phases, it was expected that considerable sharpening and intensifying of infra-red bands of material in the solid phase should occur at very low temperatures.

EXPERIMENTAL

In addition to the work of Hettner[1] on HCl at 20°K several workers have designed equipment[4] and recorded spectra at the temperature of liquid nitrogen.[5–7] Raman spectra have been obtained at liquid-hydrogen temperatures (14°K)[8,9] and ultra-violet spectra have been obtained at liquid-helium temperatures.[10] To date no infra-red spectra have been reported at extreme low temperatures, and we believe that those reported here are the first spectra to have been taken at 4°K.

A low temperature transmission cell has been developed for use with liquid helium. This cell, which will be described in a publication in the near future, has the following features.

(1) The sample is mounted in a chamber through which infra-red can be passed so that the conventional transmission is measured. This avoids possible difficulties arising in reflection cells used hitherto, due to high reflectivities[11,12] in regions of high absorption.

---

* This paper was presented at the sixth meeting of the Division of High-Polymer Physics, American Physical Society, New York City, January 27–29, 1949.

[1] G. Hettner, Zeits. f. Physik **89**, 234 (1934).

[2] W. West, J. Chem. Phys. **7**, 795 (1939).

[3] See for example, G. Herzberg, *Infrared and Raman Spectra of Polyatomic Molecules* (D. van Nostrand Company, Inc., New York, 1945), p. 531 ff.

[4] H. Rubens and G. Hertz, Ber d. Berl. Akad. **1912**, 256.

[5] G. K. T. Conn, E. Lee, G. B. B. M. Sutherland, and C. K. Wu, Proc. Roy. Soc. **A176**, 484 ff. (1940).

[6] W. H. Avery and C. F. Ellis, J. Chem. Phys. **10**, 10 (1942).

[7] W. H. Avery and J. R. Morrison, J. App. Phys. **18**, 960 (1947).

[8] A. Prikhotko, J. Phys. (USSR) **8**, 257 (1944).

[9] I. Rodnikova, J. Phys. (USSR) **10**, 236 (1946).

[10] J. F. Scott, R. L. Sinsheimer, and J. R. Loofbourow, Science **107**, 302 (1948).

[11] C. W. Price and T. S. Tetlow, J. Chem. Phys. **16**, 1157 (1948).

[12] H. O. McMahon, in press.

(2) The chamber in which the sample is mounted traverses a container which can be filled with liquid helium, the assembly being supported in a vacuum. The sample cell is sealed with silver chloride windows, which remain vacuum tight on cooling to 4°K. The cell contains helium gas which maintains the sample at the temperature of liquid helium, by heat transfer to the walls of the cell, which are in actual contact with the liquid.

(3) A small tube connects the sample cell to a pressure gauge. This assembly constitutes a gas thermometer by which the temperature of the gas actually bathing the sample is measured.

(4) The sample cell and helium container are suspended in a shell with salt windows at the appropriate level. The whole assembly can be set into the light path of a Perkin-Elmer spectrometer, without modification of the optics.

RESULTS

The infra-red spectra of films of a few polymers, polythene, rubber, polystyrene and polyvinyl chloride have been obtained at 4°K. Figures 1–3 give these data in percent absorption *versus* wave number. A modified Perkin-Elmer model 12B spectrometer was used, with direct current amplification with a Leeds and Northrup HS galvanometer. An automatic slit drive gives the actual trace directly in percent absorption. Figures 1–3 are reproduced directly from the experimental curves, with small (less than 10 percent) corrections for drift.[12a]

The most striking result is that for the most part the changes in the spectra of polymers on cooling are surprisingly small. In no case did absorption peaks disappear, although undifferentiated absorption between peaks does on the whole vanish. Furthermore, no new peaks appeared. With a few important exceptions the widths of the bands did not decrease markedly. The absence of a marked narrowing is not due to lack of sufficient resolving power of the system. The resolution was measured experimentally from the spectra of water, ammonia and acetylene in the gas phase. It agreed very well with values calculated from the refractive index of sodium chloride and the dimensions of the apparatus, and is as good as the best resolving power published for this equipment. The effective slit width in wave numbers is indicated in the figures and is of the order of 4 cm^{-1}. A few data, in small regions, were obtained under special conditions with slit widths of 1 cm^{-1} as indicated in Fig. 1. The slit widths are in general less than the width at half height of the bands so that we can definitely conclude that most bands of polymers are not less than 4 cm^{-1} wide at 4°K.

[12a] Bands of CO_2 and H_2O at 2350, 1500, and 670 cm^{-1} are superimposed on the data.

Polythene

In certain crystalline materials we have observed narrowing of bands, using the same experimental technique as was used for the polymer studies. For the one crystalline polymer examined, namely polythene, we find one band which does, in fact, show the sharpening characteristic of the crystalline materials in contrast with the other polymers which were certainly amorphous. The absorption of polythene at 720 cm^{-1} has two components. The one at 730 cm^{-1} becomes very sharp on cooling to 4°K. The width at half height is equal to that of the narrow slits used in this case, namely 1 cm^{-1} (Fig. 1). Thus this band may be intrinsically extremely sharp at 4°K. Its companion at 715 cm^{-1} remains unchanged in half width on cooling. Thus, extreme low temperatures differentiate the two components of this band, and should give some clue to their interpretation.

The frequency 720 cm^{-1} has been associated[13] with a CH_2 mode. This might be either parallel to or perpendicular to the direction of the carbon chain. The appearance of two components tentatively suggests both motions are present. The fact that one component behaves on cooling as if it were in a crystalline field, whereas the other does not, suggests further that the known formation of crystallites in polythene has an effect on one motion and not on the other. The crystallites in a polymer probably are not regions of perfect orientation but rather of alignment of chains with little orientation of a chain in a plane perpendicular to the direction of the chains. This is a reasonable conclusion from the x-ray work of Baker and Fuller[14] in polyethylene adipamides. Thus, one might expect the wagging of all CH_2's in the direction of the chains, to be in nearly identical fields due to organization by crystallite formation. The other motion occurs in non-oriented directions (perpendicular to the chain) of the crystallite and thus each CH_2 is in a different field. The first should behave like a frequency in a crystal on cooling and become sharp whereas the other should behave like a frequency in amorphous materials.

This explanation is not supported by the observations with polarized radiation,[15] in which one component of this band was observed to disappear when the radiation was parallel to the chains. The motion associated with this region is, therefore, the wagging of hydrogens across the chain. It is not clear whether it is the component at higher or lower frequency which disappears. If we assume the

[13] G. B. B. M. Sutherland and N. Sheppard, Nature **159**, 739 (1947).

[14] W. O. Baker and C. S. Fuller, J. Am. Chem. Soc. **65**, 1120 (1943).

[15] A. Elliott, E. J. Ambrose, and R. B. Temple, J. Chem. Phys. **16**, 877 (1948).

disappearing component is the higher frequency, which becomes sharp on cooling, it is the wagging across the chain which is in an oriented field, in contrast with the discussion above. Probably the crystallites in polythene, due to the packing of zig-zag chains, orient all atoms in the locality, not only in the direction of the chains but perpendicular to them.[16] So the above suggestion, that only chains as a whole are aligned, would not apply to polythene. In this event, the CH_2 wagging in the direction of the chain (if this is a normal mode) should also become sharp. It appears then that the broad band is not due to the latter motion.

On the other hand, it would be very difficult to assign the broad band to any type of motion other than that assigned to the sharp band, because the infra-red spectrum of polythene between 650 and 4000 cm^{-1} has only three regions of absorption. It would be too much of a coincidence to expect two different frequencies to be within 4 cm^{-1} of each other when other active frequencies are separated by the order of a thousand wave numbers.

Elliott, Ambrose, and Temple suggest the broad band seen with radiation polarized parallel to the chain is a motion in amorphous regions of the material. This agrees with the lack of sharpness at 4°K. However, at first sight, it cannot be attributed to the same motion as the sharp band (perpendicular CH_2 wagging), because one cannot then explain how the width of the broad band, assumed to be due to perturbations, can be less than the separation of these two frequencies at all temperatures. If the broadness is due to the variety of environments in amorphous regions, a broad band would be expected, but centered at (or at least continuously connected with) the sharp band. It is difficult to see, in general, how the lack of orientation would shift the frequency (separation of components) more than it perturbs the width of the band.

However, perhaps the environment of the amorphous regions does not form a continuous series of departures from the orientation in crystallites. The crystallites of polythene consist[16] of linear zig-zag configurations, where all C−C bonds are *trans-* to the penultimate one.[17] The amorphous region may not consist of a continuous series of displacements of random magnitudes from the *trans*-configurations. Perhaps there are only discontinuous deviations from the zig-zag configuration, caused by the energy barrier for rotation around a C−C bond. Thus, the non-crystalline parts may be caused by the occurrence of a *cis*-configuration along the chain. We can certainly expect a finite difference between the CH_2 wagging frequency in a *cis-* and in a *trans*-configuration of the order of magnitude observed. Thus, we can account for the separation of the two components. According to the above argument, the motions of CH_2 in *cis*-configurations can only occur in amorphous regions of the ma-

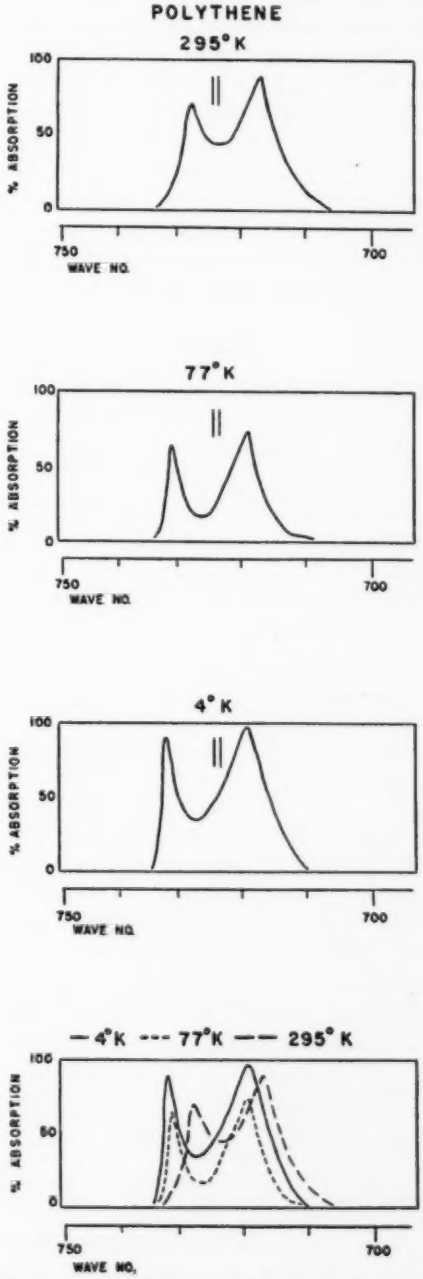

FIG. 1. Infra-red absorption spectra of polythene near 720 cm^{-1} with a 1 cm^{-1} slit width and at 295°K, 77°K and 4°K.

[16] C. W. Bunn and E. V. Garner, Proc. Roy. Soc. (London) A189, 39 (1947).

[17] The terms *cis-* and *trans-* in the following discussion refer to rotational isomerism around a single bond, where the direction of a third C−C bond connected to two already formed can only lie in one of three possible directions, of tetrahedrally directed valence bonds, rather than on a cone of continuous variation in angle. There is increasing evidence in the literature that such a restriction occurs in hydrocarbons rather than entirely free rotation. The *trans*-direction is sterically different from the *cis-*, of which there are two. In the *trans*-configuration all three C−C bonds are coplanar. This configuration may be favored energetically, accounting for the crystallization in polythene below 400°K.

terial. This accounts for the fact that the band remains broad at extreme low temperatures.[18]

Triglycerides, with long chains, have similar absorption at 720 cm^{-1}, although a third component is present at a higher frequency. This band becomes weaker and loses its structure in melting as occurs in polythene.[15] On cooling to 4°K the middle component becomes sharper.

The peak of the sharp band of polythene shifts by $4._4$ cm^{-1} on cooling; from $727._6$ cm^{-1} at 300°K to $732._0$ cm^{-1} at 4°K. The peak of the broad band shifts only by $1._9$ cm^{-1}, from $717._2$ cm^{-1} to $719._1$ cm^{-1}. The difference in shift is in part due to the change in amount of overlapping of the two bands, caused by the sharpening of the one. The positions of both peaks shift to higher frequencies, the amount being of an order of magnitude consistent with the thermal contraction of the solid. The difference in the shifts may support the above interpretation, since the effect of thermal contraction in the less dense amorphous regions can be expected to be less than in crystalline regions, so that the broad band shifts less than the sharp one.

Rubber

The sample of rubber was unstretched and frozen rapidly so it did not contain crystallites. No very sharp peaks are to be seen in the spectrum at 4°K as shown in Fig. 2. On the other hand, rubber passes through its brittle point at 200°K. This has been considered as a second-order transition point, the change in physical properties being explained by a loss of rotational and librational motion. This phenomenon, if it occurs, is not revealed in the infra-red spectrum on cooling. The width of polymer bands does not seem to be primarily determined by rotational and librational modes activated in absorption by a molecular vibration.

The absence of marked changes in the infra-red spectrum on passing through the "brittle point," or "glass-transformation interval," is in agreement with Kauzmann's[19] point of view that the glassy state (developed in rubber at very low temperature) involves inaccessibility of configurations in phase space rather than of momenta, because transitions between states of different momenta (i.e. acoustic waves) do not seem to be affected.

Some of the peaks in the rubber spectrum stand out more clearly on cooling. This is caused by reduction in absorption between peaks. This absorption may be due to rotation and libration of low frequencies, which, however, apparently are not important in the main part of the bands. This effect of cooling improves the resolution of the bands in the spectrum and enables their position to be more definitely stated. It also has the effect of differentiating bands which normally might be grouped together, and of isolating peaks from regions of amorphous absorption.

Polystyrene

Polystyrene is completely amorphous and at 300°K is already below its brittle point. The spec-

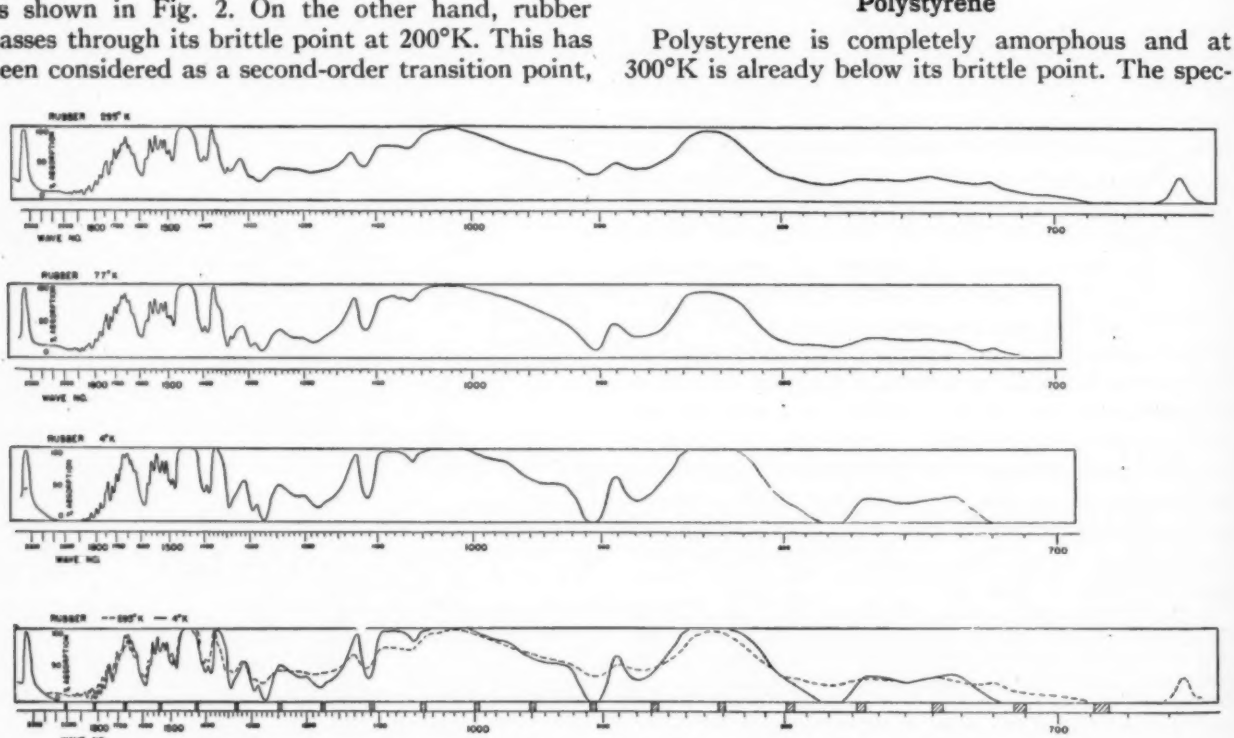

FIG. 2. Infra-red absorption spectra of rubber at 295°K, 77°K and 4°K.

[18] According to D. W. E. Axford and D. M. Rank, J. Chem. Phys. **17**, 430 (1949), the CH_2 wagging in the *trans* rotational isomer of *n*-butane in the solid state occurs at 732 cm^{-1}, in agreement with our interpretation.

[19] W. Kauzmann, Chem. Rev. **43**, 219 (1948), especially p. 234.

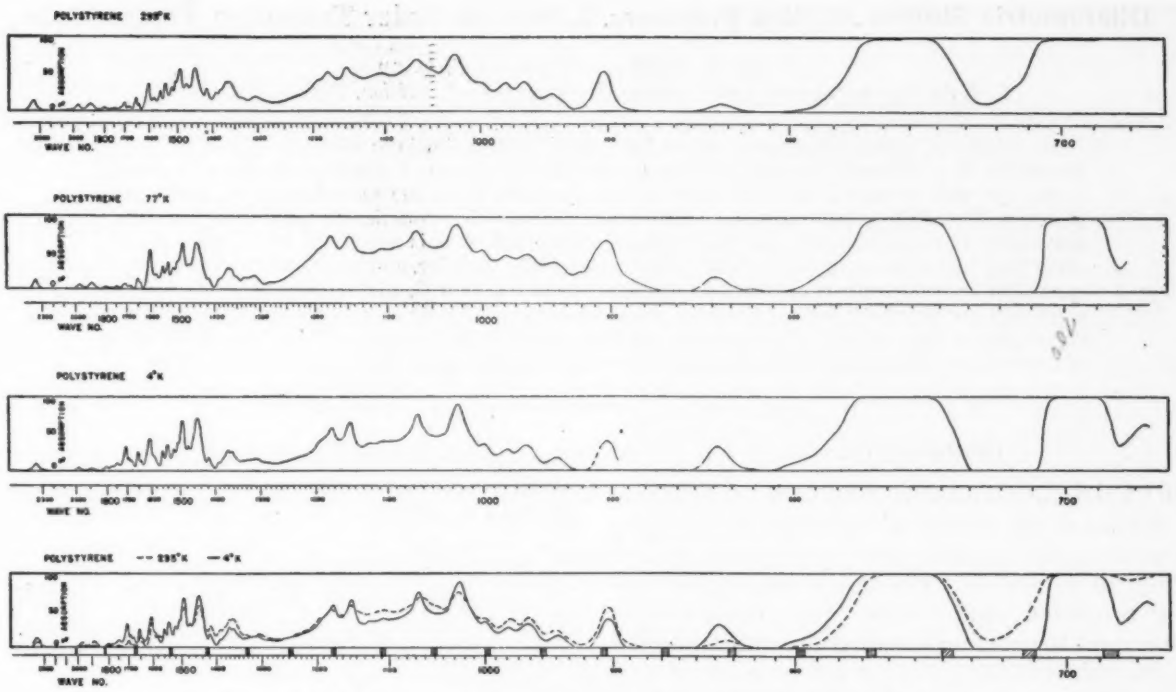

FIG. 3. Infra-red absorption spectra of polystyrene at 295°K, 77°K and 4°K.

trum of polystyrene, therefore, defines the changes to be expected in a completely amorphous polymer. The changes observed, see Fig. 3, are not large and have not yet served to interpret the spectrum. The low frequency band at 700 cm^{-1} shows a curious behavior. Unfortunately our samples were too thick to study the effect of cooling properly, but the steepening of the sides suggests some sharpening. This is probably related to the CH_2 wagging discussed in polythene. The strong broad band at 750 cm^{-1} appears to have widened on cooling at 4°K with slits 4–5 cm^{-1} wide.

Polyvinyl Chloride

The spectrum of this material has been observed and no striking changes were observed.

SUMMARY

The effect of cooling does not have the same effect on all bands in a spectrum and hence will be an aid in the interpretation in polymer spectra when there is a little internal evidence for the assignment of frequencies.

Cooling increases transparency between peaks, allowing more precise determination of their position. In several instances this serves to isolate bands from regions of amorphous absorption. Bands also seem to be characterized by the shape of the envelopes at low temperatures.

In the one case of a partially crystalline polymer, polythene, one band became very sharp. This is one of the components of absorption of 720 cm^{-1} attributed to CH_2 wagging. The contrast of this sharpening with the neighboring component which remains broad can be used to interpret this part of the spectrum.

CONCLUSIONS

It would appear from these data that the band widths of the vibration bands in the solid phase are not due to the widening by superimposed internal rotations but are due to transitions that occur equally well at room as at liquid-helium temperatures. It would also appear that the band widths of infra-red absorption bands are not a simple function of the absolute temperature and, while there is a tendency to narrow on cooling, a widening is also possible. It is, of course, possible that "rotational" and librational structure disappear at the same time that broadening occurs, caused by increased perturbations of the ground state.

The spectra at 4°K lend support to the view that infra-red absorption bands in a condensed phase are due to a quantized increase in energy of a restricted locality in the condensed phase (or, in the case of polymers, in the molecule), consisting for the most part of a bond vibration or deformation. These motions are not associated with many simultaneous changes in the quantum number of degrees of freedom such as acoustic waves, corresponding to rotations in the gas. The band widths are directly related to the statistical distribution of the absorbing group of bonds in a variety of environments.

Dilatometric Studies of High Polymers. I. Second-Order Transition Temperature

HARRY J. KOLB AND EMMETTE F. IZARD
E. I. du Pont de Nemours and Company, Rayon Technical Division, Buffalo, New York

By means of a density balance, the relationship between intrinsic viscosity and dilatometric properties is established for polyethylene terephthalate. The most pronounced property change associated with increasing intrinsic viscosity was observed to be the second-order transition temperature. The relationship between crystallinity and dilatometric properties is presented for 3 aromatic polyesters. In every case, increased crystallinity in the polymers is associated with higher second-order transition temperatures, larger transition range, higher density, and lower volume coefficients of expansion. Second-order transition temperatures, densities at 0°C, and volume of coefficients of expansion are presented for a number of polyesters and vinyl polymers to illustrate the effects of chemical structure as well as physical state on these dilatometric properties. Illustration of the effect of copolymerization on second-order transition temperatures is made with a copolyester system.

INTRODUCTION

PREVIOUS investigations have indicated the usefulness of dilatometry as a method of measuring the second-order transition temperature and crystallization of a polymer. The importance of second-order transition temperatures and crystallization with respect to other polymeric properties prompted this investigation and is reported in a set of two papers. This paper presents density data of polymers with emphasis on the second-order transition temperature, *Tg*, and its significance to the explanations of other properties; the second paper considers the density apparatus as a tool for indirectly measuring the amount and rate of crystallization in polymers and presents data accordingly.

The second-order transition temperature has been treated by a number of investigators and reference is made to a recent review article[1] by Boyer and Spencer which includes an extensive bibliography. The second-order transition temperature appears as a discontinuity in the first derivative of a primary thermodynamic quantity with respect to temperature and is unaccompanied by the usual latent heat which appears in first-order transitions. Several theories for the appearance of *Tg* have been suggested although few have been experimentally substantiated because of the complexity of the problem. Alfrey and Mark[2] indicated that the second-order transition temperature may be associated with the restricting (or freeing) of certain rotational degrees of freedom in polymer chain segments. Alfrey, Goldfinger, and Mark,[3] and Spencer and Boyer,[4] presented evidence that *Tg* was associated with kinetic phenomena and that, at this temperature, the times of the relaxation effects within the polymer are comparable to the time of experimental observation. Such views as these do much to elucidate the mechanism associated with *Tg* in a qualitative manner. The existing state of the theoretical interpretations for second-order transition temperature phenomena in polymers has already been treated adequately and reference is again made to the paper by Boyer and Spencer[1] for an extensive review.

[1] R. F. Boyer and R. S. Spencer, *Advances in Colloid Science*, Volume II (Interscience Publishers, Inc., New York, 1946), pp. 1–55.
[2] T. Alfrey and H. Mark, Rubber Chem. Tech. **14**, 525 (1941).
[3] Alfrey, Goldfinger, and Mark, J. App. Phys. **14**, 700 (1943).
[4] R. S. Spencer and R. F. Boyer, J. App. Phys. **14**, 398 (1946).

EXPERIMENTAL

Apparatus

Densities were measured with the apparatus shown in Figs. 1 and 2. The analytical balance is supported above the constant temperature bath and has a heavy wire crosspiece attached under the left pan on which to fasten a fine wire for suspending polymer plugs. Holes have been drilled under the wire crosspiece through the balance base and supporting table to allow for free suspension of the polymer plug in the thermostat by means of the wire fastened under the balance pan.

The thermostat consists of two parts: (1) an outer bath provided with a thermoregulator (Sargent No. S-81835), heater, stirrer, thermometer, and using dibutyl phthalate, as a liquid heat exchange medium, and (2) an inner bath provided with a stirrer, a thermometer calibrated to 0.1°C against Bureau of Standards thermometers, and containing the suspended polymer plug and Dow-Corning Silicone oil (100 cstks. at 25°C), the density of which has been measured to 1 part in 10,000 over the temperature range of 0 to 100°C. The capacities of the inner and outer baths are 1 l. and 28 l., respectively. During the course of this investigation the silicone oil density was rechecked monthly. The silicone oil was chosen because of low probability of attack on polymer specimens and excellent heat stability.

Procedure

During a run, the polymer plug (convenient size —1″ diameter, 2″ high) is first weighed in air and

then suspended on piano wire to 1" below the surface of the silicone oil in the thermostat. The bath is held at a given temperature until the polymer plug in the silicone oil has reached an apparently constant weight; this "instantaneous" value[5] is obtained within 15 minutes. The temperature is maintained and read to ±0.1°C for these experiments.

After the reading is made, the temperature is raised 5°–10°C and the process repeated. Usually a temperature range of approximately 0°–160°C gives enough points to allow for the calculation of *Tg*. However, this range is obviously determined by polymer type.

Polymer Characterization

The intrinsic viscosities of the polymer samples are determined in the usual manner. A 1 percent solution of polymer in solvent is prepared in a 25-ml volumetric flask, and 10 ml of this solution are transferred to an Ostwald type viscometer which is immersed in a 25°C constant temperature bath. The flow time of the solution is recorded with a stop watch on triplicate runs and the process then repeated on the pure solvent. The viscometer is rinsed with solution or solvent before these runs are made. The relative viscosities, η_r, are calculated from $\eta_r = t_s/t_o$ where t_o and t_s are the flow times of solvent and solution, respectively. The relative viscosities are obtained at different concentrations below 1 percent, and a graph of η_s/c is plotted against c where $\eta_s = \eta_r - 1$ and c = concentration of polymers in g/100 ml of solution. The intrinsic viscosity $[\eta]_0$ is given by $\lim_{c \to 0} \eta_s/c$. The solvent for the polyester determinations is a 60:40 mixture by weight of phenol and tetrachlorethane. The polymer solutions were shown to give linear curves of η_s/c *vs.* c up to concentrations of 1 percent and to conform to the Huggins equation,[6] $\eta_{sp}/c = [\eta]_0 + k'[\eta]_0^2 c$, for the samples of polyethylene terephthalate.

The compositions of the ethylene glycol and diethylene glycol terephthalate interpolymers are determined by a method involving hydrolysis of the polymer to glycol and acid, determination of 1,2 glycol with periodate and finally determination of total glycol by dichromate. This method is similar to that described by Allen and coworkers.[7]

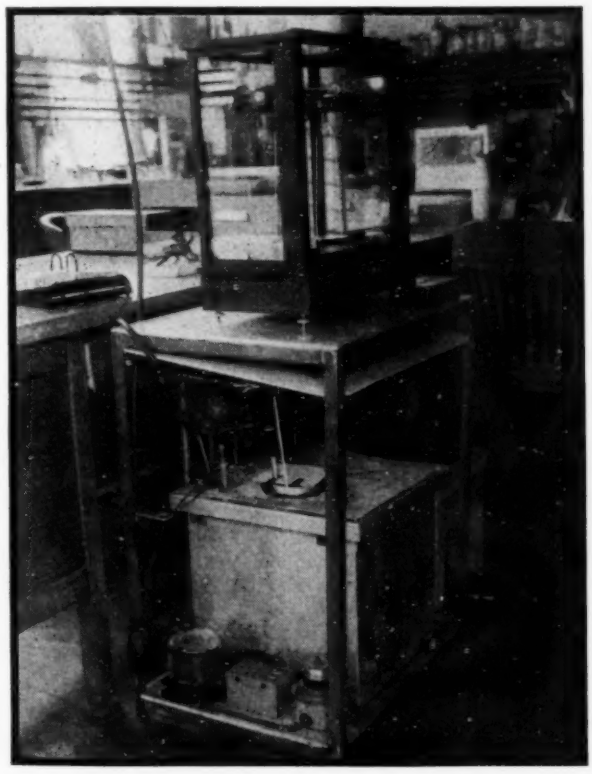

FIG. 1. Density balance.

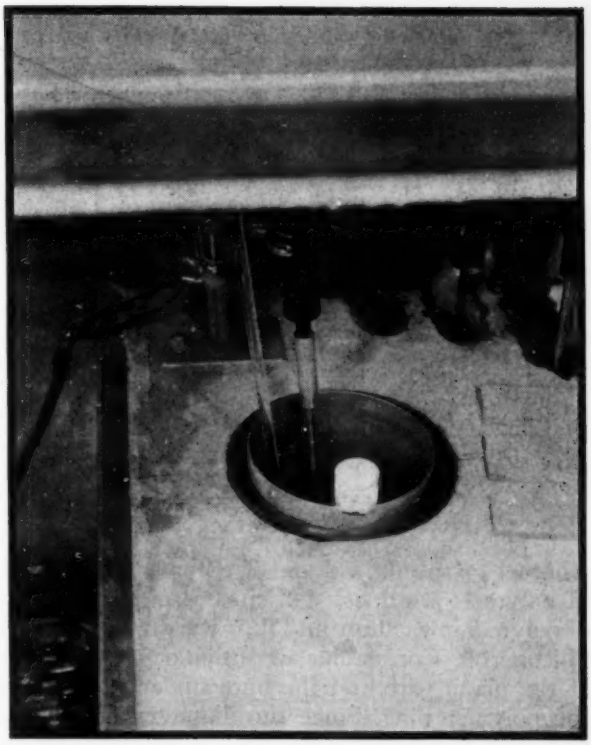

FIG. 2. Inner bath of density balance.

EXPERIMENTAL RESULTS AND DISCUSSION

With the weight of the polymer plug in air and in Silicone oil, calculations of the specific volume

[5] The "instantaneous" weight is analogous to a similar quantity described by R. S. Spencer and R. F. Boyer, J. App. Phys. **17**, 398 (1946). For further explanation, reference is made to this paper.

[6] Maurice Huggins, J. Am. Chem. Soc. **64**, 2716 (1942).

[7] Allen, Charbonnier, and Coleman, Ind. and Eng. Chem. Anal. Ed. **12**, 384 (1940).

TABLE I. Dilatometric data for polyethylene terephthalate samples of varying intrinsic viscosity.

Polymer No.	$[\eta]_0$	Tg	Transition range	ρ_0	$\beta(\times 10^4)$ Below Tg	$\beta(\times 10^4)$ Above Tg
1	0.24	51°C	44°C–56°C	1.4168	1.29	2.83
2	0.28	58	42 –61	1.4013	1.35	2.58
3	0.40	71	66 –76	1.4013	1.37	3.39
4	0.51	84	73 –94	1.3931	1.99	3.94
5	0.61	80	71 –97	1.3966	2.05	3.93
6	0.70	80	70 –88	1.3943	1.88	3.90
7	0.76	81	64 –92	1.3937	1.71	3.94
8	0.64	67	67	1.3390	1.87	9.87

$[\eta]_0$ = Intrinsic viscosity.
Tg = Second-order transition temperature (°C).
ρ_0 = Density at 0°C against water at 4°C in g/ml.
β = Volume coefficient of expansion.

and density were made with the following equation:

$$V_p = \frac{1}{\rho_p} = \frac{W_v - W_s}{W_v \cdot \rho_s},$$

where V_p = specific volume of polymer, ρ_p = density of polymer, ρ_s = density of silicone oil, W_v = weight of polymer in vacuum, and W_s = weight of polymer in Silicone oil. Corrections were made for the weight of the piano wire and the buoyant effect of air on the polymer plug. Since the diameter of the wire was only 8 mils, no corrections were made for the buoyant effect of oil on a 1″ segment below the oil surface and the effect of surface tension of the oil on the wire at the oil-air interface.

Plots of the specific volume against temperature produce curves from which Tg can be obtained. Figure 3 illustrates a typical plot for crystalline polyethylene terephthalate where the intersection of the two linear portions of the curve, defined as Tg, occurs at 80°C. The volume coefficients of expansion are calculated from the slopes of the linear portion of the curves and are given by

$$\beta = \text{Slope}/V_0,$$

where β = volume coefficient of expansion and V_0 = specific volume at 0°C.

Before listing the transition temperatures and other dilatometric data for a number of chemically different polymers it is important to show the relation of intrinsic viscosity and crystallization to the second-order transition temperature since these two physical quantities have an important bearing on transition data. It would be best to prepare chemically different polymers in comparable physical states before discussing differences in their second-order transition temperatures which are supposedly due to chemical structure. This is usually quite difficult (if not often impossible with present methods), and the best one can do under existing circumstances is to *indicate* the possible physical differences. Response of Tg to some of these differences is experimentally verified for polyethylene terephthalate in the following two sections and briefly emphasized to show that Tg as defined and measured is not a singularity depending entirely on chemical composition.

From this point on, any reference to transition temperature should automatically be considered as a second-order transition temperature unless otherwise indicated. It should also be stated that none of the polymers discussed below have oriented chains.

Intrinsic Viscosity Effects

Dilatometric data for polyethylene terephthalate samples of intrinsic viscosities 0.24 to 0.76 as measured in phenol-tetrachlorethane are presented in Table I. The transition range is the section of the curve which lies between the two linear portions of the curve and Tg is the intersection of the extensions of these two linear portions. All of the polymers in Table I exhibit some degree of crystallinity with the exception of polymer 8 which is completely amorphous. This fact bears on the following intrinsic viscosity-transition temperature discussion and prevents exact correlation because of the interference of the various degrees of crystallinity in the polymers. Nevertheless, the increasing intrinsic viscosity of polyethylene terephthalate is associated with an increasing transition temperature. The table indicates that Tg increases with $[\eta]_0$ up to a value of approximately 80°C for 0.51

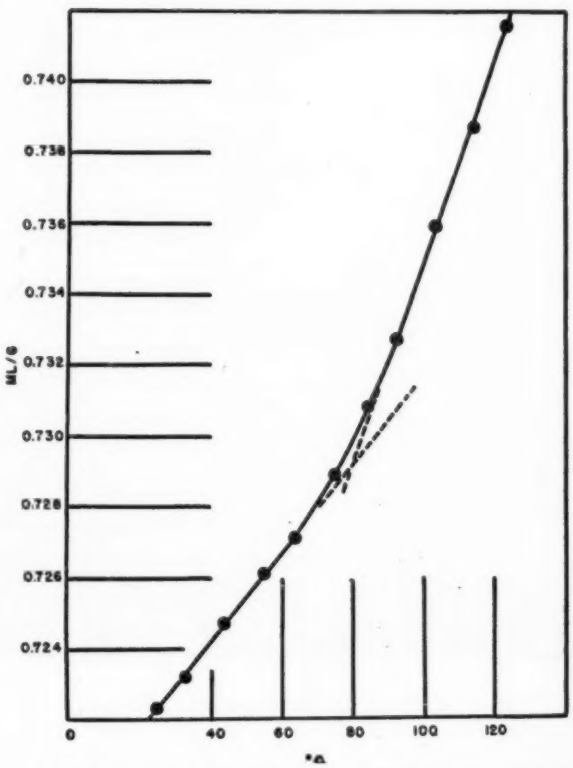

FIG. 3. Specific volume *vs.* temperature of crystalline polyethylene terephthalate.

intrinsic viscosity. Above this viscosity, the transition temperature appears to remain fairly constant. This same effect was noted by Jenckel and Überreiter[8] for polystyrene. If Tg is assumed to originate from flow of segments and molecules, it is not surprising that Tg increases with $[\eta]_0$. Above a certain $[\eta]_0$, the segment motions possibly take over entirely and operate as units of, say, 50–100. This could explain the upper Tg level of 82°C that is evident with polyethylene terephthalate. The polymers in Table I are whole polymers and definitely have molecular weight distributions which further complicate the picture. However, one important point can be made on the basis of the above discussions. When we compare second-order transition temperatures among different polymers, molecular weight has a pronounced bearing on the values quoted, and it is therefore best to attempt a correlation of Tg values above the $[\eta]_0$ where Tg becomes constant. However, this entails a rather large program of determining Tg *vs.* $[\eta]_0$ curves for every polymer and which may be more than the investigator deems advisable for the purpose in mind. In such cases, it seems reasonable to choose polymers of a high molecular weight in order to make more probable a Tg which is in or near the leveling-off section of Tg *vs.* molecular weight (or intrinsic viscosity) curve.

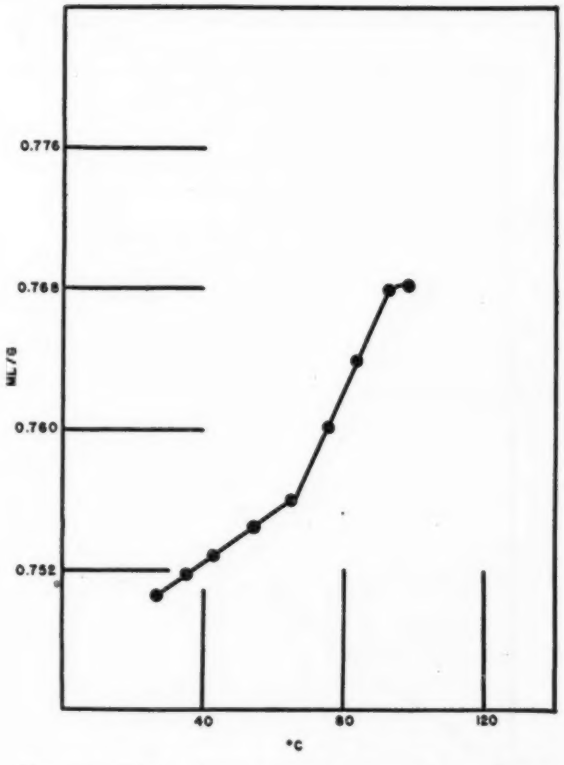

FIG. 4. Specific volume *vs.* temperature of amorphous polyethylene terephthalate.

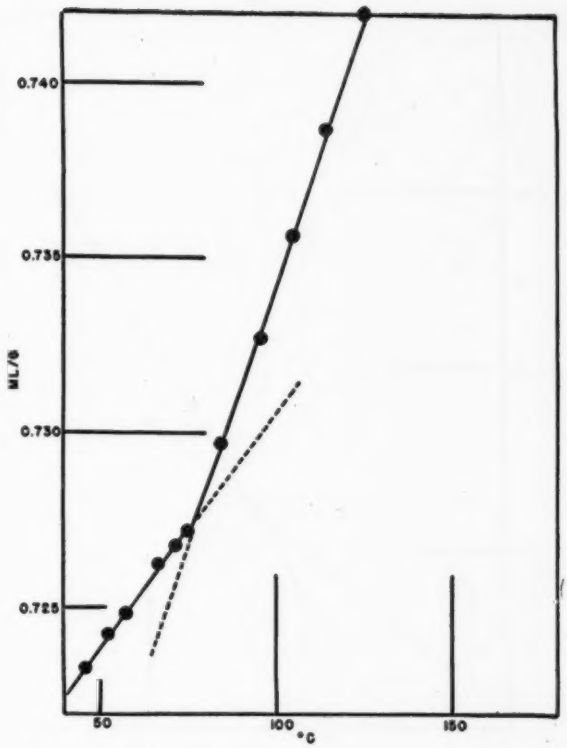

FIG. 5. Specific volume *vs.* temperature of amorphous polyethylene 1,5 naphthalate.

Effect of Crystallinity

Some polymers are capable of crystallizing, and the number and size of these crystallites have pronounced effects on the second-order transition temperature and dilatometric quantities. Some of these effects can be shown more clearly with reference to Table I. It will be noted that the density of polyethylene terephthalate increases inversely as the intrinsic viscosity. Since the molecules have lower viscous forces to overcome as they become smaller, it is understandable that they should pack better and crystallize more because of this easier movement. This explanation assumes the same treatment for all the polymers when cooling from the melt to room temperature. Polymer No. 8 is completely amorphous (x-ray) and exhibits the lowest density. The coefficients of expansion (β) of the polymers give some indication of crystallinity effects especially above the transition temperature. The amorphous polymer expands approximately 2.5–3 times the amount of partially crystalline polymers above Tg. The transition temperature and transition range are markedly affected by crystallinity; both increase as crystallinity increases. If crystal motion as well as segment and molecule motions are presumed to account for Tg, one would

[8] E. Jenckel and K. Überreiter, *Zeits. f. physik. Chemie* **A182**, 361 (1938).

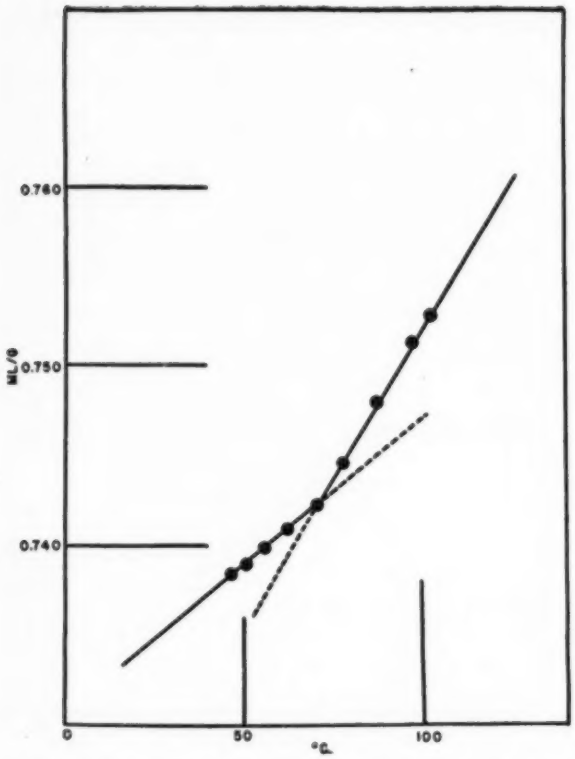

FIG. 6. Specific volume *vs.* temperature of crystallines polyethylene 1,5 naphthalate.

expect both *Tg* and transition range to increase with crystallinity. As crystallites increase in number and size, motion should become increasingly difficult within the polymer and the thermal energy necessary for the break at *Tg* would necessitate higher temperatures (or longer times—see next section). For example, the transition temperatures of amorphous polyethylene terephthalate (II), polyethylene 1,5 naphthalate (VII) and polyethylene 2,6 naphthalate (IX) are 67°, 71°, and 113°C, respectively. After the polymers are crystallized, the transition temperatures of the first two are 81° and 78°C, respectively, indicating the upward shift in *Tg* caused by crystalline material. The dilatometric curve of crystalline polyethylene 2,6 naphthalate (VIII) shows no break at all over the experimental temperature range, and comparison of *Tg* for crystalline and amorphous material is therefore impossible until the experiments can be extended.

As indicated above, the transition temperature range also becomes larger with increasing crystallinity, and the difference between the slopes of the linear portions diminishes. An inspection of Figs. 3–8 illustrates this difference. Figures 4, 5 and 7 are the specific volume-temperature curves for the amorphous polymers mentioned above, i.e., II, VII, and IX. In each case the break in the curve occurs at a single temperature, or over a short range. After crystallization, the dilatometric curves of the polymers are given in Figs. 3, 6, and 8, respectively. For polymer IX, crystallization has broadened the transition temperature into a range (polymer VIII) where it becomes impossible to pick out any linear portion within the working temperatures of this investigation.

The reason for the effect of crystallites on the transition temperature can be rationalized by the viscous flow and viscoelastic pictures. The motions of chain segments which presumably cause the appearance of *Tg* will be slowed down by the presence of "chunks" of crystallite material. As the crystallization proceeds the material will find it more difficult to move. This will cause the transition range to become broader and broader, the ultimate of which would be complete crystallization where *Tg* and the *Tg* range (as defined) may no longer exist. This is the same as stating that amorphous material is a necessary condition for *Tg* but that size, shape, and number of crystallites will alter the experimental value. Enough amorphous material must be present to act as a lubricator for the crystallites.

Time Effects

Several remarks were made concerning the viscous flow theory and relaxation time theory for the appearance of *Tg*. Spencer and Boyer[3] have shown that if the transition occurs at the temperature where the times of experimental observation are of

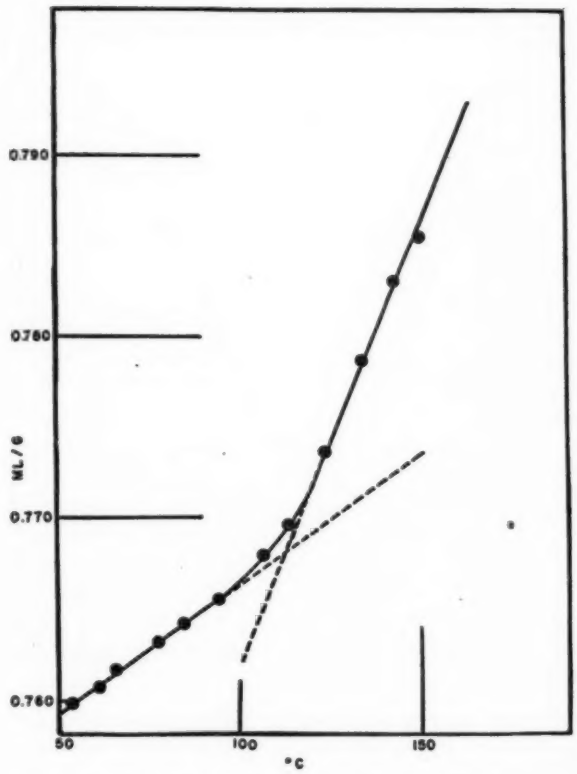

FIG. 7. Specific volume *vs.* temperature of amorphous polyethylene 2,6 naphthalate.

TABLE II. Dilatometric data for a series of ester and vinyl polymers.

Polymer	Code	Tg	ρ_0	$\beta(\times 10^4)$ Below Tg	$\beta(\times 10^4)$ Above Tg	$[\eta]_0$
Polyesters						
Ethylene glycol/terephthalic acid (Cryst.)	I	81°C	1.3937	1.71	3.94	0.76
Ethylene glycol/terephthalic acid (Amorph.)	II	67	1.3390	1.87	9.87	0.64
Ethylene glycol/hydrog. terephthalic acid	III	<25	1.2187[b]	—	—	0.75
Ethylene glycol/isophthalic acid	IV	51	1.3596	1.30	5.24	0.75
Ethylene glycol/1,4-naphthalic acid	V	64	1.36	1.74	4.92	0.52
Ethylene glycol/1,5-naphthalic acid (Cryst.)	VI	78	1.39	1.85	4.09	0.48
Ethylene glycol/1,5-naphthalic acid (Amorph.)	VII	71	1.37	2.14	4.70	0.48
Ethylene glycol/2,6-naphthalic acid (Cryst.)	VIII	ind.[a]	1.345	—	—	0.57
Ethylene glycol/2,6-naphthalic acid (Amorph.)	IX	113	1.33	1.87	6.46	0.57
Ethylene glycol/2,7-naphthalic acid	X	119	1.35	1.51	6.74	0.56
Ethylene glycol/bis-p-carboxyphenoxybutane	XI	53	1.2973	2.23	4.21	0.75
Hexamethylene glycol/bibenzoic acid	XII	ind.[a]	1.2699	—	—	0.64
Diethylene glycol/bibenzoic acid	XIII	80	—	—	—	0.66
Diethylene glycol/terephthalic acid	XIV	<25	—	—	—	
Polyvinyls						
Lucite (heat resistant)	XV	100	1.1955	2.28	5.56	
Lucite (boilable sheeting)	XVI	96	1.1945	1.80	5.47	
Lucite (5% plasticized)	XVII	78	1.1942	2.87	6.03	
Polystyrene	XVIII	88	1.0573	2.18	6.47	
Polyacrylonitrile	XIX	87[b]	1.1783	1.39	2.95	
Polyacrylonitrile (5% styrene)	XX	69	1.1777	1.56	2.70	
Polythene	XXI	<25	0.9320	—	—	
Teflon	XXII	None from 25–160	2.1968			

T_g = Second-order transition temperature (°C).
ρ_0 = Density at 0°C against water at 4°C in g/ml.
β = Volume coefficient of expansion.

[a] Transition temperature is indeterminate because of extreme crystallinity. See explanation in body of this paper.
[b] There is evidence by other investigators that T_g is higher. See explanation in body of this paper.

the same order as the relaxation time spectra, then Tg should vary with time of measurement. By extending measurements of specific volume at each temperature to periods of a day or more, they found that the transition temperature of polystyrene was no longer evident above room temperature. With the "instantaneous" readings (10 min. to 30 min.) the transition temperature was approximately 80°C. In this paper, all experimental values were taken shortly after 15 min. and would correspond to the "instantaneous" values. Differences also arise from curves obtained by heating and cooling. In every case below, the curves and extrapolated values are arrived at from data observed with the ascending temperature technique.

Effect of Chemical Composition

The influence of various structural groups within the polymer chain on the second-order transition temperature is most pronounced. To illustrate this a large number of polymers were subjected to a dilatometric analysis. A few of the experiments are represented graphically in Figs. 3–8, and all of the data are summarized in Table II.

There are some interesting comparisons that can be made between the different polymers and the different groups of polymers in Table II. When the polyester II is hydrogenated to III, the transition temperature is found to drop from 67° to well below room temperature. It appears that, for this polyester, the added bulkiness of a hydrogenated ring which tends to restrict rotation cannot offset the very large decrease in interchain attraction. The data for the polyesters of ethylene glycol with terephthalic, 2,6 naphthalic and 2,7 naphthalic acids indicate that increasing the aromaticity by symmetrical substitution will increase the transition temperature. An increase in aromaticity obtained in unsymmetrical fashion, such as for 1,4 and 1,5 naphthalates often lowers the transition temperature. The effect of this symmetrical substitution is further illustrated with diethylene glycol/bibenzoic acid (XIII) and diethylene glycol/terephthalic acid (XIV). Both polymers contain diethylene glycol, but by addition of a second benzene ring to the acid, the transition temperature jumps from <25°C to 80°C.

In the vinyl group, the Lucite samples without plasticizer exhibit Tg's in the neighborhood of 100°C instead of 57°C, which has been quoted elsewhere.[9] It will be seen from Table II that plasticizer, present within the polymer in 5 percent quantities, lowers the transition temperature to 78°C. It may well be plasticizer content or molecular weight differences that account for varia-

[9] F. E. Wiley, *Ind. and Eng. Chem., Ind. Ed.* **34**, 1052 (1942).

TABLE III. Effect of copolymerization of ethylene and diethylene glycol with terephthalic acid on the second-order transition temperature.

Composition		
Mole % [−OCH₂CH₂−O−]	Mole % [−OCH₂CH₂OCH₂CH₂O−]	Tg
97	3	81°C
84	16	77
71	29	50
64	36	46
49	51	34
36	54	31
27	73	<25
4	96	<25

tions in quoted transition values of Lucite. The sample of polystyrene has a transition at 88°C which is somewhat lower than that for Lucite but higher than the 81–82° value that other investigators[8–11] have obtained for their polystyrene samples. However, an explanation similar to that for Lucite may apply here as well.

Although the transition temperature for polyacrylonitrile is listed in Table II as 87°C, there were several observations made at the time of the experiments and from the dilatometric data, which bear on this value. If the polymer was heated above 130°C it became opaque, not completely through the plug but at the center. This effect was not noted below 130°C. It cannot be attributed to crystallization since x-ray analysis shows no structural change. Above the transition temperature, other polymers usually became soft enough to deform with the hand; polyacrylonitrile did not. The volume coefficients of expansion above Tg are roughly ½ the magnitude for other vinyl polymers. All these deviations from the normal behavior as shown by polyacrylonitrile tend to cloud the picture. Yet the dilatometric curves are quite reproducible. Lanzl[12] by another technique, has evidence that a transition temperature exists above 125°C but none in the neighborhood of 87°C.

The curves for polythene gave no break associated with a second-order transition temperature above room temperature. The deviations from linearity above 60°C are associated with a first order transition[13] rather than second. There was no indication of a transition temperature for Teflon between 25° and 160°C. Whether one exists above or below this range is a matter of speculation, but considering the characteristics of the polymer, one might favor the temperatures above 160°C.

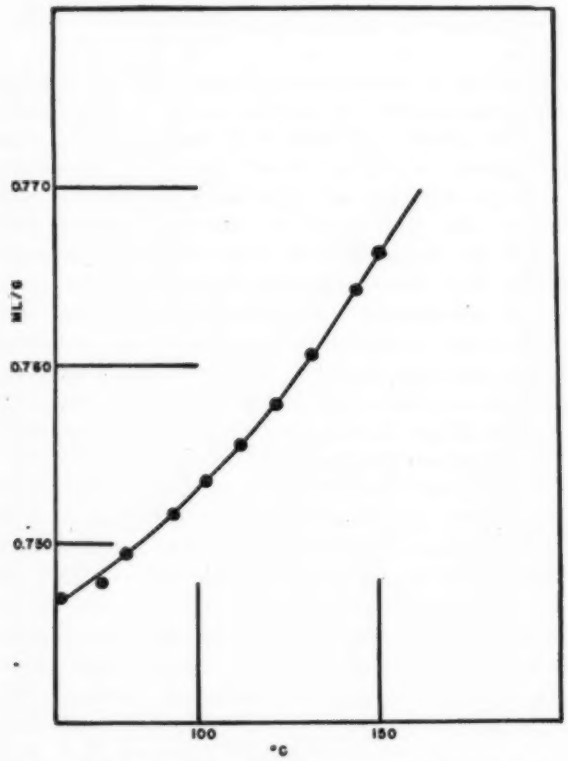

FIG. 8. Specific volume *vs.* temperature of crystalline polyethylene 2,6 naphthalate.

[10] W. Patnode and W. Scheiber, J. Am. Chem. Soc. **61**, 3449 (1939).
[11] R. F. Boyer and R. S. Spencer, J. App. Phys. **15**, 398 (1944).

Effect of Interpolymerization

The transition temperature of polyethylene terephthalate polymer dropped from 81°C to below room temperature by changing ethylene glycol to diethylene glycol in the polymer. The additional length of the diethylene glycol (with its odd number of carbon and oxygen atoms) has decreased the number of terephthalic groups which are presumably responsible for the high *inter*molecular forces in polymer II and has also added ether oxygen to the glycol which offers less restricted rotational motion than carbon-carbon bonds and consequently lowers *intra*molecular forces; the effect is therefore cumulative in the Tg for polymer XIV. Interpolymers of these two glycols and terephthalic acid were analyzed dilatometrically to determine the nature of the composition-transition temperature curve for this specific condensation polymer system. Investigations of this type have been carried out by other workers for vinyl systems such as styrene-isobutylene,[11] styrene-butadiene,[14] styrene-methacrylate,[15] and vinylchloride-vinylidene chloride.[16] The transition temperature data for polyethylene and diethylene terephthalate interpolymers are listed in Table III.

The transition temperature decreases as the diethylene glycol content increases but the curve is not characterized by any simple relation. Part of

[12] G. F. Lanzl, unpublished data.
[13] E. Hunter and W. Oakes, Trans. Faraday Soc. **34**, 282 (1938).
[14] K. Überreiter, Zeits. f. angew. Chemie **53**, 247 (1940).
[15] E. Jenckel, Zeits. f. physik. Chemie **A190**, 24 (1941).
[16] R. F. Boyer, Can. Chem. Process Ind. (August, 1944).

the complexity arises from the dependence of crystallinity on composition. Pure polyethylene terephthalate is quite crystalline when cooled from the melt under normal conditions to room temperature; pure polydiethylene terephthalate has never been made crystalline at room temperature according to present knowledge. Therefore interpolymers contain different degrees of crystallinity depending on composition and rate of cooling, and the latter influence Tg accordingly. The curves of Boyer[16] for vinyl chloride-vinylidene chloride are probably influenced by crystallinity in a similar manner. For this investigation, it is assumed that each polymer contains a statistical distribution of ethylene glycol and diethylene glycol units throughout the polymer. The interpolymers are not blends of two polymers but are prepared from acids and mixtures of the two glycols.

The addition of 5 percent styrene to acrylonitrile resulted in a polymer with a transition temperature of 69° and considerably lower than the quoted value of 87°C for pure polyacrylonitrile. In this case, both pure polymers have higher transition temperatures than the interpolymer. Enough heterogeneity has been produced by the styrene monomeric units in the chains and molecular network of the polymer to lower the transition temperature. This is more probably an *inter*molecular effect rather than *intra*molecular.

The authors wish to acknowledge the service that a number of people within the du Pont Company have given to us.

Dilatometric Studies of High Polymers. II. Crystallization of Aromatic Polyesters

HARRY J. KOLB AND EMMETTE F. IZARD
E. I. du Pont de Nemours and Company, Rayon Technical Division, Buffalo, New York

By means of both a density balance and gradient tube, experimental density data are obtained to illustrate the thermal crystallization behavior of 3 aromatic polyesters at temperatures from 90°C to 150°C. The data are discussed with reference to both amount and rate of crystallization and density curves are presented to show qualitative similarity between kinetics of polymer crystallization and the kinetics of chemical reactions. From the experimental data, a temperature, for convenience labeled the minimum crystallization temperature, is described and is shown to be 30° to 50° above the second-order transition temperature for the polyesters. In addition to thermal crystallization, data are presented to show that immersion media may initiate crystallization below the minimum temperature associated with thermal crystallization of polymers. Liquids used as immersion media for polyethylene terephthalate were water, methyl alcohol, acetone, benzene, nitromethane, and nitric acid. The last four liquids initiate crystallization of the polymer at room temperature.

INTRODUCTION

THE second of two papers on dilatometry from this laboratory is concerned with a study of crystallization in the linear polyester class of macromolecules, in particular those whose structures contain aromatic groups in the repeating units of the chain. The dilatometric approach to measure qualitatively the rate and amount of crystallization offers a rapid, easy method of obtaining information about the physical state of the polymer. The method has recently been described and used for similar studies on other high polymers by Wildshut[1] and Wood and Bekkedahl.[2]

EXPERIMENTAL

Apparatus

The densities of bulk polymer were obtained with the aid of the density balance described in the previous paper.[3] The densities of monofil and film were measured with a modification of the density gradient tube, originally applied by Linderstrøm-Lang[4] and more recently by Mark *et al.*[5] and Spencer and Boyer.[6] The density gradient tube used in this laboratory was 1 m high and 50 mm in diameter and inserted in a jacket supplied with water from a constant temperature bath at 30.0°C. At the outset the inner tube was filled with carbon tetrachloride ($\rho = 1.59$ g/ml) to the midpoint and toluene ($\rho = 0.86$ g/ml) to a point even with the outlet of the constant temperature jacket. The two liquids were then mixed by methodical shaking until a density distribution existed from top to bottom of the tube. The density range depended upon the amount of mixing performed by the operator.

The density gradient tube was originally cali-

[1] A. Wildshut, J. App. Phys. 17, 51 (1946).
[2] L. Wood and N. Bekkedahl, J. Research Nat. Bur. Stand. 36, 489 (1946).
[3] H. J. Kolb and E. F. Izard, J. App. Phys. 20, 564 (1949).
[4] K. Linderstrøm-Lang, Nature 139, 713 (1937).
[5] Tessler, Woodbury, and Mark, J. Polymer Sci. 1, 437 (1946).
[6] R. S. Spencer and R. F. Boyer, J. Polymer Sci. 1, 249 (1946).

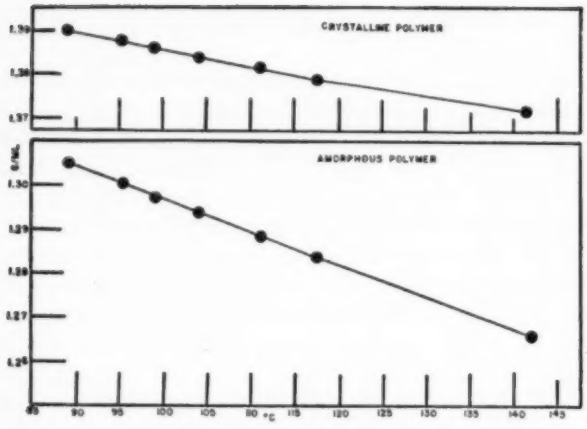

FIG. 1. Density *vs.* temperature of polyethylene terephthalate.

brated with drops of zinc chloride solutions of known density. Ten of these solutions were prepared and their densities measured with a calibrated 25 ml pycnometer at 30.0°C. Then small drops of each solution were added carefully to the tube with an eye dropper. Each drop fell to the level in the tube corresponding to its density. The positions of these salt drops were measured with a cathetometer (to ±0.05 mm) and a height *vs.* density chart was constructed from the data. About 30 colored glass floats were added to the gradient tube before the final chart was constructed. When the positions of the colored floats were recorded, the salt solution calibration allowed for the density determination of each float. After the initial run, the salt solutions were dispensed with and this obviated water diffusion in the toluene-CCl_4 mixtures and the possibility of collision between salt solution and polymer samples. The glass floats were blown from colored tubing and with different amounts of entrained air to allow for a good distribution in the tube. Two sets of floats were calibrated (from two sets of $ZnCl_2$ solutions) to cover a large range (1.00–1.5 g/ml) for general polymer work (30 floats) and a small range (1.33–1.45 g/ml) for polyethylene terephthalate work (15 floats).

TABLE I. Rate of density change of unoriented polyethylene terephthalate in silicone oil.

T(°C)	ρ_A	ρ_C	$\rho_C-\rho_A$	ρ_{22}	k_ρ (×10³)	$\frac{\rho_{22}-\rho_A}{\rho_C-\rho_A}$
89.4	1.3048	1.3900	0.0852	1.3043	0	0.00
95.4	1.3002	1.3877	0.0875	1.3000	0	0.00
99.3	1.2971	1.3861	0.0890	1.3416	9	0.50
104.2	1.2936	1.3842	0.0906	1.3399	22	0.51
111.2	1.2883	1.3817	0.0934	1.3368	56	0.52
117.7	1.2838	1.3791	0.0953	1.3364	130	0.57
141.6	1.2656	1.3702	0.1046	1.3365	650	0.68

ρ_A = density of amorphous polymer from Fig. 1 at temp., T.
ρ_C = density of crystalline polymer from Fig. 1 at temp., T.
ρ_{22} = density of initially amorphous polymer after 22 hrs. at temp., T.
k_ρ = rate constant (g ml^{-1} min.$^{-1}$) for linear section of curve.
Column 7 = fraction of density change after 22 hours.

Procedure

For the rate of crystallization studies of the polymers in Silicone oil, approximately 10 g of amorphous bulk material in plug form ($[\eta]_0=0.62$)[7] were suspended on the density balance in the inner bath containing the silicone oil. The outer bath was heated to the temperature at which rate studies were to be made and maintained at that temperature until completion of the experiment. Polymer density readings were taken at various time intervals throughout the run.

For the rate studies with polyethylene terephthalate in water, the Silicone oil was replaced with distilled water in the inner bath and amorphous unoriented monofil was immersed in the water. The density balance was used only as a thermostat for these runs. During an experiment, monofil samples were removed periodically from the constant temperature bath, tagged, and set aside for density determination in the density gradient tube. When the rate studies were completed at a given temperature, the monofil samples (0.5 cm lengths) were dropped into the gradient tube and allowed to reach an equilibrium level. The fibers reached this level in a very short time; usually they dropped slightly below the equilibrium position and then oscillated about it for a very brief time thereafter. Positions of both the glass floats and fibers were then read with the cathetometer, and with the calibration curve, densities were obtained for all the fibers.

The procedure for rate of crystallization studies of polyethylene terephthalate in acetone, benzene, methyl alcohol, nitric acid, and nitromethane, was similar to that just described. Monofil samples were immersed in the liquids at constant temperature and samples then removed at specified time intervals. Densities of the samples were obtained with the density-gradient tube.

RESULTS AND DISCUSSION

Effect of Temperature on Crystallization of Polyethylene Terephthalate

To illustrate the effect of temperature on amount of crystallization, density figures are used as indicators of the amount of crystallization of polyethylene terephthalate. However, it is understood that any exact data given below are associated with the density parameter and not crystallization. The relationship of density with crystallinity is positive and hence a density increase can be used to indicate crystallinity increase. But the quantitative relationship between density change and crystallinity has not been predetermined. On the basis of this,

[7] See reference 3 for intrinsic viscosity analysis.

discrete values of density will be associated only with trends in crystallization.

The density temperature curves for amorphous and crystalline polyethylene terephthalate have been plotted in Fig. 1 from the data for polymers No. 8 and No. 1, respectively, in Table I of the companion paper.[3] The former data are those for a completely amorphous polymer, but the latter are not representative of a completely crystalline polymer. Failure to obtain data for a completely crystalline polymer is due to the unavailability of either a large perfect crystal of polyethylene terephthalate for dilatometric studies or, an x-ray density and volume coefficient of expansion of the crystal. The density of completely crystalline polyethylene terephthalate at room temperature has been noted with x-rays as 1.46 g/ml in this laboratory and elsewhere,[8] but only a single linear coefficient of expansion along one of the principal directions of the triclinic cell has been measured.[9] Because these data are not available, the most crystalline sample of this investigation has been selected for the preliminary computations reported below.

Proceeding then to the rate of polymer crystallization in silicone oil at various temperatures, results of the study are summarized in Table I below. The values of k_p were calculated from curves similar to those in Fig. 2 and, as indicated in

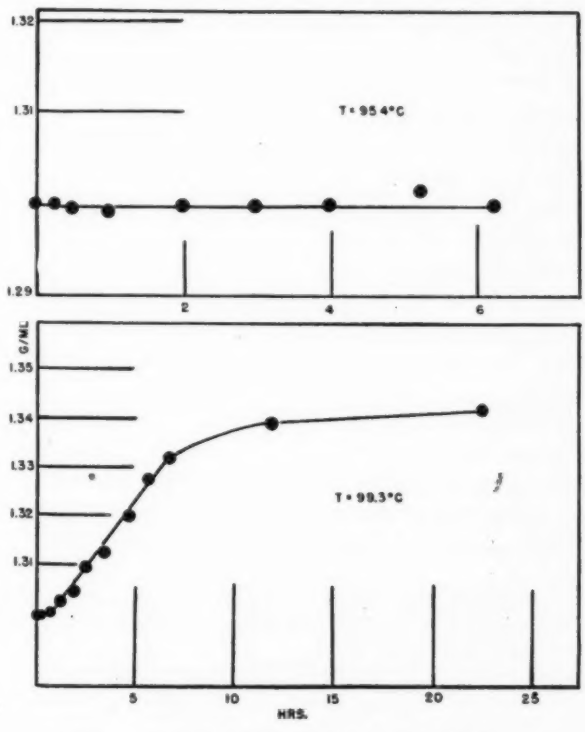

FIG. 2. Rate of crystallization of polyethylene terephthalate in silicone oil.

[8] Astbury and Brown, Nature **158**, 871 (1946).
[9] C. E. Black, III, unpublished x-ray data.

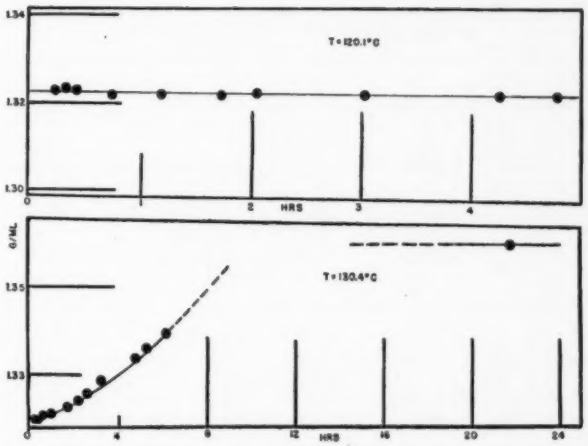

FIG. 3. Rate of crystallization of polyethylene 1,5 naphthalate in Silicone oil.

Table I, are the slopes of the linear section of the curve after the induction period. It was noted during the graphing of the data that the induction period became shorter as the temperature was increased. The slope of the linear section became greater indicating faster rate of crystallization. The curves tended toward a horizontal asymptote after finite time intervals, all increasing with temperature. It will be noted that the three principal sections of the curve in Fig. 2 bear a striking resemblance to the initiation, propagation (hence k_p), and termination steps of chemical reactions. On the basis of this, one might predict that the crystallization studies could be treated in conventional kinetic manner with more precise data. As a matter of fact, preliminary calculations of the energy of activation for the density change using the Arhennius equation gave values of 20–40 kcal./mole. This, of course, poses the interesting question as to "per mole of what." It will be remembered that all of these data are for specific polymer samples. The kinetic aspects of each are dependent on past history of the sample. For example, annealing, quenching, chain length ($[\eta]_0$), and the like will determine such factors as number of crystallite nuclei, position of chains, etc.

Although an attempt was made to determine crystallization rates at high temperatures (*ca.* 220°C), the existing apparatus was not suitable for these experiments. Polymer samples in glass tubes were then heated above 264°C, the melting point,[9] and then immersed into a constant temperature bath below but near the melting point. At various time intervals thereafter, sample tubes were removed from the bath, quickly quenched in dry ice-acetone mixtures, and subsequently analyzed in the density gradient tube. Unfortunately, the data were too inconsistent to reproduce here, but all the data indicated qualitatively that the rate of crystalliza-

TABLE II. Heat treatment of bulk polyethylene terephthalate at temperatures near its melting point.

Sample	Density at 0°C	Heat treatment	Intrinsic viscosity
A	1.3987	None	0.76
	1.4096	22 hrs. at 240°C	0.76
B	1.3833	None	0.80
	1.4048	23.5 hrs. at 240°C	—
	1.4102	Additional 63.5 hrs. at 210°C	0.75

tion near the melting point was very low. If this is true, then a maximum similar to that for rubber[10] probably exists in the crystallization rate *vs.* temperature curve for polyethylene terephthalate.

Although the rate of crystallization of the polymer may show a maximum with temperature below the melting point, there is no indication that such exists in the *degree* of crystallization *vs.* temperature curve. A glance at the last column of Table I would indicate the equilibrium position is a monotonously increasing function of temperature. This is pointed out with reservations because of the uncertainty of naming or defining an "equilibrium position." Further experiments with the annealing

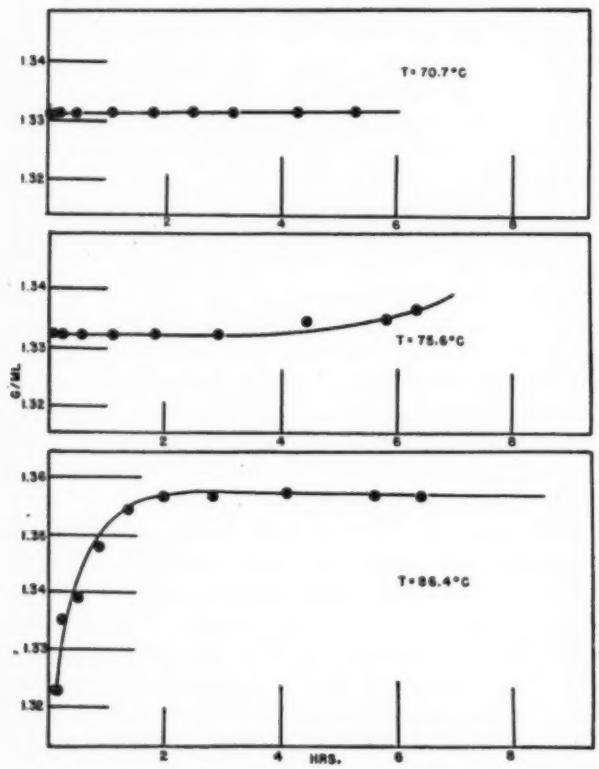

FIG. 4. Rate of crystallization of polyethylene terephthalate in water (density at 30°C).

[10] L. Wood and N. Bekkedahl, J. Research Nat. Bur. Stand. **36**, 489 (1946).

of bulk polymer at high temperatures but below the melting point supports this idea. The results of these annealing experiments are summarized in Table II.

Apparently there exists a minimum crystallization temperature for an amorphous polymer, below which the rate is so slow that the polymer can be kept for long periods without initiation of crystallization. For polyethylene terephthalate in inert media, this temperature is between 95.4° and 99.3°C (see Fig. 2). The temperature, of course, depends upon the assigned time interval before measurable crystallization takes place, and hence the absolute value is a matter of definition. The relationship between this temperature and the second-order transition temperature (Tg) is interesting to contemplate. Such questions as "Can the minimum crystallization temperature fall below the second-order transition?" and "Is the minimum crystallization temperature always a given increment from the second-order transition temperature?" are two of the more obvious.

Effect of Temperature on Crystallization of Two Polyethylene Naphthalates

The curves to illustrate the effect of temperature on the crystallization rate of amorphous polyethylene 1,5 naphthalate are represented by Fig. 3. The minimum crystallization temperature of the amorphous polymer is relatively well defined (within 10°C). As with the T_g values, these newly defined temperatures increase in the same order from polyethylene terephthalate, polyethylene 1,5 naphthalate to polyethylene 2,6 naphthalate. The results could be explained by variations in molecular symmetry and intermolecular forces. With these particular polyesters, the minimum crystallization temperature appears to fall approximately 30°–50°C above the second-order transition temperature. This fact is numerically illustrated in Table III below.

With most of these polyester samples, crystallization was associated with opacity changes as well as density changes. In some cases, as with the 2,6 naphthalate, the polymer began to turn opaque at the same instant that the density began to

TABLE III. Relationship of second-order transition temperature and minimum crystallization temperature of several amorphous polyesters.

Polymer	$[\eta]_0$	2nd-order transition temp.	Minimum crystallization temperature
Polyethylene terephthalate	0.62	67°C	95.4°– 99.3°C
Polyethylene 1,5 naphthalate	0.61	76	120.1 –130.4
Polyethylene 2,6 naphthalate	0.44	109	149.5 –152.4

increase. Opacity is not always indicative of crystallinity, nor is transparency always indicative of the amorphous state. However, in these experiments, crystallization is associated with opacity.

Effect of Immersion Media on Crystallization of Polyethylene Terephthalate

The discussion will conclude with reference to crystallization accelerated by the swelling action or activation of the immersion media. The rate curves for polyethylene terephthalate in water, illustrated in Fig. 4, graphically describe this effect. In Silicone oil, the minimum crystallization temperature for the terephthalate polymer was between 95.4° and 99.3°C. In water, this temperature has been lowered to 70.7°–75.6°C. The activation may be attributable to penetration or swelling action of the water but has not been experimentally verified.

Figure 5 illustrates the effect of other media on the crystallization rate of the terephthalate polymer. Most of these active media resemble very weak solvents. With the exception of methyl alcohol all are active enough to initiate crystallization at room temperature. Nitric acid apparently has the strongest action of those tested. In all of the experiments, the amount of crystallization definitely depends on sample size. Since it takes a finite time for penetration of the polymer, it might be expected that crystallization starts at the phase boundary and proceeds toward the center of the polymer sample. However, there is some evidence that crystallization does not take place until the liquid leaves the polymer sample. In this event, the crystallization process may proceed opposite to that expected.

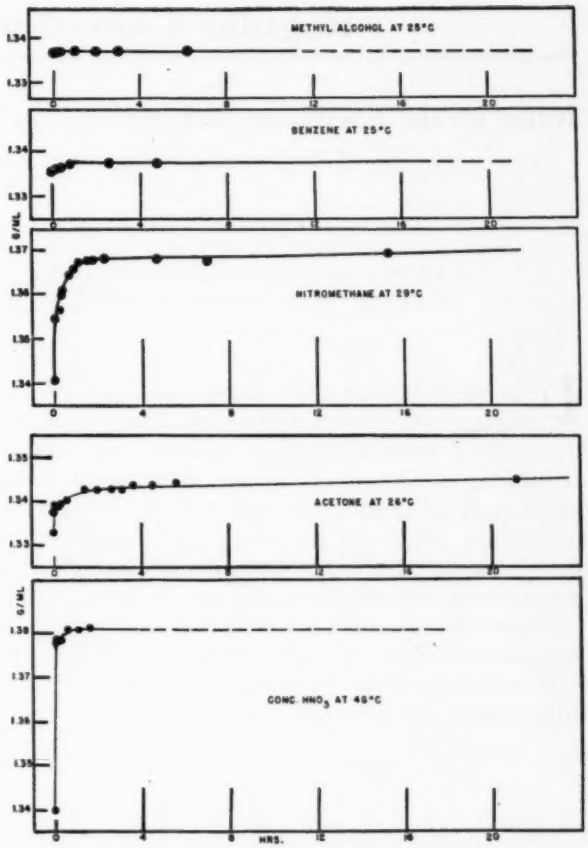

FIG. 5. Rate of crystallization of polyethylene terephthalate in various liquid media (density at 30°C).

Notes on the Excitation of Electromagnetic Waves in Cylindrical Metallic Wave Guides

A. COLINO
Madrid, Spain
(Received May 27, 1948)

In this paper very simple formulas are deduced for calculating the amplitude of modes produced in a cylindrical guide when the currents distribution is known. One example is included.

IT is well known that various modes of wave propagation exist in a cylindrical wave guide. If a radiating antenna, having a certain current distribution, is placed inside the wave guide, what modes will be produced, what will be their relative intensities, what will be the radiation resistance of the antenna? Although we suppose that all these queries have already been answered in the abundant modern bibliography, to which we unfortunately have so little access, we offer our own solutions here.

If we start from Maxwell's equations in oscillating condition ($\beta^2=\epsilon\mu\omega^2$), we have:

$$\Delta H+\beta^2 H=-\text{curl}i,$$

$$\Delta E+\beta^2 E=\frac{1}{\epsilon\omega j}(\beta^2 i+\text{grad div}i).$$

By considering the geometrical structure of the guide, it is advantageous to separate the axial (z) from the transversal (t) coordinates. Expanding the field in the wave guide in the orthogonal E and H modes,

$$E_z=\sum_\sigma E_{z\sigma}(z)F_\sigma^{\,e}(t),$$

$$H_z=\sum_\sigma H_{z\sigma}(z)F_\sigma^{\,m}(t),$$

in which $\left\{\begin{matrix}F_\sigma^{\,e}(t)\\F_\sigma^{\,m}(t)\end{matrix}\right\}$ are functions only of the transversal coordinates concerning to the $\left(\begin{matrix}\text{electric}\\\text{magnetic}\end{matrix}\right)$ σ mode, and being assumed that the condition $(\Delta_t+h_\sigma^2)F_\sigma(t)=0$ is fulfilled.

In the last formula, h_σ is determined by the conditions in the guide's contour, i.e.:

$$F_\sigma^{\,e}(C)=0 \quad \text{or} \quad \frac{\delta F_\sigma^{\,m}(C)}{\delta n}=0.$$

As we already know,

$$\int_S F_\sigma^{\,e}F_{\sigma'}^{\,e}dS=0 \quad \text{and} \quad \int F_\sigma^{\,m}F_{\sigma'}^{\,m}dS=0 \quad \text{if} \quad \sigma\neq\sigma'.$$

Replacing $\gamma_\sigma^2=\beta^2-h_\sigma^2$ by the expansions in Maxwell's equations,

$$\left(\Delta_t+\frac{\partial^2}{\partial z^2}+\beta^2\right)E_z=\sum\left(\Delta_t+\frac{\partial^2}{\partial z^2}+\beta^2\right)E_{z\sigma}F_\sigma^{\,e}$$

$$=\sum\left(\frac{\partial^2}{\partial z^2}+\gamma_\sigma^2\right)E_{z\sigma}F_\sigma^{\,e}$$

$$=\frac{1}{\epsilon\omega j}\left(\beta^2 i_z+\frac{\partial^2 i_z}{\partial z^2}+\text{grad div}i_t\right).$$

Similarly

$$\left(\Delta_t+\frac{\partial^2}{\partial z^2}+\beta^2\right)H_z=\sum\left(\Delta_t+\frac{\partial^2}{\partial z^2}+\beta^2\right)H_{z\sigma}F_\sigma^{\,m}$$

$$=\sum\left(\frac{\partial^2}{\partial z^2}+\gamma_\sigma^2\right)H_{z\sigma}F_\sigma^{\,m}=-\text{curl}i_t,$$

in which we resolve the i-vector into its components i_z and i_t.

We now make use of the orthogonal characteristics $(F_\sigma F_{\sigma'})=0$ of the F_σ functions, and also transform the differential equations in $\partial/\partial z$ by means of the Fourier transformation. To this end we submit the two portions of the equation to the operation

$$\varphi_\sigma[p]=[\varphi(z,t)F_\sigma e^{-pz}]=\int_{-\infty}^{\infty}e^{-pz}dz\int_S\varphi(zt)F_\sigma(t)dS,$$

with the result that

$$(p^2+\gamma_\sigma^2)E_{z\sigma}[p]=\frac{1}{\epsilon\omega j}[(p^2+\beta^2)L_\sigma(p)+pN_\sigma(p)],$$

$$(p^2+\gamma_\sigma^2)H_{z\sigma}[p]=-M_\sigma(p),$$

with

$$L_\sigma(p)=(i_zF_\sigma^{\,e}e^{-pz}),$$

$$M_\sigma(p)=(\text{curl}i_tF_\sigma^{\,m}e^{-pz}),$$

and

$$N_\sigma(p)=(\text{div}i_tF_\sigma^{\,e}e^{-pz}).$$

To obtain $E_{z\sigma}(z)$ and $H_{z\sigma}(z)$ we must invert the

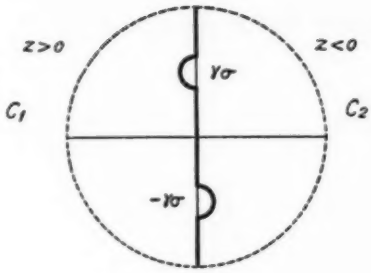

FIG. 1. Selection of the integrating contour with $z>0$ or <0.

expressions

$$E_{z\sigma}[p]=\frac{1}{\epsilon\omega j}\left[\frac{p^2+\beta^2}{p^2+\gamma_\sigma{}^2}L_\sigma(p)+\frac{p}{p^2+\gamma_\sigma{}^2}N_\sigma(p)\right],$$

$$H_{z\sigma}[p]=\frac{-1}{p^2+\gamma_\sigma{}^2}M_\sigma(p).$$

To effect the inversion we must make the operation

$$E(z)=\frac{1}{2\pi j}\int E[p]e^{pz}dp,$$

selecting the contour of integration so that the waves proceed from the excitation towards infinity and not from infinity towards the excitation. The poles of $E[p]$ and $H[p]$ are $p=\pm\gamma_\sigma j$.

For the case $z>0$ we must follow the path C_1 and in order to ensure that the integration over the whole of the infinite semi-circle C_1 is zero, z must be outside the zone of excitation. In this case it is sufficient to compute the residual quantities, so that

$$E_{z\sigma}(z)=\frac{-1}{\epsilon\omega j z\gamma_\sigma j}(h_\sigma{}^2L_\sigma(-j\gamma_\sigma)-j\gamma_\sigma N(-j\gamma_\sigma))e^{-j\gamma_\sigma z},$$

$$H_{z\sigma}(z)=\frac{-1}{2\gamma_\sigma j}M_\sigma(-j\gamma_\sigma)e^{-j\gamma_\sigma z}.$$

The interpretation of the terms N and M is intuitive. $N_\sigma=(\mathrm{div}\boldsymbol{i}_t F_\sigma{}^e e^{+j\gamma_\sigma z})$ means that the pulsating charges $\mathrm{div}\boldsymbol{i}_t$ give rise to the fields E_z. It is also evident that the infinitesimal loops caused by $\mathrm{curl}\boldsymbol{i}_t$ produce the fields H_z, $M_\sigma=(\mathrm{curl}\boldsymbol{i}_t F_\sigma{}^m e^{+j\gamma_\sigma z})$. By partial integration the terms N_σ and M_σ may be given other forms.

$$N_\sigma=(\boldsymbol{i}_t\cdot\mathrm{grad}_t F_\sigma{}^e e^{j\gamma_\sigma z}),\quad M_\sigma=(\boldsymbol{i}_t\,\mathrm{curl}_t F_\sigma{}^m e^{j\gamma_\sigma z}).$$

The power radiated by one mode in one direction may be calculated

$$W^e=\int E_t{}^e\times H_t{}^e dS=\frac{1}{4h_\sigma{}^2\gamma_\sigma\epsilon\omega}|L_\sigma h_\sigma{}^2-j\gamma_\sigma N_\sigma|^2,$$

$$W^m=\int E_t{}^m\times H_t{}^m dS=\frac{\mu\omega}{4h_\sigma{}^2\gamma_\sigma}|M_\sigma|^2.$$

In order to check our formulas, let us apply them to the case of an axial antenna in a circular wave guide, as mentioned by S. A. Schelkunoff, *Electromagnetic Waves* (D. Van Nostrand Company, Inc., 1943), p. 423. In a circular wave guide

$$(\Delta_t+h^2)F=\frac{1}{r^2}\frac{\partial}{\partial r}\left(r\frac{\partial F}{\partial r}\right)+\frac{1}{r^2}\frac{\partial^2 F}{\partial\varphi^2}+h^2F=0,$$

in which, eliminating the variable quantities $F=J_n(hr)\cos n\varphi$, the function F being abnormal. For waves E_z we have $F(C)=0=J_n(ha)\cos n\varphi$, a being the radius of the wave guide, so that $h_\sigma a=\alpha_{n,m}$, being $\alpha_{n,m}$ the root (m) of $J_n(\alpha)=0$.

To normalize the quantities F^e, it is necessary to divide each of them by

$$(F^{e2})^{\frac{1}{2}}=\left[\frac{\pi}{4}a^2J_n{}'^2(\alpha_{n,m})\right]^{\frac{1}{2}}.$$

Let us suppose that the current distribution in the aerial is the usual $I(z)=I_0\sin\beta(l-z)$ so that

$$L(j\gamma_\sigma)=J_n(hr_0)\int_0^l I_0\sin\beta(l-z)(e^{j\gamma z}+e^{-j\gamma z})dz,$$

r_0 being the distance from the center of the wave guide to the axis of the antenna, and taking z from the center of the antenna.

$$L(j\gamma_\sigma)=I_0\frac{2\beta}{\beta^2-\gamma^2}(\cos\gamma l-\cos\beta l)J_n(h_\sigma r_0),$$

and consequently,

$$E_{2\sigma}F_\sigma{}^e=\frac{2(\mu/\epsilon)^{\frac{1}{2}}I_0}{a^2\gamma_\sigma\pi}(\cos\gamma l-\cos\beta l)\times\frac{J_n(h_\sigma r_0)J_n(h_\sigma r)}{J_n{}'^2(\alpha_{n,m})}\cos n\varphi e^{-j\gamma_\sigma z},$$

which coincides with Schelkunoff's results.

Use of a Mechanical Harmonic Synthesizer in Electric Wave Filter Analysis*

S. Leroy Brown and James M. Sharp
Department of Physics, University of Texas, Austin, Texas
(Received July 27, 1948)

A mechanical method is described for graphing the effect of the variation with frequency of the series reactance (X_1) and the shunt reactance (X_2) of a filter section. This method permits the quantities $X_1/-4X_2$, $X_1X_2\{(X_1/-4X_2)-1\}$ and $X_1X_2/\{(X_1/-4X_2)-1\}$, from which the characteristics of an electric wave filter are calculated, to be graphed easily as a function of frequency. The cut-off frequencies are located directly from the graphs of N and D (where N/D is either the ratio $X_1/-4X_2$ or $(X_1/-4X_2)$) as functions of frequency, and the calculation of the attenuation and phase shift at any frequency is readily made from the ratio of corresponding ordinates of the N and D curves. The image impedance is determined from the ratio of corresponding ordinates from two additional curves which are mechanical plots of the numerator and the denominator of the expression for the square of the image impedance, $X_1X_2\{(X_1/-4X_2)-1\}$ for the mid-series image impedance, and $X_1X_2/\{(X_1/-4X_2)-1\}$ for the mid-shunt image impedance.

INTRODUCTION AND GENERAL METHOD

THE mechanical harmonic synthesizer (consisting of fifteen sine and fifteen cosine harmonic elements) may be used to graph a polynomial[1] after the polynomial has been transformed to an equation containing harmonic functions of an angle θ by a substitution for the variable of the form $R-r\cos\theta$, where R and r are arbitrary moduli. For any reactance network, the expression for the reactance may be written as a polynomial in the angular frequency ω, or as the ratio of two polynomials in ω. The synthesizer may then be used to plot the polynomials, and these curves may in turn be used to determine the variation of reactance with frequency. Except for the very simplest circuits, the expression for the reactance will be in the form of the ratio of two polynomials in ω. After the polynomial occurring in the numerator and the one occurring in the denominator are plotted with the harmonic synthesizer, the numerical value of the reactance for any value of ω is the ratio of the ordinates, corresponding to that value of ω, read from the graphs of these two polynomials. This basic method is applied herein to determine the cut-off frequencies of an electric wave filter, and to plot as a function of frequency the attenuation, phase shift, and image impedance.

The cut-off frequencies, attenuation, and phase shift of a non-dissipative electric wave filter may all be determined from the quantity $(X_1/-4X_2)^{\frac{1}{2}}$ where X_1 is the reactance of the series arm of the filter, and X_2 is the reactance of the shunt arm. This quantity is reducible to the square root of the ratio of two polynomials in ω. After a substitution of the form $\omega=R-r\cos\theta$, where the moduli are so chosen that the desired range of ω will be included, this ratio becomes the ratio of two polynomials in $\cos\theta$. The powers of $\cos\theta$ in these two polynomials may then be expanded in terms of harmonic functions of θ and multiples of θ, thus transforming the ratio to a form such that the numerator and denominator can be plotted with the synthesizer. Thus, plots of both the numerator (N) and denominator (D) of the transformed expression $X_1/-4X_2$ against θ are obtained which are easily converted to a plot of $X_1/-4X_2$ against ω. Of course, if $X_1/-4X_2$ is a perfect square, it is preferable to plot $(X_1/-4X_2)^{\frac{1}{2}}$, since this eliminates the necessity of taking square roots in the final calculation of attenuation and phase shift.

Once the curves of the numerator N *versus* θ and the denominator D *versus* θ are obtained from the synthesizer, the cut-off frequencies are readily determined. These frequencies will be those corresponding to the values of θ at which the ordinates of N and D are equal since the condition for cut-off is $X_1=-4X_2$. If N and D are plotted to the same scale, and N/D represents $X_1/-4X_2$, the points at which ordinates are equal will be apparent as the points of intersection of the two curves. If N/D represents $(X_1/-4X_2)^{\frac{1}{2}}$, then the points of intersection of the curves will be cut-off frequencies, but also points at which $N=-D$ will be cut-off frequencies.

The attenuation (a) and the phase shift (b) are respectively:

$$a=2\cosh^{-1}(X_1/-4X_2)^{\frac{1}{2}}$$

or

$$a=2\sinh^{-1}(X_1/-4X_2)^{\frac{1}{2}},$$

and

$$b=2\sin^{-1}(X_1/-4X_2)^{\frac{1}{2}} \quad \text{or} \quad b=\text{zero (or}\pm\pi).$$

Hence, the value of a in an attenuated band and the value of b in a pass band can be readily determined for any value of ω by reading the ratio $(N/D)^{\frac{1}{2}}$, or N/D as the case may be, and substituting accordingly in the above relations.

The frequency limits of the pass bands of a specific filter having been determined from the graphs N and D, the image impedance (mid-series

* Supported by ONR under Contract N6onr-266.
[1] S. Leroy Brown and Lisle L. Wheeler, J. Frank. Inst. **231**, No. 3 (1941).

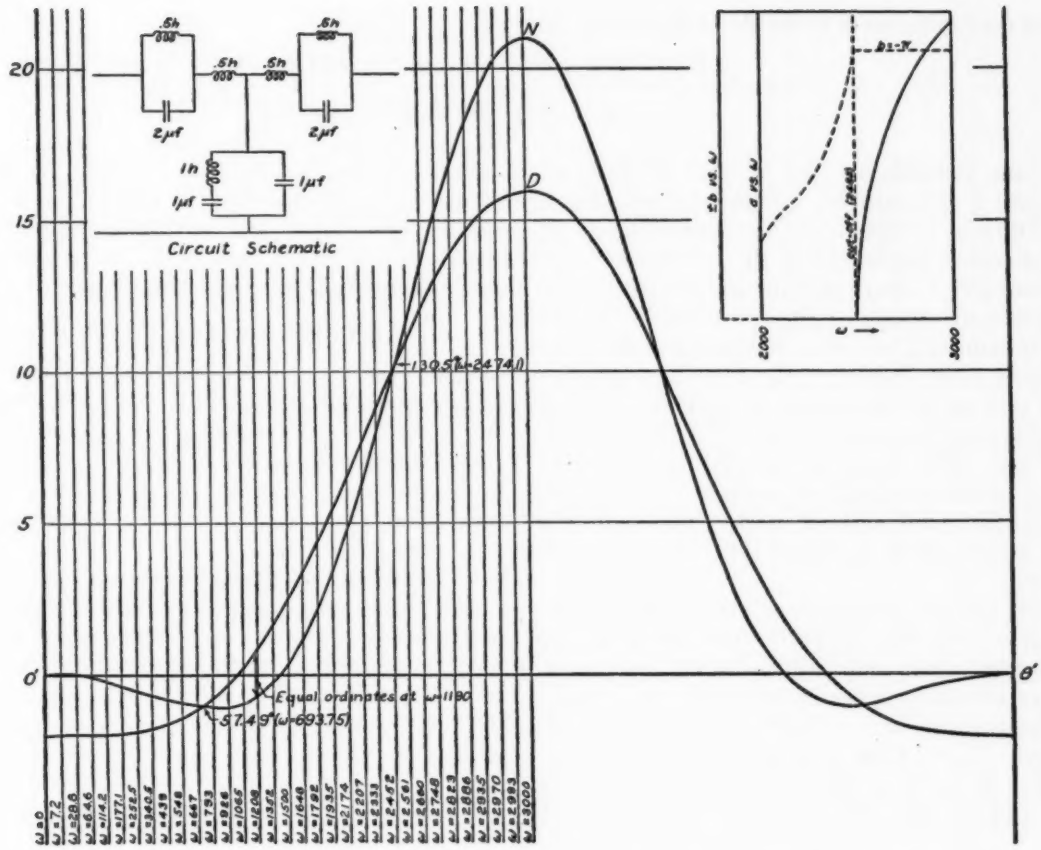

FIG. 1. Characteristics of a low pass, band-pass filter circuit, $(0<\omega<3000)$.

or mid-shunt) is then determined in an identical manner from a second pair of curves. For example, if the variation of the mid-series image impedance over the region $2000<\omega<4000$ is desired, the procedure is: Reduce the expression for the square of the image impedance, $X_1X_2\{(X_1/-4X_2)-1\}$, to the ratio of two polynomials in ω; change the variable by substituting $\omega=1000(3-\cos\theta)$; expand powers of $\cos\theta$ in terms of multiple values of $\theta(\cos2\theta$, $\cos3\theta$, etc.); plot the numerator (N) and the denominator (D) of the ratio of the two polynomials with the synthesizer; and then, the value of the mid-series image impedance at any value of ω between 2000 and 4000 is then the square root of the ratio N/D of the ordinates corresponding to the desired value of ω.

As an illustration of the method outlined above, the problem of analyzing the filter circuit (shown schematically in the figures) for the frequency range $0<\omega<3000$ will be carried out in some detail.

LOCATION OF THE BANDS

The expressions X_1 and X_2 are (see circuit diagram in figures):

$$X_1=(\omega^3-2\omega10^6)/(\omega^2-10^6), \tag{1}$$

and

$$X_2=-10^6(\omega^2-10^6)/(\omega^3-2\omega10^6). \tag{2}$$

Hence,

$$X_1/-4X_2=(\omega^3-2\omega10^6)^2/10^6(\omega^2-10^6)^24, \tag{3}$$

or

$$(X_1/-4X_2)^{\frac{1}{2}}=(\omega^2-2\omega10^6)/10^3(\omega^2-10^6)2. \tag{4}$$

It is usually possible to construct an approximate reactance diagram for the filter by an inspection of the circuit and the expressions for X_1 and X_2. For example, X_1 will obviously be infinite at $\omega=1000$ and zero at $1000\sqrt{2}$, while X_2 will be infinite at $\omega=1000\sqrt{2}$ and zero at $\omega=1000$. Thus, with these points as a guide, it is possible to predict that all the cut-off frequencies will be less than $\omega=3000$. Consequently, the substitution $\omega=1500(1-\cos\theta)$, which covers the desired frequency range, is chosen.

Substitute $\omega=1500(1-\cos\theta)$ in Eq. (4):

$$(X_1/-4X_2)^{\frac{1}{2}}=\frac{3.375(1-\cos\theta)^3-3(1-\cos\theta)}{4.5(1-\cos\theta)^2-2}. \tag{5}$$

Expand powers of $(1-\cos\theta)$, and finally expand

powers of $\cos\theta$ in terms of multiple angles in Eq. (5):

$$(X_1/-4X_2)^{\frac{1}{2}}=\frac{5.44-9.66\cos\theta+5.06\cos2\theta-0.84\cos3\theta}{4.75-9\cos\theta+2.25\cos2\theta}=N/D. \tag{6}$$

It is now possible to plot N and D with the synthesizer. For example, set the amplitudes of -9.66, 5.06 and -0.84 on the fundamental, second, and third cosine harmonics of the synthesizer, and vary θ from zero to 2π to plot the numerator against θ. The ordinate (value of the numerator) for any angle is measured from an axis which is 5.44 below the machine zero. A similar procedure is followed to obtain a plot of the denominator against the angle and, in this case, the reference axis is 4.75 below the machine zero. The bases for the ordinates of both curves are made to coincide by translating the paper on which they are drawn, with respect to the drawing board which is driven horizontally as the angle varies.

Carrying out the above procedure resulted in the curves shown in Fig. 1. Here, the abscissas are designated in values of ω rather than θ. The intersections of the two curves indicate that two of the cut-off frequencies are $\omega=693.7$ and $\omega=2474.1$. Also, since $(X_1/-4X_2)^{\frac{1}{2}}$ was plotted rather than $X_1/-4X_2$, there is a third cut-off frequency at $\omega=1190$ (where the two ordinates are equal but opposite in sign). Note that not only are the cut-off frequencies indicated by the curves but the type of band between any two cut-off frequencies is indicated; $0<N/D<1$ indicating a pass band, and $N/D<0$ or $N/D>1$ indicating an attenuated band.

ATTENUATION AND PHASE SHIFT

After the cut-off frequencies and the types of bands included between pairs of adjacent cut-off frequencies are determined, the attenuation a and phase shift b may be calculated for specific values of ω. Both of these may be calculated from the values of N and D as read from the curves in Fig. 1, $a=2\cosh^{-1}N/D$ (or $a=2\sinh^{-1}N/D$) in an attenuated band, and $b=2\sin^{-1}N/D$ in a pass band.

To obtain more nearly accurate values of the attenuation and phase shift, the change of variable may be chosen to confine the curves of N and D to a limited range of ω. For example, substitute $\omega=300(1-\cos\theta)$ in Eq. (4) to obtain curves from which the phase shift may be calculated for ω ranging from 0 to 600, and substitute $\omega=1300-700\cos\theta$ in Eq. (4) to obtain curves from which

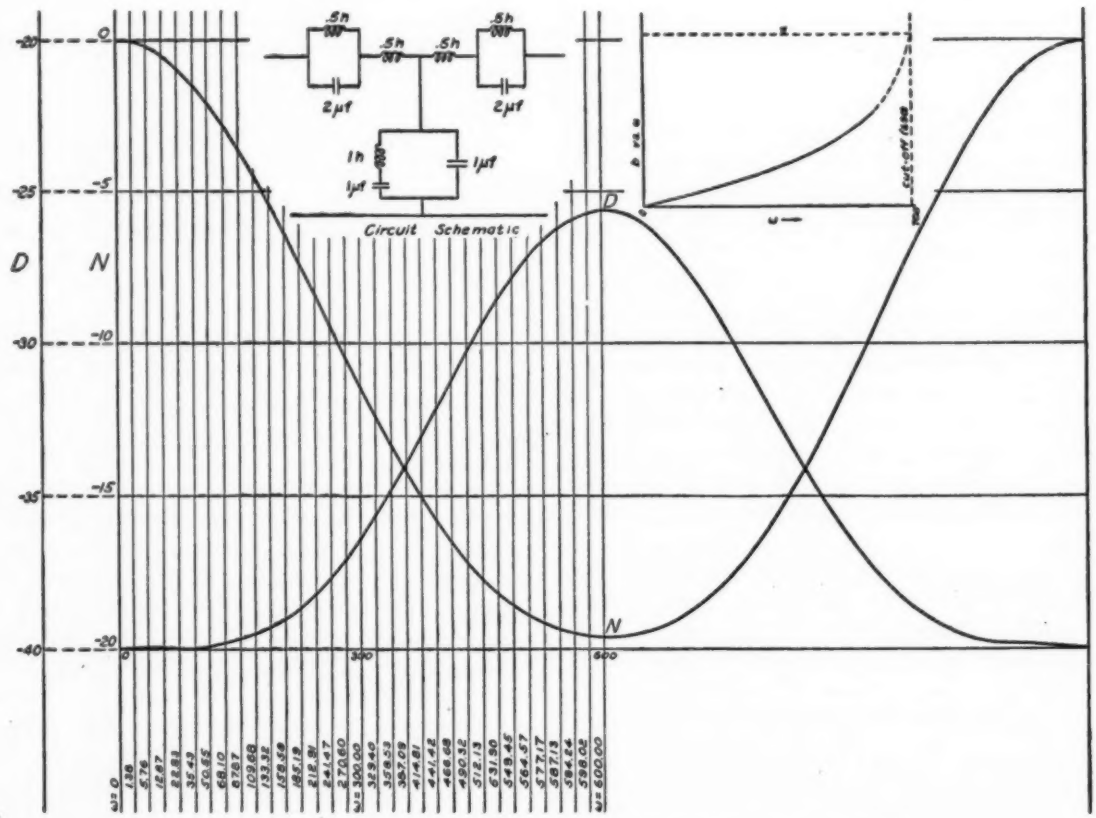

FIG. 2. Characteristics of the filter circuit in low pass region, $(0<\omega<600)$.

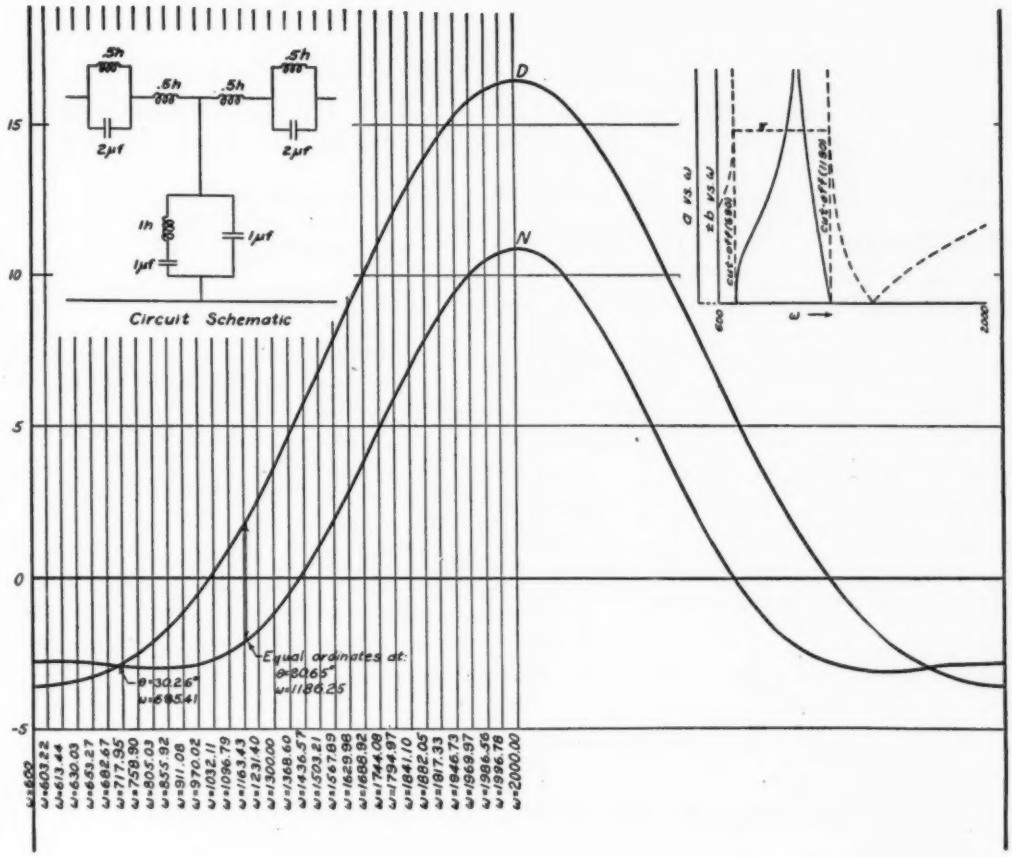

FIG. 3. Characteristics of the filter circuit in the region ($600 < \omega < 2000$).

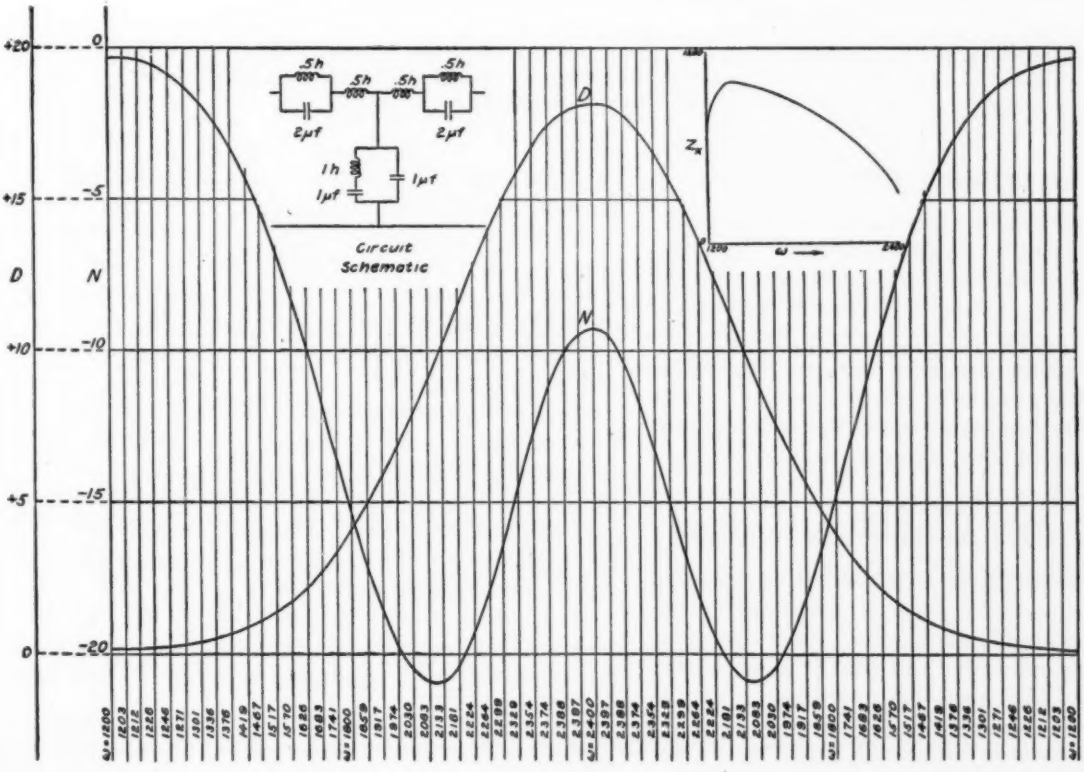

FIG. 4. Image impedance of the filter circuit ($0 < \omega < 3000$).

the attenuation (or phase shift) may be calculated for ω ranging from 600 to 2000. The curves resulting from these substitutions are shown in Fig. 2 and Fig. 3, respectively. From the values of the ordinates N and D (obtained from Figs. 1, 2, and 3) the values of attenuation and phase shift are calculated and plotted, for a limited range, in each of these figures.

IMAGE IMPEDANCE

The pass band having been found to extend from $\omega=1190$ to $\omega=2474$, the mid-series image impedance Z_K will be determined from

$$Z_K^2=X_1X_2\{(X_1/-4X_2)-1\}. \tag{7}$$

When the values of X_1 and X_2 (in terms of ω) for the specific filter circuit are substituted in Eq. (7),

$$Z_K=-j\left[\frac{\omega^6-8\omega^4 10^6+12\omega^2 10^{12}-4\cdot 10^{18}}{4\omega^4-8\omega^2 10^6+4\cdot 10^{12}}\right]^{\frac{1}{2}}. \tag{8}$$

Substitute $\omega=600(3-\cos\theta)$ in Eq. (8),

$$Z_K=-1000j\left[\frac{0.046656(3-\cos\theta)^6-1.0368(3-\cos\theta)^4-4.32(3-\cos\theta)^2-4}{0.5184(3-\cos\theta)^4-2.88(3-\cos\theta)^2+4}\right]^{\frac{1}{2}}=-1000j(N/D)^{\frac{1}{2}}. \tag{9}$$

Expand the numerator N and the denominator D in terms of cosines of multiple angles,

$$N=-10.59+7.94\cos\theta+5.16\cos2\theta-3.45\cos3\theta+0.67\cos4\theta-0.05\cos5\theta+0.001\cos6\theta, \tag{10}$$

$$D=32.82-43.37\cos\theta+12.82\cos2\theta-1.56\cos3\theta+0.06\cos4\theta. \tag{11}$$

Figure 4 shows the variation of N and D with the angle θ {Eq. (10) and Eq. (11)} plotted with the synthesizer. The angles are converted to corresponding values of ω; and finally, the image impedance $(-1000j(N/D)^{\frac{1}{2}})$ is plotted against ω. The sign of N/D is negative throughout the pass band, indicating that the image impedance is pure resistance throughout the band.

Barkhausen Noise and Magnetic Amplifiers. II. Analysis of the Noise

J. A. KRUMHANSL* AND R. T. BEYER
Brown University, Providence, Rhode Island
(Received July 27, 1948)

The Barkhausen noise is calculated for ferromagnetic cores used in magnetic amplifiers. The method of analysis follows that used in the analysis of the shot effect. The signal-to-noise ratio for a typical magnetic amplifier circuit is calculated and compared with experiment.

1. INTRODUCTION

IT was pointed out in a previous paper[1] that the limit of sensitivity of the magnetic amplifiers was perhaps to be found in Barkhausen effects in the ferromagnetic core materials. It is the purpose of this paper to present an analysis of Barkhausen noise for a simplified model of the ferromagnetic cores used in the magnetic amplifiers. The results are applied to the magnetic amplifiers discussed in I, and calculations of the signal-to-noise ratio are given.

2. THE PROBABILITY DISTRIBUTION FUNCTION

In the simplified physical model, it is assumed that the ferromagnetic core is essentially one-dimensional, reasonably satisfactory for the toroidal cores used experimentally, and that it is composed of a number of elementary magnets of magnetic moment m, which can be oriented only parallel or anti-parallel to the core axis. It is further assumed that, on the average, the behavior in all parts of the core is the same, but that the orientations of the elementary magnets in the different parts of the core are statistically independent random variables at any given time.

An e.m.f. is induced at the output terminals of any winding, surrounding the core whenever an elementary magnet flips from a parallel to an anti-parallel orientation or vice versa. The statistical problem can be solved, following methods outlined by Rice,[2] provided one knows the probability of occurrence of these processes.

It is then postulated that when the applied magnetizing force, H,[3] is changing with time, the probability of a flip occurring in a time interval, Δt,

---

* Now at Cornell University, Ithaca, New York.
[1] J. A. Krumhansl and R. T. Beyer, J. App. Phys. **21**, 432 (1949), to be referred to as I.
[2] S. O. Rice, Bell Sys. Tech. J. **23**, 287 (1944); **24**, 46 (1945).
[3] A table of the chief symbols used in this paper is included in Appendix A.

is given by $p(t)\Delta t$, where

$$p(t)=c|d\bar{B}/dH|\,|dH/dt|, \tag{1}$$

in which $\bar{B}$ is the average flux density (i.e., found from the usual $\bar{B}-H$ curve), and c is a normalizing constant.

In particular, n is defined as the net number of elementary magnets in the core, oriented in a direction parallel to the positive field direction,

$$n=n_+-n_-, \tag{2}$$

where n_+ = number oriented parallel, n_- = number oriented anti-parallel. Then n is a random variable, and $\Delta n=2$ if one flip occurs from an anti-parallel to a parallel orientation, and $\Delta n=-2$ if the opposite occurs.

The next assumption is similar to that made in the treatment of the shot effect, namely, that if Δt is made sufficiently small, the probability of more than one flip in the interval Δt is entirely negligible, and furthermore that in the time interval, Δt,

$$\Delta n\begin{cases}=2 \text{ with probability } p(t)\Delta t\\ =0 \text{ with probability } 1-p(t)\Delta t\end{cases} \quad \text{if } dH/dt>0,$$
$$\Delta n\begin{cases}=-2 \text{ with probability } p(t)\Delta t\\ =0 \text{ with probability } 1-p(t)\Delta t\end{cases} \quad \text{if } dH/dt<0. \tag{3}$$

Finally, it is assumed that events in different intervals Δt are statistically independent.

The constant c which occurs in Eq. (1) can be evaluated by considering the special process in which the initially unmagnetized core is magnetized to saturation in the positive sense. In electromagnetic units, the "volume average" flux density is

$$\bar{B}=H+(4\pi m\bar{n}/V), \tag{4}$$

where V is the volume of the core, and m is the magnetic moment of the elementary magnet. For materials of high permeability, $\bar{B}\cong 4\pi m\bar{n}/V$. In the particular process under consideration, $\bar{B}_{t=0}=0$, and $\bar{B}_{t=t_{\text{final}}}=S$, where S is the saturation value of flux density. For this process it is reasonable to assume that, on the average, $\bar{n}=0$ at $t=0$, and $\bar{n}_{\text{final}}=N$ at $t=t_{\text{final}}$ (N is the total number of magnets in the core). This means that

$$S=4\pi mN/V=4\pi m\bar{n}_{\text{final}}/V. \tag{5}$$

The final value of $\bar{n}$ can also be expressed as the sum of all changes in $\bar{n}$, i.e.,

$$\bar{n}_{\text{final}}=\textstyle\sum_i\langle\Delta n_i\rangle, \tag{6}$$

where the sum is taken over all intervals Δt_i which are included in the process. But,

$$\langle\Delta n_i\rangle=2p(t_i)\Delta t_i=2c|d\bar{B}/dH|_{t_i}|dH/dt|_{t_i}\Delta t_i, \tag{7}$$

and in the limit, as all Δt_i are made to approach zero,

$$\bar{n}_{\text{final}}=2c\int_0^{t_{\text{final}}}|d\bar{B}/dH|\,|dH/dt|\,dt=2cS. \tag{8}$$

For this process, however, $\bar{n}_{\text{final}}=N=VS/4\pi m$ and therefore, $c=V/8\pi m$. This determines $p(t)$ as

$$p(t)=V/8\pi m|d\bar{B}/dH|\,|dH/dt|. \tag{9}$$

3. AVERAGE VALUES OF INDUCED VOLTAGES

It is now possible to calculate averages of the induced output voltage. The function $f(t-t_i)$ is defined as the induced output voltage at a time, t, resulting from a flip of one elementary magnet from the anti-parallel to the parallel orientation at the time, t_i. From the method outlined by Rice in his work,[2] one finds in straightforward fashion that the ensemble averages (which are still functions of time) are

$$\bar{e}(t)=\frac{V}{8\pi m}\int_T f(t-\tau)\frac{d\bar{B}}{d\tau}d\tau, \tag{10}$$

where T is some time interval long compared to the duration of $f(t-\tau)$, and

$$\Delta^2(t)=\langle[e(t)-\bar{e}(t)]^2\rangle$$
$$=\frac{V}{8\pi m}\int_T f^2(t-\tau)\left|\frac{d\bar{B}}{d\tau}\right|d\tau. \tag{11}$$

In Eq. (11), $\bar{e}(t)$ and $\Delta^2(t)$ are the average output voltage and the mean square output voltage fluctuation, respectively.

In most practical cases, both $f(t-\tau)$ and $f^2(t-\tau)$ are extremely sharp pulses so that they may be approximated by delta functions, i.e.,

$$f(t-\tau)\cong F\delta(t-\tau),$$
$$f^2(t-\tau)\cong G\delta(t-\tau), \tag{12}$$

where F and G are constants. In this case, Eqs. (10) and (11) reduce to

$$\bar{e}(t)\cong(VF/8\pi m)(d\bar{B}/dt), \tag{13}$$

$$\Delta^2(t)\cong(VG/8\pi m)\,|(d\bar{B}/dt)|. \tag{14}$$

Let the number of turns on the output winding be N_w, and assume the core to be of uniform cross-sectional area A. Then, by setting

$$VF/8\pi m=-N_wA\times10^{-8}, \tag{15}$$

the usual expression for an induced e.m.f. can be obtained:

$$e(t)=-N_wA\times10^{-8}(d\bar{B}/dt). \tag{16}$$

On the other hand, in order to calculate G, the process must be prescribed in greater detail. For

example, if

$$f(t-\tau)=\begin{matrix}0 & t<\tau,\\ F/\sigma & \tau<t<\tau+\sigma,\\ 0 & \tau+\sigma<t,\end{matrix} \tag{17}$$

where σ is the duration of the induced pulse, then as σ becomes very small, $f(t-\tau)\cong F\delta(t-\tau)$, and $f^2(t-\tau)\cong(F^2/\sigma)\delta(t-\tau)$. Hence F^2/σ is equivalent to G in Eqs. (12) and (14). Substitution in Eqs. (13) and (14) leads at once to the value of the signal-to-noise ratio:

$$\bar{e}(t)/\Delta(t)=(\sigma V/8\pi m|d\bar{B}/dt|)^{\frac{1}{2}}. \tag{18}$$

4. FOURIER ANALYSIS OF THE NOISE

The output of this type of device is almost invariably applied to frequency selective linear filters or amplifiers. These will, of course, modify the statistical properties and averages calculated in Section 3. For this reason, an alternative representation of the output voltage, more amenable to analysis for these applications, is offered by the Fourier Series representation:

$$e(t)=\frac{a_0}{2}+\sum_{k=1}^{\infty}(a_k\cos\omega_k t+b_k\sin\omega_k t), \tag{19}$$

where $\omega_k=2\pi k/T$, and T is a long interval of time in which the voltage $e(t)$ is assumed to be periodic. In all cases, one introduces the limiting process of letting $T\to\infty$. The a_k and b_k are random variables from one experiment to another. The process for obtaining the statistical properties of the a_k and b_k is also thoroughly discussed by Rice.[2] In the present case, the time dependent flip probability, $p(t)$, tends to make the evaluation of relevant quantities rather tedious. Once this is accomplished however, Eq. (19) is a particularly useful representation of $e(t)$ when this signal is to be passed through a linear filter whose frequency response is known.

Again, the methods outlined in reference 2 may be applied directly. If the quantities α_k, β_k are defined by

$$\begin{matrix}\alpha_k\\ \beta_k\end{matrix}=\int_T\begin{matrix}\cos\\ \sin\end{matrix}\omega_k\tau f(\tau-0)d\tau, \tag{20}$$

then

$$\bar{a}_k=\frac{V}{8\pi m}\left[\alpha_k\frac{2}{T}\int_T\cos\omega_k\tau\frac{d\bar{B}}{d\tau}d\tau-\beta_k\frac{2}{T}\int_T\sin\omega_k\tau\frac{d\bar{B}}{d\tau}d\tau\right],$$
$$\bar{b}_k=\frac{V}{8\pi m}\left[\alpha_k\frac{2}{T}\int_T\sin\omega_k\tau\frac{d\bar{B}}{d\tau}d\tau+\beta_k\frac{2}{T}\int_T\cos\omega_k\tau\frac{d\bar{B}}{d\tau}d\tau\right], \tag{21}$$

and

$$\bar{e}(t)=\frac{\bar{a}_0}{2}+\sum_{k=1}^{\infty}(\bar{a}_k\cos\omega_k t+\bar{b}_k\sin\omega_k t). \tag{22}$$

It is to be noted that if the approximation, $f(t-\tau)\cong F\delta(t-\tau)$, of Eq. (12) is employed,

$$\begin{matrix}\bar{a}_k\\ \bar{b}_k\end{matrix}=\frac{FV}{8\pi m}\frac{2}{T}\int_T\begin{matrix}\cos\\ \sin\end{matrix}\omega_k\tau\frac{d\bar{B}}{d\tau}d\tau. \tag{23}$$

These are nothing more than the usual Fourier coefficients of the induced output voltage (see Eq. (13)), averaged over an ensemble of similar experiments.

However, in contrast to the shot effect case, it is found that the relations

$$\begin{aligned}&\langle(a_k-\bar{a}_k)(a_l-\bar{a}_l)\rangle\propto\delta^{kl},\\ &\langle(b_k-\bar{b}_k)(b_l-\bar{b}_l)\rangle\propto\delta^{kl},\\ &\langle(a_k-\bar{a}_k)(b_l-\bar{b}_l)\rangle=0,\end{aligned} \tag{24}$$

where δ^{kl} is the Kronecker delta, no longer hold (because of the time dependence of $p(t)$). As a result, the joint distribution of the spectrum components in any range, say $j<k<l$, although still a $2(l-j)$ dimensional Gaussian distribution,[4] will in general exhibit correlations between any two spectrum components whose frequencies differ by, or add up to, some integer multiple of the basic frequency of the periodic magnetizing force.

For this reason, the determination of the fluctuations observed at the output of a filter to which $e(t)$ is supplied, becomes impractical if one desires the ensemble averages as a function of time. Actually the time and ensemble average fluctuation is of use, since it is the quantity usually determined in practice.

5. TIME AVERAGES OF THE ENSEMBLE AVERAGES

In accordance with the discussion in the preceding paragraph, the next step is the determination of the time averages of the ensemble average voltage and fluctuation. The time average of the ensemble average voltage is

$$\epsilon=\frac{1}{T}\int_T\bar{e}(t)dt, \tag{25}$$

which reduces to

$$\epsilon=\bar{a}_0/2, \tag{26}$$

as $T\to\infty$. The value of η, the time average of the ensemble average fluctuation, may be obtained by averaging first in time and then over the ensemble. By Parseval's theorem,

$$\lim_{T\to\infty}\frac{1}{T}\int_T e^2(t)dt=\frac{a_0^2}{4}+\sum_{k=1}^{\infty}\frac{a_k^2+b_k^2}{2}. \tag{27}$$

[4] By virtue of the Central Limit Theorem of probability theory.

Averaging over the ensemble,

$$\eta=\frac{\langle a_0^2\rangle}{4}+\sum_{k=1}^{\infty}{}'\frac{\langle a_k^2\rangle+\langle b_k^2\rangle}{2}, \tag{28}$$

where the primed summation is over all values of k except those leading to ω_k which are integer multiples of the basic frequency of the magnetizing field, H. The fluctuation η is expressed in terms of $\langle a_k^2\rangle$, etc. rather than $\langle(a_k-\bar{a}_k)^2\rangle$ since all such $\bar{a}_k$, $\bar{b}_k$ are zero, except for the discrete set of values of k excluded from the sum (and these contribute a negligible amount to the fluctuation energy).

For k, such that $\bar{a}_k$, $\bar{b}_k$ vanish, one finds that

$$\langle a_k^2\rangle=\langle b_k^2\rangle=(\alpha_k^2+\beta_k^2)\frac{2V}{8\pi mT^2}\int_T\left|\frac{d\bar{B}}{d\tau}\right|d\tau, \tag{29a}$$

$$\langle a_0^2\rangle=\frac{4V\alpha_0^2}{8\pi mT^2}\int_T\left|\frac{d\bar{B}}{d\tau}\right|d\tau. \tag{29b}$$

In the limit as $T\to\infty$, the spectrum becomes dense and in the standard fashion, these substitutions are made:

$$\begin{gathered}1/T\to df,\\ \frac{(\alpha_k^2+\beta_k^2)V}{8\pi mT}\int_T\left|\frac{d\bar{B}}{d\tau}\right|d\tau\to w(f).\end{gathered} \tag{30}$$

Here f is the frequency, and $w(f)$ is the "spectral density" (see reference 2). On this basis,

$$\eta\cong\langle a_0^2\rangle/4+\int_0^{\infty}w(f)df. \tag{31}$$

It is now a simple matter to calculate the time average fluctuation at the output of a linear filter to which $e(t)$ is supplied. Let $R(f)$ be the output of the filter in response to unit amplitude input at frequency f. Then η_0, the fluctuation in the filter output voltage, is

$$\eta_0=|R(0)|^2(\langle a_0^2\rangle/4)+\int_0^{\infty}|R(f)|^2w(f)df. \tag{32}$$

The physical conclusions reached from this are much the same as those obtained for the shot effect. For instance, as is usual with noise, η_0 increases as the band width of the filter increases.

6. SIGNAL-TO-NOISE RATIO

It is now possible to give expressions for signal-to-noise ratio for typical magnetic amplifiers.[1,5] Without specifying in detail the nature of the impedance loading, the non-linear transformers, it is not possible to arrive at specific expressions; however, if one considers an ideal band pass filter,

$$R(f)=\begin{matrix}0 & f<f_1,\\ 1 & f_1<f<f_1+\Delta f,\\ 0 & f_1+\Delta f<f,\end{matrix} \tag{33}$$

and also assumes that the filter does not load the output heavily,[6] a relatively simple expression may be obtained. For the more realistic case discussed in the last section of I,[7] where an effective transfer characteristic is developed, the noise voltage calculated in Section 5 should be considered as an "open circuit" voltage. The function $R(f)$ can then be evaluated by means of the transfer characteristic,[8] once the nature of the terminating impedance is prescribed.

In general, the frequencies which are of interest are small in comparison with the reciprocal of the flip duration, so that a good approximation to $f(t-\tau)$ is obtained with Eq. (12). In such a case, Eq. (20) reduces to

$$\begin{aligned}\alpha_k&\cong\bar{F},\\ \beta_k&\cong 0.\end{aligned} \tag{34}$$

For a typical output winding of N_w turns, Eq. (15) gives

$$F=-(8\pi m/V)N_wA\times10^{-8}. \tag{35}$$

From Eq. (30),

$$w(f)=\frac{VF^2}{8\pi m}\lim_{T\to\infty}\frac{1}{T}\int_T\left|\frac{d\bar{B}}{d\tau}\right|d\tau. \tag{36}$$

The magnetizing force is again considered to be periodic with basic angular frequency ω. If the maximum value of $\bar{B}$ (assumed symmetric about $\bar{B}=0$) is denoted by $\bar{B}_{\max.}$, Eq. (36) becomes

$$w(f)=16\omega N_w^2(m/V)A^2\bar{B}_{\max.}\times10^{-16}. \tag{37}$$

From Eq. (32) the time and ensemble mean square output fluctuation is

$$\eta_0=16\omega N_w^2(m/V)A^2\bar{B}_{\max.}\times10^{-16}\int_0^{\infty}R^2(f)df. \tag{38}$$

(The contribution of the d.c. term is negligible.) In general, one must consider loading to evaluate Eq. (38). In the case of the ideal filter of Eq. (33),

$$\eta_0=16\omega N_w^2(m/V)A^2\bar{B}_{\max.}\times10^{-16}\Delta f. \tag{39}$$

When the filter passes the κth even harmonic of ω, but does not load the non-linear transformer appreciably, the signal output voltage in the No. 2

[5] Sack, Beyer, Miller, and Trischka, Proc. I.R.E. **35**, 1375 (1947).

[6] I, Eq. (17) and Eq. (18).

[7] I, Eq. (20) to Eq. (24).

[8] I, Eq. (23).

winding is given in I as

$$e_{2\kappa} = -2CN_w^2\gamma \frac{\exp\left(-\kappa \sinh^{-1}\frac{1}{\alpha D}\right)}{(1+\alpha^2D^2)^{\frac{1}{2}}} \times \kappa\omega \sin\kappa\omega t, \quad \kappa = 2, 4, 6, \cdots \quad (40)$$

where C is the direct current input on the No. 2 winding, and γ, α, D are parameters of the core, defined in I. The r.m.s. signal-to-noise ratio is then

$$\Sigma = \frac{\sqrt{2}nCN_w(0.4\pi\mu_0/l) \exp\left(-\kappa \sinh^{-1}\frac{1}{\alpha D}\right)}{4(1+\alpha^2D^2)^{\frac{1}{2}}} \times \left(\frac{\omega V}{m\bar{B}_{\max.}\Delta f}\right)^{\frac{1}{2}}. \quad (41)$$

Certain qualitative conclusions can be reached from Eq. (41):

(a) The signal-to-noise ratio Σ increases with increase in the driving frequency, and with increase in the core volume. However, more power would be required to drive the transformers under such conditions.

(b) One should use a core material with high initial permeability, which is easily saturable, and which is magnetically fine grained. These characteristics are obviously not independent, and Eq. (39) can be used qualitatively as a guide for compromise.

In order to make calculations based on Eq. (41), one must postulate values for m, and therefore, for the volume of the elementary magnet. If this volume is assumed to be 10^{-8} cm^3 (i.e., if these elementary magnets are identified with domains), then at a fundamental frequency of 1000 cycles, and with an ideal filter of band width 100 cycles, Eq. (41) gives a threshold current of about 3×10^{-9} ampere for the operating conditions of reference 5. The observed values were in the range 10^{-8} to 2.5×10^{-8} ampere. This discrepancy may have been due to extraneous pick-up in the circuits used, or to an incorrect choice of the value for the band width. An alternative would be that the elementary magnets consist of groups of domains which would flip at practically the same instant. This would increase m and thereby yield a value of Σ in better agreement with experiment. Further experimental work is being carried out in an effort to check these points.

It should also be emphasized that although the δ function approximation of the induced voltage associated with the basic flip is convenient, it is not physically accurate for the calculation of the higher frequency noise spectrum components. A finite duration of the flip would produce a non-uniform noise spectrum, and the joint distribution function of the spectrum components would then be more complex.

Finally, it should be recalled that this noise analysis is applicable only to the unloaded case, and the case in which the magnetic amplifiers are nearly unstable has not been considered.

APPENDIX A

Table of Symbols

B	Flux density.
$\bar{B}$	Volume average of B.
H	Magnetic field intensity.
S	Saturation value of B.
m	Magnetic moment of elementary magnet.
n	Net number of elementary magnets parallel to field.
$\bar{n}$	Volume average of n.
$p(t)$	Probability function for flip of one elementary magnet.
c	Normalizing constant.
$f(t-t_i)$	Induced output voltage from a single flip.
F	Strength of voltage pulse.
G	Strength of voltage-squared pulse.
σ	Time duration of induced voltage pulse.
$\bar{e}(t)$	Ensemble average of output voltage.
$\Delta^2(t)$	Ensemble average of mean square fluctuation voltage.
ϵ	Time and ensemble average of output voltage.
η	Time and ensemble average of mean square fluctuation voltage.
η_0	Time and ensemble average of mean square fluctuation voltage after filter.
Σ	Signal-to-noise ratio.
T	Period of observation of noise.
f	$1/T$.
$w(f)$	Spectral density.
$R(f)$	Filter response.
a_k, b_k	Fourier coefficients in expansion of output voltage.
$\bar{a}_k, \bar{b}_k$	Fourier coefficients in expansion of ensemble average of output voltage.
α_k, β_k	Fourier coefficients in expansion of output voltage for a single flip.
A	Cross-sectional area of core.
l	Length of core.
N_w	Number of turns on output winding.
γ	$(0.4\pi A/l)\mu_0\times10^{-8}$.
D	$(0.4\pi/l)N_1I_{10}$.
α	$\pi\mu_0/2S$.
μ_0	Initial permeability.
N_1	Number of turns on No. 1 winding.
I_{10}	Amplitude of current on No. 1 winding.

Elasticity of Zinc Crystals

C. A. Wert and E. P. T. Tyndall
Department of Physics, State University of Iowa, Iowa City, Iowa
(Received October 4, 1948)

Young's modulus, E, has been measured by dynamic and static methods for 25 zinc single crystals. The results fit a parabolic curve when $1/E$ is plotted against the square of the cosine of the orientation. From the constants of this curve and earlier data on linear compressibility by Bridgman, are derived numerical values for the coefficients of compliance of the zinc crystal, as follows: $S_{11}=8.38$, $S_{12}=0.5$, $S_{13}=-7.31$, $S_{33}=28.4$, $S_{44}=26.1$, all $\times 10^{-13}$ cm²/dyne.

Data on three crystals were taken from room temperature to 375°C. From these may be computed Young's modulus for any orientation and any temperature in the range given. Young's modulus decreases for all orientations with increasing temperature.

INTRODUCTION

ALTHOUGH the elasticity of zinc crystals has been the subject of many investigations[1] the results obtained have differed more than might be expected solely because of the use of different methods of measurement, slight differences in the purity of the zinc, etc. The writers have, during several years past and in connection with other work, made determinations of the Young's modulus of about 25 zinc single crystals, of various orientations and of zinc of high purity. Both static[2] and dynamic[3] measurements were made. Two methods of crystal growth were employed: the horizontal mold technique in use in this laboratory for some years and several modifications of Bridgman's method.

On account of the diversity of methods of measurement, growth, etc., and because of the general consistency of results obtained it seems worth while to publish these results. Observations were also made on the variation of Young's modulus with temperature from room temperature up to 375°C.

YOUNG'S MODULUS AT ROOM TEMPERATURE

As is well known the elasticity of the zinc crystal may be expressed in terms of five moduli of compliance,[4] S_{11}, S_{12}, S_{13}, S_{33}, and S_{44}. The experimental determination of these constants follows from measurement of Young's modulus, the rigidity modulus, etc., on sets of suitably oriented crystal rods. In particular the Young's modulus E_θ of a rod, the length of which makes an angle θ, with the c-axis of the zinc lattice is given by

$$1/E_\theta = S_{33}' = (S_{11}+S_{33}-S)x^2+(S-2S_{11})x+S_{11} \quad (1)$$

or

$$1/E_\theta = Ax^2+Bx+C \quad (2)$$

in which $x=\cos^2\theta$ and $S=2S_{13}+S_{44}$. The equations show that the reciprocal of Young's modulus in any direction should be a parabolic function of $\cos^2\theta$ and that only two compliances, S_{11} and S_{33}, and a combination of two others, $(2S_{13}+S_{44})$, can be obtained from experimental values of Young's modulus alone.

The experimental values were used to determine the constants A, B and C, in Eq. (2), as follows: Seven crystals with orientations, θ, between 80° and 90°, for which $\cos^2\theta$ is very nearly zero, were used to get S_{11} or C. This can be done because the value of $1/E_\theta$ for a small value of $\cos^2\theta$ depends primarily on S_{11} and very little on A and B, so that almost any previously known set of compliances may be used to get values for A and B and then each measured modulus leads to a value of S_{11}. The seven values so obtained were averaged to give

$$S_{11}=(8.38\pm 0.06)\times 10^{-13} \text{ cm}^2/\text{dyne}.$$

The constants A and B were obtained by a rather unorthodox method. By using S_{11} as given above and Read's[5] recent values, $S_{33}=28.5\times 10^{-13}$ and $S=11.3\times 10^{-13}$ cm²/dyne, to determine A and B of Eq. (2) the value of $\cos^2\theta(=x_0)$ for which $1/E_\theta$ is a minimum was found. A plot of $1/E_\theta$ against $(x-x_0)^2$ is then a straight line of a slope, A, and intercept, $C-B^2/4A$. The experimental values of crystals of orientations less than 80° were plotted thus and fitted with a straight line, the slope of which yielded A. A value of B is not obtained too accurately from the intercept and a value of B was therefore adopted halfway between such a value and the provisional value of B, which was obtained from Read's data and $S_{11}=8.38\times 10^{-13}$. The final values were: $A=25.3$, $B=-5.30$, $C=8.38$, $\times 10^{-13}$ cm²/dyne.[6]

[1] (a) P. W. Bridgman, Proc. Am. Acad. **60**, 305 (1925); (b) E. Gruneisen and E. Goens, Zeits. f. Physik **26**, 235 (1924); (c) E. Goens, Ann. d. Physik **16**, 793 (1933); (d) A. W. Hanson, Phys. Rev. **45**, 324 (1934); (e) P. W. Bridgman, Phys. Rev. **47**, 393 (1935); (f) E. P. T. Tyndall, Phys. Rev. **47**, 398 (1935).

[2] Measurement of extension under longitudinal tension; apparatus used is described briefly in Phys. Rev. **61**, 359 (1942) and J. App. Phys. **17**, 713 (1946). A few 90° crystals were also measured by the "bending beam" method, with complete agreement with the directly measured value.

[3] The composite oscillator method of Quimby was used.

[4] For a good review of elasticity of anisotropic bodies and literature reference, see R. F. S. Hearmon, Rev. Mod. Phys. **18**, 409 (1946).

[5] T. A. Read, Phys. Rev. **58**, 371 (1940).

[6] When Read's constants alone are used one obtains: $A=25.5$[5], $B=-5.40$, $C=8.35$. It is hardly necessary to add

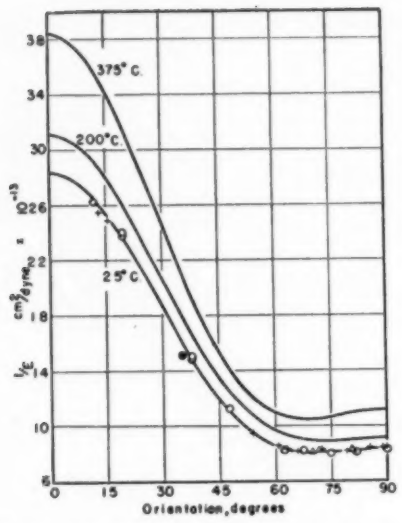

FIG. 1. Reciprocal of Young's modulus as function of orientation and temperature. On the 25°C curve circles and triangles (○●△) are for crystals measured dynamically, crosses (+) for crystals measured statically.

The lowest curve in Fig. 1 is plotted from these values of A, B, and C, and the plotted points represent the individual experimental observations. The open circles (○) and one closed circle (●) are for crystals measured dynamically at either 41 or 57 kilocycles per second. The zinc for these was Bunker Hill[7] (○) and spectrographically pure zinc[8] (●). The triangles (△) are for crystals measured dynamically by Dr. T. A. Read[9] at the Westinghouse Research Laboratories. The crosses represent crystals measured statically. These crystals were all of B. H. zinc with the exception of one made from Horsehead special zinc (New Jersey Zinc Company). The agreement of the points with the curve is in general within the experimental accuracy and no noticeable effects due to differences in growth procedure, method of measurement, or purity, seem apparent. A few of the crystals were for part of their lengths "optical mosaics,"[10] but these deviated in no detectable fashion from the others.

ELASTIC CONSTANTS

Some years ago Professor Bridgman[11] made some careful measurements of linear compressibility under hydrostatic pressure on crystals grown in this laboratory of two lots of zinc of about the same high purity as the B. H. zinc. By combining his data with the results just presented it is possible to obtain a complete set of compliances for the zinc crystal, as follows:

From the present work

$$S = 2S_{13} + S_{44} = 11.4^{6}, \tag{3}^{12}$$

$$S_{33} = 28.3^{8}, \tag{4}$$

$$S_{11} = 8.38. \tag{5}$$

From Bridgman

$$2S_{13} + S_{33} = 13.77, \tag{6}$$

$$S_{11} + S_{12} + S_{13} = 1.60. \tag{7}$$

From (4) and (6),

$$S_{13} = -7.31. \tag{8}$$

From (5), (7) and (8),

$$S_{12} = 0.5^{3}. \tag{9}$$

From (3) and (8),

$$S_{44} = 26.1. \tag{10}$$

The directly measured quantities are those given by Eqs. (3) to (7). The others, Eqs. (8) to (10), are derived, and percentage errors in the numerical values may be much greater than the experimental percentage errors in the quantities from which they are derived. The situation for S_{13} and S_{44} is not too bad. For S_{12}, however, very small errors in S_{11} and S_{13} can produce a very large error, as S_{12} is dependent largely on S_{11} and S_{13} which are almost equal in magnitude but of opposite sign. This potential error is inherent in this and other indirect methods of getting S_{12}. So far as the writers know, only Bridgman[13] has made a direct measurement of S_{12}. He obtained 0.31 and 0.48×10^{-13} cm²/dyne on

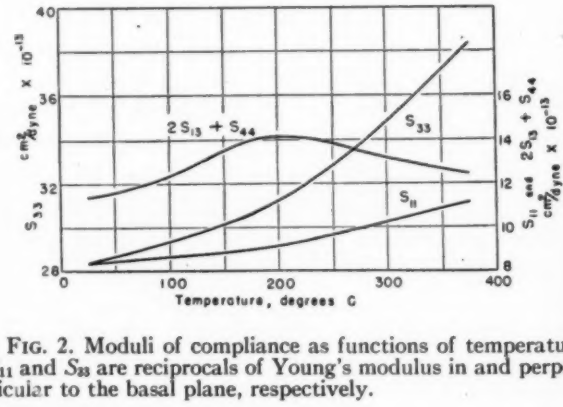

FIG. 2. Moduli of compliance as functions of temperature. S_{11} and S_{33} are reciprocals of Young's modulus in and perpendicular to the basal plane, respectively.

that the present work is, within experimental error, very nearly in agreement with Read's set of S's and that the use of his constants to get a slightly better fit is thereby justified.

[7] A commercial grade of estimated purity 99.99 percent zinc.

[8] This zinc is 99.999 percent pure. The writers are indebted to the New Jersey Zinc Company for this material.

[9] These are crystals Nos. 3, 4 and 5 of the paper by Read and Tyndall, J. App. Phys. 17, 713 (1946). No. 4 ($\theta = 70°$) was of pure B. H. zinc. Nos. 3 and 5 (72° and 81°) contained slight amounts of Pb and Sn. In communicating the results on these crystals Dr. Read stated that the $1/E$ values were slightly higher than his previous values, see reference 5.

[10] H. K. Schilling, Physics 5, 1 (1934).

[11] See reference 1, part (e).

[12] All numerical values in Eqs. (3)–(10) when multiplied by 10^{-13} are in cm²/dyne.

[13] See reference 1, part (a).

two specimens. These values and ours appear to be in as good agreement as can be expected, considering the difficulty of direct measurement and the inherent inaccuracy of indirect measurement.

The results of the writers agree well, as has been pointed out, with Read's[5] results. Of the older determinations the results of Goens[14] are closest to the present work.

ELASTICITY AND TEMPERATURE

Three crystals ($\theta=20°$, 38° and 75°) were measured by the dynamic method at a series of temperatures between 25° and 375°C. From these data S_{11}, S_{33} and $S=2S_{13}+S_{44}$ were computed as functions of temperature. A slight and obvious adjustment was made so that the value at 25°C should agree with the value on the lowest curve in Fig. 1, for each of the three crystals. From the plotted curves of S_{11} and S_{33} in Fig. 2 it is seen that Young's modulus decreases in each of the two principal directions (parallel and perpendicular to the C-axis) in the crystal, in agreement with the behavior of most metals. The third constant, S, is not the reciprocal of any of the usual elastic moduli in any direction. Its behavior may be due to increases in magnitude of S_{44} and S_{13}, but with the rate of increase in the positive constant, S_{44}, eventually getting less than that of the negative one, S_{13}. Computation of Young's modulus for temperatures between 25° and 375°C shows a decrease with rising temperature for all orientations. Two curves of $1/E_\theta$ at elevated temperatures are shown in Fig. 1 for comparison with the 25°C curve.

[14] See reference 1, part (c). Also see tabulation in reference 4, p. 429.

Electric-Field Modulation of Ultrasonic Signals in Liquids*

A. W. NOLLE**
Acoustics Laboratory, Massachusetts Institute of Technology, Cambridge, Massachusetts
(Received November 19, 1948)

An experiment is performed to determine whether the presence of a periodic transverse electric field produces modulation, either of amplitude or of phase, of a continuous progressive ultrasonic wave train passing through the liquid. One object of the experiment is to ascertain whether the application of an electric field to a polar liquid influences either the compressibility or the viscosity of the liquid through molecular orientation. The results of a related investigation in which an electric field was applied in the direction of wave travel, published in 1945 by Barone and Giacomini, were inconclusive. The present experiments reveal phase modulation in a number of conducting liquids. This is explained as a thermal effect involving the temperature dependence of velocity of sound. No evidence is found of phase modulation resulting from dipole orientation in non-conducting polar liquids. Amplitude modulation, which would result from change of attenuation, is not found in any liquid. A variety of organic liquids is investigated. Limits of sensitivity of the apparatus are given.

I. INTRODUCTION

APPLICATION of an electric field to a polar liquid produces, in the statistical sense, an orientation of the permanent molecular dipoles in the direction of the field. Such orientation might influence to a small degree the compressibility or the viscosity of the liquid, and therefore might influence the acoustic velocity of the acoustic attenuation. In 1945 Barone and Giacomini,[1] who had speculated on this possibility, as well as on the possibility that an electric or magnetic field might render a polar liquid anisotropic in compressibility, published the results of an inconclusive experiment designed to test for the existence of an electric effect. Their apparatus included a 5-mc crystal-controlled oscillator, whose quartz crystal was immersed in nitrobenzene and faced a parallel reflector 5-mm distant. A slight change in the frequency of oscillation was detected when an electric potential of 4000 volts was applied between the reflector and the front electrode of the crystal. It was not established whether the change of frequency was the anticipated result of molecular orientation, or the result of heating.

If indeed the presence of an electric field does modify the velocity of sound in a liquid, the application of a periodic electric field to a liquid, through which a steady acoustic signal is passing, should produce phase modulation of the emergent signal. Phase modulation should also accompany the initial a.c. heating of the liquid if the liquid is a conductor, as demonstrated in the final section of this paper. These two types of phase modulation can be distinguished on the basis of linear or

* This work was supported in part under Contract NObs-25391, Task No. 1, with the Bureau of Ships.
** Permanent address: Department of Physics, University of Texas, Austin 12, Texas.
[1] A. Barone and A. Giacomini, Ricerca Scient. e Ricost. 15, 264 (1945). For abstract, see R. H. Bolt and A. Giacomini, J. Acous. Soc. Am. 20, 341 (1948).

square-law dependence upon the intensity of the electric field, and on the basis of the phase relation between the phase modulation and the periodic electric field. Furthermore, if the presence of an electric field should modify the viscosity, and thus the acoustic attenuation in the liquid, the application of a periodic electric field would produce amplitude modulation of the acoustic signal. The present experiment is designed to test for the presence of these several types of modulation in acoustic signals transmitted through various liquids subjected to an alternating electric field. Provision is made for identifying the types of modulation which may be found. It will be observed that this experiment considers electric fields perpendicular to the direction of wave propagation, whereas Barone and Giacomini were concerned with fields parallel to the direction of propagation.

II. METHOD

The experimental apparatus is indicated schematically in Fig. 1. Electric signal of frequency 10 mc, power about 5 watts, is applied to a 3/8" diameter resonant quartz crystal operating in a small water tank. A similar crystal, about 10-cm distant from the source crystal, serves to receive the ultrasonic signal. The electrical output of the receiving crystal is applied to a narrow-band communications receiver. The test liquid is located in a narrow rectangular glass cell, 7 cm long, which is introduced into the water bath in such fashion that the ultrasonic signal traverses the length of the cell. Along the walls of the glass cell are plane parallel electrodes, 5 cm long, composed of platinum foil or of silver paste baked on the sides of the cell. The electrode separation is 1.6 cm. An alternating potential at 400 c.p.s. can be applied to the electrodes at r.m.s. voltages up to 1300.

The communications receiver is used with normal tuning to test for the presence of amplitude modulation, or in a detuned condition to detect phase

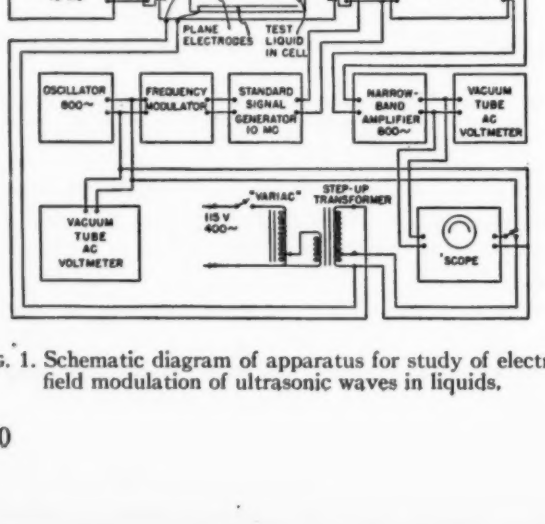

FIG. 1. Schematic diagram of apparatus for study of electric-field modulation of ultrasonic waves in liquids.

(frequency) modulation. Since the effects sought in the liquid sample are presumably independent of the polarity of the field, any modulation present should be at 800 c.p.s. A selective audio amplifier and a vacuum tube voltmeter serve to measure the modulation frequency output of the receiver. The degree of modulation is measured by a substitution method in which the input of the receiver is connected to a standard signal generator. The standard signal is set equal in amplitude and frequency to the signal from the receiving crystal. The frequency or amplitude modulation of the standard signal generator (at 800 c.p.s.) is adjusted to produce the same modulation frequency output voltage from the receiver as that created by the unknown signal.

When phase modulation is studied, an oscilloscope is used to provide phase comparison of the 800-c.p.s. modulation output of the receiver with the 400 c.p.s. voltage applied to the test cell. An initial adjustment of the system is made with the input of the receiver connected to the output of the standard signal generator, frequency-modulated at 800 c.p.s. The 800-cycle modulating signal is applied to the horizontal input of the oscilloscope, and the modulation output of the receiver is applied to the vertical plates. The receiver and the selective audio amplifier are tuned to provide an in-phase (straight-line) pattern on the oscilloscope. Then the receiver input is connected to the output of the receiving crystal, and the horizontal input of the oscilloscope is connected to the 400-c.p.s. test cell voltage. If the phase modulation produced in the test cell is the result of direct dependence of acoustic velocity upon electric field strength, the phase pattern should be a figure "8" lying on its side; if the phase modulation is the result of a.c. heating of the test liquid, the phase pattern should be a "U" or an inverted "U."

In some instances a pad of glass wool was placed in the end of the test cell to reduce standing waves. This procedure has the disadvantage that the glass wool contaminates some conducting liquids in such fashion as to increase their conductivity. Whether or not an absorbing pad was used, measurements were made at several slightly different frequencies in order that the effects of standing waves could be, to a first approximation, averaged out.

III. RESULTS

A variety of liquids, polar and nonpolar, conducting and nonconducting, were studied. In no case was there evidence of amplitude modulation; that is, there was no evidence of an electric field effect upon acoustic attenuation.

Phase modulation was found in the case of conducting liquids, but no such effect was found in the case of non-conducting liquids. The "conducting"

liquids are specifically those whose specific resistance is not greater than 5×10^6 ohms-cm, while the "non-conducting" liquids are those whose specific resistance is not less than 10^8 ohms-cm. It happened that none of the liquids considered had a specific resistance intermediate between these values. The phase test already described, as well as additional tests made in some cases as described in the following paragraphs, indicated that the phase modulation found in conducting liquids is a heating effect. Thus, no evidence was found for a direct electric field effect upon acoustic velocity in either polar or nonpolar liquids.

In the case of alcohol-water mixtures, appreciable phase modulation was found in mixtures containing 0.10, 40, and 95 percent alcohol by weight, but in the mixture containing 17 percent alcohol, whose temperature coefficient of sound velocity is zero,[2] modulation was undetectable. This finding is in agreement with the supposition that the modulation effect is due to the heating mechanism described in the final section of this paper. Also the phase of the modulation produced by water-rich mixtures was opposite to that of the modulation produced by alcohol-rich mixtures, as would be predicted from the opposite signs of the temperature coefficients of sound velocity for water and alcohol.

In those cases in which phase modulation produced an audio signal well above noise level, it was possible to measure the relative degree of modulation for several values of voltage applied to the test cell. A plot of the degree of modulation as a function of modulating voltage then indicated that the degree of modulation is proportional to the square of the modulating voltage, in agreement with the view that the modulation is due to heating. Experimental confirmation of the square-law relation was obtained in tests on *n*-butyl alcohol, conductivity water, and 1.0 molar potassium chloride solution.

It was observed in the study of water that amplitude modulation and unusually intense phase modulation are generated when voltage is applied for sufficient time to heat the sample above some 80°C. It appears likely that this phenomenon results from a variable diffraction pattern produced by electric distortion of gas and vapor bubbles which appear in the heated water, rather than from any fundamental property of the liquid. Amplitude and phase modulation at 400 c.p.s. may be observed when the glass wool absorbing material is allowed to protrude into the space between the electrodes. Probably this is an anomalous effect associated with mechanical motion of the glass fibers. Phase modulation at 800 c.p.s. was found in diethyl ether (which is nonconducting) when platinum foil electrodes were employed, but vanished when the foils were replaced by silver paste electrodes baked on the cell walls. Thus the modulation produced with foil electrodes is assumed to be a mechanical phenomenon.

[2] A. Giacomini, J. Acous. Soc. Am. **19**, 701 (1947).

TABLE I. List of liquids investigated.

Liquid	Class
n-butyl acetate	II
n-butyl alcohol	I
n-butyl chloride	II
Carbon tetrachloride	IV
Chlorobenzene	II
Chloroform	II
Dibutyl ether	II
Dibutyl phthalate	II
Diethyl ketone	I
Ethyl alcohol absolute	I
Ethyl alcohol plus water (except following entry)	I
Ethyl alcohol 17% by weight in water	V
Ethyl methyl ketone	I
n-hexane	IV
n-hexyl alcohol	I
Methyl acetate	I
Methyl propyl ketone	I
Nitrobenzene	I
Potassium chloride solutions	I
Trichloroethylene	II
Water	I

Notation: I, polar liquid with conductivity sufficient for observation of thermal modulation; II, polar liquid with very small conductivity, no observable modulation; III, nonpolar liquid with conductivity sufficient for observation of thermal modulation; IV, nonpolar liquid with very small conductivity, no observable modulation; V, conducting liquid having zero temperature coefficient of sound velocity, no observable modulation.

A list of the liquids which have been investigated appears in Table I, in which the liquids are designated as "conducting" or "non-conducting," polar or nonpolar. All experimental measurements were made in the temperature range 27–28°C.

The sensitivity of the apparatus was such that amplitude modulation should be observable for a liquid whose acoustic attenuation changes by 5×10^{-4} db/cm in an electric field of one kilovolt/cm. Sensitivity to phase modulation is such that a detectable signal should result from testing a liquid in which the relative change in phase velocity $(\Delta c/c)$ is 2×10^{-8} in an electric field of one kilovolt/cm. In view of the failure of the experiment to reveal linear amplitude or phase modulation, it is concluded that any dependence of acoustic velocity or attenuation upon electric field, in the "non-conducting" liquids listed above, is less than these limits.

IV. THE THERMAL MODULATION EFFECT

The thermal modulation observed in conducting liquids is easily explained by the nature of the temperature changes which accompany the heating of a sample of liquid by the passage of alternating current. Let the resistance of the liquid sample be R, and the voltage between electrodes be $E\sin\omega t$. The rate of heat generation in joules/sec. is

$$dQ/dt=(E^2/R)\sin^2\omega t, \qquad (1)$$

while the integrated heat delivered to the sample is

$$Q=\int_0^t dQ/dt=(E^2/2R)[t-(1/2\omega)\sin 2\omega t]. \quad (2)$$

In practice, the experiment is performed in a time short compared to the thermal lag of the liquid in its containing cell, in order that large voltage may be applied to the cell without producing severe temperature changes. Thus, the heating is essentially adiabatic. In this case, the temperature increase as a function of time is

$$T-T_0=Q/K=(E^2/2RK)[t-(1/2\omega)\sin 2\omega t], \quad (3)$$

where K is the heat capacity in joules/C° of the portion of liquid in the region of current flow.

If s denotes the length of the acoustic path in the region of heated liquid, the total phase delay of the acoustic signal in this region is $\omega_c s/c$, where ω_c is the radian frequency of the acoustic signal, and c its phase velocity. It is convenient to assume that the temperature dependence of the reciprocal phase velocity is expressible as

$$1/c=1/c_0+\alpha(T-T_0)+\beta(T-T_0)^2+\cdots. \quad (4)$$

Then, for small temperature changes, the radian phase delay of the acoustic signal in the heated region is

$$\phi=\omega_c s/c_0+(\omega_c s\alpha E^2/2RK)[t-(1/2\omega)\sin 2\omega t], \quad (5)$$

where the expression (3) for $(T-T_0)$ has been employed.

The instantaneous frequency of the acoustic signal which emerges from the heated region is

$$\omega_c'=\omega_c-d\phi/dt=\omega_c-(\omega_c s\alpha E^2/2RK)[1-\cos 2\omega t]. \quad (6)$$

The first term in the bracket represents a steady change of frequency which persists during the period of uniform temperature rise, and which produces only an initial surge in the f-m detector. The second term represents periodic frequency modulation which gives rise to audio detector output as measured in the present experiment. Thus, the peak frequency deviation effective at the detector, in c.p.s., is

$$\text{frequency deviation}=\nu_c s\alpha E^2/2RK. \quad (7)$$

A numerical example will illustrate the orders of magnitude found in the experiment. The following data apply to a test conducted on 0.05-molar potassium chloride solution:

$\nu_c=10^7$ c.p.s.,
$s=5$ cm,
$\alpha=(-)1.3\times10^{-8}$ sec./cmC°
(water data of Giacomini[2]),
$E=36.4$ v (peak value),
$R=26.5$ ohms,
$K=56$ joules/C°.

The peak frequency deviation calculated from these values by the relation (7) is 0.29 c.p.s. The observed peak frequency deviation is 0.17 c.p.s. Similar approximate agreement† was found in measurements of potassium chloride solutions whose molar concentrations were 0.02, 0.2, 0.5, and 1.0.

The reasonable agreement found here between theory and experiment indicates that the modulation technique can be refined to provide rapid measurements of the temperature coefficient of sound velocity in conducting liquids. In designing apparatus for this purpose, it would be advisable to work at a frequency somewhat lower than 10 mc, to provide a longer liquid path length than that used in the present work, to eliminate the acoustic impedance mismatch between liquid and glass cell walls (for example by using half-wave-length walls), and to operate at higher acoustic power (preferably with interrupted signals of one or two seconds duration, to avoid unnecessary heating at high acoustic level). These modifications would facilitate measurements upon liquids having small velocity temperature coefficients.

† The direction of the disagreement revealed here is that expected from the conditions of the experiment. As a result of the relatively large current densities which were required in the potassium chloride measurements, considerable irreversible chemical reaction occurred at the electrode surfaces with eventual formation of precipitate. Thus, the electric power applied to the cell was not all expended in volume heating of the liquid. Nevertheless, the values of α, calculated from the various potassium chloride solutions, while subject to the inaccuracy just stated, all agree within less than 5 percent with one another; therefore, the major effects of changes in concentration are accounted for as changes of cell resistance, in agreement with the theory outlined above. The present apparatus is not considered sufficiently precise to evaluate small changes in α due directly to changes of concentration.

Inter-Particle Interference Effects in the Small Angle X-Ray Scattering from Fine Powders*

LOUIS H. LUND** AND GEORGE H. VINEYARD
University of Missouri, Columbia, Missouri
(Received October 25, 1948)

Simple formulas for calculating the small angle x-ray scattering from aggregates of identical spherical particles, taking into account the interference between different particles, are given. The case of independent clumps of particles and the case of a more general arrangement describable by a radial density function are considered. Calculated curves of scattered intensity *vs.* angle for likely arrangements of both types are presented. The assumption that each particle scatters independently is seen to be a poor approximation whenever there is a significant amount of clumping or whenever the average density of the sample is as much as one third of the density corresponding to close packing. Estimates of particle size from the small angle scattering are shown to be seriously affected.

INTRODUCTION

THE use of small angle x-ray scattering for measuring the sizes of small particles has been described by numerous workers,[1] but it seems to have been assumed in almost every treatment[2] that the total scattered intensity could be adequately calculated as the sum of the intensities scattered by the individual particles. It is the purpose of this article to point out that the effect of interference between the rays scattered from the individual particles may easily be taken into account, that it can strongly affect the scattering, and to present calculations of the scattering patterns from aggregates of spherical particles possessing a variety of likely arrangements.

METHODS OF CALCULATION

We consider aggregates of identical spherical particles, and limit our attention to small scattering angles. The case of non-spherical particles and of heterogeneous aggregates may also be handled by straightforward methods, but the complicated calculations do not seem worthwhile at present. Suppose the sample to be irradiated by a collimated, monochromatic beam of x-rays having the direction of the unit vector $\mathbf{S}_0$. The coherent part of the electric field scattered in the direction of the unit vector $\mathbf{S}$ by the nth particle, whose center is at $\mathbf{r}_n$, may be written***

$$E_n = A\Phi(kR)\exp\{(2\pi i/\lambda)(\mathbf{S}-\mathbf{S}_0)\cdot\mathbf{r}_n\}, \qquad (1)$$

where λ is the wave-length of the x-rays, 2θ is the angle between $\mathbf{S}$ and $\mathbf{S}_0$, $k=(4\pi\sin\theta/\lambda)$, R is the radius of the particle, A is the number of electrons which it contains, and

$$\Phi(kR)=\{3/(kR)^3\}(\sin kR - kR\cos kR). \qquad (2)$$

E_n is measured in electron units.

Equation (1) is valid for scattering angles which are small compared to the angle of the first Bragg line in the case of crystalline particles, or the angle of the corresponding first peak in the case of amorphous particles, and is, of course, not dependent upon the nature of the molecular arrangement inside the particle.

$A\Phi(kR)$ may now be regarded as the form factor for the particle, precisely analogous to the ordinary

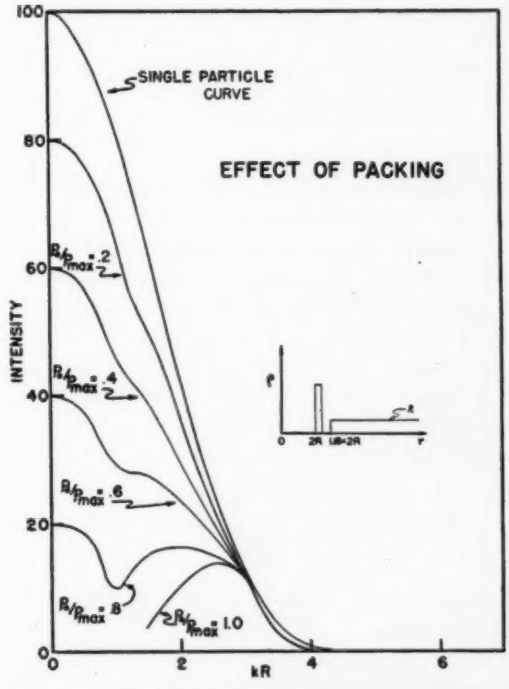

FIG. 1. X-ray scattering from samples with various amounts of packing. Radial density as shown in inset.

* Part of this work is from a thesis submitted by Louis H. Lund to the Univ. of Mo. toward the Ph.D. degree.

** Now at the University of Missouri School of Mines and Metallurgy, Rolla, Mo.

[1] Among others, A. Guinier, *Radiocristallographie* (Dunod, Paris, 1945), Chap. XII; C. G. Shull and L. C. Roess, J. App. Phys. **18**, 295, 308 (1947).

[2] Kratky (Zeits. f. Elektrochemie **48**, 587 (1942)) has treated a rather special case of interference between particles. K. L. Yudowitch (Ph.D. Thesis, U. of Mo., 1948) has taken into consideration a few of the cases discussed in the present paper. P. G. Bergmann [Phys. Rev. **74**, 1209(A) (1948)] has considered a very general situation, but has not interpreted his calculations for any actual cases.

*** See A. Guinier, reference 1.

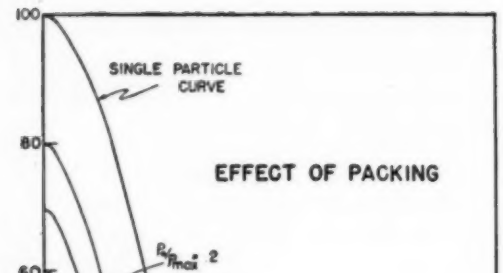

FIG. 2. X-ray scattering from samples with various amounts of packing. Radial density as shown in inset.

form factor for an atom, and the total scattered intensity from the aggregate may be calculated by summing expression (1) over all particles of the aggregate and taking the square of its absolute value. Since the aggregate will ordinarily contain enough particles so that no special orientation will be discernible, one may average the result over all possible directions of $\mathbf{S}-\mathbf{S}_0$, and obtain[3] for the total scattered intensity I,

$$I=A^2\Phi^2(kR)\sum_n\sum_m(\sin kr_{nm})/kr_{nm}, \qquad (3)$$

where $r_{nm}=|\mathbf{r}_n-\mathbf{r}_m|$.

Two general types of arrangements of the particles are considered as likely. In the first possibility, small groups of particles might clump together in definite ways at the time of formation of the aggregate, with the different clumps of particles rather well separated. For simplicity, suppose the sample contains C independent, identical clumps, with N particles in each clump. The scattering from different clumps could then be assumed independent, and the total scattering from the sample would be

$$I=CA^2\Phi^2(kR)\sum_{n=1}^{N}\sum_{m=1}^{N}(\sin kr_{nm})/kr_{nm}, \qquad (4)$$

analogous to the Debye scattering formula for a molecular gas.

In the second (and more general) type of arrangement, special clumps of particles may not be discernible, but the average number of particles with centers between r and $r+dr$ from any one particle may be written $4\pi r^2\rho(r)dr$, where $\rho(r)$ is a radial density function for particles, analogous to the radial density function for molecules in a liquid. Letting the average number of particles per unit volume of the sample be ρ_0, assuming the entire sample to be sufficiently large, and, on the average, isotropic, Eq. (3) may then be rewritten, again analogously to the conventional procedure in liquid scattering theory, as

$$I=MA^2\Phi^2\left[1+\int_0^\infty 4\pi r^2(\rho-\rho_0)(\sin kr/kr)dr\right]. \qquad (5)$$

Here M is the total number of particles in the sample.

If the sample were known to contain very nearly identical spherical particles, Eq. (5) would allow the determination of the radial density function ρ from the Fourier transform of $kI(k)$,**** just as in the determination of liquid structures. Actual samples usually contain a variety of sizes and shapes of particles, and Eq. (5) would not then be accurately applicable. In fact the introduction of any further degree of variation in the sample besides $\rho(r)$ means that at least one more unknown function enters into the determination of $I(k)$, and a measurement of the latter cannot then suffice for a unique determination of any of the unknown functions.

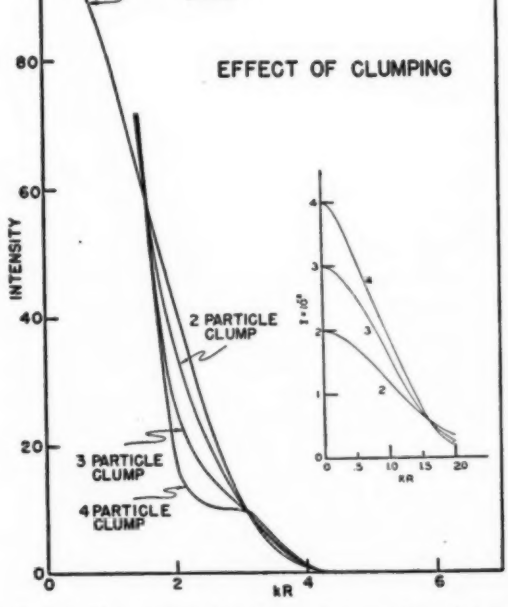

FIG. 3. X-ray scattering from clumps of particles.

[3] Compare N. S. Gingrich, Rev. Mod. Phys. 15, 90 (1943).

**** This has also been pointed out by Bergmann, reference 2.

The curious result has been announced by Guinier[4] that, "When the system is not too compact, and is composed of irregular particles, the scattered intensity is diminished because of interference between the particles in the ratio $(1-d'/d)$, d being the electronic density on the interior of the particle and d' the mean electronic density of the whole system, but the course of the curve is not much modified." In deriving this conclusion, Guinier assumes that the effect of the particles surrounding any one particle is to contribute, on the average, a *uniform* electronic density, equal to d', everywhere outside that particle. One readily shows, however, that no possible arrangement of particles exists which gives uniform average electronic density outside any one particle. Assuming randomly oriented particles, this average external density must always come to zero just at the boundary of a given particle. For the case of uniform spherical particles, the random arrangement with which Guinier is concerned would actually be represented by the following radial density function (for particles):

$$\rho(r)=0, \quad 0\leq r<2R$$
$$\rho(r)=\rho_0, \quad r\geq 2R.$$

Applying Eq. (5), one then finds

$$I=MA^2\Phi^2(kR)[1-8((4\pi/3)R^3\rho_0)\Phi(2kR)]$$
$$=MA^2\Phi^2(kR)[1-8(d'/d)\Phi(2kR)],$$

disagreeing with Guinier's result both at zero angle, through the factor 8, and in angular dependence through the term $\Phi(2kR)$. This last term alters the value of the zero angle slope of the $\ln I$ *vs.* k^2 curve, and thus affects the determination of particle sizes by conventional methods. It appears to us that inter-particle interference may not be safely neglected with any arrangement of particles whatsoever, unless d'/d is much less than 1.

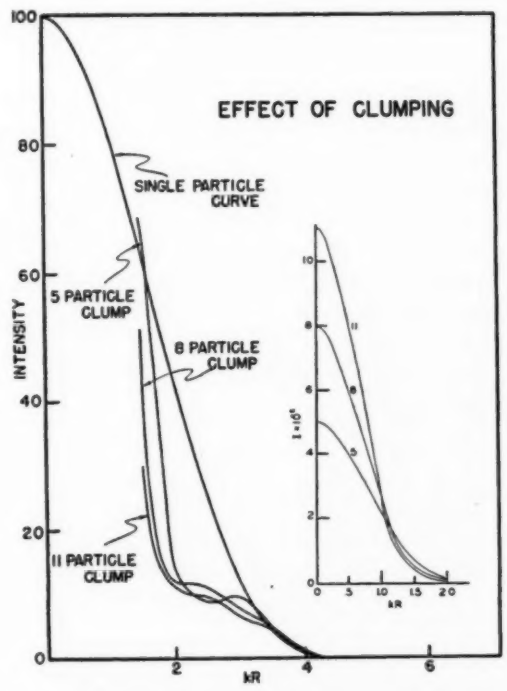

FIG. 4. X-ray scattering from clumps of particles.

[4] A. Guinier, J. d. Chim. Phys. **40**, 133 (1943).

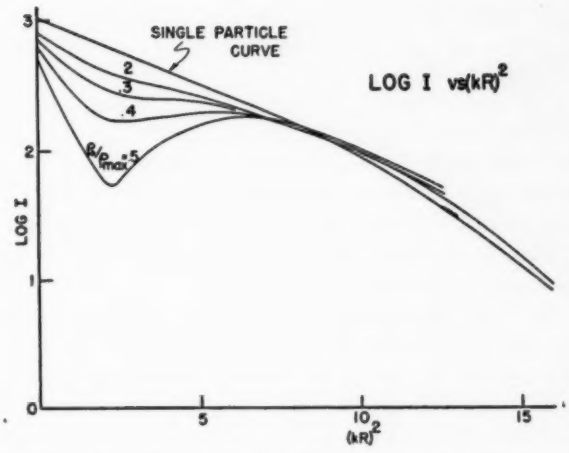

FIG. 5. Calculations of Fig. 2 replotted as logarithm of scattered intensity *vs.* $(kR)^2$.

CALCULATIONS FOR SOME SPECIFIC CASES

In order to give an idea of the extent and nature of inter-particle interference effects in some situations of likely occurrence, numerical calculations from the above formulas have been made in the following specific cases:

I. The integral in Eq. (5) has been evaluated elsewhere[5] for $\rho(r)$ of the form shown as insets in Figs. 1 and 2. These $\rho(r)$ are idealizations designed to represent the principal effects of packing at various average densities, and are discussed in the paper of Gingrich and Warren. The peak at $2R$ represents approximately $5\rho_0/\rho_{\max}$ nearest neighbor particles in each instance. The accompanying curves in these figures show the intensity calculated using these $\rho(r)$'s in Eq. (5), for various values of the parameter $\rho_0/\rho_{\max}$, where ρ_0 is the actual density in particles per unit volume, and $\rho_{\max}$ is the density of particles per unit volume corresponding to close packing of spheres. Shown also for comparison is the single particle curve, $MA^2\Phi^2(kR)$, which is simply the sum of the intensities scattered by the individual particles. The unit of intensity is so chosen that $MA^2\Phi^2(0)=100$, and MA^2 is the same for all the plots.

It is clear that the introduction of $\rho(r)$ into the calculations produces marked departures from the single particle curve, especially for values of $\rho_0/\rho_{\max}$

[5] N. S. Gingrich and B. E. Warren, Phys. Rev. **46**, 248 (1934).

near to 1. The $\rho_0/\rho_{max}=1$ curve in Fig. 1 goes negative at about $kR=1.2$ and so has not been completely drawn.

The $\rho_0/\rho_{max}=0.5$ curve in Fig. 2 shows a maximum at $kR=2.5$, with the ratio of the intensity of this maximum to that of the central maximum about 3 to 1. These figures are in close agreement with recent experimental data[6] showing a maximum in the intensity curve attributable to interference between the particles.

II. The intensity has also been calculated using Eq. (4) for clumps of 2, 3, 4, 5, 8, and 11 particles. The 2-particle clump consisted of two particles in contact. In the 3-particle clump the particles were centered on the corners of an equilateral triangle, each particle touching all others, and in the 4-particle clump, the particles were at the corners of a regular tetrahedron, each particle touching all others. The 5-particle clump was in the form of two tetrahedra possessing a common base. Three additional particles, each added to the center of one of the 3 faces of one of the 2 tetrahedra possessing a common base, gave the 8-particle clump. Three more particles, each added to the center of the 3 faces of the remaining tetrahedron, resulted in the 11-particle clump. The following table shows the frequency of occurrence of the distances in the clumps.

TABLE I. Frequency of occurrence of the distances in the clumps.

Clump	0	$2R$	$2.18R$	$3.27R$	$3.34R$	$3.99R$	Total
2-particle	2	2					4
3-particle	3	6					9
4-particle	4	12					16
5-particle	5	18		2			25
8-particle	8	36		8	12		64
11-particle	11	54	6	14	24	12	121

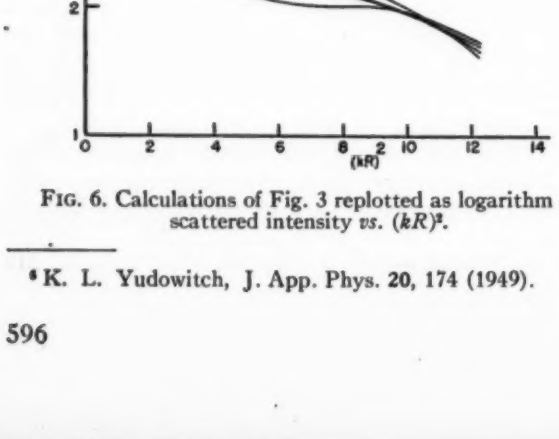

FIG. 6. Calculations of Fig. 3 replotted as logarithm of scattered intensity *vs.* $(kR)^2$.

[6] K. L. Yudowitch, J. App. Phys. **20**, 174 (1949).

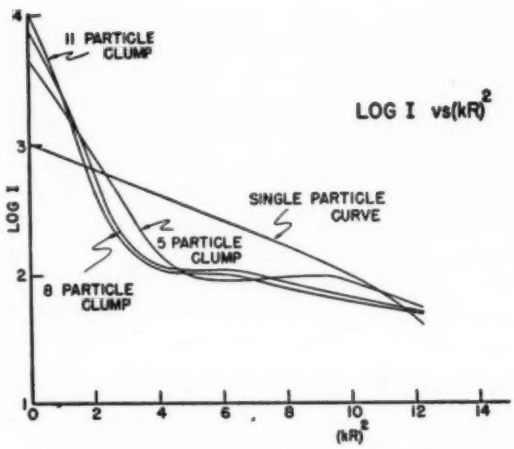

FIG. 7. Calculations of Fig. 4 replotted as logarithm of scattered intensity *vs.* $(kR)^2$.

The results of these calculations are shown in Figs. 3 and 4. There is a tendency, with increasing number of particles per clump, for the intensity curves to develop a plateau or even a slight maximum in the region between $kR=2$ and $kR=3$.

Since the single particle curve for spherical particles may be closely approximated, in the region $0\leqq kR\leqq 1.5$, by

$$I=A^2M\exp\{-(kR)^2/5\}, \tag{6}$$

the radius of the spherical particle may be expressed directly in terms of α, the slope of the straight line portion of the curve obtained from a plot of $\ln I$ *vs.* k^2. Thus,

$$R=2.24(-\alpha)^{\frac{1}{2}}. \tag{7}$$

For samples assumed to be made up largely of identical spherical particles, Eq. (7) has been rather extensively used for particle size determination.

To show a possible source of error in such determinations, we have plotted in Figs. 5, 6 and 7, $\log I$ *vs.* $(kR)^2$ for the intensity curves of Figs. 2–4. It is clear that if the particles in the sample are so arranged that their distribution in space cannot be considered purely random, but describable either in terms of a $\rho(r)$ function or in terms of clumping, Eq. (7) no longer suffices for an accurate determination of R. Indeed, a calculation of the slope, for example, of the straight line portion of the 11-particle curve of Fig. (7) shows it to be 6.63 times as large as the slope of the single particle curve. Use of Eq. (7), then, would result in the determination of an R which is too large by a factor of about 2.6.

It is easy to show, however, that the $\log I$ *vs.* $(kR)^2$ curves corresponding to calculation of I from Eqs. (4) and (5) are linear over a small range of $(kR)^2$. Hence, it is possible to modify Eq. (7) so

that R can again be calculated from the slopes of the straight line portions of the log$I$ *vs.* $(kR)^2$ curves.

The preceding considerations make it clear, however, that use of Eq. (7) without modification is justified only when the arrangement of the particles in the sample is known to be such as to preclude such typical interference effects as we have considered.

Finally, it should be noted that slit width corrections, and range-of-wave-length corrections are usually needed, besides inter-particle interference corrections, before quantitative agreement with experiment can be had.

Synthesis of n-Reactance Networks for Desired Transient Response

PIERRE R. AIGRAIN
Centre d'Etudes et de Recherches de la Marine Francaise, Ecole Normale Superieure, Paris, France
AND
EVERARD M. WILLIAMS
Carnegie Institute of Technology, Pittsburgh 13, Pennsylvania
(Received November 5, 1948)

This paper deals with the problem of synthesizing a network with n-reactances and an associated necessary number of resistances which will have a transient response most nearly equal, in the least square sense, to a desired transient response when excited with some particular input voltage or current impulse. A method is derived for this synthesis in the cases for which the Laplace transform of the input impulse contains no poles or one pole at $s=0$. The significance of this method with relation to synthesis techniques based on steady-state considerations is discussed, and the method is illustrated for a simple case.

NETWORKS synthesized for desired transient response are used extensively in communication systems. Examples of such networks are video coupling systems, delay lines, and telegraph line equalizers; this aspect of their purpose is, however, obscured because their synthesis is usually based on steady-state concepts. Synthesis methods originating from steady-state considerations have been applied by Lee,[1] Wheeler,[2] Butterworth,[3] Marcuvitz,[4] and others for quite general cases and by Kallman,[5] Blewett and Rubel,[6] for structures used as delay transmission lines. Synthesis of a network from steady-state considerations, however, insures only that the network has good transient properties rather than that the network synthesized is the optimum for the number of circuit elements used. The purpose of this paper is to describe a general method derived from transient considerations for synthesis of networks with an arbitrary number of reactances n (and some necessary associated number of resistance elements) which will have the closest possible transient response to some desired response. This method is applicable to several forms of input signal and it is not necessary that the desired output be of the same form as the input. The term closest possible, or optimum approximation, is used in the "least square" sense.

The method of attack on the problem is the following: let the desired response and the actual response of the network be designated as $f(t)$ and $g(t)$, respectively. The least square integral D, is[7]

$$D=\int_0^\infty [g(t)-f(t)]^2 dt. \tag{1}$$

This integral is a measure of departure of the actual response from the desired response and has an ideal value of zero when the actual response and

[1] Y. W. Lee, "Synthesis of electric networks by means of the fourier transforms of Laguerre's Functions," J. Math. and Phys. **11**, 83–113 (1932).
[2] H. A. Wheeler, "Wide-band amplifiers for television," Proc. I.R.E. **27**, 429–437 (1939).
[3] S. Butterworth, "On the theory of filter amplifiers," Exp. Wireless and Wireless Eng. **7**, 536–541 (1940).
[4] N. Marcuvitz, "Distortionless correction of video networks," M.E.E. Thesis, Polytechnic Institute of Brooklyn, June 1941.
[5] Heinz E. Kallman, "Equalized delay lines," Proc. I.R.E. **34**, 646 (1946).
[6] J. P. Blewett and J. H. Rubel, "Video delay lines," Proc. I.R.E. **35**, 1580 (1947).

[7] If $f(t)$ is the Dirac delta-function, this definition must be revised in order to obtain a convergent integral. The case considered in detail in this paper uses the Dirac function but the integral is left in the above form so that it may be followed more readily. The revised error integral with the Dirac function should in fact be:

$$D=\int_0^\infty [g(t)^2-2f(t)g(t)]dt.$$

It may readily be verified that the results (5) will be obtained if this convergent integral is used. The error integral for this case has been discussed by Hansen; see W. W. Hansen, "Transient response of wide-band amplifiers," Proc. Nat. Elec. Conf. **1**, 544–553 (1944).

desired response are identical. The actual response $g(t)$ will be written in terms of circuit parameters $\xi_1, \xi_2 \cdots$ and substituted in the above integral. The optimum values of these parameters will then be determined by solving the simultaneous equations:

$$\partial D/\partial \xi_1 = 0, \quad \partial D/\partial \xi_2 = 0, \quad \text{etc.}$$

The steps of this procedure are very considerably simplified by using Laplace transforms.[8] The details of this procedure vary slightly with the form of the input signal; it will be illustrated for an input "delta" impulse, or impulse of infinite amplitude, infinitesimal duration and unit area.

The impulse response of a circuit is described by its "operational transfer impedance," which will be designated by $G(s)$ or, using a common notation,[8]

$$G(s) = Lg(t) = \int_0^\infty (e^{-st} g(t))dt, \; g(t) = L^{-1}G(s). \quad (2)$$

It is demonstrable that for physically realizable circuits $G(s)$ is the quotient of two polynominals, the denominator being of degree n (the number of reactances) and the numerator of degree less than n. The knowledge of $G(s)$ is sufficient for the determination of a circuit[9,10] so that the problem becomes one of finding the coefficients of the numerator and denominator polynominals of $G(s)$ which will minimize the integral D. If the zeros of the denominator are $s_1, s_2 \cdots s_n$ the partial fraction expansion of $G(s)$ may be written

$$G(s) = \sum_{p=0}^{n} \frac{A_p}{s - s_p}, \quad (3)$$

in which the coefficients $A_1, A_2 \cdots A_n$ are defined by this expansion. The optimum circuit will be that corresponding to the resulting $G(s)$ when $s_1, s_2 \cdots A_1, A_2 \cdots$ have the values which minimize the integral (1). These values are obtained from equations of the families:

$$\partial D/\partial A_p = 0, \quad \partial D/\partial s_p = 0. \quad (4)$$

Using the notation (involving the desired transient response $f(t)$):

$$F(s) = Lf(t) = \int_0^\infty e^{-st} f(t)dt,$$

the following identities may be derived:

$$\frac{\partial D}{\partial A_p} = \frac{\partial}{\partial A_p}\int_0^\infty [f(t) - L^{-1}G(s)]^2 dt$$

$$= 2\int_0^\infty [f(t) - L^{-1}G(s)]L^{-1}\frac{1}{s - s_p}dt$$

$$= 2\int_0^\infty [f(t) - L^{-1}G(s)]e^{s_p t}dt$$

$$= 2[F(-s_p) - G(-s_p)].$$

$$\frac{\partial D}{\partial s_p} = 2\int_0^\infty [f(t) - L^{-1}G(s)]L^{-1}\frac{A_p}{(s - s_p)^2}dt$$

$$= 2A_p\int_0^\infty [f(t) - L^{-1}G(s)]te^{s_p t}dt$$

$$= 2A_p\int_0^\infty \frac{\partial}{\partial s}[f(t) - L^{-1}G(s)]e^{s_p t}dt$$

$$= 2A_p\left[\frac{\partial}{\partial s}F(s) - \frac{\partial}{\partial s}G(s)\right]_{s=-s_p}.$$

Therefore the system of equations corresponding to (4) is:

$$F(-s_p) = G(-s_p), \quad (5)$$

$$\frac{\partial}{\partial s}F(s)_{s=-s_p} = \frac{\partial}{\partial s}G(s)_{s=-s_p}. \quad (6)$$

These are the $2n$ simultaneous equations necessary for the determination of $A_1 \cdots A_n$ and $s_1, s_2 \cdots s_n$. If, for example, the desired response $f(t)$ is a delta impulse delayed by a time unity, so that

$$F(s) = e^{-s},$$

the coefficients of $G(s)$ must be such that

$$G(-s_p) = e^{s_p},$$

$$\frac{\partial}{\partial s}G(s)_{s=-s_p} = -e^{s_p}.$$

If the input function is some function of time, $y(t)$, other than the delta impulse for which the above analysis was carried out the Eqs. (5) and (6) involve the transform of $y(t)$, which will be designated $\phi(s)$, and become

$$G(-s_p) = \frac{F(-s_p)}{\phi(-s_p)},$$

and

$$\frac{\partial}{\partial s}G(s)_{s=-s_p} = \frac{\partial}{\partial s}\left[\frac{F(s)}{\phi(s)}\right]_{s=-s_p}.$$

[8] See, for instance, M. F. Gardner and J. L. Barnes, *Transients in Linear Systems* (John Wiley and Sons, Inc., New York, 1942).

[9] Ernst Guillemin, *Communication Networks* (John Wiley and Sons, Inc., New York, 1931–35).

[10] O. Brune, "Synthesis of a finite two-terminal network whose driving-point impedance is a prescribed function of frequency," J. Math. and Phys. **10**, 191–236 (1931).

If $\phi(s)$ has poles of its own, however, the s_p will have to include these poles. Unless $G(s)$ is taken more generally than previously assumed the above condition may very well result in more equations than unknowns so that the method herein described is generally applicable only to input functions for which $\phi(s)$ has no poles. In the important case of the step function input, for which $\phi(s)=1/s$, the problem can be handled by satisfying Eqs. (5) and (6) for the poles of $G(s)$ exclusively, then adding to $G(s)$ a constant term which will make the response at zero frequency equal to the final value of $f(t)$. This constant term requires an added resistance in series with the synthesized network.

The results of this analysis can be expressed in the following general form:

Let the circuit transfer impedance of an n-reactance network, the Laplace transform of a specified input and the Laplace transform of an (arbitrary) desired response function of time $f(t)$ be $G(s)$, $\phi(s)$ and $F(s)$ respectively. The Laplace transform of the input must contain no poles except for the case in which this transform is $\phi(s)=1/s$. For the circuit response to be the best obtainable approximation (in the least square sense) to the desired response $f(t)$ it is necessary that:

$$G(s)=\frac{F(s)}{\phi(s)}, \quad \frac{\partial}{\partial s}G(s)=\frac{\partial}{\partial s}\frac{F(s)}{\phi(s)}$$

at the opposite (negative) of each pole of $G(s)$.

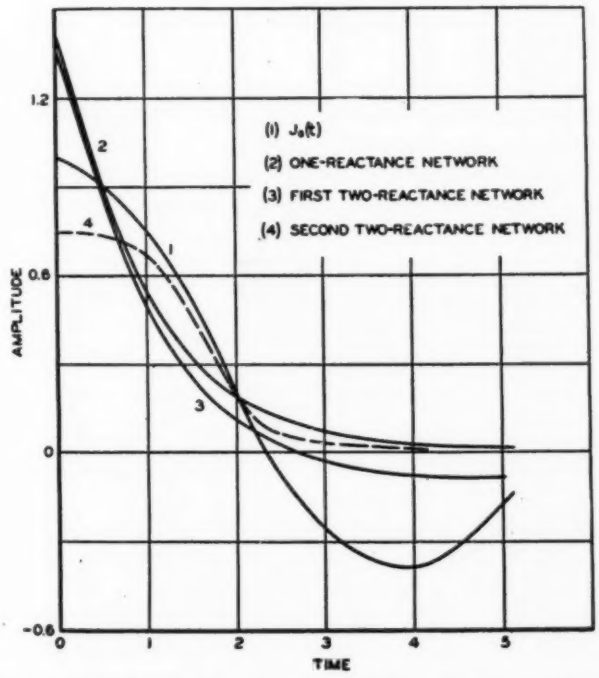

FIG. 1. Form of $J_0(t)$ response together with responses of one-reactance and two two-reactance approximations.

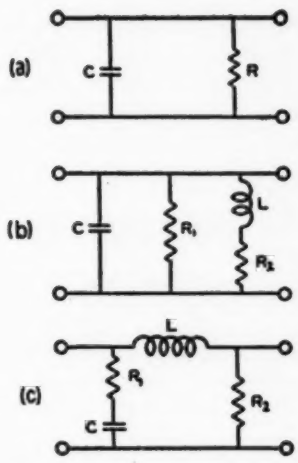

FIG. 2. Circuits corresponding to curves of Fig. 1 synthesized for current pulse input (milliamperes), time in microseconds, and voltage output.

(a) one-reactance approximation:

$R=1410$ ohms
$C=0.00071$ mf

(b) first two-reactance approximation:

$R_1=1230$ ohms $\quad L=772$ microhenries
$R_2=1080$ ohms $\quad C=0.0009$ mf

(c) second two-reactance approximation:

$R_1=2250$ ohms $\quad C=0.0006$ mf
$R_2=1450$ ohms $\quad L=420$ microhenries

Application of this method in any particular instance may result in several optimum transfer impedances, each of which is optimum with respect to adjacent values of its parameters. The best of these transfer impedances may be selected by evaluating the integral (1) for each.

The system of simultaneous equations obtained from (5) or (6) solves the problem entirely from a mathematical point of view. This system, however, often contains transcendental terms which render the process of obtaining the actual roots quite possibly uneconomical unless highly specialized computers are available. This difficulty arises, for instance, in the delay line problem. When a small number of reactances is involved, however, a direct solution is practicable; such a case is illustrated in the appendix. Owing to the difficulty of completing solutions, in general the method described in this paper is believed to be of use primarily as a check on circuit designs derived by other means and because of its interest in connection with network theory. In connection with network theory, for example, it should be observed that Eqs. (5) and (6) do not involve the relative values of $G(s)$ and $F(s)$ on the imaginary axis of the s plane (i.e., phase and amplitude response of the circuit under consideration, compared with those of an ideal circuit having exactly the desired response) but rather they involve the relative values of $G(s)$ and $F(s)$ in a region of the complex s plane situated

entirely to the right of the imaginary axis, since all the poles of $G(s)$ must lie in the left-hand side of the s plane. These loci offer an explanation for the not entirely satisfactory results obtained by design methods based exclusively on steady-state phase and amplitude response.

APPENDIX

As an example of the application of the method described in this paper assume that it is desired to find circuits with a transient response to the delta-impulse which is most nearly $J_0(t)$ (Bessel Function of first kind and order zero). The approximation will be found for the one-reactance and two-reactance cases. In the case of $J_0(t)$

$$F(s) = LJ_0(t) = (1+s^2)^{-\frac{1}{2}}.$$

The solution of the system of Eqs. (5) for one-reactance can be shown to be

$$G(s) = 1.41/(s+1), \quad g(t) = 1.41e^{-t}.$$

and for two-reactances there are two possible solutions,

$$G(s) = \frac{0.19+1.37s}{0.27+1.03s+s^2}, \quad g(t) = 1.37[1-0.377t]e^{-0.52t};$$

or

$$G(s) = \frac{5.40+0.75s}{3.73+3.86s+s^2}, \quad g(t) = 0.75[1+5.28t]e^{-1.93t}.$$

The responses of these circuits are shown in Fig. 1 together with $J_0(t)$ for comparison. The two solutions for the two-reactance case represent optimum circuits with respect to nearby values of the parameters; one of these circuits is, however, possibly better (and therefore the best possible two-reactance approximation) than the other; this could be selected by comparing the integral (1) for the two circuits.

The actual circuits represented by the above solutions depend upon the units of current, voltage, and time and upon whether the functions $G(s)$ are regarded as admittances or impedances, or, in effect, whether the input and output signals of interest are of voltage or current. If it is assumed, for instance, that the desired networks (four terminal) are excited with a delta-pulse of current (milliamperes) and the selected $J_0(t)$ output is a voltage signal, timed in microseconds, the simplest circuits represented by the three solutions are those shown in Fig. 2.

An Electro-Mechanical Device for Solving Non-Linear Differential Equations

CARL A. LUDEKE
University of Cincinnati, Cincinnati, Ohio
(Received August 16, 1948)

This paper introduces an electro-mechanical device for solving some non-linear differential equations. Solutions are obtained with sufficient accuracy and speed so that an entire domain of solutions can be quickly investigated. The procedure not only avoids the limited point of view inherent in the solutions obtained by most mechanical means, but also retains sufficient accuracy so that its solutions can be used as a starting point for numerical methods if further accuracy is desired. Examples are given of results obtained on some non-linear differential equations.

INTRODUCTION

THE purpose of this paper is to show that it is possible to construct a simple electro-mechanical apparatus capable of investigating, with considerable accuracy, phenomena described by non-linear differential equations; and that this mechanical procedure finds its place beside the topological and analytical methods used in non-linear mechanics today. The subject of non-linear differential equations is very incomplete, and the chief advances to date have been accomplished by combining the qualitative and all-inclusive procedures of topological methods with the quantitative but more restricted methods of expansions in terms of suitable parameters.[1] However, both of these methods have serious limitations; and there is need for some method of investigation which has the ease and breadth of operation of topology, is suitable for

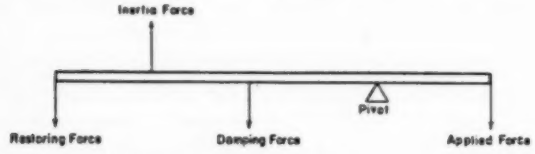

FIG. 1. Diagram of system.

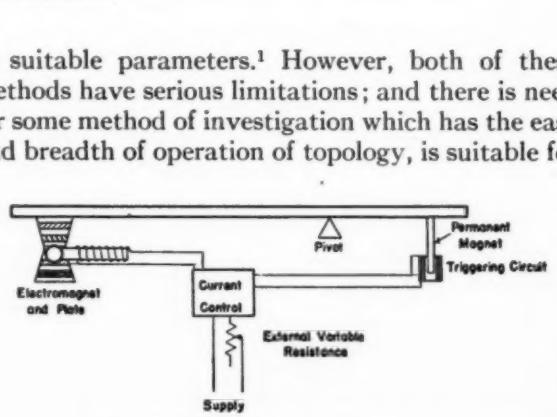

FIG. 2. Diagram of damping system.

[1] The reader will find good introductions to the present methods of solving non-linear differential equations in the following: N. Minorsky, *Introduction to Non-Linear Mechanics* (Edwards Brothers, Ann Arbor, Michigan, 1947); K. O. Friedricks and J. J. Stoker, pp. 1–78 of a set of notes corresponding to a series of twenty lectures organized under the Program of Advanced Instruction and Research in Mechanics at Brown University and delivered during the winter semester of the academic year 1942–43.

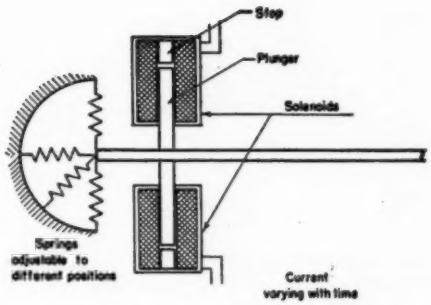

FIG. 3. Diagram of restoring system.

numerical solutions, and is not limited to a narrow field of parametric values.

If we turn to mechanical aids as a solution to our difficulties, we must first consider two methods already in common usage, namely; integration by numerical methods with the aid of computing machines, and integration by means of the differential analyzer. Both of these methods are accurate and applicable to a wide variety of problems, but they too have limitations.

In a previous paper,[2] the author indicated that many of the difficulties of existing methods could be overcome by generating physical solutions to the differential equations under consideration. We cannot, of course, expect such solutions to have the same accuracy as mathematical solutions, but a physical solution with reasonable accuracy can often point the way toward the proper general mathematical approach, or if a specific solution is needed to greater accuracy it can certainly be used as a starting point for numerical computations. This general idea is of course not new,[3] the real problem is involved in constructing a physical system which represents the differential equation with sufficient accuracy and at the same time allows the parameters involved to be changed through a large range with ease and accuracy. With these general points in mind, let us turn now to a consideration of the differential equation which the analog is to represent.

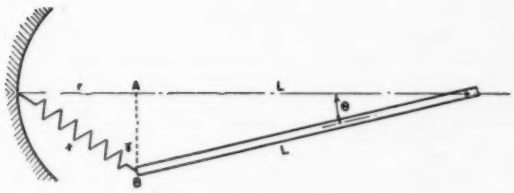

FIG. 5. Diagram of non-linear spring.

THEORY

If we restrict ourselves to systems with one degree of freedom, one general non-linear differential equation dealing with vibration phenomena would be of the form:

$$d^2\theta/dt^2+\psi_1(\theta, t)(d\theta/dt)^n+\psi_2(\theta, t)=\psi_3(t), \quad (1)$$

in which, as indicated, ψ_1 and ψ_2 are functions of θ and t, ψ_3 is a function of t only, and n is a constant. In Eq. (1) the first term can be considered as an inertia "force," the second term a damping "force," the third term a restoring "force," and the term on the right side of the equation, an applied "force." The terms containing ψ_1 and ψ_2 would contribute to the non-linearity of the equation because each is a function of the dependent variable, θ. Equation (1) can be represented by the physical system shown diagrammatically in Fig. 1, in which a horizontal beam pivoted about a horizontal axis perpendicular to the axis of the beam is acted on by the four forces previously mentioned.

Consider first the damping force represented by the term $\psi_1(\theta, t)(d\theta/dt)^n$. This term can be simulated by the device shown in Fig. 2. In this device, damping is produced by means of an electromagnet and a plate inserted between the magnet poles and fastened to the beam. The plate can be made with varying cross section, varying thickness, and of strips of different material so as to get many types of functions $\psi_1(\theta, t_0)$. By means of a triggering circuit and current control, n can be made to assume various values. Further variations in ψ_1 with respect

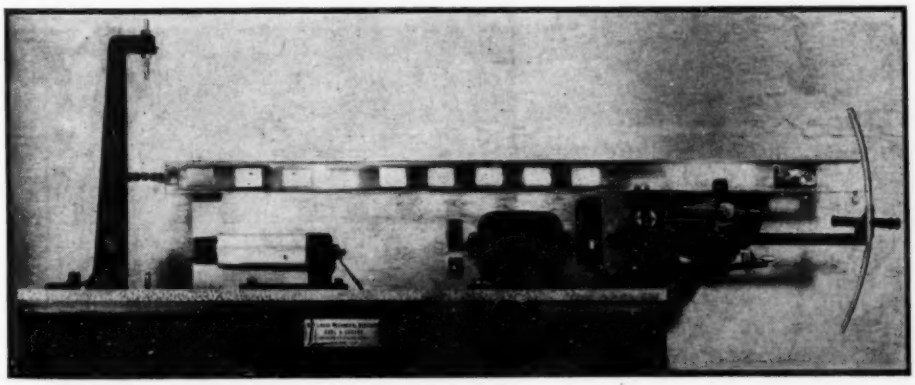

FIG. 4. Photograph of non-linear mechanical generator.

[2] C. A. Ludeke, J. App. Phys. **17**, 603–609 (1946).
[3] Lord Kelvin, Proc. Roy. Soc. London **24**, 269 (1876).

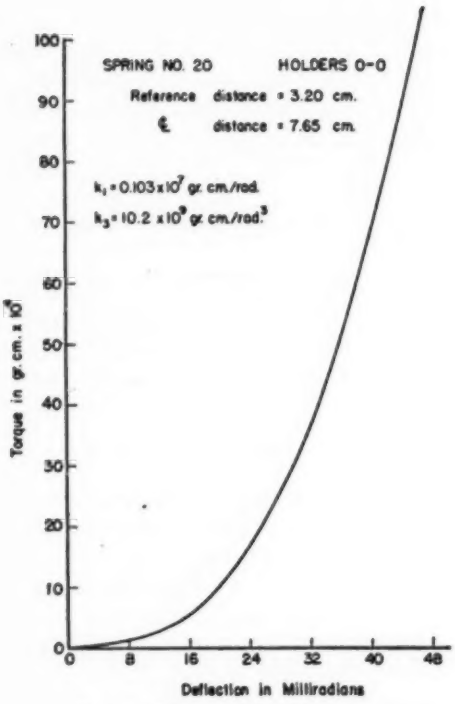
SPRING NO. 20 HOLDERS 0-0
Reference distance = 3.20 cm.
ℓ distance = 7.65 cm.
$k_1 = 0.103 \times 10^7$ gr. cm./rad.
$k_3 = 10.2 \times 10^9$ gr. cm./rad.^{3}
Torque in gr. cm. x 10^3
Deflection in Milliradians

FIG. 6. Torque deflection curve.

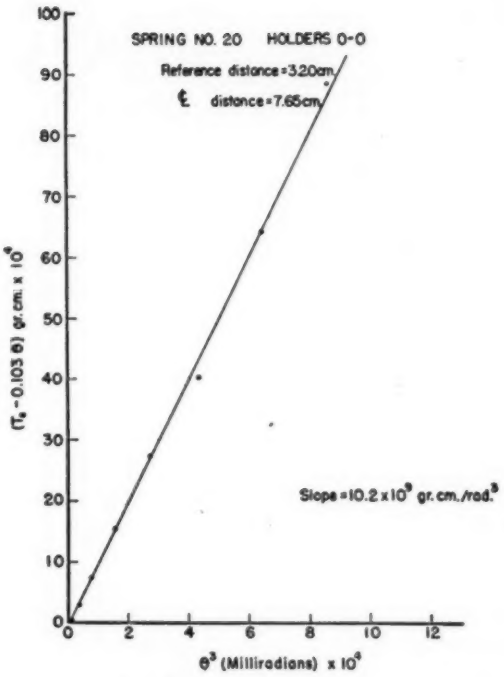
SPRING NO. 20 HOLDERS 0-0
Reference distance = 3.20cm.
ℓ distance = 7.65cm.
Slope = 10.2×10^9 gr. cm./rad.^{3}
$(T_0 - 0.103\,\theta)$ gr. cm. x 10^3
θ^3 (Milliradians) x 10^6

FIG. 7. Determination of k_3.

to t only can be accomplished by an external variable resistance. If negative damping is desired, an ironclad solenoid with plunger and stop can be used in conjunction with the triggering circuit and current control. Such a device will put energy into the system as a function of θ, t and $d\theta/dt$.

Consider next the restoring force represented by the function $\psi_2(\theta, t)$. This force can be generated by means of a spring system and a solenoid with plunger and stop as shown in Fig. 3. The spring system is used to introduce a restoring force which is a function of θ, while the solenoid introduces a force which varies with time. By changing the position of the stop the solenoid can also be used to introduce a force which is a function of displacement.

Finally, the applied force represented by $\psi_3(t)$ can be introduced by means of rotating unbalances, and by masses moving with reciprocating motion perpendicular to the plane of the beam and its axis of rotation.

After some consideration as to the type of non-linear problems which seemed of immediate importance, it was decided to restrict Eq. (1) in the initial stages of the investigation to the form,

$$I(d^2\theta/dt^2)+\beta(d\theta/dt)+f(\theta)=P_0 \sin\omega t, \qquad (2)$$

in which I, β, P_0, ω, are constants; and all of the non-linearity is introduced in the function $f(\theta)$. Before constructing an apparatus to generate the type of motion described mathematically by Eq. (2) it was necessary to decide on the form of $f(\theta)$ and P_0. An odd function of the form $k_1\theta+k_3\theta^3$ where k_1 and k_3 are constants seemed most suitable for $f(\theta)$; and since the forcing function was to be simulated by a rotating unbalance, P_0 was chosen in the form $mrl\omega^2$. Thus Eq. (2) becomes

$$I(d^2\theta/dt^2)+\beta(d\theta/dt)+k_1\theta+k_3\theta^3=mrl\omega^2 \sin\omega t, \qquad (3)$$

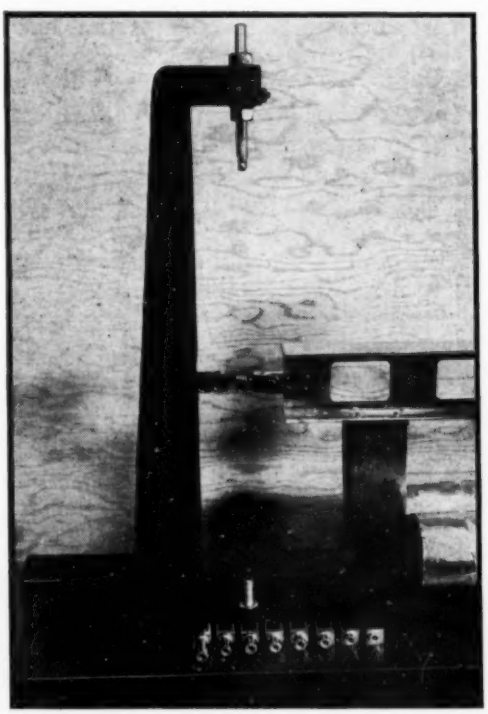

FIG. 8. Photograph of non-linear spring holders.

in which:

I = the moment of inertia of the vibrating system,
β = the coefficient of viscous damping,
k_1 and k_3 are constants used in fitting the torque-deflection curve,
m = the mass of the unbalance,
r = the radius of the unbalance,
l = the distance from the center of rotation of the unbalance to the center of rotation of the system,
ω = the constant angular velocity of the unbalance,
θ = the angular displacement of the vibrating system,
t = the time.

Having decided upon Eq. (3) as representing the non-linear system to be investigated, it remains to be seen just how satisfactorily a mechanical analog can be constructed.

APPARATUS

In Fig. 4 is shown a photograph of the apparatus exclusive of the recording drum. The base of the vibrator consists of a heavy casting which is securely fastened to a concrete pier. The base itself is made in the form of a lathe bed with two T rails onto which the component parts of the vibrator are clamped. On the right end of this base is clamped a cast iron support which serves as a mounting for the ball bearings about which the vibrating structure pivots. The basic part of the vibrating structure is a balanced aluminum I beam which pivots on steel pins that are inserted in the above-mentioned bearings.

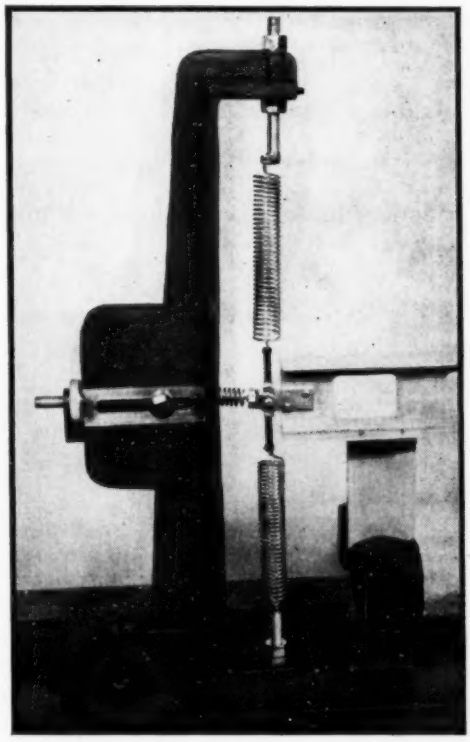

FIG. 9. Photograph of combination spring holder.

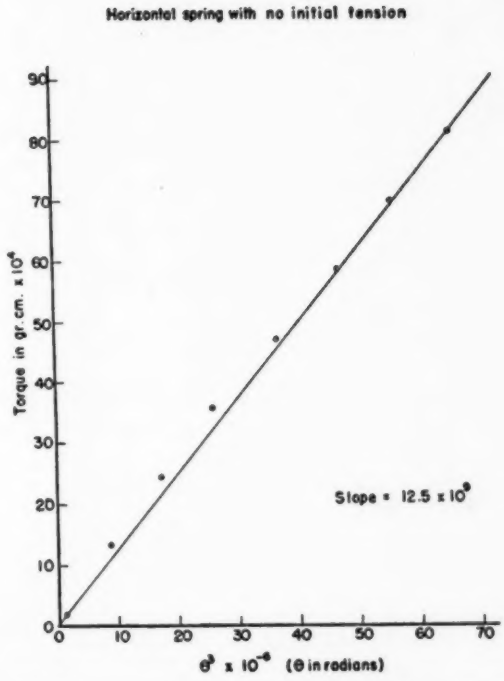

FIG. 10. Torque *versus* cube of deflection for a horizontal spring with no initial tension.

On the right end of the I beam there are mounted two unbalances which rotate on a shaft parallel to the axis about which the beam rotates and perpendicular to the beam itself. These unbalances are rotated by means of a $\frac{1}{2}$ hp 110-volt d.c. shunt wound motor which is clamped just to the left of the casting which supports the bearings. The motion is transmitted from the motor to the unbalances by means of (a) enclosed change gears; (b) a universal joint which is mounted with the intersection of its pin center lines on the axis of rotation of the beam so that the beam is free to pivot while the universal joint rotates; (c) a shaft and pair of spiral gears which transmit the motion from the universal joint to the unbalance shaft itself.

At the left end of the base is clamped a cast iron spring support to which one end of the spring system is fastened. This support contains adjustments for varying the tension in the spring system. The other end of the spring system is fastened to the beam itself by means of a ball bearing pivot which reduces friction losses to a minimum. To the right of the spring support and to the left of the motor there is fastened to the base an electromagnet whose pole pieces have a narrow gap which is parallel to the beam. Into this gap is inserted an aluminum strip which is fastened to the beam and vibrates with it. This constitutes the electro-magnetic damper.

In operation, the rotating unbalances supply the forcing energy which causes the beam to rotate. The restoring force is supplied by the spring system and the damping force is supplied by the electromagnet.

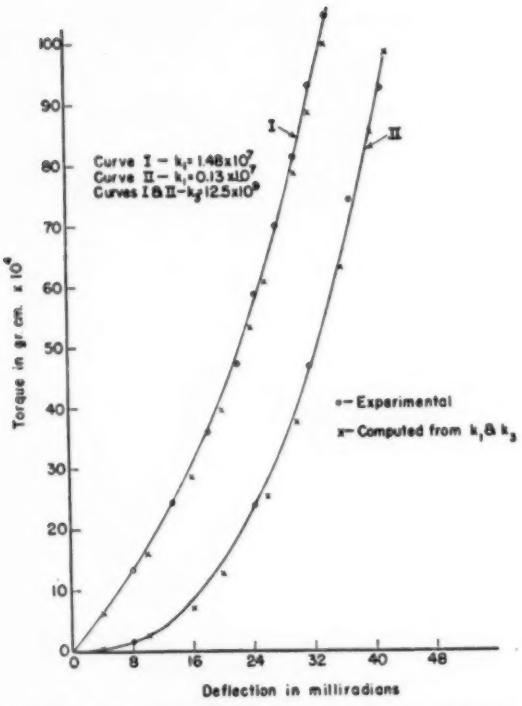

FIG. 11. Typical torque deflection curves obtained with the combination spring holder.

We see therefore that the vibrator simulates the system described by Eq. (3).

The two parts of the apparatus which need careful checking are the spring system and the electromagnetic damper. Consider first the spring system shown diagrammatically in Fig. 5, where:

r = length of spring when beam is horizontal,
θ = angle through which beam is depressed,
x = length of spring when beam is depressed through angle θ,
τ_i = tension in spring when $\theta = 0$,
$AB \cong \theta L$.

As θ changes, the component of τ_1 in the direction of AB is given by,

$$\tau_i \cos\gamma = \tau_i \theta L (r^2 + \theta^2 L^2)^{-\frac{1}{2}}. \quad (4)$$

The elongation due to displacement θ is given by,

$$x - r = (r^2 + \theta^2 L^2)^{\frac{1}{2}} - r. \quad (5)$$

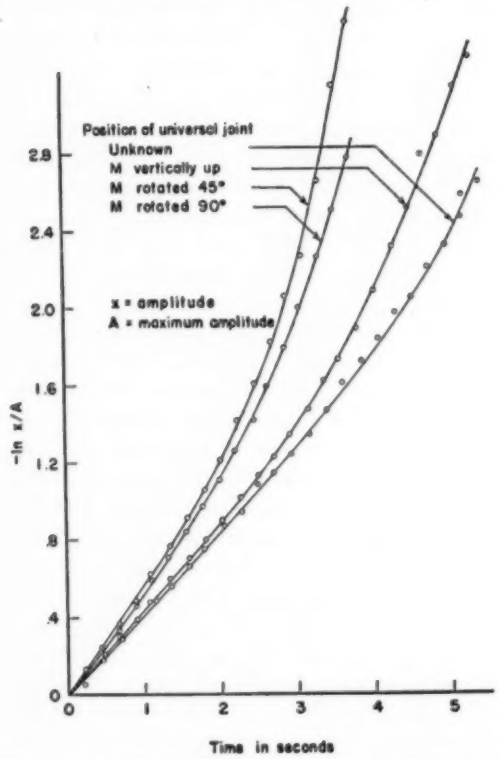

FIG. 12. Logarithmic decrement curves obtained with universal joint in fixed positions.

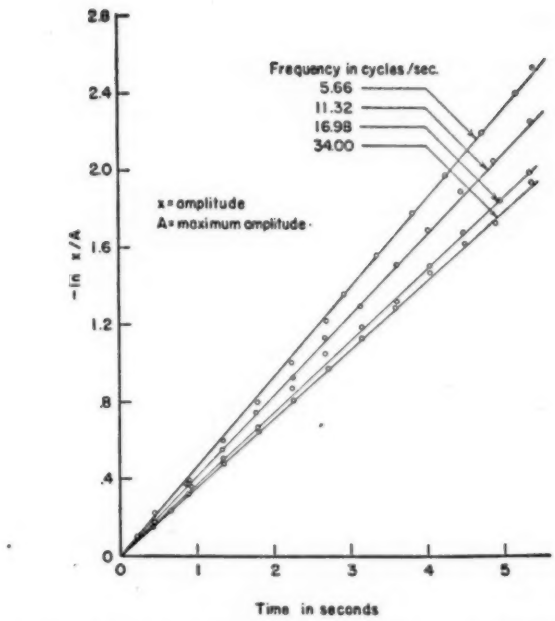

FIG. 13. Logarithmic decrement curves obtained with universal joint rotating.

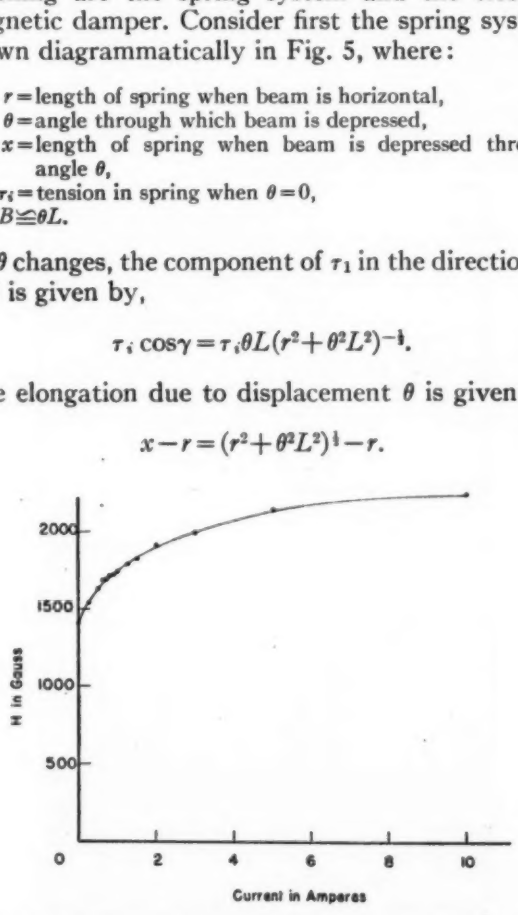

FIG. 14. Relationship between the field strength and the current in the electromagnetic damper.

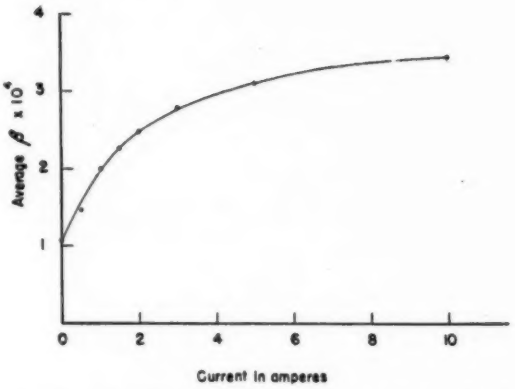

FIG. 15. Relationship between the coefficient of viscous damping and the current through the damper.

The total tension, τ, in the direction AB is,

$$\tau = \{K(x-r)+\tau_i\}\cos\gamma \qquad (6)$$

in which K is the spring constant. The restoring torque is $T=\tau L$, or

$$T=\{K[(r^2+\theta^2L^2)^{\frac{1}{2}}-r]+\tau_i\}\theta L^2(r^2+\theta^2L^2)^{-\frac{1}{2}}. \qquad (7)$$

Neglecting the higher powers of θ, we get

$$T\simeq K'\theta[\tau_i/Kr+\tfrac{1}{2}C^2(1-\tau_i/Kr)\theta^2] \qquad (8)$$

in which $K'=KL^2$ and $C=L/r$.

$T\simeq k_1\theta+k_3\theta^3$ in which k_1 and k_3 are constants. (9)

A typical torque deflection curve with the values of k_1 and k_3 is shown in Fig. 6. The determination of k_3 is shown in Fig. 7. The fact that $(T-k_1\theta)$ *versus* θ^3 plots as a straight line is proof that the spring system does give torque deflection curves of the form described by Eq. (9).

Since the non-linearity is a function of the spring length it was found simpler to use a single spring with a set of different length holders than to try and construct a set of springs similar in every respect except length. A photograph of the non-linear spring system and holders is shown in Fig. 8. Since in this system, because of the initial tension in the

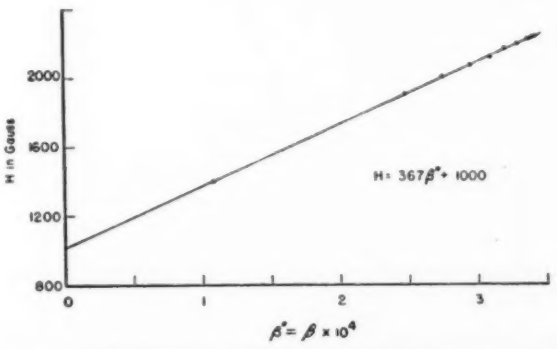

FIG. 16. Relationship between the coefficient of viscous damping and the field strength of the damper.

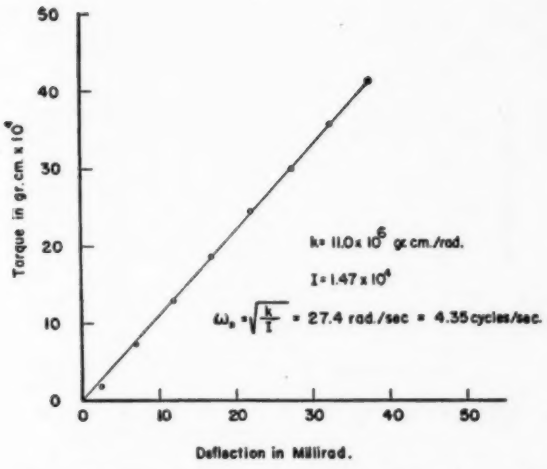

FIG. 17. Torque deflection data of linear spring No. 2.

spring, the linear and non-linear parts of the restoring torque are introduced simultaneously and must then be separated by analysis, it was found advantageous to construct another spring system in which the linear and non-linear parts of the restoring torque could be introduced separately so that no analysis was necessary. This was accomplished by means of the system shown in Fig. 9. The horizontal spring is adjusted in length by means of the knurled nut until it has zero initial tension. Thus according to Eq. (9) it produces a torque proportional to θ^3. The linear torque is then introduced by the vertical springs. This means that several sets of vertical springs can be used with each horizontal spring. Thus k_3 and k_1 are known characteristics of the springs no matter what combination is used.

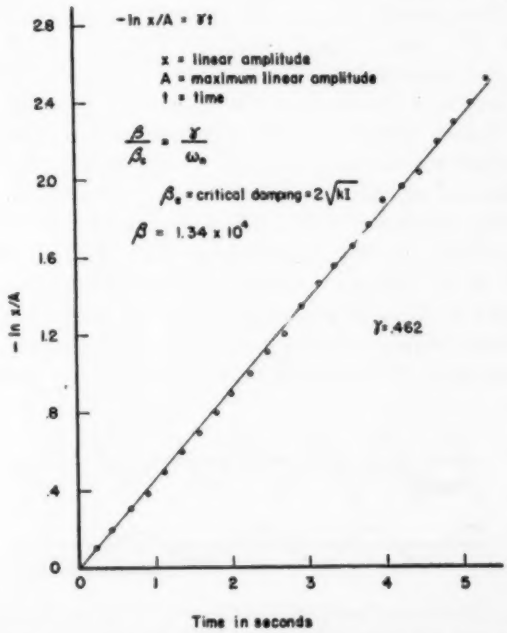

FIG. 18. Logarithmic decrement data of linear spring No. 2.

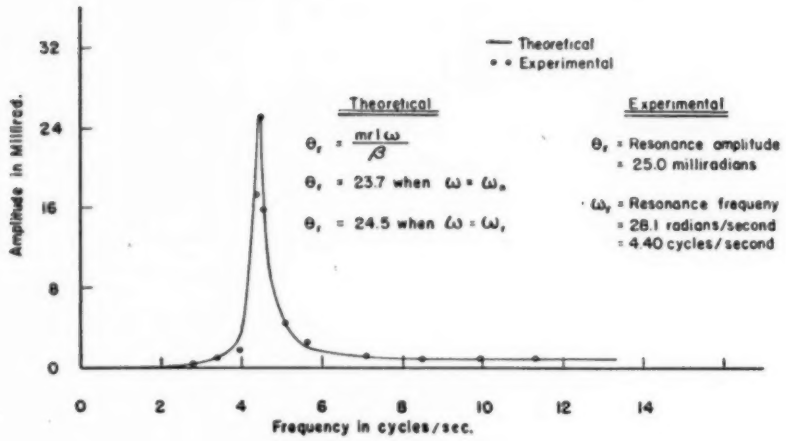

FIG. 19. Resonance data of linear spring No. 2.

This proved very successful as shown in Figs. 10 and 11. Thus it is entirely possible to satisfactorily duplicate a restoring force which can be represented by the first two terms of an odd power series.

Before considering the electromagnetic damper itself, let us consider the damping inherent in the machine due to friction and air damping. We first observe that if the universal joint is not rotating, the damping, though very small, is not viscous because the logarithmic decrement curve is not a straight line. This is shown for several positions of the universal joint in Fig. 12. However, if the universal joint is rotating, the inherent damping is small but viscous. We note also a slight dependence of damping on the rate at which the universal joint is rotating. These results are shown in Fig. 13.

Convinced now that the inherent damping is small and viscous, we can turn to the examination of the electromagnetic damper. By means of a bismuth spiral inserted between the poles, a plot was made of field strength *versus* current. This is shown in Fig. 14 and discloses the fact that when the current has reached 10 amperes the magnet is saturated. A set of four linear springs was used to calibrate the damper; resonance data was taken, and from it the coefficient of viscous damping was computed. The results are shown in Fig. 15, which plots β as a function of the current. Using the results of Figs. 14 and 15 it is possible to establish a relationship between H and β. This is shown in Fig. 16, and since the inherent damping is very small and viscous, the relationship between H and β is given by a linear expression,

$$H = 367\beta \times 10^4 + 1000, \tag{10}$$

as it should be. Thus it is experimentally possible to introduce controlled viscous damping into the system represented by Eq. (3).

As to the method of recording the motions of the system, they may be recorded directly on a rotating drum by means of spots of light, as in a previous paper,[2] or they may be recorded by means of an electric pickup and oscilloscope. If recorded electrically the results can be altered by differentiating circuits to get the results in any coordinates desired.

A typical set of test data on a linear system is shown in Figs. 17 through 19. The system considered does not contain the electromagnetic damper and the results clearly show that even though the damping is supplied only by the friction inherent in the machine, satisfactory results are obtainable. When the electromagnetic damper is used we know the results are correct because they were used in calibrating the damper and Fig. 16 plotted as a straight line.

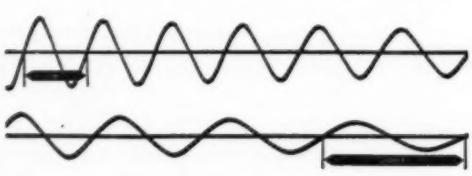

FIG. 20. Solution generated by the free vibration of a system with a non-linear restoring force. Note the dependence of the period on the amplitude.

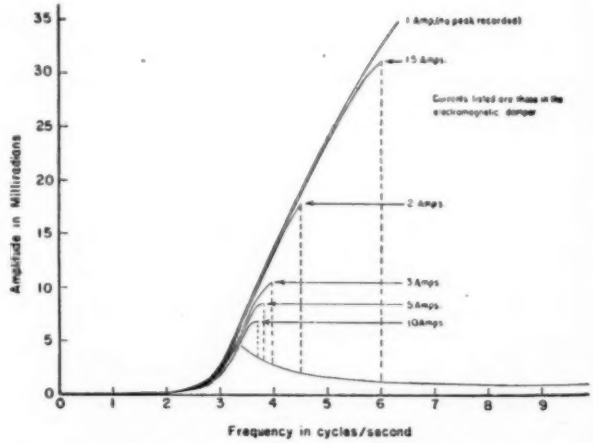

FIG. 21. Typical resonance curves obtained from the forced vibrations of a system with a non-linear restoring force of the type shown in Fig. 6.

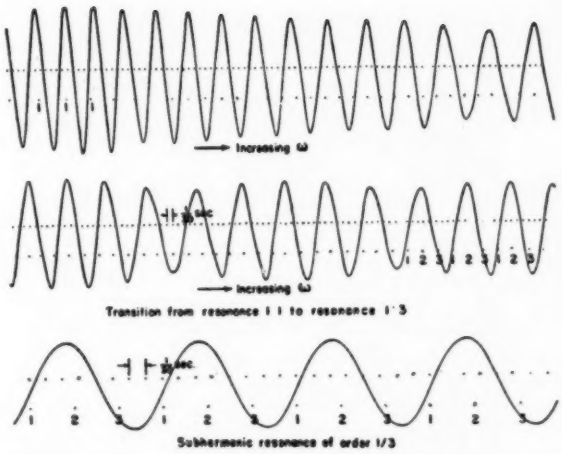

FIG. 22. The transition in a non-linear system from ordinary resonance to subharmonic resonance of order one-third. The lower spots (some are numbered) indicate cycles of the unbalance. The upper spots are the timing spots. In the lower picture the recording drum has been speeded up to get a better record of the wave form after the transition is complete.

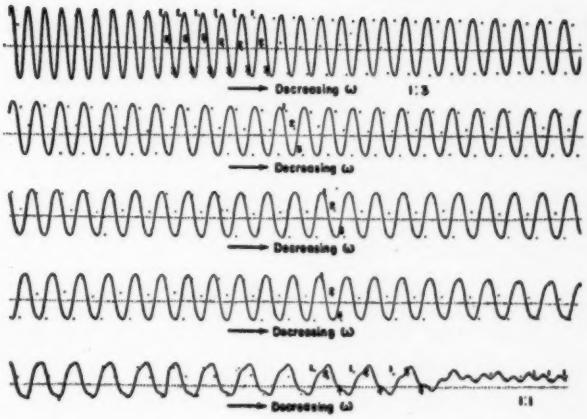

FIG. 23. Transition in a non-linear system from subharmonic resonance of order one-third to regular resonance. The cycles of the unbalance are recorded differently than in Fig. 22 but are clearly marked. The very closely spaced spots again represent timing intervals of 1/30th of a second. Note the very definite change in wave form and phase relationship during the transition.

CONCLUSIONS

It has been demonstrated that an accurate analog can be constructed for determining solutions of some problems in non-linear mechanics. The parameters affecting the solutions can be readily changed and solutions obtained rapidly enough to make the investigation of the variation of solution with change in parameter a very simple process. Critical values of parameters can be easily determined, stability conditions investigated, and transition phenomena recorded. It is not the purpose of this paper[4] to present an analysis of results obtained on non-linear systems; however it seems proper to present the following results as examples of what may be obtained. Figure 20 shows the dependence of frequency on amplitude in non-linear free vibrations. The results were obtained by removing the rotating unbalances (so that the right side of Eq. (3) was zero) and then giving the beam an initial displacement. Figure 20 shows the jump phenomena in a non-linear system as a function of the damping. Figures 21–23 show some interesting transition phenomena in subharmonic resonance as displayed by non-linear systems.

[4] The author has in preparation a paper, soon to be published, on the results obtained by using the apparatus, herein described, on certain non-linear systems.

ACKNOWLEDGMENTS

The present apparatus has evolved during the past several years and the author wishes to acknowledge the assistance afforded him by a Sigma Xi Grant-in-Aid, Purchase Order (535)43-27402-E U. S. Army Air Forces, Navy Contract No. (bs) 28378, and a Cottrell Grant-in-Aid from the Research Corporation.

A Torsion Balance for Measuring Forces in Low Density Gas Flows

I. ESTERMANN
Department of Physics, Carnegie Institute of Technology, Pittsburgh, Pennsylvania

AND

E. D. KANE
Department of Engineering, University of California, Berkeley, California

(Received November 8, 1948)

A torsion balance, designed to measure the force on a flat plate (or other simple geometry) in a low density gas flow, is described. The balance has been used with two interchangeable torsion member sizes, with diameters of 0.00064″ and 0.00090″, which measured forces up to a maximum of 0.6 milligram and 2.4 milligrams, respectively. Calibrations (obtained in still air using weights) were reproducible within ±0.005 mg and ±0.04 mg for the two sizes. Data obtained for a flat plate in a gas stream under large molecular mean free path conditions are presented.

INTRODUCTION

RESEARCH at the University of California on flow of low density air through supersonic nozzles brought up the problem of measuring forces on objects small compared to the molecular mean free path. Specifically, it was desirable to measure the net force (in the macroscopic flow direction) normal to a flat plate about 0.019″ square placed near the exit of a supersonic wind-tunnel nozzle. The flow conditions were variable over a range which required measuring forces of approximately 0.1 to 2 milligrams.

DESCRIPTION OF FORCE BALANCE

The target plate (see Fig. 1) was fastened to a vertical quartz fiber with dry shellac. The fiber in turn was cemented to a torsion member, consisting of a tungsten wire. A force on the target in the flow direction resulted in twisting of the torsion member. The motion of the fiber holding the plate was restricted by the shield indicated in Fig. 1. The torsion member was then twisted to return the pointer to the zero position, and the angle of twist was read on an engraved scale.

The arrangement of the balance in the wind tunnel is shown in Fig. 2. The torsion member was twisted by means of a flexible shaft which was turned externally through a Wilson seal. The frame on which the balance was mounted was in turn fastened to a mechanism which permitted adjustment of the position of the balance assembly and target over the cross section and along the axial (flow direction) centerline of the wind-tunnel nozzle.

CALIBRATION

The balance is shown in a vertical position in Figs. 1 and 2. For calibration, the balance was placed in a horizontal position and weights, in 0.1-milligram increments, were placed on the quartz fiber at the target. Two different tungsten torsion wire diameters were used, 0.00064 and 0.00090 inch. The distance of the weights from the torsional support fiber was 1.40 inches for the 0.00064-inch diameter member and 1.39 inches for the 0.00090-inch member. The torsion member was twisted to bring the pointer to zero position, as in operation, and the angle of twist was determined as a function of the force at the target. The resulting data are plotted on Figs. 3 and 4. Multiplying the ordinates of Figs. 3 and 4 by the respective lever arms would give the calibration data in terms of moments. The procedure was to load the balance with progressively larger weights in 0.1-mg steps, and then to unload, noting the angle of twist in each case. Some hysteresis effect and scatter is evident from examination of Figs. 3 and 4, amounting to a maximum deviation about a straight line of about ±0.04 mg for the 0.00090″ fiber and ±0.005 mg for the 0.00064″ fiber.

The calibration procedure required a total time of about one hour. To determine the magnitude of possible long time creep effects, a 0.1-mg weight was left on the target (using the 0.00064″ diameter torsion member) for 24 hours, and the angle of twist was determined. The shift in angle was 0.2 degree.

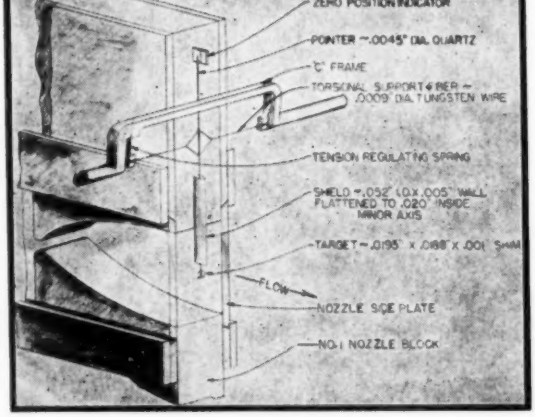
ZERO POSITION INDICATOR
POINTER ~.0045" DIA. QUARTZ
'C' FRAME
TORSIONAL SUPPORT FIBER ~ .0009 DIA. TUNGSTEN WIRE
TENSION REGULATING SPRING
SHIELD ~.052" I.D. x .005" WALL FLATTENED TO .020" INSIDE MINOR AXIS
TARGET ~.015" x .018" x .001" SHIM
FLOW
NOZZLE SOE PLATE
NO. 1 NOZZLE BLOCK

FIG. 1.

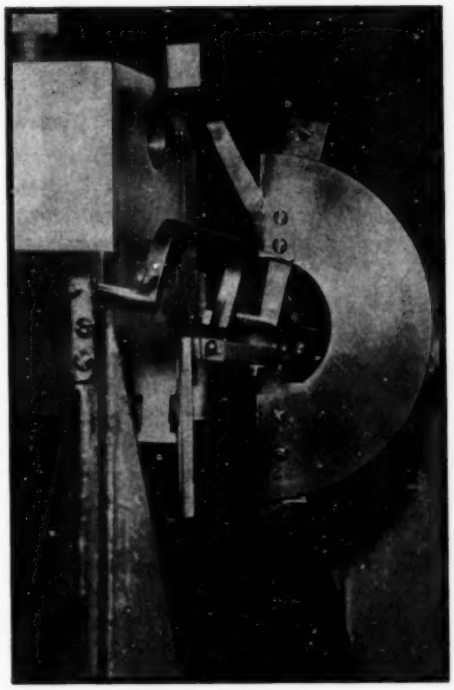

FIG. 2.

The calibration was checked before and after about six days' operation in the wind tunnel for the 0.00090-inch torsion member. The points obtained checked the original calibration, the deviations in every case being no greater than those found initially.

OPERATION

The wind tunnel was operated over a range of static pressures from about 10 to 80 microns, as measured by a Pirani gage connected to the wall of the test chamber in which the nozzle was located. The characteristics of the wind tunnel are such that an increase in the test chamber pressure is accompanied by an increase in the macroscopic gas velocity and a decrease in the gas temperature. The force on the target, placed at the axial centerline of the nozzle, was determined at each test chamber pressure.

The enlarged view of the target, supporting fiber and shield in Fig. 5 indicates that the projected area of the fiber (1.71×10^{-4} in.^{2}) is comparable to that of the target (3.67×10^{-4} in.^{2}, corresponding to an exposed length between target and shield $=0.038$ inch). The measured forces obtained with the balance were divided by the total projected area (5.38×10^{-4} in.^{2}) of target and fiber, and are shown on Fig. 6 as a function of test chamber pressure (the 0.00090″ tungsten fiber was used for these runs). The ordinate of Fig. 6 is the equivalent force (divided by the total projected area), acting at a distance of 1.39 inches from the torsion member, which produces the same moment as the actual force distribution on the target and fiber. At each pressure setting of the wind tunnel, the angle of twist was read on the balance, first by gradually increasing the twist until the pointer (Fig. 1) was at the zero position, then by increasing the twist still further and decreasing it until the zero position was reached again. The angle of twist did not check exactly in each case; the spread obtained on repeating the procedure at least three times as indicated by the high and low points on Fig. 6. The maximum spread in values, obtained at the 60-micron test chamber pressure, was ±1.9 percent about the mean value of the force.

This variation was attributed first to mechanical sticking of the fiber against the shield. However, the shield was remade once, and removed and checked several times, without correcting the difficulty. The effect was not present when the balance was checked in still air. The possibility that side forces caused by the flowing gas would force the fiber against the shield was checked, but calculations showed that even forces of the same magnitude as those measured would deflect the fiber less than 0.002″. As a

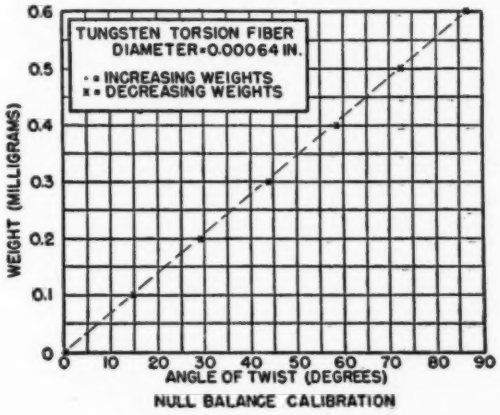

FIG. 3.

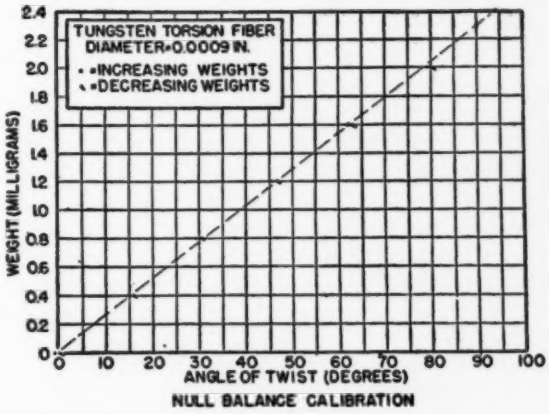

FIG. 4.

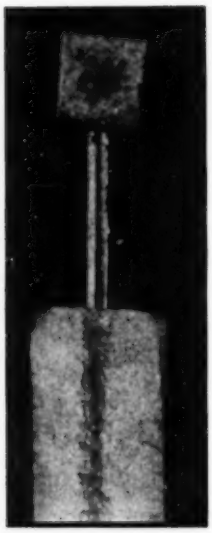

FIG. 5.

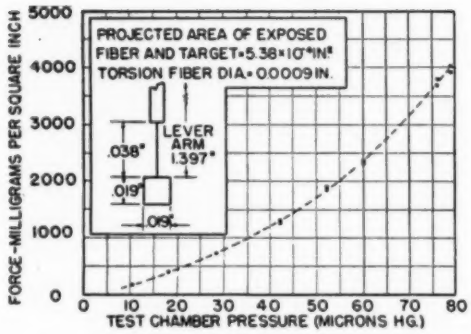

FIG. 6. Force per unit area on target and fiber *versus* test chamber pressure.

tentative explanation, it is considered possible that a static charge may build up on the quartz fiber as a result of the flowing gas. This would cause electrostatic forces between the fiber and (grounded) shield which might account for the observed sticking. Modifications to permit an investigation of this effect are planned.

APPLICATION OF RESULTS

The force measured on the target plate and supporting fiber can be interpreted to give information concerning the condition of the gas producing the force. For example, if the static pressure in the gas is known, then the Mach number (the dimensionless ratio of free stream speed to speed of a sound at a point in the flow) can be determined from this type of drag data.[1] Alternately, if the Mach number and static pressure are known (or an equivalent combination of variables), then information can be obtained from the force balance measurement regarding the nature of the molecular interaction with the surface of the target. These statements are based on the assumption that the molecular mean free path is large compared to the dimensions of the target, so that the analysis methods of kinetic theory can be applied and collisions between oncoming and reflected molecules can be ignored. In the wind tunnel in which Fig. 6 was obtained, it is estimated that the mean free path $=0.020''$ (approximately the side dimension of the target) when the test chamber pressure is 80 microns. At 20 microns, the mean free path increases to an estimated $0.10''$. The minimum ratio of mean free path to target dimension for which the interaction between the gas molecules may be neglected is not known. Also, the effect which the shield may have on the forces on the target and support fiber would have to be considered in interpreting measurements obtained with the balance.

[1] H. S. Tsien, "Superaerodynamics, mechanics of rarefied gases," J. Inst. Aeronautical Sci. **13**, 643–664 (1946).

ACKNOWLEDGMENT

This work was done at the Department of Mechanical Engineering of the University of California in Berkeley as part of ONR contracts with the Department of Engineering, University of California (No. N7-ONR-295-Task 3) and with the Physics Department, Carnegie Institute of Technology (No. N7-ONR-303-Task 3). The torsion balance described was constructed by Mr. C. E. Beeson.

A Resonance Effect in the Synchrotron*

E. D. COURANT**
Cornell University, Ithaca, New York
(Received September 27, 1948)

The effect of the resonance occurring at $n=-d(\log H)/d(\log r)=\frac{3}{4}$ between the second harmonic of the frequency of radial oscillations and the frequency of revolution of the particles in a synchrotron is analyzed. It is shown that this resonance will lead to an increase in the amplitude of the radial oscillations if the first Fourier coefficient of the azimuthal variation of n is too large. The effect may occur even if the value of n at the equilibrium orbit is different from $\frac{3}{4}$, because the orbit will drift back and forth periodically due to the phase oscillations and may cross the place where $n=\frac{3}{4}$.

A criterion is derived for the condition that the increase in the amplitude of the oscillations per unit time due to this resonance be less than the decrease in the amplitude due to the magnetic damping, i.e. that there be a net damping effect. It turns out that this condition reduces to the requirement that the first Fourier component of the azimuthal inhomogeneities of the magnetic field be less than about 10^{-3}. If this condition is not satisfied the resonance effect will reduce the intensity of the beam unless the equilibrium value of n is sufficiently far from $\frac{3}{4}$.

I. INTRODUCTION

IT has been pointed out[1] that the motion of the particles in an accelerator becomes unstable, due to second- and higher order terms in the equations of motion, when the frequencies of some of the modes of oscillation of the orbit are commensurable with each other or with the frequency of revolution. An example of such an effect is the disappearance of the beam of the Berkeley synchro-cyclotron at the point where the magnetic field index $n=-d(\log H)/d(\log r)=0.2$, i.e. where the radial oscillation frequency is twice the vertical oscillation frequency.[2]

A similar effect may be expected in a synchrotron at the point where $n=\frac{3}{4}$, i.e. where the radial oscillation frequency is half the frequency of revolution. Energy will be fed from the revolutions of the particles into the radial oscillations if the corresponding coupling term in the equations of motion is different from zero. The coupling term, as we shall see, is proportional to the first Fourier component of the azimuthal inhomogeneities of the magnetic field index n.

In a synchrotron the situation is complicated by the slow radial oscillations associated with the phase oscillations, hereafter referred to as the "synchrotron oscillations." These oscillations may be regarded as a slow periodic shift of the radius of the orbit around which the rapid radial and vertical oscillations take place. If n changes with the radius the value of n at the orbit, and therefore the frequencies of the radial and vertical oscillations, will vary as the orbit radius varies. Thus if n at the equilibrium orbit is equal or near to $\frac{3}{4}$, it will pass through the value $\frac{3}{4}$ during each cycle of the synchrotron oscillations, and while it is near that value the radial oscillations may be built up by the resonance with the frequency of revolution. If the increase of amplitude due to this effect is greater than the decrease due to magnetic damping[3] a net increase of the amplitude of oscillations will result and the particles will be lost to the beam when the amplitude becomes too great. It is therefore desirable to estimate the magnitude of this resonance effect and to formulate criteria which must be satisfied in order that the effect be harmless.

II. THE EQUATIONS OF MOTION

If the magnetic field in the synchrotron is not constant azimuthally the equation of motion for the fast radial oscillations (hereafter referred to simply as the "radial oscillations") is

$$d/dt(m\dot{r})=mr\dot{\theta}^2-e(r\dot{\theta}B_z-\dot{z}B_\theta). \tag{1}$$

Let us assume that, to the first order in the deviations from the equilibrium orbit $r=R$,

$$B_z=m\omega/e[1+f_0(\theta)-(n-f_1(\theta))x/R] \tag{2}$$

where $x=r-R$ and f_0 and f_1 are small functions of θ. The azimuthal component of the field will then be of the form

$$B_\theta=m\omega/e[g_0(\theta)+g_1(\theta)x/R+h_1(\theta)z/R] \tag{3}$$

where g_0, g_1 and h_1 are also small functions of θ. Equation (1) then becomes, to first order in x and z,

$$\ddot{x}+(1-n)\omega^2x=-\omega^2[Rf_0(\theta)+xf_1(\theta)-(\dot{z}/\omega)g_0(\theta)] \tag{4}$$

if the slow increase of the mass is neglected.

If we assume that x and z are approximately given by the Kerst-Serber equations:[3]

$$x=x_0\cos(1-n)^{\frac{1}{2}}\omega t+x_1 \quad x_1\ll x_0$$
$$z=z_0\cos n^{\frac{1}{2}}\omega t+z_1 \quad z_1\ll z_0$$

* Work done under contract with the Brookhaven National Laboratory under the auspices of the Atomic Energy Commission.

** Author's present address: Brookhaven National Laboratory, Upton, New York.

[1] D. M. Dennison and T. H. Berlin, Phys. Rev. **69**, 542 (1946).

[2] Sewell, Henrich, and Vale, Phys. Rev. **72**, 739 (1947).

[3] D. W. Kerst and R. Serber, Phys. Rev. **60**, 53 (1941).

and note that $\theta=\omega t$, we see that the forcing term on the right-hand side of Eq. (4) contains components of the frequencies

$$k\omega,\ (k\pm(1-n)^{\frac{1}{2}})\omega,\ (k\pm n^{\frac{1}{2}})\omega$$

where k may be any integer.

Now if $n=\frac{3}{4}$, $(1-n)^{\frac{1}{2}}=\frac{1}{2}$ and therefore the frequency $(1-(1-n)^{\frac{1}{2}})\omega$ is equal to the resonance frequency $(1-n)^{\frac{1}{2}}\omega$. Thus, if $f_1(\theta)$ is given by a Fourier series beginning with the term $\alpha\cos\theta$, the right-hand side of Eq. (4) contains a term

$$-\tfrac{1}{2}\omega^2\alpha x_0\cos(1-(1-n)^{\frac{1}{2}})\omega t.$$

Now in the synchrotron the equilibrium radius R oscillates slowly about its mean value, and if n is not constant spatially, n and therefore the frequency $(1-n)^{\frac{1}{2}}\omega$ will also oscillate slowly. If the value of n at the mean radius R_0 is near $\frac{3}{4}$ it is likely that during the course of this slow oscillation R will pass through the point where $n=\frac{3}{4}$; since the frequency of the oscillations of R is small compared to ω, the electrons will spend many periods in the vicinity of $n=\frac{3}{4}$ and large amplitudes may be built up. The equation of motion is now (in complex form)

$$\ddot{x}_1+\omega_1^2x_1=-\tfrac{1}{2}\alpha\omega^2x_0\exp i\int_0^t\omega_2dt' \qquad (5)$$

where $\omega_1=(1-n)^{\frac{1}{2}}\omega$ and $\omega_2=\omega-\omega_1$, and where we have included only the forcing term with frequency ω_2.

To solve Eq. (5) we note that ω_1 is a slowly varying function of time; more precisely, $|\dot{\omega}_1|\ll\omega_1^2$ and $|\ddot{\omega}_1|\ll\omega_1^3$. We may therefore use the WKB solutions

$$\omega_1^{-\frac{1}{2}}\exp\left[\pm i\int_0^t\omega_1(t')dt'\right]$$

as the two fundamental solutions of the homogeneous part of Eq. (5), and obtain for the solution of the complete equation

$$\begin{aligned}x_1=\tfrac{1}{4}i\alpha(\omega^2/\omega_1)x_0\Big\{&\exp i\phi_1(t)\\&\times\int_0^t\exp i[\phi_2(t')-\phi_1(t')]dt'\\&-\exp[-i\phi_1(t)]\\&\times\int_0^t\exp i[\phi_2(t')+\phi_1(t')]dt'\Big\}\end{aligned} \qquad (6)$$

where

$$\phi_1(t')=\int_0^{t'}\omega_1(t'')dt'';\quad \phi_2(t')=\int_0^{t'}\omega_2(t'')dt''.$$

This solution satisfies the initial conditions $x_1=\dot{x}_1=0$ at $t=0$.

III. THE DAMPING CONDITIONS

The condition for stability of the motion is that the increase in amplitude of x_1 due to the resonance, over a given time interval, must be less than the decrease due to damping in the same time interval. We must, therefore, compare the rate of increase of x_1 with the rate of damping.

To estimate the integrals in Eq. (6) we note that the integrand of the second integral oscillates rapidly throughout the interval of integration, while the integrand of the first integral varies slowly whenever n is near $\frac{3}{4}$. We may therefore neglect the second integral compared to the first, and estimate the first integral by applying a modification of the "method of stationary phase" (see Appendix).

It is convenient to split the integral up into contributions of the individual periods of the synchrotron oscillations. The amplitude of resonance oscillations after N periods is

$$x_1(t_N)=-\tfrac{1}{2}i\alpha\omega x_0\sum_{m=0}^{N-1}y_me^{if(t_m)} \qquad (7)$$

where t_m is the end of the mth period of the synchrotron oscillations, and

$$y_m=\int_{t_m}^{t_{m+1}}\left[\exp i\int_{t_m}^t(\omega_2-\omega_1)dt'\right]dt. \qquad (8)$$

We shall see in the Appendix that, if n passes through the value $\frac{3}{4}$ during the mth period of synchrotron oscillations,

$$y_m=2^{\frac{1}{2}}(\pi/n_2\omega\Omega)^{\frac{1}{2}}\{1/[X(X-Y)]^{\frac{1}{4}}\} \qquad (9)$$

where Ω is the circular frequency of the synchrotron oscillations, X is their amplitude divided by the mean orbit radius R_0, YR_0 is the distance from the mean orbit to the place where $n=\frac{3}{4}$, and $n_2=dn/d(\log r)$. The expression (9) is valid provided that

$$X-Y>\Omega/\omega(X\omega/8n_2^2\Omega)^{\frac{1}{3}}. \qquad (10)$$

Ω/ω is of the order of 10^{-2} [4] and X, the relative amplitude of the synchrotron oscillations, is also of this order or somewhat greater, while n_2 is of the order of unity. Therefore the condition (10) means essentially that $X-Y$ must be more than about Ω/ω.

If the oscillations just reach to $n=\frac{3}{4}$, i.e. if $X=Y$, Eq. (9) must be replaced by

$$y_m=[2\pi/3^{\frac{1}{3}}\Gamma(\tfrac{2}{3})][n_2X\omega\Omega^2]^{-\frac{1}{3}} \qquad (11)$$

which is of the same order of magnitude as (9), while

[4] See, for example, D. Bohm and L. Foldy, Phys. Rev. **70**, 249 (1946).

if the oscillations fail to reach to $n=\frac{3}{4}$,

$$y_m=(\pi/9n_2\omega\Omega)^{\frac{1}{3}}[\tfrac{1}{2}X(Y-X)]^{-\frac{1}{6}} \times\exp-\{(2^{5/2}/3)n_2(\omega/\Omega)[(Y-X)^3/X]^{\frac{1}{2}}\}. \quad (12)$$

Because of the exponential factor, this is smaller than (9) or (11). However, it is comparable to these expressions as long as the exponent is not large compared to 1, i.e. as long as

$$Y-X<[(3/2^{5/2}n_2)(\Omega/\omega)X^{\frac{1}{2}}]^{\frac{2}{3}}.$$

If we assume that n_2 is of the order of $3/2^{5/2}$ and that Ω/ω and X are of the same order, this means that the contribution to the amplitude becomes appreciable if the amplitude of the synchrotron oscillations is of the order of half of the distance from the mean orbit to the "dangerous" radius.

If ω_2 is a strictly periodic function of time, $t_m=mT$ where T is the period of the synchrotron oscillations; $f(t_m)=mf(T)$, and y_m is independent of m, so that Eq. (7) becomes

$$x_1(NT)=-\tfrac{1}{2}i\alpha\omega x_0 y\sum_{m=0}^{N-1}e^{imf(T)}. \quad (13)$$

Thus the contributions of successive periods cancel out by interference, unless $f(T)$ happens to be an integral multiple of 2π. However, two factors destroy the regular phase relationship indicated in Eq. (13). In the first place, the amplitude and frequency of the synchrotron oscillations are not constant, but change during the course of the acceleration cycle. Therefore, both y_m and $f(t)$ will change. Furthermore, scattering by the gas and fluctuations in the r-f voltage and the magnetic field may destroy the phase relations between the contributions of successive cycles. If the phase relations are destroyed completely, the contributions of the individual cycles have to be added with random phases, and the mean increment of amplitude per cycle is

$$\xi=[x_0^2+|x_1(T)|^2]^{\frac{1}{2}}-x_0\approx|x_1(T)|^2/2x_0. \quad (14)$$

To ensure stability of the motion, this must be less than the decrease in amplitude per cycle due to the damping. The damping given by the theory of Kerst and Serber[3] is proportional to $E^{-\frac{1}{2}}$ where E is the energy of the particle. Thus the decrease per cycle of the synchrotron oscillations is

$$\Delta x=\tfrac{1}{2}x_0\Delta E/E=\tfrac{1}{2}x_0(\omega/\Omega)(eV\sin\psi_0/E) \quad (15)$$

where V is the r-f voltage on the gap and ψ_0 is the equilibrium phase angle.

If we use the expression (9) for y_m the condition $\xi<\Delta x$ becomes

$$\alpha^2<(2^{\frac{1}{2}}n_2/\pi)[X(X-Y)]^{\frac{1}{2}}eV\sin\psi_0/E. \quad (16)$$

If the phases of the successive increments of amplitude are not random, Eq. (13) is still not valid because of the slow change of Ω and X with energy, and we must return to Eq. (7). Let us write

$$f(t_m)-f(t_{m-1})=2\pi p_m$$

where

$$p_m=\Delta/\Omega_m$$

and Δ is the mean value of $\omega_2-\omega_1$ and Ω_m is the value of Ω during the mth period of the synchrotron oscillations. Successive terms of the sum in (7) will be in phase whenever p_m passes through an integral value. We may, therefore, expect a substantial contribution to x_1 for each integral value through which p passes as Ω changes.

In the vicinity of the time t_0 when $p=k$ we have

$$f(t)=f(t_0)+2\pi k(m-m_0)+\pi p'(m-m_0)^2+\cdots$$

where $p'=dp/dm=(2\pi/\Omega)dp/dt$. Since k, m and m_0 are integers,

$$\exp[if(t_m)]\approx\exp i[f(t_0)+\pi p'(m-m_0)^2]. \quad (17)$$

To evaluate the part of the sum in Eq. (7) due to the terms near t_0 we neglect the variation of y_m with m and replace the sum by an integral, obtaining

$$\sum\exp[if(t_m)] \approx\int_{-\infty}^{\infty}\exp i[f(t_0)+\pi p'(m-m_0)^2]dm =(-ip')^{-\frac{1}{2}}\exp[if(t_0)]. \quad (18)$$

To evaluate p' we use the relation[4]

$$\Omega=\omega(beV/E)^{\frac{1}{2}} \quad (19)$$

with

$$b=[\cos\psi_0/2\pi(1-n)]=[2\cos\psi_0/\pi],$$

obtaining

$$p'=[\sin\psi_0/2b](\Delta/\omega). \quad (20)$$

p will pass through an integral value once in $1/p'$ cycles. Thus we have a contribution to x_1 equal to $1/p'^{\frac{1}{2}}$ times the contribution of one cycle, occurring once in $1/p'$ cycles. Even if, as we have assumed, scattering and fluctuations of the r-f voltage and magnetic field are not strong enough to destroy the phase relations between successive cycles, they may be expected to destroy phase relations over an interval of $1/p'$ cycles. The contributions of successive integral values of p will then add with random phases, so that the mean increase in amplitude per cycle is again given by Eq. (14), and the condition (16) for stability of the motion still holds. However, there is an additional condition: the increase in amplitude at a single integral value of p must be less than the effective semi-aperture of the vacuum chamber:

$$\tfrac{1}{2}(x_0/p'^{\frac{1}{2}})\alpha\omega y_m<A$$

where A is the effective semi-aperture. This condi-

tion reduces to

$$\alpha^2 < (n_2/\pi)[2X(X-Y)]^{\frac{1}{2}}(eV/bE)^{\frac{1}{2}}(\Delta/\omega) \times (A^2 \sin\psi_0/x_0^2) \quad (21)$$

if we again use Eq. (9) for y_m.

This is a less stringent condition than (16) as long as

$$2(\Delta/\omega)(A^2/x_0^2) > (eVb/E)^{\frac{1}{2}};$$

with $\Delta/\omega = 0.01$, $x_0/A = \frac{1}{2}$ this is equivalent to $ebV/E < 0.064$, which is satisfied in most synchrotrons now in existence or being planned. The significant condition for damping is therefore (16).

If we take as typical numerical values $n_2 = 1$, $X = 0.05$, $Y = 0.03$, $eV = 4000$ ev, $\sin\psi_0 = \frac{1}{2}$, $E = 5$ Mev (near injection), the condition (16) becomes

$$\alpha < 3 \times 10^{-3}$$

which must be satisfied in order that the motion be damped near the beginning of the synchrotron phase of the acceleration cycle. For higher energies the damping condition becomes more severe because of the factors $1/E$ and $(X(X-Y))^{\frac{1}{2}}$ in Eq. (16). However, the damping of the synchrotron oscillation amplitude X, which is proportional to $E^{-\frac{1}{4}}$,[4] will soon reduce it below the value Y, so that the synchrotron oscillations no longer reach to $n = \frac{3}{4}$ and therefore the amplitude x_1 is no longer built up.

IV. DISCUSSION

We have seen that in order that damping of the radial oscillations be assured, the first Fourier component of the azimuthal variation of the coefficient n of radial variation of the magnetic field must be of the order of 10^{-3} or less. This is probably a difficult condition to fulfill, especially near the beginning of the acceleration cycle when there are comparatively large stray magnetic fields. However, this condition need only be satisfied if the synchrotron oscillations extend beyond the point where $n = \frac{3}{4}$. If the synchrotron is designed so that the mean equilibrium orbit is far from this point this resonance effect may be avoided. And even if the value of n at the equilibrium orbit is near $\frac{3}{4}$ there will be some electrons which execute oscillations of sufficiently small amplitude that they do not reach the dangerous radius. The effect of this resonance thus will be to reduce the intensity of the beam, but not to eliminate it altogether.

The design value of n in the 70-Mev synchrotron of the General Electric Company is just $\frac{3}{4}$.[5] However, the actual value may easily differ from $\frac{3}{4}$ by a small amount. It has been observed in this synchrotron that electrons emerge from the vacuum chamber throughout the acceleration cycle.[6] This may well be explained by the resonance effect discussed here.

Similar resonances will occur at other values of n at which the various oscillation frequencies are commensurable. Thus there will be a coupling between the vertical oscillations and the revolution frequency, exactly analogous to the resonance treated here, at $n = \frac{1}{4}$, due to the relation $2\omega_z = \omega$. Since most synchrotrons are designed with $n > \frac{1}{2}$ the most serious other resonance occurs at $n = 0.64$, where the relations

$$2n^{\frac{1}{2}} - (1-n)^{\frac{1}{2}} = 1$$

and

$$n^{\frac{1}{2}} + 2(1-n)^{\frac{1}{2}} = 2$$

lead to resonance between the vertical and horizontal oscillations and the first and second Fourier components of the azimuthal variations of the magnetic field, respectively. In a circular synchrotron these resonances would, however, be less serious than the one at $n = \frac{3}{4}$ because the forcing terms corresponding to the right-hand side of Eq. (5) will contain higher powers of the small oscillation amplitudes x_0 and z_0. In the case of a two-section race track, on the other hand, the second Fourier component of the magnetic field as well as the oscillation amplitude x_0 will necessarily be comparatively large, and the corresponding resonance may be serious. This resonance will occur at a value of n different from 0.64 because of the different relations between n and the oscillation frequencies when straight sections are present.[7] Similarly, in a four-section race track resonances involving the fourth harmonic of the rotation frequency may be serious, although they will necessarily be of fifth or higher order in the oscillation amplitudes.

It is a pleasure to acknowledge some very helpful discussions with Professor H. A. Bethe.

APPENDIX

We must evaluate the integral

$$y_m = \int_{t_m}^{t_{m+1}} \left[\exp i \int_{t_m}^{t} (\omega_2 - \omega_1) dt' \right] dt \quad (A1)$$

where the interval from t_m to t_{m+1} represents one period of the synchrotron oscillations. The integrand is an oscillatory function of varying period; we may expect the main contribution to the integral to come from that region in the interval of integration where the integrand varies least rapidly, i.e. where $|\omega_2 - \omega_1|$ is smallest. There are two possibilities: either the amplitude of the synchrotron oscillations is suffi-

[4] Elder, Gurewitsch, Langmuir, and Pollock, J. App. Phys. 18, 810 (1947).

[6] R. V. Langmuir and H. C. Pollock, private communication to H. A. Bethe.

[7] D. M. Dennison and T. H. Berlin, Phys. Rev. 70, 764 (1946).

ciently great so that n passes through the value $\frac{3}{4}$, i.e. $\omega_2-\omega_1$ passes through zero, or the maximum (minimum) value of n during one period may be less (greater) than $\frac{3}{4}$, so that $\omega_2-\omega_1$ is of the same sign throughout.

In the first case one might attempt to estimate the integral (A1) by the method of stationary phase, i.e. by expanding the exponent in the integrand in power series around each of the points where $\omega_2-\omega_1$ vanishes, and neglecting all powers beyond the second. However, for this method to be valid it is necessary that the points where the phase is stationary be well separated, so that the contribution from each may be taken separately. It turns out that this condition is not always satisfied in our case.

We may, however, estimate the integral by a slight modification of this method, which has the advantage that it is valid whether $\omega_2-\omega_1$ passes through zero or not. We expand the exponent in the integral (A1) around a point where its *second* derivative vanishes. There will be two such points, since $\omega_2-\omega_1$ is approximately periodic and therefore has a maximum and a minimum in each period; we choose the one at which $|\omega_2-\omega_1|$ is smaller. Let this point be t_0. We may assume, without loss of generality, that t_0 is at the center of the interval from t_m to t_{m+1}, for if it is not, we merely have to redefine the phase which we designate as the "beginning" of a period. We have, in the vicinity of t_0,

$$f(t)\equiv\int_{t_m}^{t}(\omega_2-\omega_1)dt'=f(t_0)$$
$$+(\omega_2-\omega_1)_0(t-t_0)+\tfrac{1}{6}(\ddot{\omega}_2-\ddot{\omega}_1)_0(t-t)^3+\cdots \quad \text{(A2)}$$

where $(\omega_2-\omega_1)_0$ is the value of $\omega_2-\omega_1$ at t_0, and $(\ddot{\omega}_2-\ddot{\omega}_1)_0$ is its second time derivative at t_0. In the following, we shall omit the subscript 0. We neglect terms of higher order in $t-t_0$ than the third.

We now substitute Eq. (A2) in Eq. (A1):

$$y_m=\exp(if(t_0))\int_{t_m}^{t_{m+1}}\exp i[(\omega_2-\omega_1)(t-t_0)$$
$$+\tfrac{1}{6}(\ddot{\omega}_2-\ddot{\omega}_1)(t-t_0)^3]dt. \quad \text{(A3)}$$

If $\omega_2-\omega_1$ and $\ddot{\omega}_2-\ddot{\omega}_1$ have the same sign or if $|\omega_2-\omega_1|^2<|\ddot{\omega}_2-\ddot{\omega}_1|$ the main contribution to the integral comes from a region around t_0 whose width is of the order of $(6/(\ddot{\omega}_2-\ddot{\omega}_1))^{\frac{1}{2}}$ or less. If $\omega_2-\omega_1$ and $\ddot{\omega}_2-\ddot{\omega}_1$ are of opposite signs and $|\omega_2-\omega_1|^3>|\ddot{\omega}_2-\ddot{\omega}_1|$ the main contribution will come from the interval between $t-[6(\omega_2-\omega_1)/(\ddot{\omega}_2-\ddot{\omega}_1)]^{\frac{1}{2}}$ and $t+[6(\omega_2-\omega_1)/(\ddot{\omega}_2-\ddot{\omega}_1)]^{\frac{1}{2}}$. Thus, if $[6/(\ddot{\omega}_2-\ddot{\omega}_1)]^{\frac{1}{2}}$ and $2[6(\omega_2-\omega_1)/(\ddot{\omega}_2-\ddot{\omega}_1)]^{\frac{1}{2}}$ are both less than the period $t_{m+1}-t_m$ we may replace the limits of integration by $-\infty$ to ∞. Using the relations[8]

$$\int_0^\infty\cos(x^3+\alpha x)dx=\tfrac{1}{3}\alpha^{\frac{1}{2}}K_{1/3}[2(\alpha/3)^{\frac{1}{2}}],$$

$$\int_0^\infty\cos(x^3-\alpha x)dx=(\pi\alpha^{\frac{1}{2}}/3^{\frac{1}{2}})$$
$$\times\{J_{1/3}[2(\alpha/3)^{\frac{1}{2}}]+J_{-1/3}[2(\alpha/3)^{\frac{1}{2}}]\} \quad \text{(A4)}$$

we find that, if $(\omega_2-\omega_1)_0$ and $(\ddot{\omega}_2-\ddot{\omega}_1)_0$ are of opposite signs, which is the case if $\omega_2-\omega_1$ passes through zero during the period,

$$y_m=(2^{\frac{1}{2}}\pi/3)[(\omega_1-\omega_2)/(\ddot{\omega}_2-\ddot{\omega}_1)]^{\frac{1}{2}}[J_{1/3}(\gamma^{\frac{1}{2}})$$
$$+J_{-1/3}(\gamma^{\frac{1}{2}})], \quad \text{(A5)}$$

where

$$\gamma=8/9[(\omega_1-\omega_2)^3/(\ddot{\omega}_2-\ddot{\omega}_1)],$$

while if $(\omega_2-\omega_1)_0$ and $(\ddot{\omega}_2-\ddot{\omega}_1)_0$ are of the same sign, i.e. if $\omega_2-\omega_1$ has the same sign throughout the oscillation period,

$$y_m=(2/3)^{\frac{1}{2}}[(\omega_2-\omega_1)/(\ddot{\omega}_2-\ddot{\omega}_1)]^{\frac{1}{2}}K_{1/3}(|\gamma|^{\frac{1}{2}}). \quad \text{(A6)}$$

Now $(\ddot{\omega}_2-\ddot{\omega}_1)_0$ and $(\omega_2-\omega_1)_0$ may easily be expressed in terms of the characteristics of the synchrotron oscillations:

$$(\ddot{\omega}_2-\ddot{\omega}_1)_0=-[\omega n_2/(1-n)^{\frac{1}{2}}R]d^2R/dt^2$$

where $n_2=dn/d(\log r)$, and d^2R/dt^2 is evaluated at the maximum of the oscillation. If we assume that the oscillation is sinusoidal with circular frequency Ω and amplitude XR_0,

$$R=R_0(1+X\cos\Omega t),$$

we have

$$(1/R)(d^2R/dt^2)\approx-\Omega^2X.$$

Since the maximum will occur near $n=\frac{3}{4}$, we have $(1-n)^{\frac{1}{2}}\approx\frac{1}{2}$, and

$$(\ddot{\omega}_2-\ddot{\omega}_1)_0\approx 2n_2\omega\Omega^2X.$$

It may also be shown without difficulty that

$$(\omega_2-\omega_1)_0\approx 2n_2\omega(X-Y)$$

where YR_0 is the distance from the mean orbit to the place where $n=\frac{3}{4}$. We may now verify that the conditions enabling us to make use of the relations (A4) and (A5) are satisfied. We have

$$[6/(\ddot{\omega}_2-\ddot{\omega}_1)]^{\frac{1}{2}}=[3/\omega\Omega^2n_2X]^{\frac{1}{2}},$$

which is less than the period $2\pi/\Omega$ if $3\Omega/\omega n_2X<8\pi^3\approx 250$. This condition will always be satisfied in practice. The other condition is

$$[6(\omega_2-\omega_1)/(\ddot{\omega}_2-\ddot{\omega}_1)]^{\frac{1}{2}}=[6(X-Y)/X\Omega^2]^{\frac{1}{2}}<\pi/\Omega$$

[8] G. N. Watson, *Bessel Functions* (Cambridge University Press, New York, 1944), second edition, p. 190.

which is satisfied as long as $6(X-Y)/X<\pi^2$ which is certainly always the case.

The Bessel functions in Eqs. (A5) and (A6) are easily estimated when their arguments are either large or close to zero. When $\gamma \gg 1$

$$y_m \approx 2^{\frac{1}{2}}(\pi/n_2\Omega\omega)^{\frac{1}{2}} \cos\phi/[X(X-Y)]^{\frac{1}{2}}$$

where ϕ is a phase angle. On the average, we may put $\cos\phi = 2^{-\frac{1}{2}}$, so that

$$y_m \approx 2^{\frac{1}{2}}(\pi/n_2\Omega\omega)^{\frac{1}{2}}[X(X-Y)]^{-\frac{1}{2}}. \quad \text{(A7)}$$

If $\gamma \ll 1$

$$y_m \approx \tfrac{1}{3}(\pi/n_2\Omega\omega)^{\frac{1}{2}}[\tfrac{1}{2}X(Y-X)]^{-\frac{1}{2}} \exp(-|\gamma|^{\frac{1}{2}}) \quad \text{(A8)}$$

and if $\gamma = 0$, i.e. if the oscillations just reach to the point where $n = \frac{3}{4}$,

$$y_m \approx 2\pi(n_2 X\omega\Omega^2)^{-\frac{1}{2}}/3^{\frac{1}{2}}\Gamma(\tfrac{2}{3}). \quad \text{(A9)}$$

Thus y_m is comparatively large if $\gamma \geqslant 0$, i.e. if the oscillation at least reach to $n = \frac{3}{4}$, and y_m is small if $\gamma < 0$, i.e. if n is never equal to $\frac{3}{4}$ during the oscillation period.

On the Design of Networks for Constant Time Delay

M. H. Hebb*
The Sharples Corporation, Philadelphia, Pennsylvania

C. W. Horton and F. B. Jones
The University of Texas, Austin, Texas

(Received November 19, 1948)

Design formulae for five low pass electrical networks are obtained. These design formulae are based on the concept of "group delay time" which represents the delay for a signal composed of a narrow band of frequencies. The dependence on the circuit parameters of the deviation of the group delay time from a constant value is investigated for a simple L–C line, an m-derived section, a type B compensating network, and for two other networks. The relative performance of these networks is discussed, and the properties of the image impedance are summarized briefly.

INTRODUCTION

THE theory of four-terminal electrical networks governs the design of both artificial lines and filters. In the latter, attention is directed toward obtaining the required dependence of attenuation on frequency. Usually, phase shift is not of much concern. The emphasis is reversed for artificial delay lines. Here the phase shift, which fixes the delay, is primary in importance and the attenuation characteristics secondary.

An ideal delay network produces an output which is identical with its input, except for a delay in time independent of the character of the input. This is equivalent to saying that there must be no attenuation at any frequency and that the phase shift shall be proportional to frequency. Obviously, these conditions will never be obtained exactly, and an approximation to them will have to be accepted. It is the purpose of this analysis to investigate the design of networks which approach ideal delay over a limited range of frequencies.

SIMPLE L–C LINE

As an illustration, we consider the artificial line composed of series inductances L and shunt condensers C which is shown in Fig. 1. This is a low pass filter of the constant-K type. It passes without attenuation frequencies up to a cutoff frequency

$$f_c = 1/\pi(LC)^{\frac{1}{2}}. \quad (1)$$

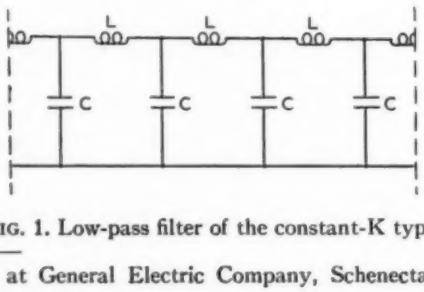

FIG. 1. Low-pass filter of the constant-K type.

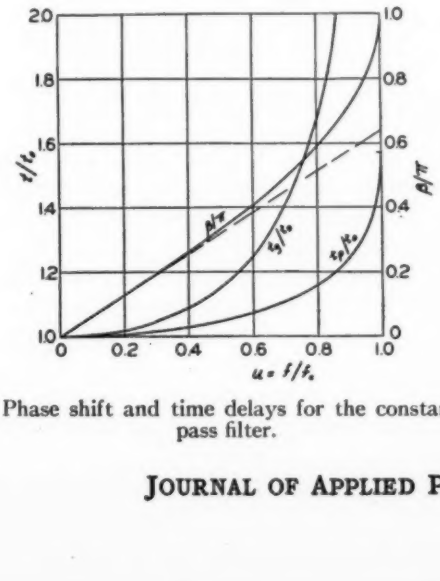

FIG. 2. Phase shift and time delays for the constant-K low pass filter.

* Now at General Electric Company, Schenectady, New York.

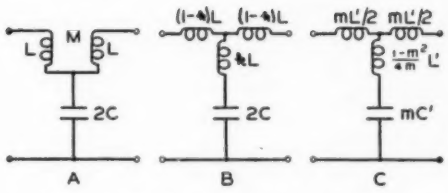

FIG. 3. The m-derived filter section.

The phase shift per section produced by this filter is given, in multiples of $\pi=180°$, by the curve marked β/π in Fig. 2. This is obtained from the formula

$$\sin(\beta/2)=(1/2)\omega(LC)^{\frac{1}{2}}=f/f_c=u, \qquad (2)$$

in which $\omega=2\pi f$ is the angular frequency. It will be observed that the phase shift is approximately proportional to the frequency for frequencies which are low compared to cutoff. Thus, if the frequencies which are to be transmitted by the line are all low compared with the cutoff frequency, the behavior of the line will be substantially ideal. In this region the time delay t_0 will be the low frequency value of

$$t_p=\beta/\omega=\beta/2\pi f, \qquad (3)$$

i.e., from Eq. (2)

$$t_0=(LC)^{\frac{1}{2}}=1/\pi f_c. \qquad (4)$$

The delay time for a sinusoidal signal of frequency f is t_p as given by Eq. (3). It will be called the "phase delay time." Since the phase shift β is not proportional to the frequency, the phase delay t_p is not constant at the low frequency value t_0 but rises with frequency to the value $\pi t_0/2$ at cutoff. The plot of t_p/t_0 against $u=f/f_c$ is shown in Fig. 2.

Besides the phase delay time t_p, there is another delay time of even greater importance. This is the "group delay time" denoted t_g. It represents the delay for a signal composed of a group of frequencies in the vicinity of f. It can be shown that

$$t_g=d\beta/d\omega=t_p+\omega(dt_p/d\omega)=t_p+u(dt_p/du). \qquad (5)$$

The delay measured in signalling along the line will be t_g rather than t_p.[1] From Eq. (2) we get

$$t_g=t_0/(1-u^2)^{\frac{1}{2}}, \qquad (6)$$

which is also plotted in Fig. 2.

In what follows we shall restrict our examination of delay times to the group delay time t_g. In any frequency range *that includes zero*, the maximum deviation of t_p from t_0 will not exceed the maximum deviation of t_g from t_0.

Suppose that a line of the type under consideration is to be constructed to produce a total delay time t. The highest frequency f_1 which the line will be required to transmit is specified, as well as the variation in delay time which can be tolerated. Then the fraction $f_1/f_c=x$ can be determined. For example, if the delay time t_g is not to deviate from its low frequency value by more than 2.0 percent, one finds from Fig. 2 that the highest frequency which can be used is $0.2f_c$, so that $x=0.2$. The total number of sections required is approximately $n=t/t_0$ and from Eq. (4) $n=\pi f_c t=\pi f_1 t/x$. Clearly, the more stringent are the limits put on the variation of the time delay, the smaller is x and hence the greater is n. The principal objection to the simple low pass line is that the required number of sections is large. If the sections could be modified to produce a linear phase shift and constant delay over a greater portion of the pass band, higher values of x could be used and a smaller number of sections would be required.

m-DERIVED SECTION

It is common practice in the design of artificial lines to use the T section of Fig. 3A in which the two series inductances L have mutual inductance M and are connected series aiding. An equivalent form of the circuit is given in Fig. 3B, in which the coupling coefficient $k=M/L$ is negative for the series-aiding connection. In Fig. 3C the elements have been re-labelled in terms of the parameter

$$m=((1-k)/(1+k))^{\frac{1}{2}}, \qquad (7)$$

and in this form the circuit is recognized as m-derived from the filter of Fig. 1. The advantage of this section, compared with the previous one, is that the parameter m or k can be adjusted to extend the fraction of the pass band over which the time delay is approximately constant.

In terms of the parameter m, the phase shift per

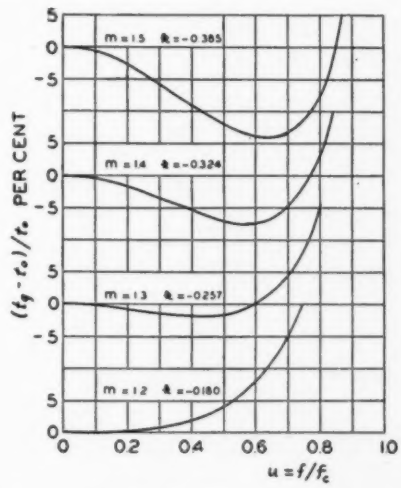

FIG. 4. The dependence of the group time delay on frequency for the m-derived section.

[1] The phase and group delays are equivalent to the reciprocals of the phase and group velocities which are introduced when velocity is dependent on frequency.

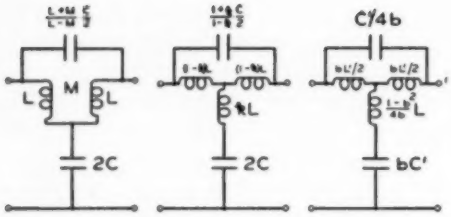

FIG. 5. Equivalent forms of the type B phase compensating network.

section β is given by

$$\tan(\beta/2)=mu/(1-u^2)^{\frac{1}{2}}, \tag{8}$$

in which $u=f/f_c$ and the cutoff frequency is

$$f_c=1/\pi(L'C')^{\frac{1}{2}}=1/2\pi(LC(1+k))^{\frac{1}{2}}. \tag{9}$$

From Eqs. (5) and (8) we find the group delay

$$t_g=\frac{t_0}{(1-u^2)^{\frac{1}{2}}[1+(m^2-1)u^2]}, \tag{10}$$

with $t_0=m/\pi f_c$. Figure 4 shows the variation of this delay through the pass band with several choices for the value of m. One may see by comparison with Fig. 2 that the m-derived filter does indeed maintain a more nearly constant time delay over a wider portion of the pass band than does the constant-K filter. Before making a closer comparison, we shall present three other delay networks.

TYPE B PHASE COMPENSATING NETWORK

Another circuit with good delay characteristics is the constant resistance section of Fig. 5, which is known as the type B Phase Compensating

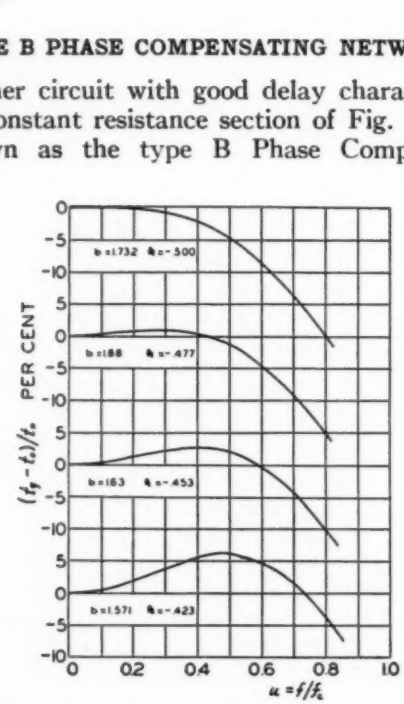

FIG. 6. The dependence of the group time delay on frequency for the type B network.

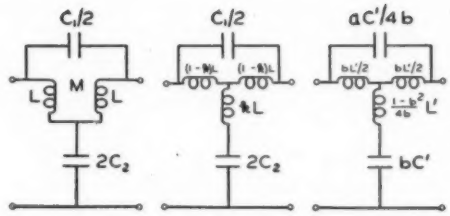

FIG. 7. The generalized bridged-T network.

Network.[2] In order for the three forms shown to be equivalent, one must have

$$k=M/L=(1-b^2)/(1+b^2). \tag{11}$$

The type B network differs from the m-derived filter in the presence of the bridging condenser which is so chosen as to make the image impedance a pure resistance.

It is convenient to write

$$u=f/f_c,\quad f_c=1/\pi(L'C')^{\frac{1}{2}}=1/2\pi(LC(1+k))^{\frac{1}{2}}. \tag{12}$$

Here f_c is the frequency at which the phase shift produced by the section is π. On account of the all-pass characteristics of the constant-resistance network, there is no cutoff at f_c as there was for the two previous filters. In terms of the parameter $b=((1-k)/(1+k))^{\frac{1}{2}}$, the phase shift β is given by

$$\tan(\beta/2)=bu/(1-u^2), \tag{13}$$

and the group time delay by

$$t_g=t_0\frac{1+u^2}{1+(b^2-2)u^2+u^4}, \tag{14}$$

where $t_0=b/\pi f_c$.

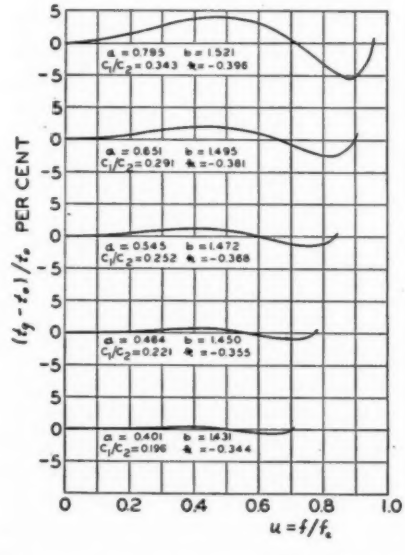

FIG. 8. The dependence of the group time delay on frequency for the generalized bridged-T network.

[2] A. T. Starr, *Electric Circuits and Wave Filters* (Sir Isaac Pitman and Sons, Ltd., London, 1940), p. 197.

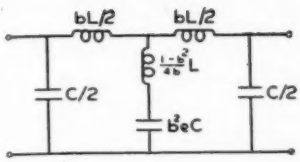

FIG. 9. The capacitance-shunted network.

Figure 6 shows the deviation of the time delay (14) from its low frequency value for several choices of b. Since b is greater than unity, k is negative, i.e., the inductances in Fig. 5A are connected series aiding. It will be noticed that the curves of Fig. 6 are concave downward, whereas those of Fig. 4 for the m-derived filter are concave upward. The accuracy with which a constant delay is maintained is about the same for the two networks.

GENERALIZED BRIDGED-T CIRCUIT

The appearance of the curves of Figs. 4 and 6 suggests that even better phase characteristics could be realized by a circuit intermediate to the m-derived and type B sections. Such a circuit can be obtained as a generalization of the type B circuit, by relaxing the requirement on the bridging condenser that it make the image impedance resistive. Figure 7 shows three equivalent forms of the circuit. The coupling coefficient k and the parameter b are still related by the formulas

$$k=(1-b^2)/(1+b^2), \quad b=((1-k)/(1+k))^{\frac{1}{2}}. \quad (15)$$

The bridging condenser $C_1/2$ is related to the new variable $a=b^2C_1/C_2$. There are now two parameters a (or C_1) and b (or k) which can be adjusted to secure optimum delay characteristics.

We write

$$f_c=1/\pi(L'C')^{\frac{1}{2}}=1/2\pi(LC_2(1+k))^{\frac{1}{2}} \quad (16)$$

and express the frequency f as the ratio $u=f/f_c$.

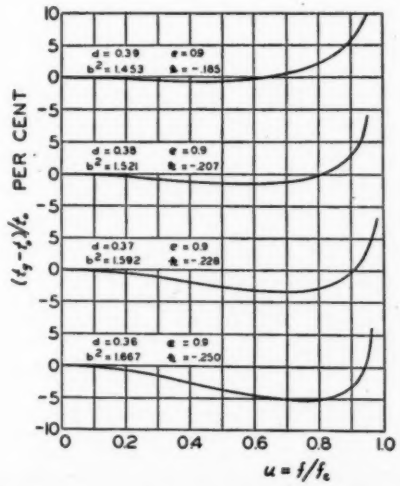

FIG. 10. The dependence of the group time delay on frequency for the capacitance-shunted network.

Then the phase shift is found from

$$\tan(\beta/2)=\frac{bu}{(1-u^2)^{\frac{1}{2}}(1-au^2)^{\frac{1}{2}}}. \quad (17)$$

When a lies between zero and unity, f_c is the lowest cutoff frequency of the filter. The group time delay is

$$t_0=t_0\frac{[1-au^4]}{[1+(b^2-a-1)u^2+au^4](1-u^2)^{\frac{1}{2}}(1-au^2)^{\frac{1}{2}}} \quad (18)$$

with $t_0=b/\pi f_c$. The generalized bridged-T network includes the m-derived and type B circuits as special cases. The first corresponds to $a=0$ and the second to $a=1$.

In Fig. 8 we have plotted delay curves for several values of the parameters. It will be observed that the curves first loop above and then below the axis. The parameters have been so chosen that these loops are approximately equal in height. On account of the algebraic complexity of Eq. (18) the adjustment was made numerically.

THE CAPACITANCE-SHUNTED NETWORK

It may not be feasible in some cases to use either of the bridged-T circuits because of their high pass properties. Since this is a consequence of the bridging capacitances, it seems possible that we can replace them by a pair of shunting capacitances, as in Fig. 9. Here again there are two parameters e (or C) and b (or k) which may be varied in order to obtain good performance.

In this analysis we write

$$f_c=(1/\pi)(e/LC)^{\frac{1}{2}}. \quad (19)$$

In terms of the variable $u=f/f_c$,

$$\tan\frac{\beta}{2}=u\left(\frac{e}{d}\right)^{\frac{1}{2}}\left(\frac{(1-du^2)}{(1-u^2)(1-eu^2)}\right)^{\frac{1}{2}}, \quad (20)$$

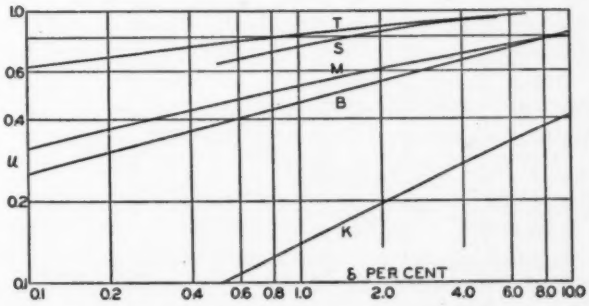

FIG. 11. The dependence of the useful fraction of the pass band on the error in the group time delay. The ordinate, u, is the fraction of the pass band within which the deviation of the group time delay from the low frequency value is less than $\pm\delta$ percent. K: constant-K network, M: m-derived network, B: type B network, T: generalized bridged-T network, S: capacitance-shunted network.

where $d=e/(1+eb^2)$, and, as before, $k=(1-b^2)/(1+b^2)$. Thus, when e is between zero and one, f_c is the lowest cutoff frequency.

The group time delay is

$$t_g=\frac{t_0[(1-eu^2)(1-du^2)+(e-d)(1-u^2)u^2]}{((1-u^2)(1-eu^2)(1-du^2))^{\frac{1}{2}}[(1-u^2)(1-eu^2)+(eu^2/d)(1-du^2)]} \tag{21}$$

with $t_0=(e/d)^{\frac{1}{2}}/\pi f_c$.

Figure 10 shows the delay curves for several pairs of values of the parameters e and b.

COMPARISON OF THE NETWORKS

We are now in a position to make a comparison between the five networks which have been examined. For this purpose, we plot in Fig. 11 the fraction of the pass band over which the network can be used, against the maximum variation in time delay from the low frequency value. In the m-derived, type B, and capacitance-shunted networks the useful fraction of the pass band is taken as the value of u at the axis crossing ($t_g=t_0$). With the generalized bridged-T circuit where there are two crossings, the value of u at the larger is used. For the constant-K filter which has no axis crossings, the fraction of the band is just the value of u at which the specified error in delay is obtained.

Figure 11 shows clearly the relative performance of the several networks. The m-derived section is slightly better than the type B both being much superior to the constant-K section. The generalized bridged-T circuit represents a further improvement. The capacitance-shunted network approaches the performance of the generalized bridged-T network. It will be noted that the separations of the curves becomes less to the right of the figure, where deviation from constant time delay is large.

Figure 12 summarizes the manner in which the design parameters depend on the tolerance allowable in t_g. It is seen that most of the curves become flatter with a decreasing tolerance. This means that the selection of components becomes more critical as the tolerance is decreased.

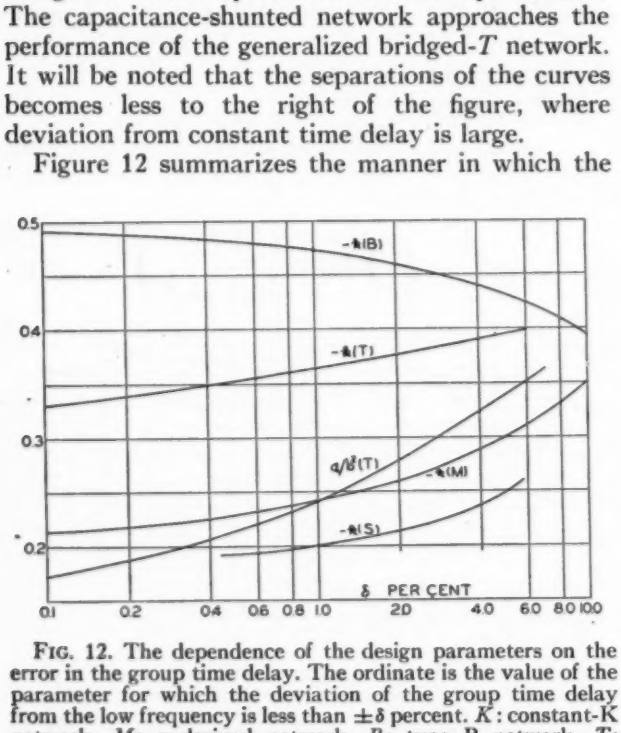

FIG. 12. The dependence of the design parameters on the error in the group time delay. The ordinate is the value of the parameter for which the deviation of the group time delay from the low frequency is less than $\pm\delta$ percent. K: constant-K network, M: m-derived network, B: type B network, T: generalized bridged-T network, S: capacitance-shunted network.

THE IMAGE IMPEDANCE

The foregoing discussion has been written entirely from the viewpoint of group time delay. However, we are occasionally interested in achieving a constant image impedance over the frequency range of interest. In this section the properties of the image impedance throughout the pass band are reviewed briefly.

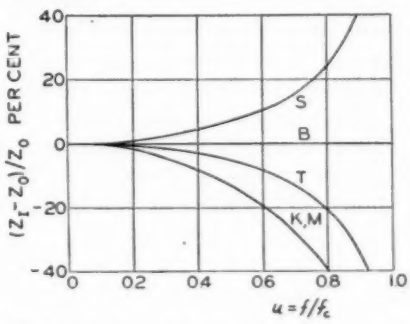

FIG. 13. The deviation of the image impedance from its low frequency value as a function of frequency. K: constant-K network, M: m-derived network, B: type B network, T: generalized bridged-T network, S: capacitance-shunted network.

Let Z_I = image impedance at $u=f/f_c$ and Z_0 = image impedance at $u=0$.

For the simple L-C line the image impedance at the mid-series section is

$$Z_I=Z_0(1-u^2)^{\frac{1}{2}}. \tag{22}$$

This is also the mid-series image impedance of a mid-series m-derived section with a constant-K prototype. The type B phase-compensating network has a constant image impedance, R, for all frequencies. The image impedance of the generalized bridged-T network is given by

$$Z_I=Z_0((1-u^2)/(1-au^2))^{\frac{1}{2}}, \tag{23}$$

while the image impedance of the capacitance-shunted network is

$$Z_I=Z_0\left(\frac{(1-eu^2)}{(1-u^2)(1-du^2)}\right)^{\frac{1}{2}}. \tag{24}$$

Plots of these four image impedances are shown in Fig. 13.

An Apparatus to Depict the Load-Elongation Diagram of Yarn at Five Cycles per Second*

FRANCIS BREAZEALE AND JOHN WHISNANT
Research Department, American Enka Corporation, Enka, North Carolina
(Received December 20, 1948)

An apparatus is described which presents on a cathode-ray oscilloscope the load-elongation hysteresis diagram, loading and unloading, of a length of yarn. The frequency may be adjusted from 1.7 to 5 cycles per second, the constant minimum load per cycle at any value from several grams to several thousand grams, and the percent extension per cycle from several percent down to several tenths of one percent. The growth of the sample as a function of time is automatically plotted, and, in addition, the stretch modulus of the sample at any time may be determined from the setting of an amplifier dial.

As way of illustration of the type of data which may be obtained with this apparatus, there are shown both the absolute and percent energy losses exhibited by tire cords of widely different constructions. For the somewhat arbitrary condition of load increment 2 kilograms over a minimum load of 0.6 kilogram, at a frequency of 5 cycles/second, both the percent and absolute energy losses increase very rapidly with increasing twist in the plies, less rapidly with increasing twist in the cord. Of interest, also, is the extremely high energy losses shown by cords which are made by plying together two plies of originally zero twist, thus giving a cord whose ply and cord twist are approximately the same, and in the same direction: Some other interesting features regarding energy losses in cords are pointed out.

I. INTRODUCTION

IN realization of the fact that the elastic and hysteresis energy loss properties of yarn may be quite different under some of the dynamic conditions to which they are subjected in use, as compared to nearly static conditions, an apparatus has been constructed which depicts on an oscillograph screen the stress-strain hysteresis loop of a length of yarn, extended and released at a rate as high as 5 cycles/second, and which also allows the ready determination of the dynamic stretch modulus[1] of the sample at any time. The growth of the sample is automatically recorded on graph paper as a function of time. Inasmuch as the behavior of tire cord at reasonably high frequencies of loading and unloading is of considerable practical interest, especially from the hysteretic energy loss standpoint, it was thought appropriate to illustrate the performance of this apparatus with such data taken from tire cords. However, this apparatus is by no means limited to the accommodation of tire cords; comparatively fine single yarns may be examined as well.

There appear to be two especially significant papers relating to energy losses in tire cords. The first is: "Hysteresis and related elastic properties of tire cords," by H. Wakeham and Edith Honold.[2] In this investigation, tire cords were subjected to extension and release therefrom at a frequency of 1 cycle-second. The load was generally on the order of 1.4 kilogram, and the value for energy loss for a cotton cord of 18/4/3 construction, when converted to our form of expression, was 2.1×10^5 ergs/gram/cycle. The second paper of interest in this connection is "Method for the absolute measurement of dynamic properties of linear structures at sonic frequencies," by W. James Lyons and Irven B. Prettyman.[3] In this investigation, a length of cord was subjected to elongation and release therefrom at frequencies from 100 to 300 cycles/second. By the very nature of this test, however, the stress (or strain) amplitude was very small. The energy loss in a cotton cord of 11/4/2 construction was found to be about 2.5×10^4 ergs/gram/cycle, which differs almost by a factor of 10 from that found by Wakeham and Miss Honold. This great discrepancy was noted by Lyons and Prettyman and they ventured the opinion that it was probably due to the great difference in strain amplitude between the two methods of measurement. As a comparison, we may state that under an incremental load of about 50 percent greater than that employed by Wakeham and Miss Honold (2.0 kilo as compared to 1.4 kilo), we found for a cotton cord of 11/4/2 construction a value of 3.5×10^5 ergs/gram/cycle, just about as expected.

When we wish fully to simulate the stress increment and release therefrom to which a cord in a tire is subjected at a nominal running speed, we must satisfy two conditions: First of all, the frequency of load application and release should be on the order of perhaps 0.01 second, since it is recognized that the cords in a tire are only subjected to this treatment for that small fraction of a revolution just before the particular section of tire concerned is in contact with the road, during its period of contact, and immediately thereafter. The second condition we must meet is that the incremental load be the same as that in a tire. (Incidentally, we neglect the compression to which the cords are certainly sub-

* Read before the Fall Meeting of the Fiber Society, Boston, Massachusetts, September 10, 1948.

[1] Here defined as the constant relating load (L) on, and resulting strain ($\Delta l/l$) of the specimen, hence: S.M. $= L.\ l/\Delta l$.

[2] H. Wakeham and Edith Honold, J. App. Phys. 17, 698 (1946).

[3] W. James Lyons and Irven B. Prettyman, J. App. Phys. 19, 473–480 (1948).

jected during the part of a cycle, since there seems to be no practical means of duplicating this condition in an apparatus of the general nature we are discussing.) It is evident that to fulfill these two conditions would be an extremely difficult job from the apparatus standpoint. It is further obvious that in each of the two investigations already noted, there is a compromise between frequency and incremental load. In the apparatus here to be described, it is felt that, although it, too, is a compromise, it is one in the much less objectionable direction, namely, the load increments are realistic, but the frequency (5 cycles/second) may leave something to be desired. As a matter of fact, it is noted in Lyons' paper that the energy loss per cycle of his cotton cord mentioned above was independent of frequency in the range 60 to 300 cycles/second. Furthermore, the comparatively close agreement between the values of Wakeham and Miss Honold on one hand, and ours on the other for cotton cord, indicates that the energy loss/cycle is also substantially independent of frequency in the range 1–5 cycles/second. And thirdly, when one calculates Lyons' and Prettyman's data on a rayon cord on the basis of percent energy loss/cycle, one finds this to be about 4–5 percent, which, as we will see later, is about the minimum value which we find. All in all, it seems, therefore, that the energy loss/cycle in such a test, while of course strongly dependent on the strain amplitude, may be considered to be only slightly dependent on the frequency in the range 1–300 cycles/second. It is therefore believed that for investigations of the type herein discussed, the compromise in the direction already indicated is by far the preferable one.

II. APPARATUS

Figure 1 is a schematic diagram of both the mechanical and electronic components of the apparatus. This assembly is also shown in Fig. 2, to which the components designated by capital letters refer.

A strain gauge,[4] *A*, is mounted on the end of a reciprocating shaft which is motivated by a cam enclosed in an oil box, *B*. This cam has two cuts, either of which may be used; a sine-wave one and a saw-tooth one. In the experiments herein to be described, the saw-tooth one is used. This cut, of course, imparts to the strain gauge a reciprocating motion of *constant* velocity. The amplitude of this motion is 5.0 mm. The cam is driven, through a set of speed reduction gears (hidden by the shield, *C*), by a $\frac{1}{4}$-hp motor, *D*. The gears are easily interchangeable to give a frequency variation of from 1.7 to 5 cycles per second, in several steps. In this investigation, a frequency of 5 cycles/second was used throughout. Also driven from the cam shaft through a clutch is a Microtorque potentiometer,[5] *E*, continuously rotatable through 360 degrees. This unit is tapped at two places 180 degrees apart and is provided with a single rotating brush. It will be appreciated that the constant angular velocity, which is imparted to the brush, results in a saw-tooth voltage output. Each of the clutch plates is fixed with a shoe so that they always assume the same relative position when engaged; and thus the position of the brush on the potentiometer will always be maintained in synchronization with the cam shaft and thereby in synchronization with the traverse position of the strain gauge.

On the right hand side of the bench may be seen the take-up and elongation-recording unit, *F*. Such a device is necessary inasmuch as the yarn grows when subjected to the minimum tension, in addition to the rapid extension and release, as mentioned. The take-up device proper consists of a long, finely threaded screw, to the right-hand end of which is fixed a ratchet wheel, which is, in turn, advanced by

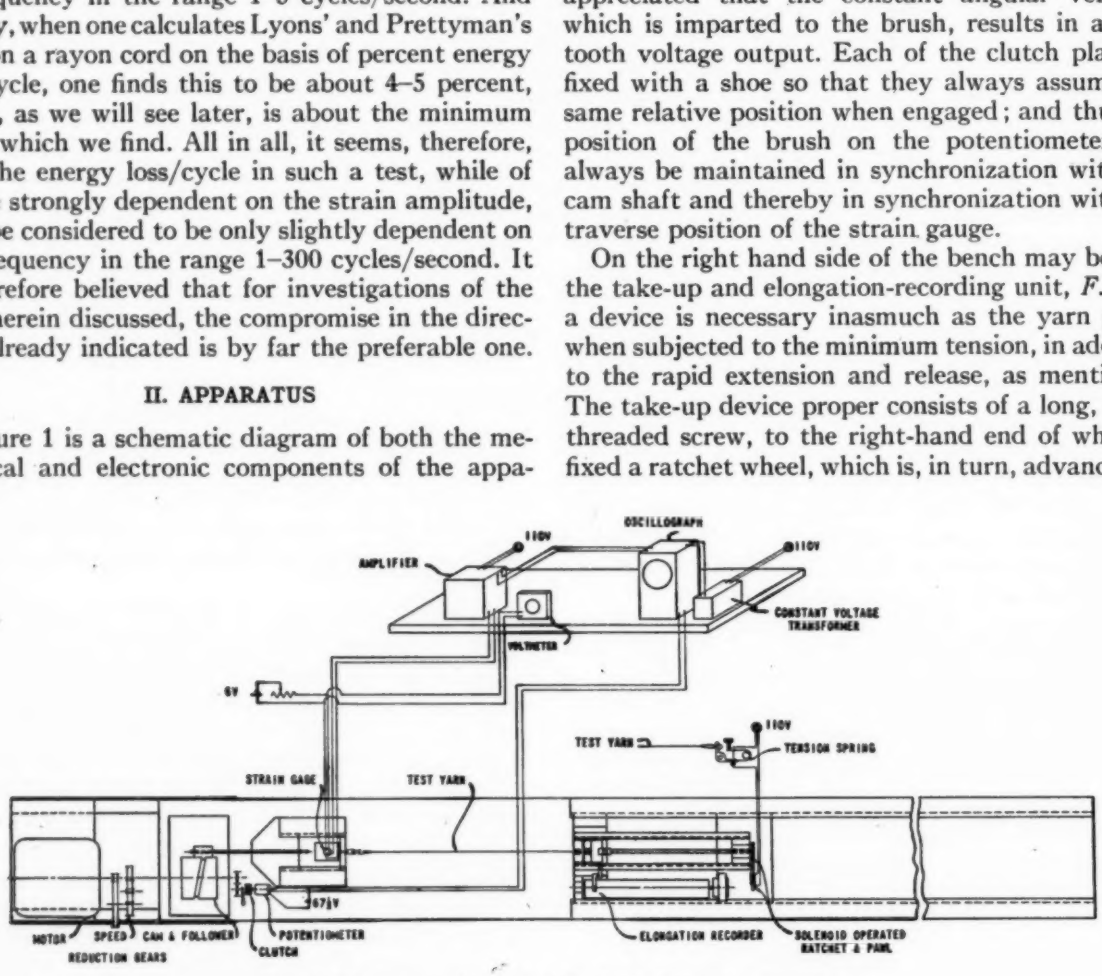

FIG. 1. Diagrammatic view of the load-elongation recorder.

[4] Manufactured by Statham Laboratories, Los Angeles 36, California.
[5] Manufactured by Autoflight Instruments, Pasadena, California.

means of a solenoid-actuated pawl. The left-hand end of the screw runs through a sliding carriage, which runs between ways, and to which the other end of the yarn specimen is attached. This solenoid is energized when the tension in the thread falls below a certain predetermined value, and thus allows an electrical contact in its circuit to close. By choice of the stiffness of the spring, and also by the setting of its compression means, the yarn tension below which the electric contact will close, may be determined. The growth of the yarn, that is to say, the advance of the thread-anchoring mechanism by the screw, is recorded by means of a pen or pencil riding on the drum which is turned at constant speed by an electric clock motor. Provision is made for wrapping the drum with a piece of ordinary graph paper for this purpose. The whole take-up unit just described may be clamped in any position along the main ways of the bed, and thus any desired initial length of yarn between about 25 and 240 cm may be used.

General reference will now be made to the electronic components, which are also shown in diagrammatic form in Fig. 1 and in Fig. 2. The strain gauge has the following characteristics: maximum load, 4.5 kilograms; output linear, within ½ percent; maximum exciting voltage, 16 volts; output to high impedence (such as used in the present application), 22 millivolts per kilogram. The very considerable gain of the amplifier into which it feeds, enables a smaller exciting voltage (6) to be used. This is advantageous from the standpoint of keeping the unit stable. The voltage is supplied from a 6-volt Hotshot battery, with a 1000-ohm variable resistance in series so that a constant voltage, which is read on the voltemeter, V, may be employed. The output of the strain gauge feeds through shielded cable, into an amplifier, W, specially constructed for us by the G. C. Wilson Company.[6] This amplifier shows a flat response between 2 and 15 c.p.s., and a maximum voltage amplification of approximately 3×10^3. Its output, which is fed directly to the vertical deflecting plates of the cathode-ray oscillograph, is controlled by a rotatable knob whose position is graduated in terms of output voltage, for a constant input. The Microtorque potentiometer is supplied with 67½ volts to its two taps by means of B-batteries. The output from it then consists of the voltage between the brush and one of the taps. This voltage is fed directly to the horizontal deflecting plates of the oscillograph. The oscillograph itself, X, is an RCA Model 160. It is powered through a Sola[7] constant-voltage transformer. It was found necessary to use this transformer to minimize wandering of the pattern on the screen. Not shown in Fig. 1,

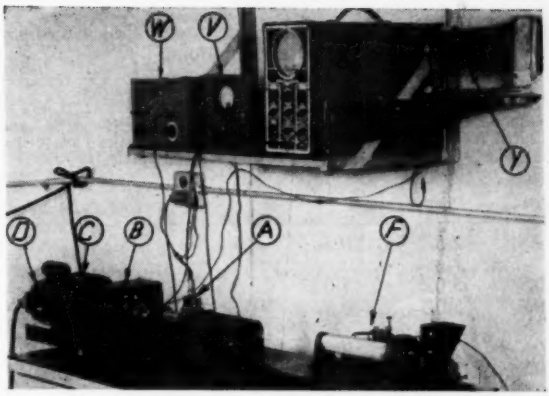

FIG. 2. General view of the load-elongation recorder.

but shown in Fig. 2, is a camera, Y, mounted on a swinging holder so that it may easily be brought into position when the image on the screen is to be photographed. The camera is equipped with an Eastman Ektar lens, which is used at f:4.7. The distance between the oscillograph screen and the lens is about 28 cm. Eastman Super-XX film is employed in the form of a 12-exposure film pack.

III. APPARATUS CALIBRATION AND CALCULATION OF RESULTS

The percent energy loss shown by any specimen is, of course, directly calculated from the ratio of the area of the hysteresis loop to the area underneath it. The stretch modulus of the specimen is directly determined from the vertical displacement of the spot on the oscillograph screen, the setting of the amplifier dial, and the length of the specimen. Calibration of the apparatus to determine the relationship between amplifier dial setting and applied load is effected by running several lengths of piano wire, whose elastic modulus was determined by conventional methods. There is an instrumental consideration which makes it necessary to calibrate the instrument with a known, practically perfectly elastic material before hysteresis measurements on yarn may be accurately conducted. This is the slight time lag in both the strain gauge itself and the strain gauge amplifier. Fortunately, there is a ready means by which these two effects may be compensated instrumentally. This is done by rotating the potentiometer and its pointer so that in testing a practically perfectly elastic body, such as a long piece of steel piano wire, the pattern on the oscillograph becomes a straight line. It has been found that this occurs with a potentiometer rotation of approximately 10° in the direction to make the strain lag behind the stress. For a testing frequency of 5 cycles/second, this corresponds to a time lag of only 0.0056 second.

When it comes to the determination of absolute energy loss for the cords, there is some question as to

[6] Chatham, New Jersey.
[7] Manufactured by the Sola Electric Company, Chicago, Illinois.

TABLE I. Stretch moduli and energy losses shown by cords of various constructions.

Final construction turns/inch		% extension	% energy loss	Stretch modulus	Energy loss/ cycle/gram of yarn $\times 10^5$ ergs.
Cord	Plies			$\times 10^9$ dynes	For 2-kilo load over 0.6-kilo. minimum
5.4*S*	2.5*Z*	0.5	6.1	3.6	0.9
5.0*S*	5.0*Z*	1.0	6.6	3.0	—
5.0*S*	5.0*Z*	0.5	—	3.4	
5.0*S*	7.9*Z*	0.5	4.0	2.5	1.1
5.0*S*	7.9*Z*	1.0	7.2	2.6	
5.0*S*	7.9*S*	0.5	7.5	2.8	1.3
4.7*S*	7.7*S*	1.0	7.7	3.0	
4.9*S*	9.9*S*	0.5	7.6	2.1	2.2
4.5*S*	9.5*S*	1.0	12.8	2.2	
5.4*S*	14.4*S*	0.5	5.9	1.6	4.3
5.0*S*	14.7*S*	1.0	11.4	1.5	
4.9*S*	3.0*Z*	0.5	4.8	3.6	0.8
4.9*S*	3.0*Z*	1.0	5.2	3.0	
5.0*S*	7.8*Z*	0.5	5.3	2.6	—
5.0*S*	7.8*Z*	1.0	—	2.5	
5.0*S*	7.8*Z*	0.5	5.0	2.7	0.9
5.0*S*	7.5*Z*	1.0	4.9	2.7	
5.0*S*	9.0*S*	0.5	5.1	2.4	1.7
5.0*S*	9.5*S*	1.0	9.5	2.3	
4.4*S*	11.8*S*	0.5	8.9	1.8	4.3
4.0*S*	11.0*S*	1.0	15.7	1.9	
4.2*S*	14.0*S*	0.5	9.9	1.7	7.2
4.0*S*	13.4*S*	1.0	20.9	1.6	
3.5*Z*	15.5*Z*	0.5	6.9	1.8	5.7
4.2*Z*	14.7*Z*	1.0	16.8	1.5	
6.4*Z*	14.7*Z*	0.5	8.4	1.7	4.8
7.2*Z*	14.2*Z*	1.0	14.9	1.7	
7.1*Z*	8.4*Z*	0.5	6.4	—	1.3
6.8*Z*	8.0*Z*	1.0	8.3	2.8	
7.2*Z*	7.6*Z*	0.5	14.3	2.2	4.0
8.0*Z*	8.5*Z*	1.0	17.0	2.0	
7.3*S*	6.9*Z*	0.5	5.4	2.5	1.2
7.3*S*	6.9*Z*	1.0	6.9	2.6	
6.5*S*	11.0*S*	0.5	9.2	2.1	2.7
5.3*S*	10.0*S*	1.0	12.7	2.2	
4.6*S*	4.5*S*	0.5	8.0	3.1	1.5
5.0*S*	5.0*S*	1.0	9.7	2.8	
4.8*S*	5.0*Z*	0.5	6.2	3.3	1.0
4.9*S*	4.9*Z*	1.0	6.5	3.2	
7.5*Z*	4.8*Z*	0.5	4.0	3.3	0.7
7.5*Z*	4.8*Z*	1.0	5.9	3.0	
8.1*Z*	4.6*S*	0.5	4.3	2.8	1.0
8.0*Z*	4.9*S*	1.0	6.9	2.8	
7.7*S*	5.5*Z*	0.5	3.0	2.7	1.2
7.7*S*	5.1*Z*	1.0	8.3	2.7	

TABLE I.—*Continued.*

Final construction turns/inch		% extension	% energy loss	Stretch modulus	Energy loss/ cycle/gram of yarn $\times 10^5$ ergs.
Cord	Plies			$\times 10^9$ dynes	For 2-kilo load over 0.6-kilo. minimum
6.7*S*	8.0*Z*	0.5	6.2	2.3	1.4
6.6*S*	7.8*Z*	1.0	7.4	2.6	
5.9*Z*	10.5*Z*	0.5	7.3	2.3	2.5
5.4*Z*	9.9*Z*	1.0	13.5	2.2	
5.8*Z*	12.5*Z*	0.5	9.7	1.9	4.2
5.6*Z*	12.1*Z*	1.0	17.5	2.0	
9.6*Z*	5.0*S*	0.5	5.2	2.4	1.07
9.6*Z*	5.0*S*	1.0	5.4	2.3	
9.1*S*	2.1*Z*	0.5	4.9	2.5	—
8.3*Z*	14.0*Z*	0.5	9.6	1.7	—
8.3*Z*	14.0*Z*	1.0	—	1.6	
7.9*S*	2.3*Z*	0.5	4.0	3.0	0.8
8.0*S*	2.5*Z*	1.0	5.9	3.0	
7.9*S*	2.3*S*	1.0	4.4	3.0	0.7
8.0*S*	2.4*S*	0.5	4.2	3.2	
8.0*Z*	8.1*Z*	0.5	5.5	2.5	1.1
7.5*Z*	8.2*Z*	1.0	6.0	2.7	
8.5*Z*	13.0*Z*	0.5	7.7	1.9	4.0
8.5*Z*	13.0*Z*	1.0	13.9	1.7	
7.8*S*	2.9*Z*	0.5	4.5	2.8	—
7.8*S*	2.6*Z*	0.5	4.0	2.9	0.7
7.8*S*	2.6*Z*	1.0	4.0	2.7	
8.9*Z*	13.0*Z*	0.5	7.7	1.8	3.4
8.0*Z*	12.5*Z*	1.0	12.3	1.7	
9.0*Z*	8.5*Z*	1.0	13.2	2.0	3.2
9.0*Z*	9.5*Z*	0.5	6.2	2.5	1.4
8.5*Z*	9.0*Z*	1.0	9.5	2.8	
9.0*Z*	9.3*Z*	0.5	11.9	2.1	—
9.0*S*	9.3*S*	0.5	9.1	1.9	5.0
10.0*S*	9.8*S*	1.0	19.0	1.8	
9.6*S*	1.4*Z*	0.5	5.7	2.5	1.2
9.8*S*	1.5*Z*	1.0	6.1	2.6	
12.6*Z*	2.0*Z*	0.5	7.1	2.0	1.9
11.5*Z*	0.9*Z*	1.0	8.3	2.2	
12.6*Z*	3.7*Z*	0.5	6.9	2.2	1.6
12.0*Z*	5.0*Z*	1.0	7.7	2.2	
12.0*Z*	7.6*Z*	0.5	7.4	2.3	2.2
11.4*Z*	7.5*Z*	1.0	11.3	2.2	
10.5*Z*	9.5*Z*	0.5	13.6	2.0	4.0
10.0*Z*	9.0*Z*	1.0	16.3	2.0	
11.8*Z*	14.5*Z*	0.5	—	2.4	2.6
11.4*Z*	14.5*Z*	1.0	13.4	1.9	
10.5*Z*	13.0*Z*	0.5	6.9	2.3	1.8
9.9*Z*	12.8*Z*	1.0	9.9	2.3	
10.0*Z*	9.6*Z*	0.5	—	2.2	—

the best scheme by which various cords may be compared in this regard. The one which we adopt here, and which seems to be of practical interest, is to give the energy loss per gram of cord, per cycle, when it is subjected to a certain load increment and release therefrom. It is advantageous to do this since in a tire it is incremental load and release therefrom, per cycle, which is important since the load determines the elongation of the cords, and thus their hysteresis losses. For that reason, as will be seen, the data which we obtained at two different percent elongations (0.5 and 1.0) are recalculated in terms of a given load increment. This was taken somewhat arbitrarily to be 2.0 kg. The picture we have, then, is of the absolute energy loss per gram of a cord subjected to a minimum load of 0.6 kg which is increased by 2.0 kg, and released back to 0.6 kg, 5 times per second.

The arithmetic fashion by which these computations are made from the data are as follows:

Assuming that in the load increment contemplated, the load-elongation relationship is linear, which it is to a good approximation, we have the following relationships for the energy involved, E, the application of a load, L, to a cord of length, l, resulting in an elongation, Δl,

$$E=(L\times\Delta l/2),\quad \text{stretch modulus,}\quad \text{S.M.}=\frac{L\times l}{\Delta l},$$

thus,

$$\Delta l=(L\times l/\text{S.M.}),\quad \text{and,}\quad E=(L^2\times l/2\ \text{S.M.}). \quad (1)$$

Inasmuch as we wish to express energy in terms of 1 gram of yarn, we multiply the above equation by the reciprocal of the weight of l cm of yarn, and the expression for the energy involved then becomes:

$$E'=(L^2/2\ \text{S.M.}\times d), \quad (2)$$

where:

d = linear density of cord in gm/cm.

When this last expression is multiplied by the percent energy loss, determined as described above, the final expression for the energy loss per gram of yarn per cycle when subjected to the chosen stress increment of 2 kg, then becomes:

$$E=\frac{2\times 10^{10}}{\text{S.M.}\times d}\times\text{percent energy loss ergs.} \quad (3)$$

There are two more computations that are necessary before the data may be substituted in Eq. (3). The first is to determine the percent extension which any particular cord would undergo when it is subjected to a stress increase of 2.0 kg over 0.6 kg. This, of course, is determined by the stretch modulus, and for $L=2$ kg, it becomes: $2\times 10^8/\text{S.M.}$ The second is to use the data on percent energy losses of the particular cord at 0.5 and 1.0 percent extension to determine what the energy loss would be at the extension calculated as mentioned directly above. Inasmuch as the extensions in this range are almost all within the limit 0.5 and 1.0 percent, and since, in general, the percent energy loss of 0.5 and 1.0 percent extension do not differ too markedly, a linear interpolation or extrapolation is employed. As a matter of fact, it so happens in this data that for the majority of those few cases where there is considerable difference in percent energy loss between 0.5 and 1.0 percent extension, the extension which would occur at 2 kg falls rather close to the upper limit. This is added assurance that the calculated values of energy loss at this region are probably quite valid.

IV. DATA

The data now to be presented in tabular form consist of percent energy loss shown by cords of various constructions when elongated at both 0.5 percent and 1.0 percent, together with the stretch modulus of these cords at these two elongations. In addition, there is shown in graphical, as well as tabular form, the absolute energy loss per gram of cord per cycle, for some of these various cords when subjected to an incremental load of 2 kg over a minimum load of 0.6 kg. This latter type of data is significant as a measure of the heat generated in the cords of a running tire. Incidentally, by far the best way of presenting these data, both for the percent energy losses and the absolute energy losses, is by means of three-dimensional models, in which the vertical axis is either percent energy loss or absolute energy loss, and the two horizontal axes are ply twist as exists in the cord, and cord twist. Unfortunately, however, the difficulties of interpreting a photograph taken of such models as constructed here rules out this mode of presentation.

First, it is appropriate to make several general remarks concerning Table I. It will be noted that the first two columns give the cord and ply twist as it exists in the cord in turns/inch either right (S) or left (Z). The next column gives the percent extension imposed on the particular specimen. This is followed by the percent energy loss calculated as described above, and the stretch modulus also calculated as described. The last column is the absolute energy loss/cycle and, as will be appreciated from the description of the previous section, it is calculated for those experiments in which *both* 0.5 percent and 1.0 percent extension data are available. It will be noted that in several pairs of runs the data on percent energy loss for one of the extensions is not recorded. These omissions are due to the fact that good photographs were not obtained in several cases. However, percent energy loss of the other member of the pair is recorded for the sake of presenting as much data as possible, although the absolute energy loss cannot be calculated unless the

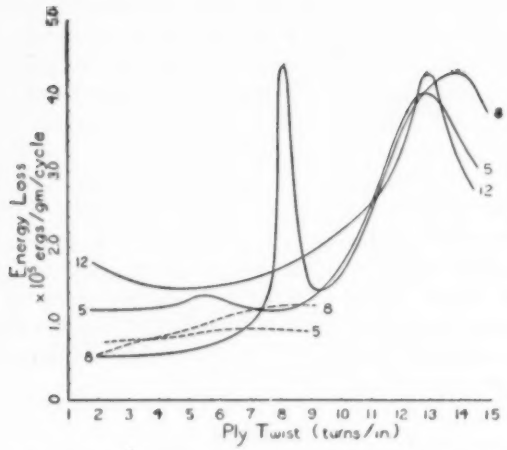

FIG. 3. Absolute energy loss per extension cycle *vs.* ply twist, for cord twists of 5, 8, and 12 turns/inch, as calculated for a load increment of 2 kilo. over a minimum load of 0.6 kilo. (——) twist in cord and plies in the same direction; (- - - -) in opposite directions.

percent extension, at which data is available, is very nearly that which would be occasioned by the application of the 2-kg. load.

Perusal of the table reveals that the percent energy loss increases much more rapidly with increased singles twist than it does with increased cord twist, and that when the singles and cord twist are the same and in the same direction, percent energy losses are abnormally high. The same is true for the absolute energy loss, and the possible reasons thereof will be discussed presently.

The curves of Fig. 3, showing absolute energy loss as influenced by construction, are taken directly from the corresponding three-dimensional models; hence, the data points are not shown. It is believed all absolute energy values are correct within ±5.0 percent. It will be noted that the solid curves indicate cord and ply twist in the same direction, whereas the dotted lines represent cords whose ply and cord twist are in opposite directions. The reason that the dotted lines are restricted to a region of comparatively low cord and ply twist, is that to obtain opposite twists at all high values, the plies would have to be subjected to such a high initial twist that sufficient tension could not be put on them in the twister to maintain an even twist and yet not break them.

When viewing the curves in Fig. 3, one is immediately struck by two features: The first is that the energy loss shown by the cord increases very rapidly with twist in the plies (starting at about 7–8 turns/inch), as compared with increase in twist in the cord; the second that where twist in the cord and the plies is approximately the same, and in the *same direction*, there is an abnormally high loss in all cases. This is doubtless due to the fact that for all such cords the twist in the plies is zero, or very nearly so, when the plying operation is commenced. This may result in a great deal more area of contact between the two plies than ordinarily occurs. As far as the very rapid increase of energy loss with increasing twist in the plies is concerned, this probably is due to the fact that in each ply 720 filaments are in contact, and at high twist the innermost filaments are under considerable compressive forces, which would certainly give rise to considerable frictional forces between them when the ply is periodically elongated and released. Another point of interest is in the region where both the solid and dotted curves are seen. They lie fairly close together (except where the ply and cord twist is the same) indicating that whether the twist in the plies and cord is the same or opposite, the energy losses of such cords are about the same. As regards the energy loss of cords of the standard construction (10.5*S* in the cord; 1.0*Z* in the plies), it may be said that it is about 1.5×10^5 ergs/gram/cycle. In the region bounded by singles twist: 1–9 turns/inch and cord twist: 1–10 turns/inch (except for the humps), the energy loss is under this value; and between singles twist: 1–5 turns/inch and cord twist: 1–8 turns/inch, it is under 1.0×10^5 ergs/gram/cycle. It may be of interest to compare this value with that of a cotton cord of 11/4/2 construction. When run under the same conditions discussed, its energy loss at 0.5 percent extension was found to be 14 percent; at 1 percent extension, 18 percent; and the absolute energy loss for a stress increment of 2 kg (over 0.6 kg), 3.2×10^5 ergs/gram/cycle. It is probable that this high value of absolute energy loss in cotton cords is not primarily due to a high intrinsic hysteresis loss property of cotton, but rather arises from the fact that cotton fibers must be twisted together to form threads, and further, that the plies have a fairly high twist. This is, perhaps, then, an analogous situation to a rayon cord with high twist in the plies, which, as we have seen, is accompanied by high energy losses.

ACKNOWLEDGMENTS

It is a pleasure to make acknowledgment to the following individuals who had a large part in the design and construction of the apparatus: Mr. Paul Green and Mr. Raymond Ross, Jr., design; Mr. Woodfin Clayton and Mr. Howard Perrits, construction.

Transition Temperatures of Methyl Methacrylate Polymers at Ultrasonic Frequencies

THOMAS F. PROTZMAN
Mendenhall Laboratory of Physics, Ohio State University, Columbus, Ohio
(Received January 19, 1949)

The velocity of sound in methyl methacrylate polymers (Plexiglas) has been measured at temperatures from 24° to 90°C, and frequencies from three to eleven megacycles. Optical diffraction methods were used to determine the sound velocity within a maximum error of 1 percent. This low experimental error made possible a detailed study of the sound velocity-temperature relationships. A previously unreported transition of a new type has been found. The sound velocity decreases linearly with increasing temperature, with an abrupt increase of slope occurring when a transition temperature is reached. The transition temperature is found to decrease linearly with frequency, falling from 64°C at three megacycles to 49°C at eleven megacycles. The observed transitions apparently are not manifestations of elastic relaxational effects and are tentatively attributed to the excitation of some mode of molecular motion, for example, molecular vibrations.

INTRODUCTION

USING the optical diffraction methods of Shaeffer and Bergmann[1] we have measured the velocity of longitudinal waves in methyl methacrylate polymers[2] at frequencies of three, five, nine, and eleven megacycles. The high precision of these measurements made possible a detailed study of the variation of the velocity of sound with temperature, which revealed a new type of transition in the neighborhood of 60°C.

EXPERIMENTAL PROCEDURE

The polymer samples were cut from cast methyl methacrylate sheet. The sample size was $2\frac{1}{2}'' \times \frac{3}{4}''$ × thickness of sheet. The cut surfaces of the sample were filed flat and smooth, and the samples were annealed in an oil bath at 120°C after preparation.

X cut quartz crystals, with aluminum or silver electrodes, were cemented to a machined surface of the polymer so that the sound waves were propagated parallel to the cast surfaces of the polymer. The fundamental frequencies of the crystals were one and three megacycles.

For measurement the samples were placed in a temperature-controlled oil bath equipped with a stirrer. Two plate-glass windows on the sides of the tank allowed the light to pass through the bath and the sample. Sufficient time was allowed at each temperature for the sample to come to equilibrium.

An *H*-4 mercury-arc lamp served as light source. The mercury green line was isolated with Corning glass filters. As indicated in Fig. 1, parallel light from the lens, L_1, was projected through the sample, *P*, and focused by the lens, L_2, on a photographic plate.

The quartz crystals were excited by a Hartley oscillator tuned to a suitable harmonic of the crystal. The radiofrequency voltage applied to the crystal faces varied from 500 to 1000 volts. The mechanical damping of the sample and the oil bath resulted in marked broadening of the resonant response of the crystals. The frequency of the oscillations was measured with a General Radio Precision Wave Meter type 724A.

Separation of the diffraction lines recorded on the photographic film was measured with a traveling microscope.

PRECISION OF MEASUREMENT

The diffraction of light from a sound grating obeys the law[1]

$$n\lambda = d \sin\theta,$$

where n is the order of diffraction; λ, the wavelength of the light; θ, the diffraction angle; and d, the grating space, may be identified with the wavelength of the sound. For small angles of diffraction this expression becomes

$$n\lambda = \theta d.$$

Expressing d, the sound wave-length, in terms of sound velocity, V, and frequency, f; and expressing θ in terms of arc length, D, and radius, R (cf. Fig. 1), we get

$$V = (nfR\lambda)/D.$$

The maximum error in measurement of V then is,

$$\Delta V/V = \Delta R/R + \Delta D/D + \Delta f/f + \Delta\lambda/\lambda.$$

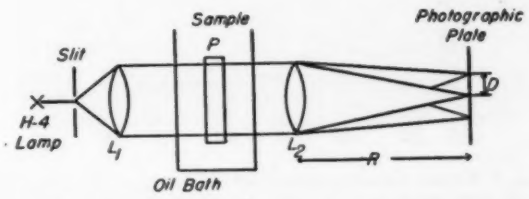

FIG. 1. Schematic diagram of optical system.

[1] C. Shaeffer and L. Bergmann, Sitz.-Ber. Berliner Akad., 155 (1934).

[2] The methyl methacrylate polymers used in these measurements are manufactured by the Rohm & Haas Co., Philadelphia, Pa., and sold under the trade name "Plexiglas." Plexiglas II and Plexiglas IA designate unplasticized and plasticized polymers respectively.

TABLE I.

Sample	Sheet thickness (inches)	Softening point ASTM heat distortion
Plexiglas II	½	90°C
Plexiglas IA	1	81°C
Plexiglas IA	½	76°C

The errors in f and λ are negligible compared with those in D and R. In these measurements the error in R is estimated at $\Delta R/R \approx 0.5/100$ and that in D at $\Delta D/D \approx 0.5/100$. Thus the maximum error in the sound velocity is of the order of 1 percent. The relative error in any given series of measurements should be less than this figure as the distance R was kept fixed.

EXPERIMENTAL RESULTS

The characteristics of the samples used in these measurements are listed in Table I.

Figures 2 and 3 show the results of measurements on samples of Plexiglas IA and II at three megacycles, plotted against centigrade temperature and inverse absolute temperature. The fact that the sound velocity varies linearly with both centigrade temperature and inverse absolute temperature results from the limited range of temperatures covered in these experiments.

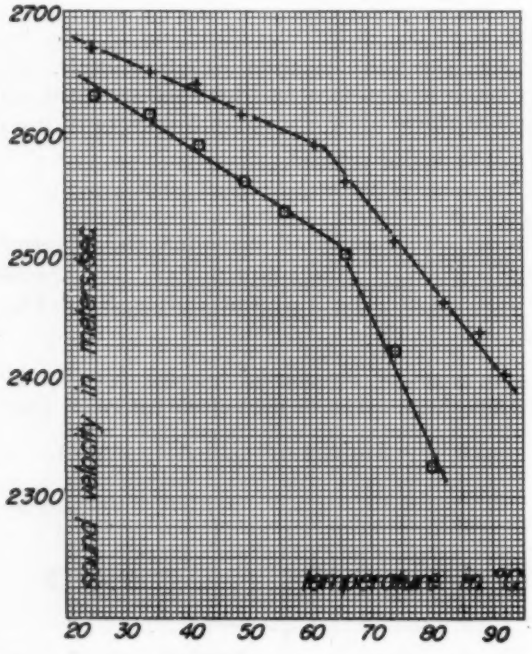

FIG. 2. Sound velocity measured at 3 megacycles as a function of temperature. Crosses: ½" Plexiglas II; circles: 1" Plexiglas IA.

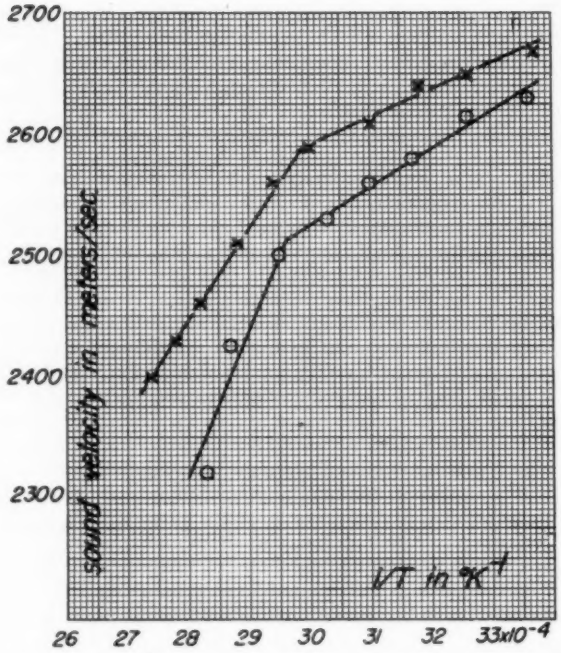

FIG. 3. Sound velocity measured at 3 megacycles as a function of inverse absolute temperature. Crosses: ½" Plexiglas II; circles: 1" Plexiglas IA.

A sharp transition in the sound velocity curves will be noted in the region of 60°C. Abrupt transitions of this type have not been reported by other workers with polymeric materials. However, other workers with polymeric materials have reported experimental errors of 5 percent to 20 percent in the

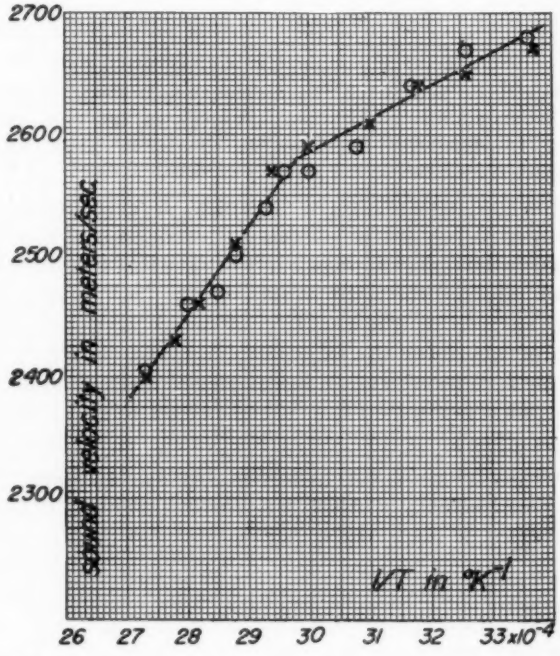

FIG. 4. Sound velocity measured at 3 megacycles as a function of inverse absolute temperature. Crosses and circles: duplicate samples of ½" Plexiglas II.

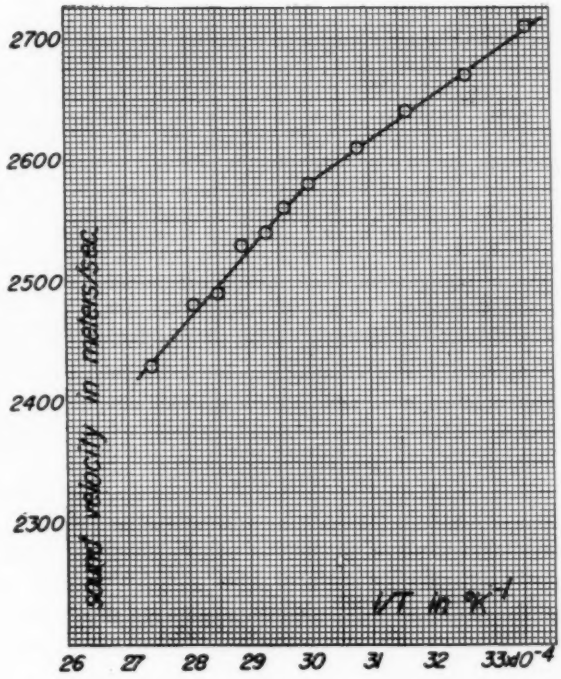

FIG. 5. Sound velocity of ½" Plexiglas II measured at 5 megacycles.

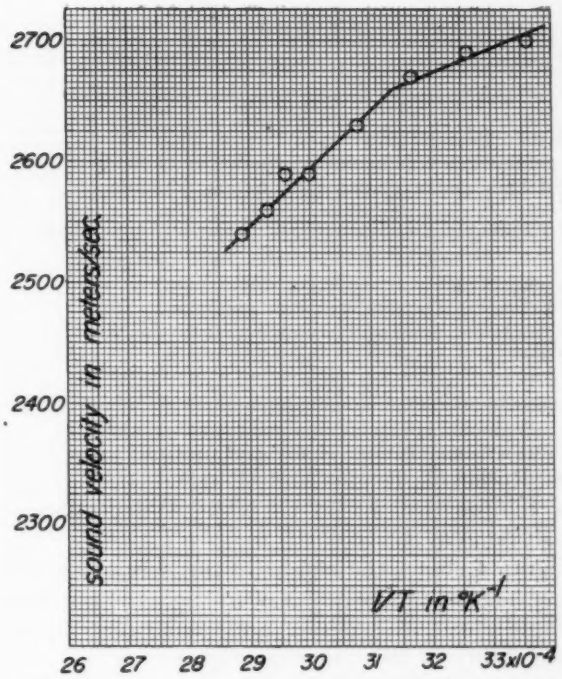

FIG. 7. Sound velocity of ½" Plexiglas II measured at 11 megacycles.

velocity of sound which would effectively mask these transitions. It is, therefore, impossible to determine at this time whether these transitions are unique with methyl methacrylate polymers.

A transition in the cubical expansion coefficient of polystyrene has been observed by Alfrey, Goldfinger, and Mark[3] and interpreted by them as a second-order transition. Boyer and Spencer[4] list similar results for polyethylene, Styraloy, Buna S, Nylon, and Saran. Transitions have also been observed in

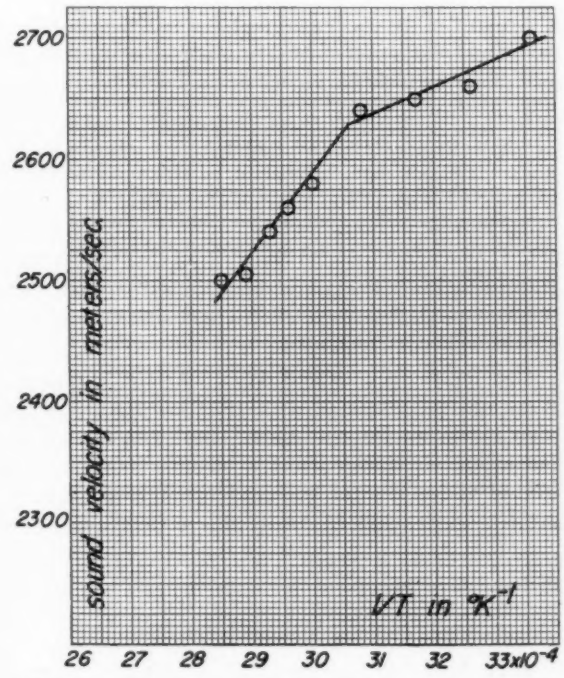

FIG. 6. Sound velocity of ½" Plexiglas II measured at 9 megacycles.

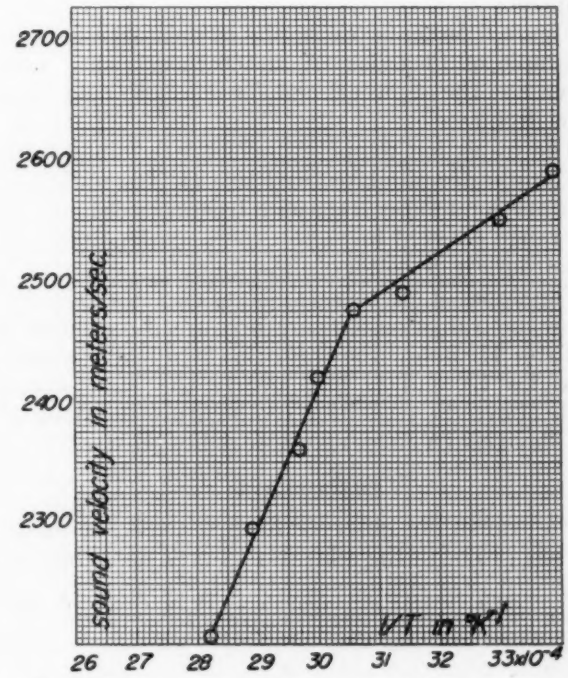

FIG. 8. Sound velocity of ½" Plexiglas IA measured at 9.6 megacycles.

[3] Alfrey, Goldfinger, and Mark, J. App. Phys. 14, 700 (1943).
[4] Boyer and Spencer, J. App. Phys. 15, 398 (1944).

TABLE II.

Sample	Thickness (inches)	Frequency (Mc)	Transition temperature °K	Transition temperature °C	Slope: $dV/d(1/T)$ Below transition temperature	Slope: $dV/d(1/T)$ Above transition temperature
Plexiglas II	½	3	336	63	2.6×10^5	7.5×10^5
		5	333	60	3.6	5.5
		9	327	54	2.0	7.2
		11	322	49	2.0	4.7
Plexiglas IA	1	3	338	65	3.1	12.5
Plexiglas IA	½	9.6	326	53	3.0	11.0

the cubical expansion of methyl methacrylate polymers. Robinson, Ruggy, and Slantz[5] report a transition temperature of 71°C, while Wiley[6] finds a transition at 67°C.

Figure 4 shows the results of measurements at 3 megacycles on two samples of Plexiglas II cut from a single sheet of polymer and illustrates the reproducibility of these measurements.

Figures 4, 5, 6, and 7 show the results of measurements on a sample of Plexiglas II at frequencies of 3, 5, 9, and 11 megacycles. Increasing sound absorption made it impossible to obtain measurements at 9 and 11 megacycles at the higher temperatures. Inspection of these graphs shows that the transition is strongly frequency dependent. The transition temperature is observed to decrease with increasing frequency.

Figure 8 presents the results of measurements on a sample of Plexiglas IA at 9.6 megacycles. This curve has the same general form as the curves at other frequencies.

The transition temperatures as determined from the graphs are tabulated in Table II. The variation of transition temperature with frequency is linear in the range covered in these experiments as may be seen from Fig. 9, a plot of these data.

The slopes of the sound velocity curves above and below the transition temperatures are also tabulated in Table II. Below the transition temperature both Plexiglas IA and II give nearly the same slope, while above the transition temperature the slope of the Plexiglas IA curves is appreciably greater.

DISCUSSION

The transitions observed in these experiments do not seem to be of the relaxational type described by

[5] Robinson, Ruggy, and Slantz, J. App. Phys. **15**, 343 (1944).

[6] F. Wiley, Ind. Eng. Chem. **34**, 1052 (1942).

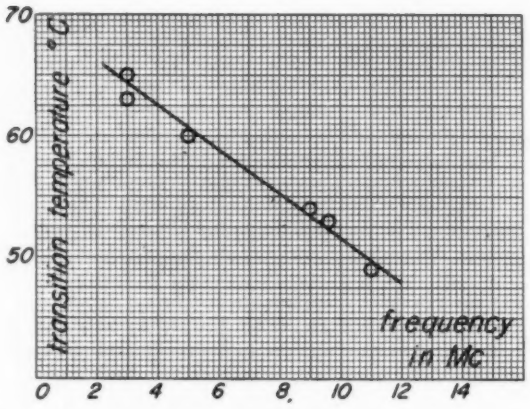

FIG. 9. Observed sonic transition temperatures as a function of sound frequency.

Alfrey.[7] According to the relaxational theories, thermal transitions in polymers occur at temperatures at which the mechanical relaxation time, τ, of the polymer is of the same order of magnitude as the experimental time scale, t. Assuming that the temperature dependence of the relaxation time is the same as that of the viscosity, that is,

$$\eta = Ae^{B/T}, \quad \tau = \eta/M = (A/M)e^{B/T},$$

and assuming that the elastic modulus, M, is independent of temperature, Alfrey obtains for the transition temperature the relation:

$$T_0 = B/(\ln M - \ln A + \ln t).$$

According to this relation, a decrease in experimental times scale (i.e., an increase in frequency) should result in an increase in the transition temperature. The observed variation of the transition temperature as a function of frequency is opposite to this, as shown in Fig. 9.

It might be possible to modify the assumptions about the temperature variation of the viscosity and elastic modulus so as to obtain a frequency variation of the transition temperature in accord with these results. However, these assumptions are based on a solid foundation of experimental evidence. It appears more probable that the observed transition is not of the relaxational type.

As the frequency dependence of the transition point is independent of the plasticization of the polymer, it must be concluded that the transition results from a change in the mode of molecular motion of the polymer molecules, such as, for example, the excitation of molecular vibrations.

[7] T. Alfrey, *Mechanical Behavior of High Polymers* (Interscience Publishers, Inc., New York, 1948), p. 79.

Letters to the Editor

On Blowing Bubbles for Bragg's Dynamic Crystal Model

CYRIL STANLEY SMITH
Institute for the Study of Metals, University of Chicago, Chicago, Illinois
April 4, 1949

BRAGG and Nye[1] have described the use of rafts of small bubbles floating on soap solution to demonstrate on a two-dimensional basis several aspects of the structure and behavior of crystals and crystalline imperfections. Their model is of great value in both instruction and research. They have shown that dislocations and grain boundaries become more apparent as the size of bubbles becomes smaller, and describe a method of blowing bubbles in a rotating cup which will give uniform bubbles as small as 0.12 mm in diameter.

There is a simpler method of blowing these small bubbles—nothing but a fine jet delivering air in the center of a nozzle through which soap solution is flowing under constant hydrostatic head. By varying the head, and consequently the velocity of the soap stream, any size of bubble over a large range can be produced with a single set-up. The double nozzle, shown in Fig. 1, is easily made even by an inexperienced glassblower in a few minutes, using a pinpoint flame for the final necking down of the air tube. Exact centering of the air jet seems to be unnecessary, and the precise dimensions are unimportant. The jet is supported, pointing downwards, about half an inch above the surface of a clear pool of soap solution in a flat dish or tray.

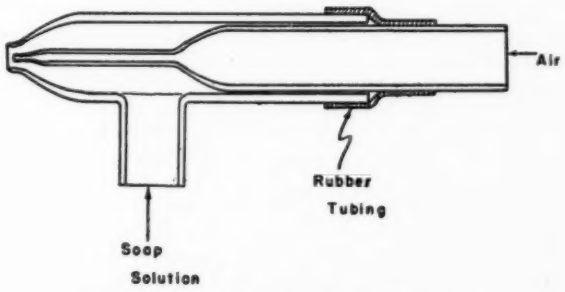

FIG. 1. Nozzle for blowing small soap bubbles.

Bubbles of 0.24-mm diameter were produced by the use of a nozzle of 0.34-mm internal diameter for the soap solution, an internal air jet of 0.085-mm internal diameter, air under pressure of 50-cm water, and soap solution under a head of 100 cm from a constant-level reservoir. Uniform bubbles of 0.31-, 0.41-, and 0.58-mm diameter were obtained at heads of 45, 20, and 9 cm, respectively. Bubbles of about 0.3-mm diameter seem to be the best for general use. The crystal rafts composed of them are barely resolvable with the naked eye, but dislocations are very conspicuous as black lines 3 to 12 mm long. The lengths of the dislocations are almost independent of the size of the bubbles, but are spread over more bubbles as the latter become smaller and "harder." On straining "crystals" made up of such bubbles, the movement of dislocations, their splitting, interaction, and occasional annihilation are very conspicuous, as are grain boundaries composed entirely of dislocations and those of more disordered structure.

The soap solution used was a mixture of 7.5 grams triethanolamine oleate (made from ethanolamine and oleic acid), 34 grams glycerine, and 58.5 grams water. The addition of some dye (phenolphtalein) gave a dark red color to the body of the solution and prevented reflections from the tank bottom.

[1] W. L. Bragg and J. F. Nye, "A dynamic model of crystal structure," Proc. Roy. Soc. 190A, 474–481 (1947).

Method of Measuring Spherical Aberration of an Electron Microscope Objective

CECIL E. HALL
Massachusetts Institute of Technology, Cambridge, Massachusetts
February 17, 1949

IT is generally recognized in electron microscopy that the displacement of a diffraction image from the in-focus paraxial image of the diffracting crystal is a function of the spherical aberration constant of the objective lens.[1,2] The effect seems not, however, to have been utilized for measuring aberration constants. The purpose of this communication is to report recent results which demonstrate that the spherical aberration constant can in fact be measured by this method when the image quality is such that paraxial focus can be determined critically. The principle involved may be illustrated by considering the case for axial illumination. Under these conditions, the relative aperture of the diffracted beam is 2θ, where θ is the Bragg angle. The product of dimensionless aberration constant, C (as defined in reference 1) and the focal length, f, is given by the equation, $Cf=r/(2\theta)^3$, where r is the displacement of the diffraction image from its position of coincidence with the paraxial image when the latter is in focus at the Gaussian plane. It is assumed that the relative aperture for paraxial imaging is small compared to twice the Bragg angle, as was the case in these experiments. A complication is introduced into the calculations when the incident illumination is not precisely axial with respect to the objective lens, but this can be taken into account. Actually, the microscope (RCA Type B) was never in perfect alignment during the tests.

The (200) diffraction images from magnesium oxide were selected for the test because they are relatively bright, frequently occurring and readily identifiable through their characteristic interference bands.[2] Twice the Bragg angle is 0.0222 radian for the 65,000-volt accelerating potential used. Test objects were prepared by collecting magnesium oxide from a burning magnesium ribbon on a standard specimen screen. At a magnification of about 20,000× the (200) images were easily selected by eye. A through-focus series was recorded, consisting of ten one-inch exposures on a standard ten-inch plate. The increments of the objective current were kept sufficiently small near focus that the relative displacements of diffraction images between exposures was about 100A referred to the object plane. True focus was selected as the setting at which the first Fresnel fringes disappear at the edges of the crystal producing the diffraction. (The lens had been compensated for asymmetries by a modification of the method devised by Hillier and Ramberg.)[3]

In a particular test, the through-focus characteristics of 13 separate diffraction images were recorded, providing a fair distribution of displacements at various azimuths throughout 360°. The displacements were plotted radiating from a common center in proper azimuth. The end points lie on the intersection at the image plane of the cone of rays whose angle with the illuminating pencil is 2θ, when the paraxial pencil is in focus. Since the illumination was not axially perfect (the illuminating pencil made an angle of about 2×10^{-3} radian with the lens axis), the figure was eccentric. The displacements were about 700A on the average and it is judged that they can be determined to within ±75A with respect to the paraxial

image. The results yielded a value of 0.56 cm for the length Cf. Since the focal length is 0.35 cm, the dimensionless constant, C, is 1.6. It is of interest to note that this same lens had been used previously for a dark-field investigation, from which it was concluded that the value of Cf must be 2 cm or less in order to account for the observed resolution in dark-field images of small crystallites.[2]

The results of these tests show that diffraction images may be used as a convenient and reasonably accurate means for measuring the spherical aberration constant of electron microscope objectives under conditions of actual use, without special equipment or alterations to the microscope. The test should be applied with some caution, however. Since the selection of paraxial focus is rather critical, errors might occur if the objective lens field is unsymmetrical or if the resolution is inferior for other reasons. A single measurement of a displacement at one azimuth could scarcely be accepted as reliable unless the alignment is perfect—and imperfect alignment seems to be the rule, rather than the exception. The measurement of displacements at several azimuths is, in fact, a critical test for the perfection of alignment. A more detailed report of these studies will appear at a later date.

[1] V. K. Zworykin, G. A. Morton, E. G. Ramberg, J. Hillier, and A. W. Vance, *Electron Optics and the Electron Microscope* (John Wiley and Sons, Inc., New York, 1945).
[2] C. E. Hall, J. App. Phys. **19**, 198 (1948).
[3] J. Hillier and E. G. Ramberg, J. App. Phys. **18**, 48 (1947).

A Note on the Maximum Height of Reflection of a Radio Wave in a Curved Ionosphere Layer

JOHN M. KELSO
Electrical Engineering Department, The Pennsylvania State College, State College, Pennsylvania
March 9, 1949

IN the course of a theoretical study of radio wave propagation in a curved ionosphere, a certain peculiarity in the reflection heights was noted. In the ionosphere a signal is reflected at various levels, the heights of which depend upon the frequency of the signal and on its angle of incidence on the layer. If the ionosphere is assumed to be composed of plane strata, theory indicates that reflections may occur at all levels up to, but not above, the level of maximum ionization. However, if the ionosphere is assumed to consist of spherical shells, there is an upper limit to the possible heights of reflection, the limit lying below the level of maximum ionization.

To show this effect, we consider Bouger's rule, as given by Mitra.[1] This equation relates the index of refraction, μ, at a point a radial distance, r, from the center of the earth, and the sine of the angle θ, the angle that a ray makes with a radial line, to the values μ_0, r_0, $\sin\theta_0$ at some specified point, such as the point of incidence on the layer. The relation is,

$$\mu r \sin\theta = \mu_0 r_0 \sin\theta_0. \tag{1}$$

If the curvature approaches zero, this equation becomes,

$$\mu \sin\theta = \mu_0 \sin\theta_0, \tag{2}$$

which is the ordinary expression of Snell's law in a plane ionosphere.

Using the notation of Hàcke,[2] we now assume that the electron density is a parabolic function of height,

$$P_1(x) = (1 - x^2/T^2). \tag{3}$$

In this expression $P_1(x)$ is the ratio of the electron density, N, at a point x, to the maximum electron density, N_m, which occurs at the point $x=0$. The quantity x is the distance of the point in question from the level where the electron density is a maximum, and since we are concerned with points below the maximum level, x is always negative. This distance is measured in "scale-units," i.e., multiplication of x by $H=kT/(mg)$,

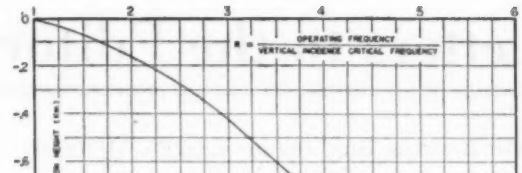

FIG. 1. The highest distance, measured in kilometers down from the level of maximum ionization, at which reflections can occur, plotted as a function of the ratio of the operating frequency to the vertical incidence critical frequency. For the special case of a layer in which $H=10$ km, and the level of maximum ionization appears at a distance of 6488.81 km from the center of the earth.

the "scale height" of the region, gives the distance in kilometers. When the parameter T is multiplied by H, we obtain the semi-thickness of the layer in kilometers.

The square of the index of refraction is then given by

$$\mu^2 = 1 - P_1(x)/R^2 \tag{4}$$

where R is the ratio of the operating frequency to the vertical incidence critical frequency.

The condition for reflection is that, at the point r_r, the ray become perpendicular to the radial direction, i.e., that $\theta=90°$, whence $\sin\theta=1$. In the plane ionosphere case, this gives the value of x_r, the height of reflection in scale units,

$$x_r = -T(1 - R^2\cos^2\theta_0)^{\frac{1}{2}}, \tag{5}$$

where a negative sign has been used because reflections cannot occur for positive values of x. This result shows that for each value of x_r in the range $-1.848 < x < 0$, there is a value of the product $R\cos\theta_0$ which will produce this x_r. Thus, reflections occur for all heights lying below the level of maximum ionization and above the bottom of the parabolic region.

If one solves for x_r in a curved ionosphere, the resulting expression is a quartic equation. Since this is rather complicated to discuss, this case will be treated by another method.

Using the value of μ from Eq. (4), and writing $r=R_0+x$, where R_0 is the radial distance from the center of the earth to the level of maximum ionization, we substitute these into Bouger's rule as given in Eq. (1). At the point of wave reflection $\sin\theta=1$, and thus we have $\mu r=$ constant, for given conditions of incidence. It will now be shown that, for a given constant, there are two values of the height x for which μr has the specified value. We do this by differentiating the product with respect to x,

$$\frac{\partial(\mu r)}{\partial x} = \frac{2x}{T^2R^2}(R_0+x)^2 + 2(R_0+x)\left(\frac{T^2R^2 - T^2 + x^2}{T^2R^2}\right). \tag{6}$$

Setting the right-hand side equal to zero, and solving for x, we obtain

$$x = \frac{-R_0}{4} + \tfrac{1}{4}(R_0^2 - 8(T^2R^2 - T^2))^{\frac{1}{2}}. \tag{7}$$

The solution with a negative sign before the square root is neglected because it leads to a value of x far outside of the ionosphere layer. Since Eq. (7) gives a negative root of $\partial(\mu r)/\partial x = 0$ for all values of R greater than unity, there is always a minimum value of the product μr corresponding to each of these values of R. This means that the product μr is a double valued function of R. The points above the level at which this minimum occurs cannot be points of reflection, because signals for which the μr product has the proper value for a reflection would already have passed through a lower

level at which μr was also such that reflection would occur there. Thus, if the signal reaches the level of maximum reflection height, x_m, it must then penetrate the region.

A numerical example has been chosen to illustrate the preceeding results. We let $R_0=6488.81$ km, and $H=10$ km. (This is an approximation to conditions in the E-layer.) Then we calculate x_m from Eq. (7), and plot the results as a function of R in Fig. 1. In this figure, x_m is shown in kilometers, rather than in scale units.

Although the results obtained here can be obtained numerically from the exact Chapman relation,[3] on which the parabolic approximation used in Eq. (3) is based, the parabolic approximation gives results which are very close to the exact case, and which can conveniently be expressed in closed form.

This work has been taken from a more extensive study which is to be submitted for publication in the near future. The work has been done at the Radio Propagation Laboratory of The Pennsylvania State College with the support of the Geophysical Research Directorate of the Cambridge Field Station, AMC U. S. Air Force.

[1] S. K. Mitra, *The Upper Atmosphere* (Calcutta, 1947).
[2] J. E. Hacke, Jr., Proc. I.R.E. **36**, 724 (1948).
[3] S. Chapman, Proc. Phys. Soc. **43**, 26 (1931).

Tensor Field Equations in a Region of Variable Refractive Index

P. D. P. Smith
Westmount, Quebec, Canada
February 21, 1949

FOR problems in electromagnetic theory and communications, the dielectric constant and magnetic permeability, ϵ and μ, are usually specified functions of the coordinates and time.

Since the tensor form of the field equation is most readily adapted to different systems of coordinates, it would appear useful to have Maxwell's equations in tensor form suitable for use in a region of varying μ and ϵ.

The equations in vector notation are

$$\begin{cases} \mathbf{U}=\text{curl}\mathbf{H}-\dot{\mathbf{D}}, \\ 0=\text{curl}\mathbf{E}+\mathbf{B}, \end{cases} \tag{1}$$

$$\begin{cases} \mathbf{D}=\epsilon\mathbf{E}, \\ \mathbf{B}=\mu\mathbf{H}. \end{cases} \tag{2}$$

Corresponding to (1) in tensor form are

$$F^{ij}=\partial_j F^{ij}, \quad 0=\partial_i\varphi_{jk}+\partial_j\varphi_{ki}+\partial_k\varphi_{ij}. \tag{3}$$

For a metric, the square of the "radar" distance between two events can be used, which in orthogonal coordinates is

$$ds^2=g_{ij}dx^i dx^j=c^2dt^2/\mu\epsilon-\alpha^2dx^{1^2}-\beta^2dx^{2^2}-\gamma^2dx^{3^2}. \tag{4}$$

The quantity $g^{\frac{1}{2}}=|g_{ij}|^{\frac{1}{2}}\alpha\beta\gamma/(\mu\epsilon)^{\frac{1}{2}}$ and $g_{11}=-\alpha^2$, $g_{22}=-\beta^2$, $g_{33}=-\gamma^2$ and $g_{44}=1/\mu\epsilon$ with $x^4=ict$. If the usual relation

$$F^{ij}=g^{\frac{1}{2}}\varphi^{ij} \tag{5}$$

is used in (3), then taking

$$\varphi_{23}=\beta\gamma B_1, \quad \varphi_{41}=i\alpha E_1$$

leads to

$$(\epsilon/\mu)^{\frac{1}{2}}F^1/\beta\gamma=\text{curl}_1\mathbf{H}-(\epsilon/\mu)^{\frac{1}{2}}\cdot 1/\beta\gamma c\cdot\frac{\partial}{\partial t}\{(\epsilon/\mu)^{\frac{1}{2}}\beta\gamma D_1\} -[\mathbf{H}\times\text{grad}\log(\mu/\epsilon)^{\frac{1}{2}}]_1 \tag{6}$$

which is unsatisfactory. The first equation in (3) is still valid if (5) is replaced by

$$F^{ij}=g^{\frac{1}{2}}\cdot(\epsilon/\mu)^{\frac{1}{2}}\varphi^{ij} \tag{7}$$

since $(\epsilon/\mu)^{\frac{1}{2}}$ is a scalar. In this case the following identifications can be used:

$$\varphi_{23}=\beta\gamma B_1, \quad \varphi_{41}=i\alpha E_1, \quad F^{23}=\alpha H_1, \quad F^{41}=i\beta\gamma D_1, \quad \text{etc.} \tag{8}$$

Also,

$$F^i=g^{\frac{1}{2}}\rho\frac{dx^i}{ds}=\alpha\beta\gamma\rho\dot{x}^i/c(1-v^2/v_0^2)^{\frac{1}{2}}$$

where $v_0=c/(\mu\epsilon)^{\frac{1}{2}}$.

The first equation in (3) now gives

$$\rho\alpha\dot{x}^1/c(1-v^2/v_0^2)^{\frac{1}{2}} =1/\beta\gamma\{\partial_2(\gamma H_3)-\partial_3(\beta H_2)\}-1/\beta\gamma\frac{\partial}{\partial t}\{\beta\gamma D_1\} \tag{9}$$

which is the same as the first equation of (1) when β and γ do not vary with time. The equation

$$\rho/(1-v^2/v_0^2)^{\frac{1}{2}}=1/\alpha\beta\gamma\cdot\partial_1\{\beta\gamma D_1\}+\,+\,=\text{div}\mathbf{D}$$

also follows from (8) and (3).

Thus Maxwell's equations for a region of varying μ and ϵ are given by (3) and (7), and the terms may be identified from (8) for any system of normal orthogonal coordinates.

Comments on Biconical Antennas

P. D. P. Smith
Westmount, Quebec, Canada
February 21, 1949

IN an interesting paper, Tai has applied my formulation of the biconical dipole problem to calculate the impedance to a higher approximation for the special case of small cone angles. With regard to his comment "Smith's approximate expression, $(y_t)_1$[2], is actually not a very good one, at least for small-angle cones,"[1] I would like to point out that in the range of $\beta l\leq 1.6$ in which I was interested, the real part of my expression is virtually identical with Tai's best approximation, and the imaginary part differs by less than 5 percent. I further believe that there is good evidence that the higher order waves become less important with increasing cone angle,[2] although they are very important for thin dipoles, so that my approximation will improve as the cone angle increases.

Tai's results show that my approximation should be limited to dipoles for which $\beta l\leq 2$, but I feel that his statement might lead to misconception.

In his second to last paragraph he remarks, "For those antennas whose angles are not small, Smith's approximation is not a very good one." It seems that one of the "nots" is a misprint.

[1] C. T. Tai, J. App. Phys. **19**, 1158 (1948).
[2] P. D. P. Smith, J. App. Phys. **19**, 19 (1948).

The Formation of Recrystallization Nuclei

Paul A. Beck*
University of Notre Dame, South Bend, Indiana
March 14, 1949

IN his paper on "Das Wesen der Rekristallisationskeime"[1] van Arkel critically reviewed the older "high stress point" and "low stress point" theories of the formation of recrystallization nuclei, and concluded that neither one is satisfactory. The "low stress point" theory of recrystallization nuclei must be incorrect because it is difficult to conceive of an increase in the number of low stress points with increasing deformation; thus this theory cannot account for the increasing number of nuclei with increasing deformation. On the other hand van Arkel's results showed that, even after a moderate amount of deformation, a crystal loses its tendency to grow at the expense of its more severely deformed neighbors. Thus, it is unlikely that highly stressed regions in the metal may act as

nuclei. Van Arkel developed a theory, originally suggested by van Liempt, which combines the advantages of both former conceptions, without their disadvantages. According to the van Liempt–van Arkel theory the high stress points in a deformed metal are potential locations of nuclei. But this theory assumes that, in order to actually become active as a nucleus, a high stress point first has to transform spontaneously into a relatively stress-free lattice portion, which is then capable of growing. This theory will account for the increase of the number of nuclei with increasing deformation and avoids the difficulty of having to assume the growth of unstable deformed lattice regions. The only difficulty with this conception has been that no definite picture could be devised for the spontaneous transformation of small highly stressed lattice regions into unstressed ones. Van Arkel himself did not make any attempt to develop a more detailed mechanism for this rather critical part of the process.

Recently E. Orovan and R. F. Cahn[2] discovered the process designated by them as "polygonization." This process allows the transformation of an elastically bent crystal lattice into a polygon-shaped structure in which sections of stress-free "straight" lattice are separated by regions with high concentration of dislocations. It appears that energy is gained if the elastic stress, which is distributed fairly evenly over a relatively large lattice region of the bent metal crystal, is removed by the section-wise straightening process. The work of Guinier and Lacombe[3] indicates that these regions of high dislocation concentration are identical with the "sub-boundaries," previously discovered by Lacombe.[4] According to Cahn, the time necessary for polygonization at a certain annealing temperature is shorter (the dislocations diffuse faster) if the elastic stresses are greater.

It is rather tempting to make the assumption that polygonization constitutes the missing link in the van Liempt–van Arkel theory of the formation of recrystallization nuclei. Certainly, polygonization is a mechanism by which stressed lattice regions may transform into stress-free sections. The local stresses in a deformed metal vary between wide limits. The most severely stressed lattice regions are likely to occur near grain boundaries and slip zones. During the annealing process, the regions of highest stress will be first to undergo polygonization. At this early stage many of the polygonized, relatively stress-free lattice regions are directly adjacent to relatively highly stressed lattice regions which did not as yet undergo polygonization. The former will then have a tendency to grow into the latter by a process of ordinary boundary migration, as distinct from polygonization. Energy is gained by the transfer of atoms across the grain boundary from the stressed lattice region into the unstressed one. For any given stressed lattice region, the question whether it will become stress free by polygonization or by being absorbed by a growing stress-free grain by means of boundary migration, will depend on the length of the incubation period necessary for polygonization to take place at this point and on the occurrence in its neighborhood during this period of a growing stress-free grain. A high stress point, which became stress-free by polygonization, is capable of growing, provided that it is surrounded by lattice regions which at that time still contain sufficient stress energy to compensate for the increase in surface energy resulting from the growth of the stress-free nucleus. As stated by W. G. Burgers,[5] a further condition apparently necessary for the fast growth of a nucleus is that it should have a favorable lattice orientation with respect to the average orientation of its environment. The number of nuclei formed per unit volume and unit time at a certain instant will then depend on the number of high stress points just completing polygonization at that time, for which the various conditions for growth by boundary migration are favorable.

It was found by Kornfeld[6] that there exists a definite incubation period at the beginning of the recrystallization process during which no nuclei are formed. Mehl and his collaborators[7,8] discovered that, even after nucleation has started, the rate of nucleation is at first relatively low, but that it increases exponentially with the annealing time. Anderson and Mehl[8] mentioned the possibility that the increasing rate of nucleation may be a result of action at a distance emanating from the new grains already formed, and activating new nuclei in other parts of the metal. However, they regarded this suggestion themselves with apparent misgivings. Later Burgers[9] attempted to explain the increasing rate of nucleation by assuming the "stimulation" of potential nuclei by the advancing boundary of a recrystallized grain. This hypothesis would require, however, that the new grains would form in direct contact with some other ones already existing. It is well known and clearly seen in the photographs published by Stanley and Mehl[7] that this is relatively seldom the case. Most new grains appear to grow from nuclei distinctly separated from the grains already growing. Both of these views are rather unsatisfactory and inadequate to explain the increasing rate of nucleation with annealing time. The hypothesis of nucleation by polygonization, as discussed above, can explain the increase in the rate of nucleation if the further assumption is made that the number of favorable lattice regions with the highest stress content (and, therefore, the first to become active) is relatively small and that the number of lattice regions with decreasing stress energy is progressively larger. If the length of annealing time required for polygonization at any given point is determined by the stress level at that point, then the stress distribution in the cold-worked metal corresponds to a three-dimensional timetable, where each lattice region is assigned a definite incubation period for polygonization, depending upon the local stress. Consequently, the assumed increasing frequency of occurrence of lattice regions with decreasing stress levels is translated into an increasing rate of nucleation after longer annealing periods. The idea of explaining the increasing rate of nucleation by assigning an incubation period to each point of potential nucleation, and by assuming a certain distribution of these incubation periods, was briefly suggested in 1942.[10]

* Associate Professor of Metallurgy.
[1] A. E. van Arkel, Zeits. Metalle **22**, 217 (1930).
[2] R. F. Cahn, in a *Report of a Conference on the Strength of Solids* (The Physical Society Bristol, July, 1947), p. 136.
[3] A. Guinier and P. Lacombe, "L'etat 'polygonise' du cristal metallique," Metaux et Corrosion **23**, 212 (1948).
[4] Paul Lacombe and Louis Beaujard, J. Inst.Metals **74**, 1 (1947).
[5] W. G. Burgers, Physica **9**, 987 (1942).
[6] M. Kornfeld and F. Sawizki, Physik. Zeits. Sovietunion **8**, 528 (1935).
[7] J. K. Stanley and R. F. Mehl, Trans. A.I.M.E. **150**, 260 (1942).
[8] W. A. Anderson and R. F. Mehl, Trans. A.I.M.E. **161**, 140 (1945).
[9] W. G. Burgers, Nature **160**, 398 (1947).
[10] Discussion of reference 7 by P. A. Beck.

Notes on "Wave Guides for Slow Waves"*

W. WALKINSHAW
Atomic Energy Research Establishment, Malvern, England
February 3, 1949

THE writer wishes to point out that the solution of the wave equations given by Professor Brillouin in his paper is of limited application and that a more general solution of the problem may be made. The circular corrugated guide is taken as an example since this is of interest in the design of electron accelerators.

The limitation arises because of the approximations which are made in deriving the solution. Applying Brillouin's analysis to the above case the following relationship between frequency, phase velocity and guide dimensions is obtained[1,2]

$$\frac{F_1(ka)}{F_0(ka)}=\frac{k}{\chi}\frac{J_1(\chi a)}{J_0(\chi a)} \qquad (1)$$

where

$$\begin{cases} F_0(ka)=J_0(ka)Y_0(kb)-Y_0(ka)J_0(kb) \\ F_1(ka)=J_1(ka)Y_0(kb)-Y_1(ka)J_0(kb) \end{cases} \quad (2)$$

$k=2\pi/$free space wave-length, $\beta=2\pi/$guide wave-length, $\chi^2=k^2-\beta^2$, $a=$radius of iris, $b=$radius of wave guide. Thus $b-a=$slot depth.

This solution is obtained on the assumption that the wall thickness of the slots is negligible and that the slot width is small compared with the guide wave-length. For most cases of practical interest these conditions are not fulfilled sufficiently well for the above result to give the relationship between phase velocity and guide dimensions to the accuracy required.

A substantial improvement in accuracy may be obtained by the following analysis. We derive the fields inside the slots and in the axial region of the guide by the same method which is clearly discussed by Brillouin. We differ from the latter in the method of matching these fields at the mouths of the slots. Whereas Brillouin has not taken the secondary waves into account in improving the accuracy of the frequency Eq. (1), the present method leads to an infinite determinant which is an accurate solution of the problem. (*a*) From the expansion for the fields inside the slots, we get the following expressions for the tangential components at the slot mouth ($r=a$)

$$\begin{cases} E_z=\sum_0^\infty B_s\cos\frac{2\pi s}{d}z+\sum_1^\infty D_s\sin\frac{2s-1}{d}\pi z \quad \text{for} \quad |z|<\frac{d}{2}=0 \quad (3) \\ \text{for}\frac{d}{2}<|z|<\frac{D}{2} \\ Z_0H_\phi=\sum_0^\infty iB_s\frac{k}{\Gamma_s}\frac{F_1(\Gamma_s a)}{F_0(\Gamma_s a)}\cos\frac{2\pi s}{d}z \\ \qquad +\sum_1^\infty iD_s\frac{k}{\Gamma_s}\frac{F_1(\Gamma_s a)}{F_0(\Gamma_s a)}\sin\frac{2s-1}{d}\pi z \quad (4) \end{cases}$$

where

$$\begin{aligned} \Gamma_s^2&=k^2-\left(\frac{2\pi s}{d}\right)^2 \quad \text{for cos terms} \\ &=k^2-\left(\frac{2s-1}{d}\pi\right)^2 \quad \text{for sin terms,} \end{aligned} \quad (5)$$

d is the slot width and D is the pitch of the periodic structure leaving a wall thickness $(D-d)$ between slots, over which the boundary condition requires the tangential electric field to vanish. The origin of the z axis has been taken at the center of the slot and the field expressions above refer to the slot at the origin. The fields for the slot with center at $z=nD$ are obtained by multiplying the above expressions by $\exp(-i\beta_0 nD)$ where $\beta_0 D$ is the phase change per slot along the guide.

(*b*) From the expansion for the fields in the axial region of the guide, the tangential components at the slot mouths ($r=a$) are[2]

$$\begin{cases} E_z=\sum_{-\infty}^\infty A_m\exp[-i\beta_m z] \quad (6) \\ Z_0H_\phi=\sum_{-\infty}^\infty\frac{ik}{\chi_m}A_m\frac{J_1(\chi_m a)}{J_0(\chi_m a)}\exp[-i\beta_m z] \quad (7) \end{cases}$$

where

$$\begin{cases} \beta_m D=\beta_0 D+2\pi m \\ \chi_m^2=k^2-\beta_m^2 \\ \beta_0=2\pi/\text{guide wave-length.} \end{cases}$$

The fields given by (3) and (4) must now be matched to the fields given by (6) and (7). From the electric fields, by multiplying (3) and (6) by $\cos\frac{2\pi s}{d}z$ and then by $\sin\frac{2s-1}{d}\pi z$ respectively and integrating over the region $|z|<D/2$, we get the following relationships between the coefficients

$$\left.\begin{aligned} B_0 d&=\sum_{-\infty}^\infty A_m C_{0m} \\ \tfrac{1}{2}B_s d&=\sum_{-\infty}^\infty A_m C_{sm} \\ \tfrac{1}{2}D_s d&=\sum_{-\infty}^\infty A_m S_{sm} \end{aligned}\right\} \quad (8)$$

where

$$C_{sm}=\int_{-D/2}^{D/2}\cos\frac{2\pi s}{d}z\exp[-i\beta_m z]dz \quad (9)$$

$$S_{sm}=\int_{-D/2}^{D/2}\sin\frac{2s-1}{d}\pi z\exp[-i\beta_m z]dz. \quad (10)$$

The magnetic fields given by (4) and (7) are now treated in a similar manner but in this case the integrations are carried out over the range $|z|<d/2$. On the metal wall, the field given by (7) will be automatically matched by the induced surface current. Thus we get after substituting for B_s and D_s from (8), the following infinite set of linear equations for the coefficient A_m

$$\sum_{-\infty}^\infty A_m\left[\frac{k}{\Gamma_s}\frac{F_1(\Gamma_s a)}{F_0(\Gamma_s a)}C_{sm}-\frac{k}{\chi_m}\frac{J_1(\chi_m a)}{J_0(\chi_m a)}C'_{sm}\right]=0 \quad (11)$$

$$\sum_{-\infty}^\infty A_m\left[\frac{k}{\Gamma_s}\frac{F_1(\Gamma_s a)}{F_0(\Gamma_s a)}S_{sm}-\frac{k}{\chi_m}\frac{J_1(\chi_m a)}{J_0(\chi_m a)}S'_{sm}\right]=0. \quad (12)$$

In which C'_{sm} and S'_{sm} are given by (9) and (10) by replacing D by d. Integration of (9) and (10) gives

$$\begin{cases} C_{sm}=D\left[\dfrac{\sin\left(\beta_m+\frac{2\pi s}{d}\right)\frac{D}{2}}{\left(\beta_m+\frac{2\pi s}{d}\right)D}+\dfrac{\sin\left(\beta_m-\frac{2\pi s}{d}\right)\frac{D}{2}}{\left(\beta_m-\frac{2\pi s}{d}\right)D}\right] \quad (13) \\ S_{sm}=iD\left[\dfrac{\sin\left(\beta_m+\frac{2s-1}{d}\pi\right)\frac{D}{2}}{\left(\beta_m+\frac{2s-1}{d}\pi\right)D}-\dfrac{\sin\left(\beta_m-\frac{2s-1}{d}\pi\right)\frac{D}{2}}{\left(\beta_m-\frac{2s-1}{d}\pi\right)D}\right]. \quad (14) \end{cases}$$

The coefficients of A_m in (11) and (12) form an infinite determinant which must be zero, these giving an accurate expression for the frequency equation.

When the argument of the Bessel functions are imaginary it is convenient to replace (2) by

$$\begin{aligned} F_0(\Gamma_s a)&=K_0(\gamma_s b)I_0(\gamma_s a)-I_0(\gamma_s b)K_0(\gamma_s a) \\ F_1(\Gamma_s a)&=K_0(\gamma_s b)I_1(\gamma_s a)+I_0(\gamma_s b)K_1(\gamma_s a) \end{aligned}$$

where

$$\gamma_s^2=-\Gamma_s^2.$$

By using three rows and columns of the determinant ($m=0$, -1, $+1$, $S=0,1$ from (11), $S=1$ from (12)), agreement (see Table I) has been found with measured values[3] for guides having five slots per free space wave-length.

TABLE I.

	a	b	λ_g	(Measured)	(Theoretical)
Guide I (iv)	1 cm	3.894 cm	10	*9.968 cm	9.980
Guide II (v)	1.5 cm	4.002 cm	10	*9.915 cm	9.915
Guide III (vi)	2 cm	4.171 cm	10	**9.820 cm	9.810

* From 3 row determinant.
** From 4 row determinant.

[1] L. Brillouin, J. App. Phys. **19**, 1023 (1948).
[2] E. L. Chu and W. W. Hansen, J. App. Phys. **18**, 996 (1947).
[3] W. Walkinshaw, Proc. Phys. Soc. **61**, 246 (1948).
[3] Mullett and Loach, Proc. Phys. Soc. **61**, 271 (1948).

Ground Plane Field of the Wide Angle Conical Dipole

P. D. P. Smith
Montreal, Quebec
February 14, 1949

As part of a program of calculating the field patterns of a wide angle conical dipole, formula (4) has been deduced. It is intended merely as a preliminary estimate.

By making certain assumptions, it is possible to obtain a simple formula for the ground plane* field of a wide angle conical dipole. This work follows from that of another paper, *The Conical Dipole of Wide Angle*,[1] and symbols defined in that paper will be used here with the same meaning.

The field strength on the ground plane, at a great distance r_0 from the apex of the dipole, is

$$E_s = -j30e^{-i\beta r_0}/r_0) \int_{-l}^{+l} J_0(\beta r \sin\theta) \cdot I(z) \cdot d(\beta z), \qquad (1)$$

where $I(z)$ is the current passing a horizontal plane, z=constant. The factor $J_0(\beta r \sin\theta)$ appears because all parts of a ring element of current are not equidistant from the measuring point.

The current terms are calculated from their corresponding waves by the relation

$$I = \int_0^{2\pi} H_\phi \cdot r \sin\theta \cdot d\phi.$$

The following assumptions are then introduced:

(1) On the cones, only the principal and first higher order current terms need be considered.

(2) On the spherical caps, only the first, ($k=1$), term need be considered.

(3) For the small values of βr involved,

$$(\beta r)^{\frac{1}{2}} J_{n+\frac{1}{2}}(\beta r) \propto (\beta r)^{n+1}. \qquad (\beta r \leq 2),$$

(4) The term $J_0(\beta r \sin\theta)$ can be replaced by $J_0(\frac{3}{4}\beta l \sin A)$. This is equivalent to assuming the same currents are flowing on a cylinder of radius $\frac{3}{4}l \sin A$.

From assumptions (1) to (3), and from formulas (3), (4), and the equation for the magnetic field of the principal waves on page 12 of reference 1, the current on the cones becomes

$$I = (P/K^2 g_t)^{\frac{1}{2}} \cdot \{Ky_t \cdot \cos\beta(r-l) - j \cdot \sin\beta(r-l) + K^2 y_t/60 \cdot (r/l)^{n+1} \cdot ((2n+1)\sin^2 A (dn/d\mu_1)/(n^2+n-2)(n^2+n))\}, \qquad (2)$$

while on the spherical end caps the current is

$$I_e = (P/K^2 g_t)^{\frac{1}{2}} (K^2 y_t/120)(\sin^2\theta/\cos A). \qquad (3)$$

To obtain (3) use is made of the equations appearing between (7) and (8) of reference 1. The factor $(P/K^2 g_t)^{\frac{1}{2}}$ is introduced to make the total radiated power P watts. K is the characteristic impedance of a bi-conical transmission line of semi-angle A, and $y_t = g_t + jb_t$ is the effective admittance terminating this line at a radius l, as described on pages 11 and 12 of reference 1.

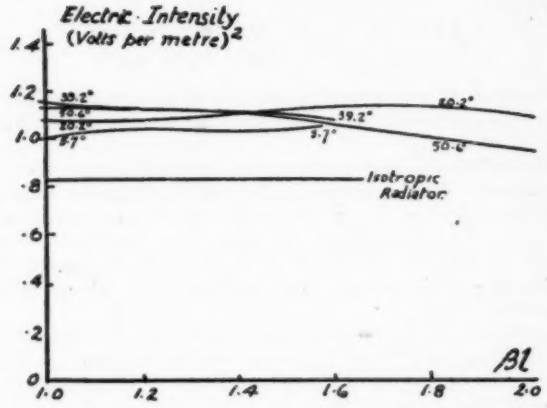

FIG. 1.

Using (2) and (3) in (1) gives, with assumption (4),

$$E_s = -j \cdot 60/r_0 \cdot e^{-i\beta r_0} \cdot (P/K^2 g_t)^{\frac{1}{2}} \cdot J_0(\tfrac{3}{4}\beta l \sin A) \times [Ky_t \chi + j\mu_1(1-\cos\beta l)].$$

$$\chi = \mu_1 \sin\beta l + \beta l[\mu_1 K/60 \cdot ((2n+1)\sin^2 A (dn/d\mu_1)/(n^2+n)(n^2+n-2)(n+2)) + K\psi/120],$$

$$\psi = \{(1-\mu_1) - \tfrac{1}{3}(1-\mu_1^3)\}/\mu_1. \qquad (4)$$

n and $(-\sin^2 A (dn/d\mu_1))$ are given in Fig. 3 of reference 1 as functions of $(\mu_1 = \cos A)$.

It is difficult to set an upper limit to the error in this approximation, but there is a difference between the currents from formulae (2) and (3) at the rim of the caps ($\theta = A$, $r = l$). This difference varies from 10 percent to 20 percent of the principal wave current, so errors are presumably of this order of magnitude, combined with the errors inherent in assumption (4).

Figure 1 shows values of $|E|^2$ on the ground plane, calculated from (4) for semi-angles of 5.7°, 20.2°, 39.2°, and 50.6°. They are substantially constant over this range of βl, with a slight tendency to drop at large values of $l \sin A$, due to the factor $J_0(\frac{3}{4}\beta l \sin A)$. These intensities are calculated for a 27.7 kilowatt source at a distance of 1000 meters from the dipole. Because the impedance rises rapidly at small cone angles, the intensity from a 5.7° dipole is considerably below that of a thin wire dipole. At larger cone angles this effect is offset by the end loading of the spherical caps.

* By ground plane is meant that plane in which one pole is the mirror image of the other.

[1] P. D. P. Smith, J. App. Phys. **19**, 11–23 (1948).